Changes of the tropical tropopause layer in reanalysis and climate model data

Dissertation

zur Erlangung des Doktorgrades

an der Mathematisch-Naturwissenschaftliche Fakultät

der Christian-Albrechts-Universität zu Kiel

vorgelegt von

Viktoria Mohr

Helmholtz-Zentrum für Ozeanforschung Kiel
Forschungsbereich 1
– Maritime Meteorologie –

Kiel, September 2013

Erster Gutachter: Prof. Dr. Douglas Maraun

Zweiter Gutachter: Dr. Kirstin Krüger

Tag der mündlichen Prüfung: 28.11.2013

Zum Druck genehmigt: 28.11.2013

gez.:

Abstract

The main entrance region for trace gases which are emitted in the troposphere reaching the stratosphere, is the tropical tropopause layer (TTL). Chemical and dynamical processes within the TTL control the amount of trace gases entering the stratosphere.
In this study a Lagrangian analysis of the upper TTL is presented, using backward trajectory calculations with a kinematic method. The Lagrangian approach is applied in order to determine the main entrainment regions of air masses into the stratosphere - the Lagrangian cold points (LCP)- with the new reanalysis product ERA Interim. Further, it is evaluated how well climate models are able to reflect the basic LCP temperature and distribution. Additionally, future simulations are analyzed in order to understand the evolution of the TTL in a changing climate. This calculation is carried out employing ERA Interim data for the period 1979-2011 and different CCMs from CCMVal-2 and one model from the CMIP5 project, analyzing one decade in the past (1990s) and two decades in the future (2040s and 2090s).
As shown by ERA Interim, the main air mass entrainment is located over the tropical West Pacific, where more than 50% of the air masses enter the stratosphere on annual average. Generally, the analyzed climate models are able to capture this main entrance region for stratospheric air masses. Further, it is shown that also other convective regions, like South America, West Africa and the Indian Ocean play a larger role as entrainment regions in the reanalysis and the climate models compared to previous studies. During NH winter the West Pacific becomes even more important as entrance region for air masses to the stratosphere (62%), which is also simulated by most of the climate models.
A new diagnostic method for analyzing the impact of the tropical widening on the upper TTL is presented in this thesis. By analyzing the meridional extension of the LCPs a significant broadening of the upper TTL is detected by ERA Interim of 1.2° lat/dec on the annual average between 1979-2011, indicating an increase of air mass entrainment into the stratosphere. However, the broadening of the upper TTL revealed larger transitions prior to the year 2000 than afterwards, possibly due to changes in the stratospheric circulations at the same time. Most of the climate models reveal a slight positive change of the width of the upper TTL as well for the time period 1990-1999, though the results are not significant. For the future scenarios the climate models project an increase of the LCP temperature around 1 K from the 1990s to the 2090s. Additionally, by determining the spatial evolution of the LCP occurrence, all climate models agree with each other by projecting an increase of the air mass entrainment over the West Pacific by 2% to 8% annually averaged. Simultaneously, a slight broadening of the upper TTL within the whole tropics and in particular over

the main entrance region, the West Pacific is projected by the climate models on the annual average. These results suggest that the role of the tropical West Pacific as main entrance region for air masses into the stratosphere will be even more pronounced in a changing climate.

Zusammenfassung

Der Haupteintragungsort für Spurengase, die in der Troposphäre emittiert werden und bis hinauf in die Stratosphäre gelangen, ist die tropische Tropopausenschicht (TTL). Chemische und dynamische Prozesse innerhalb dieser Schicht kontrollieren den Anteil an Spurengasen, die tatsächlich in die Stratosphäre transportiert werden.
In dieser Arbeit wird mithilfe von Rückwärtstrajektorien eine Lagrange Untersuchung der oberen TTL durchgeführt, die auf der kinematischen Methode basiert. Diese Lagrange Näherung dient dazu den Haupteintragungsort von Luftmassen in die Stratosphäre, der durch den Lagrangen Kältepunkt (LCP) bestimmt wird, anhand des neuen Reanalyseproduktes ERA Interim zu ermitteln. Desweiteren werden unterschiedliche Chemie Klimamodelle (CCM) in Bezug auf ihre grundsätzliche Darstellung der LCP Temperatur und Verteilung evaluiert. Zukunftssimulationen werden ausgewertet, um die Entwicklung der Eigenschaften der TTL in einem sich ändernden Klima zu untersuchen. Unter Anwendung des ERA Interim Datensatzes (1979-2011) und unterschiedlichen CCMVal-2 CCMs und einem Modell des CMIP5 Projektes, werden diese Berechnungen für ein Jahrzehnt in der Vergangenheit (1990er Jahre) und zwei Jahrzehnte in der Zukunft (2040er und 2090er Jahre) durchgeführt. Basierend auf den Ergebnissen von ERA Interim, befindet sich der Haupteintragungsort für Luftmassen über dem tropischen West Pazifik, wo mehr als 50% der Luftmassen im Jahresmittel die Stratosphäre erreichen. Generell sind die unterschiedlichen CCMs fähig diesen Haupteintragungsort für Luftmassen wiederzugeben. Weiter wird gezeigt, dass auch andere konvektiv dominierte Regionen neben dem West Pazifik, wie Süd Amerika, das Westliche Afrika und der Indische Ozean zwar eine untergeordnete Rolle als Haupteintragungsort für Luftmassen in die Stratosphähre spielen, sich hier jedoch im Vergleich zu früheren Studien stärker hervorheben. Während des norhemisphärischen Winters wird dem West Pazifik eine noch ausgeprägtere Rolle als Haupteintragungsort für Luftmassen in die Stratosphäre zuteil, welcher auch von den Klimamodellen wiedergegeben wird.
Um die Verbreiterung der oberen TTL zu untersuchen, wird in dieser Arbeit ein neues Diagnoseverfahren vorgestellt. Indem die meridionale Ausbreitung der LCPs untersucht wird, kann man eine signifikante Verbreiterung der oberen TTL von 1.2° Breitengrad pro Dekade, basierend auf ERA Interim von 1979-2010, feststellen, welche eine Zunahme des Luftmassentransportes in die Stratosphäre andeutet. Die Verbreiterung der oberen TTL weist jedoch eine stärkere Zunahme vor dem Jahr 2000 auf als in den Jahren danach, was möglicherweise auf Änderungen in der stratosphärischen Zirkulation in dieser Zeit zurückzuführen ist. Die meisten der Klimamodelle lassen eine positive Änderung der Breite der oberen TTL zwischen 1990 und 1999 erkennen, jedoch sind die Ergebnisse nicht signifikant.

Die Zukunftssimulationen zeigen eine Zunahme zwischen den 1990er und 2090er Jahren der gemittelten LCP Temperatur von 1 K auf. Ferner stellte sich bei allen Klimamodellen bei Betrachtung der LCP Häufigkeit eine Zunahme des Luftmasseneintrages über dem West Pazifik um 2% bis 8% von den 1990er bis 2090er Jahren heraus. Gleichzeitig wurde eine schwache Verbreiterung der oberen TTL im gesamten tropischen Bereich im Jahresmittel insbesondere über dem Haupteintragungsort für Luftmassen, dem West Pazifik, von den Klimamodellen projiziert. Diese Ergebnisse deuten an, dass die Rolle des tropischen West Pazifiks als Haupteintragungsregion für Luftmassen in einem sich ändernden Klima noch an Bedeutung dazugewinnen wird.

Contents

Chapter 1

Introduction

The tropical tropopause layer (TTL) is the transition region between the tropical troposphere and stratosphere, ranging from approximately 14 to 18.5 km and is laterally bounded by the sub-tropical jets at around 30° (Fueglistaler et al., 2009). It is the main entrance region for all trace gases being transported from the troposphere to the stratosphere, among them water vapor and halogenated Very Short Lived Substances (VSLS). VSLS are defined as trace gases with atmospheric lifetimes less than six months. The last years brought the discovery of VSLS significantly contributing to the stratospheric ozone depletion, in addition to the long-lived ozone depleting substances (ODS) like chlorofluorocarbons (CFCs), (e.g WMO, 2003; Salawitch et al., 2005; WMO, 2007). VSLS are mainly of natural origin and have, by definition, atmospheric lifetimes shorter than 6 months. When chemically active trace gases enter the stratosphere through the TTL, their concentration is controlled by the dynamical and chemical processes within this layer. But also a change of the meridional extension of the TTL, hence the entrance region, could have a large impact on the amount of trace gases that can enter the stratosphere from below. It is crucial to a better understanding of key processes in the TTL in order to improve predictions of the stratospheric chemical composition in a changing climate.
Trace gases, which are emitted from the Earth's surface and the oceans, can reach the TTL through upward transport by tropical deep convection until they reach the TTL. Once they reach the level of zero radiative heating (LZRH), the ascending branch of the Brewer-Dobson Circulation (BDC) carries them further upward into the stratosphere. The short and long-term variability of trace gases, are linked to the variability of the minimum temperature in the upper TTL, the so-called cold point tropopause (CPT) (Randel et al., 2004). Only these temperatures are low enough to allow dehydration of the moist tropospheric air to the observed low values of water vapor in the stratosphere (Brewer, 1949).

Recently, a widening of the tropical belt was identified by several studies, which are mainly based on observations of different atmospheric characteristics within the troposphere (e.g. Seidel et al., 2008; Davis and Rosenlof, 2012). The tropical belt is meteorologicaly defined via the large scale atmospheric circulation systems like the position of the jet streams and the Hadley circulation (Fueglistaler et al., 2009). Changes in the Hadley cell and the BDC in turn could effect the meridional extent of the TTL, which is also reflected by changes

in the mid-latitude storm tracks (Gettelman et al., 2009). Changes in the tropical width, associated with a displacement of atmospheric circulation systems like the Hadley cell, would also alter the structure and the transport in the TTL (Fueglistaler and Haynes, 2005). Most of the previous studies use atmospheric features of the troposphere to identify a change in the tropical borders. In contrast, this study uses transport characteristics in the upper TTL, which is stratospheric influenced, to analyze whether the upper TTL reflects a broadening of the tropical belt as well.

The cause for the change of the tropical belt was analyzed by Lu et al. (2009) using reanalysis data and two GFDL model simulations. One simulation is forced by observed sea surface temperatures (SSTs) and sea ice, the other is additionally forced by estimated radiative forcing from natural (solar and volcanic aerosol) and anthropogenic sources (well-mixed greenhouse gases GHG, tropospheric and stratospheric ozone, and tropospheric aerosols). They use the frequency of high tropopause days to define tropical borders. Although the model indicates a weaker broadening compared to observations, the authors attributed this change to direct radiative forcing from natural and anthropogenic sources. Chemistry Climate model (CCM) simulations based on future atmospheric scenarios under the influence of GHGs and CFCs, suggest a warming and a lifting of the cold point tropopause until the end of the 21st century (Gettelman et al., 2010). Based on future simulations from Coupled Model Intercomparison Project Phase 5 (CMIP5), Hu et al. (2013) analyzed a poleward shift of the Hadley circulation indicating a broadening of the tropical belt until the end of the 21st century.

This study aims to investigate transport processes in the upper TTL and a possible widening of this region in past, present and future climate. A Lagrangian transport model, which is applied in this study, is a useful tool to investigate the question of possible transport changes in the TTL. Trajectories obtained from Lagrangian model studies can be used to analyze the individual pathways, the density and the temperature history of air parcels. The Lagrangian cold point (LCP), the lowest temperature of a trajectory, is the so-called "dry point" controlling the amount of water vapor that can reach the stratosphere. Since no washout occurs above the LCP and air is ascending, the LCP determines the uppermost boundary of the TTL. One of the first Lagrangian studies that analyzed the transport in the TTL was by Jackson et al. (2001) based on forward trajectories driven by large scale meteorological datasets. The authors initialized trajectories on the 150 hPa level within four main convective regions and noted that the majority of trajectories stayed within the troposphere and that hence, the LCP was not captured well. Using Lagrangian calculations forward and backward in time based on ERA-40 data, Fueglistaler et al. (2004) revealed the importance of different geographical regions for the troposphere-stratosphere-transport (TST), highlighting the West Pacific as main contributor for stratospheric air. Several Lagrangian ECMWF based studies showed differences in predicted water vapor during El Niño and La Niña conditions (Bonazzola and Haynes, 2004), and good agreement of the water vapor amount derived with the Lagrangian approach compared to radiosonde and satellite measurements (Fueglistaler and Haynes, 2005). Another study by Krüger et al. (2008) presented a long term climatology of TTL processes using ERA-40 and operational ECMWF data based on diabatic heating rates. The authors showed that there is a disagreement

between the diabatic and the kinematic method in the calculated amount of air masses reaching the stratosphere within different regions. Their trajectories indicated improved performance of the Lagrangian approach using the "diabatic method", where diabatic heating rates are used instead of vertical winds ("kinematic method") to drive vertical motion. However, Ploeger et al. (2010) showed a reduction of the differences between the two different methods (kinematic and diabatic) using the new ECMWF reanalysis ERA Interim. Kremser et al. (2009) analyzed two CCMVal-1 CCMs (E39/C and FUB-CMAM-CHEM) for different reference years and seasons, which indicate a fairly good geographical distribution of the LCPs compared to ERA-40 data during an ENSO neutral event. However, the CCMs seem to have difficulties in reproducing LCP temperatures well and partly the LCP distributions during El Niño or La Niña events.

This Lagrangian study is based on the new ERA Interim assimilation from 1979-2011, which revealed improved vertical velocity fields compared to the older ECMWF products (Dee et al., 2011; Monge-Sanz et al., 2012). Model output of different CCMs from CCMVal-2 and of one CMIP5 model, simulating the recent past and the future until the end of the 21st century, are analyzed as well. These CCMs use advection schemes for the transport of the chemical compounds, which are driven by vertical and horizontal winds; no diabatic heating rates were available. As a consequence, this study is based on the kinematic method for both applications, reanalysis and the climate model data. The applied CCMs take into account a well-resolved stratosphere and stratospheric ozone chemistry, but most of the models use prescribed SSTs as lower boundary. The model from CMIP5 has a well-resolved stratosphere as well and includes a fully coupled ocean, however stratospheric chemistry is missing. One essential goal of this study is to analyze how well those climate models are able to reproduce recent changes and variabilities, enabling us to evaluate the TTL changes in a future climate.

In the present study, long-term changes of the upper TTL of ERA Interim and different climate models will be investigated in more detail. By analyzing the LCP temperature and geographical distribution and with a new method the poleward extension of the LCPs, the following questions will be addressed:

- *How is the upper TTL represented in ERA Interim reanalysis?*
- *Where is the main entrance region for trace gases into the stratosphere using ERA Interim?*
- *How well do the different climate models reproduce upper TTL characteristics from ERA Interim?*
- *Is there a change in the width of the upper TTL in ERA Interim and climate models in the past and the present?*
- *Does the TTL change in a future climate?*

Outline

An overview of main atmospheric processes in the atmosphere and in the TTL is presented in chapter 2. One of the main questions - whether a broadening of the tropical belt is also reflected in the upper TTL - will be introduced and motivated there. Chapter 3 describes the different datasets and methods, which are applied within this study in more detail. Furthermore, the fundamentals for the Lagrangian transport model, the model setup and analysis method are described. In chapter 4, climatologies of the LCP and their occurrence within different regions is presented and discussed for ERA Interim and for different climate models for the recent past. The analysis of the broadening of the upper TTL is based on a new method defining the poleward extension of the LCP distribution (chapter 5). The annual and seasonal change of the LCP distribution is analyzed for the whole tropics and for different geographical regions within the tropics based on ERA Interim and seven climate simulations. In chapter 6, future changes of the TTL, which can be attributed to changes in temperature, occurrence and poleward extent of the LCP, are analyzed using three climate models. A conclusion and outlook is presented in chapter 7.

Chapter 2

Basics

2.1 Structure of the atmosphere

The atmosphere of the Earth is a complex system formed by physical and chemical processes. Based on the vertical structure of the temperature, the atmosphere is divided into different layers, which are defined by characteristic properties and processes. Figure 2.1 shows a typical temperature profile of the atmosphere. Two temperature maxima are visible, one at the surface and one at the stratopause (50 km).

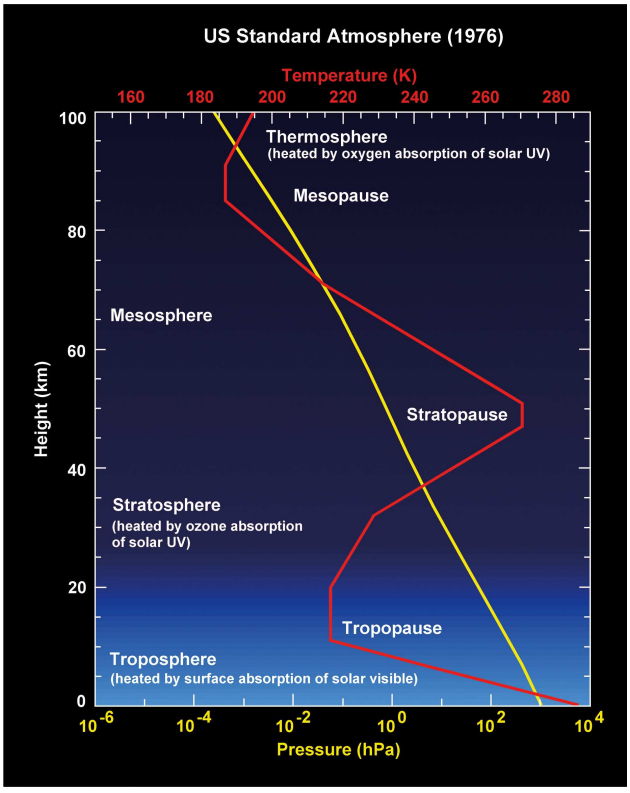

Fig. 2.1: Temperature and pressure profiles through the layers of the atmosphere (Gottwald et al., 2006).

The first layer, the troposphere, begins at the surface and extends up to 9 to 13 km at higher latitudes and up to 17 to 18 km in the tropics. Most of the atmospheric mass is contained within the troposphere (90%) (Labitzke and Loon, 1998). Since most of the weather events occur in this layer, it is also known as "advection" or "weather" layer. The word troposphere is derived from the Greek, where "tropos" means "change", which describes the behaviour of the well mixed turbulent troposphere. In general, the temperature decreases monotonically from the surface to the tropopause, which separates the troposphere from the stratosphere above. The highest tropopause is located in the tropics. The high surface temperatures and the high amount of water vapor there provide energy for deep convection, deepening the tropopsphere. From the equator to the poles the height of the tropopause drops rapidly. The lowest temperatures of the tropopause are reached at the equator. Within the tropics the tropopause becomes the transition layer, where most of the exchange of air masses between the troposphere and the stratosphere takes place (see section 2.3.1).
The stratosphere is the second atmospheric layer above the surface. It extends up to the stratopause in approximately 50 km height, which separates the stratosphere from the mesosphere. In the stratosphere the majority of natural ozone is produced. The ozone absorbs the harmful UV-radiation from the sun and converts the evolved electromagnetic radiation into heat, which leads to the inverse temperature gradient. Thus, the temperature increases steadily with altitude in this layer, which makes the stratosphere dynamically stable. The stratosphere got its name from its characteristic, where the Latin word "stratus" means "layered".
In the mesosphere, the temperature decreases again with altitude up to the mesopause. During polar summer, the mesopause is located at around 90 km above the surface, where the lowest temperature of the atmosphere exist. This coldest place of the atmosphere occurs due to the braking of gravity waves combined with the preferred eastward propagation of gravity waves in the mesopause region during summer (Labitzke and Loon, 1998). On the respective winter hemispheres the mesopause can be found at higher altitudes at around 100 km with higher temperatures. The mesopause separates the mesosphere from the thermosphere, which is located above. The thermosphere extends up to the limit of the atmosphere at 500-600 km altitude (Malberg, 1997). The temperature increases strongly due to the absorption of X-rays and gamma radiation from the sun. There, the physical processes and laws of meteorology are not longer valid. Due to the very low air density in that altitude, thermal conduction is not possible any more.

2.2 Global circulation

Three circulation cells are located in the lower atmosphere, surrounding the Earth. The Hadley cell, the Ferrel cell and the Polar cell. They were observed already in the 18th century. The Hadley cell (HC) describes an atmospheric large scale meridional circulation in the tropical troposphere. Due to the surface temperature gradient between the equator and the poles, evolving from the high solar insolation at the equator diminishing towards the poles, energy is transported polewards. Warm humid air rises at the equator, which

moves poleward near the tropopause, where the air cools and sinks slowly between 30° and 35° latitude. The Coriolis effect turns the equatorward flow of the HC near the surface to the west resulting in a northeast and southeast component on the northern and southern hemisphere respectively. These so-called trade winds are the dominating wind system in the tropics, converging at the equator to the Inter Tropical Convergence Zone (ITCZ). The schematic in Figure 2.2 illustrates some atmospheric features, which are described in this section.

At the poleward edges of the trade winds, the vertical component of the circulation is directed downward, resulting in the subtropical high pressure belt. From around 35° to 70° latitude prevailing westerlies dominate this part of the Earth's surface. Typical for this zone are the development of wave-motions due to large horizontal temperature gradients. They can propagate up into the higher atmosphere with different wave-lengths (see section 2.2.1). Between 60° and 70° latitude the polar front is located, separating two main air masses, the cold polar air and the subtropical warm air. The polar cell describes a circulation within the troposphere, located on the poleward side of the polar front, where still relatively warm air rises at around 60°. The air sinks at the poles, resulting in a cold and dry high pressure area at surface. In contrast to the Polar and Hadley cells, which are thermally direct cells, the Ferrel cell is a thermally indirect cell and represents the reverse flow of them. The Ferrel cell is located equatorward of the HC towards the polar front and describes a poleward and eastward flow near the surface.

On each hemisphere, two narrow air currents from east to west between the troposphere and the stratosphere can be found reaching high wind speeds of around 100 m/s. At around 30°, in the zone between the tropical and extratropical tropopause region (see section 2.3.1), the subtropical jets are located. They emerge from the Coriolis effected poleward flow of the air of the HC. At the polarfront the strongest jet streams, the polar jets, evolve. Both jets are formed due to large meridional temperature gradients, which cause tropopause breaks in that regions as well.

2.2.1 Brewer Dobson circulation

In 1949, Alan Brewer was the first scientist detecting a global meridional circulation in the stratosphere. He carried out trace gas measurements over South England. One of the observed quantity was atmospheric humidity. It can be measured by the "frost point", which is the temperature below the water vapor content of an air mass that will condensate. He observed very low values of water vapor in the stratospheric air, which were found immediately above the tropopause. The frost point of the stratospheric air experienced a rapid drop of ∼20 K. Due to this observation, Brewer suggested that this phenomena in the stratosphere can only be explained by a slow mean upwelling motion of air from the tropical tropopause into the stratosphere (Brewer, 1949). Only in the tropical tropopause the temperatures are low enough to dehydrate the air to the values observed over South England (mid-latitudes). From the tropical stratosphere the air moves poleward and sinks into the troposphere in extra tropical and polar regions. This phenomenon is also the explanation why the tropical atmosphere contains much less ozone than the observed values of the polar air, even if ozone

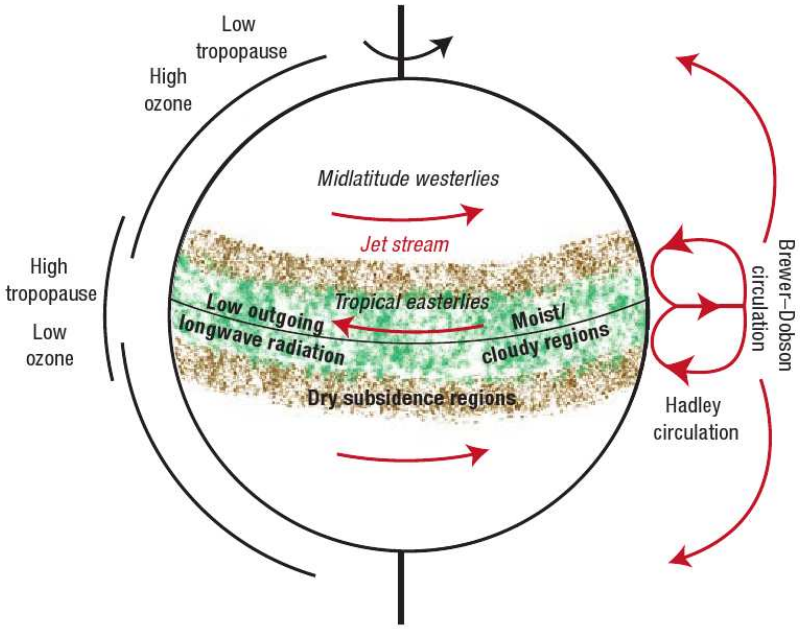

Fig. 2.2: A schematic of atmospheric phenomena to distinguish the tropics (Seidel et al., 2008).

is mostly produced in the tropical stratosphere. Even then Dobson et al. (1929) speculated about a poleward movement of air in the stratosphere based on the ozone distribution from very few available observations at that time. However, only in 1956 he revived his thoughts due to the increased number of ozone measurement and the previous work from Alan Brewer (Dobson, 1956). This slow mean upwelling motion in the tropics from the upper troposphere into the stratosphere and poleward and downward movement in the stratosphere is called the Brewer Dobson Circulation (BDC).

The BDC results from atmospheric waves in the troposphere. Planetary and gravity waves develop through temperature differences between ocean and land or from interactions of winds with the Earth surface. Those waves can propagate from the troposphere into the stratosphere and mesosphere respectively, whilst their amplitudes grow with decreasing air pressure. There are seasonal differences in matters of the strength and the behavior of the BDC. The westerlies, which are located in the extratropical troposphere, are strongest during winter (Labitzke and Loon, 1998). Additionally, in the stratosphere westerly winds exist on the winter hemispheres, whereas during summer easterlies are present. Planetary waves, which transfer energy, are able to propagate vertically as well when westerlies are dominating and hence penetrating into the stratosphere. This gives the BDC a greater significance during winter. In the stratosphere only planetary waves with wave-number 1-3 can propagate (Charney and Drazin, 1961). When easterlies or too strong westerlies arise these waves can not propagate into the stratosphere. Gravity waves are able to propagate further and

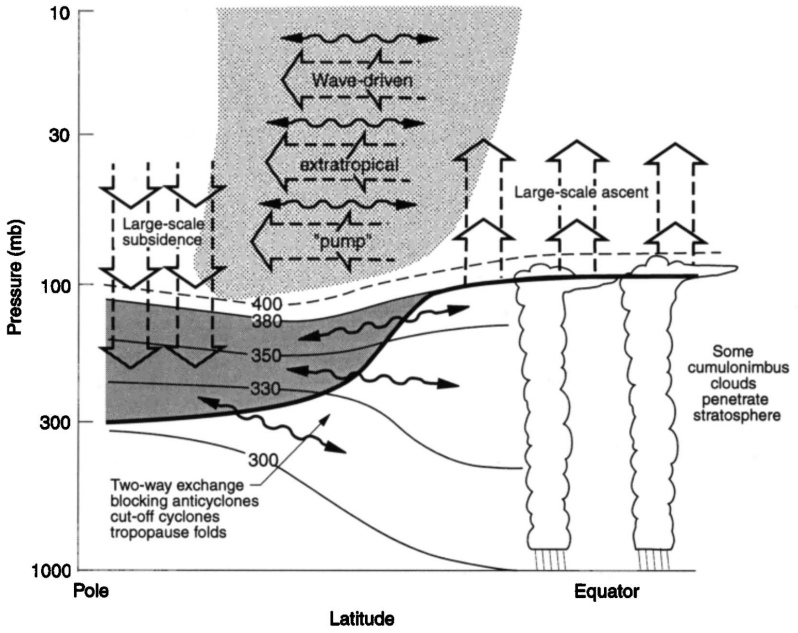

Fig. 2.3: Schematic of the Brewer Dobson circulation (Holton et al., 1995). The thick black line denotes the position of the tropopause, whereas the wavy-arrows visualize meridional transport by eddy motions.

break due to instability in the mesosphere. When the waves break, impulse and energy is delivered to the atmosphere. Within the developed wave braking area, the so-called “surf zones”, which are mainly located in the extratropical region, horizontal mixing takes place (McIntyre and Palmer, 1983). Additionally, the westerlies in the mid latitudes slow down, caused by the wave induced impulse and energy transfer. The resulting deceleration and the unbalanced quasi-geostrophic equilibrium leads to a northward stream component, which drives the residual circulation. This phenomenon is also called the “wave driven extra tropical pump”, (Holton et al., 1995, Figure 2.3). This definition refers to the pumping effect of the poleward stream on the tropical and polar air masses. Figure 2.3 shows a schematic of the BDC, with upwelling at the equator and the wave-driven poleward flow with the resulting large-scale subsidence at high altitudes (Holton et al., 1995).

2.3 The tropopause

The tropopause is the boundary between the troposphere and the stratosphere. It is typically characterized by a temperature inversion layer in the atmosphere from the surface (Figure 2.1) and was discovered at the beginning of the 20th century. In the 1890s Richard Assman a German Meteorologist, carried out several unmanned balloon flights and found some indications of an inversion layer in the higher atmosphere. However, he was skeptical about the measured temperatures and forced future manned balloon flights. In July 1901, two German balloonists, Reinhard Üring and Arthur Berson, were appointed to carry out

the first manned balloon measurements to high altitudes. During the implementation of the balloon flight, both scientists fainted despite of a good oxygen supply at approximately 10 to 11 km. However, they were able to strain the security leash in time to sink back to the Earth surface alive. In May 1902, Leon Teisserenc de Bort, in France, and Richard Assman in Germany, published about the existence of the tropopause and an overlying stratosphere at the same time. They used instruments lifted up by several unmanned balloons to high altitudes during the year 1901, obtaining comparable results to the manned balloon measurements (Labitzke and Loon, 1998).

Due to different physical and chemical characteristics within the stratosphere and the troposphere, the height of the tropopause can be defined by several ways. Based on the vertical temperature profile of the atmosphere there exists the thermal tropopause, which was defined by the World Meteorological Organization (WMO). After this definition, the tropopause was assumed as "lowest level at which the temperature lapse rate decreases to 2° C/km or less, and also the average lapse rate between this level and all higher levels within 2 km does not exceed 2° C/km" (WMO, 1957). In other words, the tropopause is defined by its static stability, which increases from the troposphere to the stratosphere. Another common "thermal" definition for the tropopause is the "cold point tropopause" or "cold point temperature" (CPT). Thus, the tropopause can be also approximated by the temperature minimum. These two definitions are most appropriate for the tropics

Dynamically, the stratosphere can be distinguished from the turbulent troposphere due to its high static stability, associated with monotonically increasing potential temperature values within the stratosphere.

The potential temperature θ of an air parcel at the given pressure p and the current temperature T, is defined as the temperature the air parcel needs if it would be brought to a reference pressure p_0, dry-adiabatically. It is defined as following:

$$\theta = T \cdot (p_0/p)^{\kappa}; \tag{2.1}$$

$\kappa = R/c_p$ =0.286 represents the adiabatic exponent for dry air where R=287 $J/(kg \cdot K)$ is the specific gas constant, c_p=1003 $J/(kg \cdot K)$ the heat capacity at constant pressure and p_0=1000 hPa the reference pressure. The potential temperature (Equation 2.1), is a conserved quantity and the vertical gradient of θ is a measure of stability in the atmosphere. As the stratosphere has a widely stable stratification, θ is increasing with height and thus, a geometric allocation is possible. Figure 2.4 presents a vertical cut of zonally averaged potential temperature and temperature for January 1993 from United Kingdom Meteorological Office (UKMO) analyzes. The extratropical tropopause can be approximated by the "dynamical" definition. Here, the tropopause is defined by a surface of constant potential vorticity (PV), which is a measure of the horizontal wind shear. Based on observations, the extratropical tropopause was found near the 2PVU surface (Holton et al., 1995). Due to the dependence on the Coriolis force, potential vorticity becomes zero at the equator and the dynamical tropopause is not valid anymore. Within the tropics the 380 K θ level is often used to approximate the tropopause. In Figure 2.3 the 380 K θ level, which approximates the tropopause in the tropics is located in the lower boundary of the "stratospheric overworld" (isentropes are entirely in the stratosphere), but it should be kept in mind that the actual

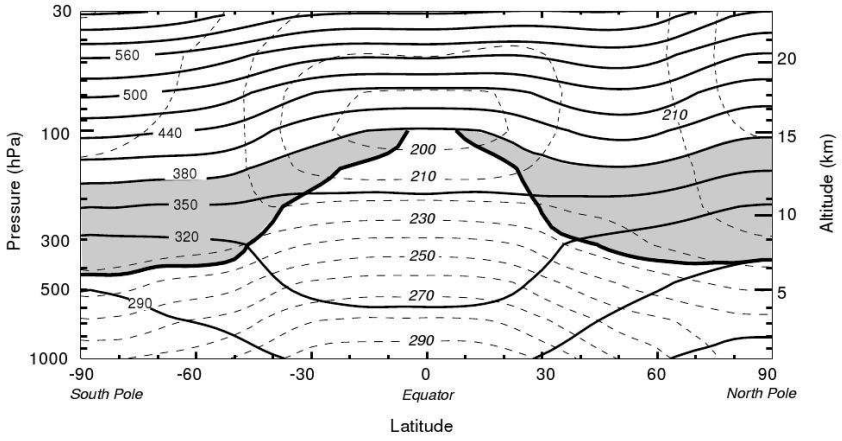

Fig. 2.4: Latitude-altitude cross section for January 1993 showing longitudinally averaged potential temperature (solid line) and temperature (dashed line), dynamical tropopause is marked by the heavy solid line of the 2 PVU ($1PVU = 10^{-6}m^2/s\ K/kg$) potential vorticity contour. The shaded area, where the isentropes cross the tropopause, represents the lowermost stratosphere (Holton et al., 1995).

boundary is somewhat variable (Holton et al., 1995).
Due to different concentrations of chemical species between the troposphere and the stratosphere there also exists a "chemical" definition of the tropopause. Based on the change of the correlation of ozone (O_3) and Carbon monoxide (CO) between the troposphere and the stratosphere, Zahn et al. (2004) defined a "chemical" tropopause in the tropics. The authors showed that their chemically derived tropopause revealed a constant value of 2 PVU. Thus, the "chemical" and "dynamical" tropopause can be identical.

A definable structure of the tropopause is not possible everywhere. At the borders of the large scale atmospheric circulation systems tropopause-breaks come along with the existence of jet streams (see section 2.2). From the equator to the poles, the height of the tropopause drops rapidly in the area of the subtropical and polar jets, especially when the jet is strong and the connected fronts intense (Geerts and Linacre, 1997). The extense height of the tropopause in the tropics and the lower tropopause height in the extratropics is controlled by the upwelling branch of the BDC in the tropics, which induces cooling and lifts the tropopause, whereas the downwelling branch in the extratropics induces warming and lowers the tropopause (Birner, 2010b).
As the tropical tropopause differs in respect to physical and chemical characteristics and reveals rather a transition layer than a sharp boundary, the tropical tropopause layer will be introduced in more detail in the following section.

2.3.1 The tropical tropopause layer

The tropical tropopause layer (TTL) is referred to be the main entrance region for atmospheric trace gases like water vapor and other relevant climate gases like ozone depleting

substances (ODS), traveling from the Earth surface up to the higher atmosphere. Thus, the TTL acts as a "gate to the stratosphere" (Fueglistaler et al., 2009) and is essential if we want to understand the chemical composition of the stratosphere.
The TTL is not a sharp, well-defined boundary between the troposphere, which is mainly dominated by convection, and the stratosphere, which is mainly controlled by radiation. The TTL can be regarded as an interface between these two dynamically different regimes, where properties of the troposphere and the stratosphere can be observed (Fueglistaler et al., 2009). The idea of a transition layer between the stratosphere and the troposphere is not new. Bjerknes and Palmén (1937) registered multiple tropopause structures in radiosoundings and named the region in between the "sub-stratosphere". Thereupon, in the following publications the tropopause is defined as "transition layer" rather than a sharp intersection. Highwood and Hoskins (1998) and Folkins et al. (1999) were the first publications mentioning the TTL.
Although the TTL is more an interface among the troposphere and the stratosphere, it is still valuable to distinguish between these two regimes. Large differences are observable, when looking at the time scale of the vertical transport of chemical species. In the troposphere, the vertical transport can take place within only some hours, when air is lifted up by moist convection, or within several days in the mid latitudes via baroclinic eddy motions (Holton et al., 1995). On the other hand in the stratosphere vertical transport is driven by radiative heating or cooling and takes place on much longer timescales like months to years. This significant difference of the timescales of the vertical transport is also the main reason why it is possible to distinguish between the characteristics of the troposphere and the stratosphere (Holton et al., 1995). Furthermore, there is a rapid change of the chemical composition, like the decrease of water vapor mixing ratio and the increase in ozone mixing ratio, when entering the stratosphere from below.
As the TTL is a transition layer where different characteristics of the troposphere and the stratosphere occur, different definitions for the TTL exist. If the definition of the TTL is more motivated by chemical tracers, clouds or thermodynamics, upper and lower boundaries could be set higher or lower. E.g. Sherwood and Dessler (2001) set their boundaries of the TTL from "the level of neutral buoyancy of the most buoyant tropospheric air at 150 hPa to 50 hPa, to the absolute highest possible overshooting height". This definition corresponds to the "entrainment zone" based on laboratory experiments of atmospheric boundary layers from Deardorff et al. (1980). The definition of the TTL from Fueglistaler et al. (2009) is mainly motivated by the large-scale dynamical structures that can be observed, thus levels with important temperature and circulation characteristics are mainly distinguished. Corresponding to Fueglistaler et al. (2009), vertically the TTL extends approximately from the height of main convective outflow at 150 hPa (14 km altitude or 355 K) to the height where the lapse rate has its maximum at about 70 hPa (18.5 km altitude or 425 K). The temperature minimum is located in the upper part of the TTL at approximately 90 hPa (17 km altitude or 380 K). The level of zero radiative heating (LZRH) with radiative heating above and cooling below, is located slightly above the level of main convective outflow at 125 hPa (15.5 km altitude or 360 K). Laterally, the TTL is bounded by the position of the subtropical jets (Fueglistaler et al., 2009).

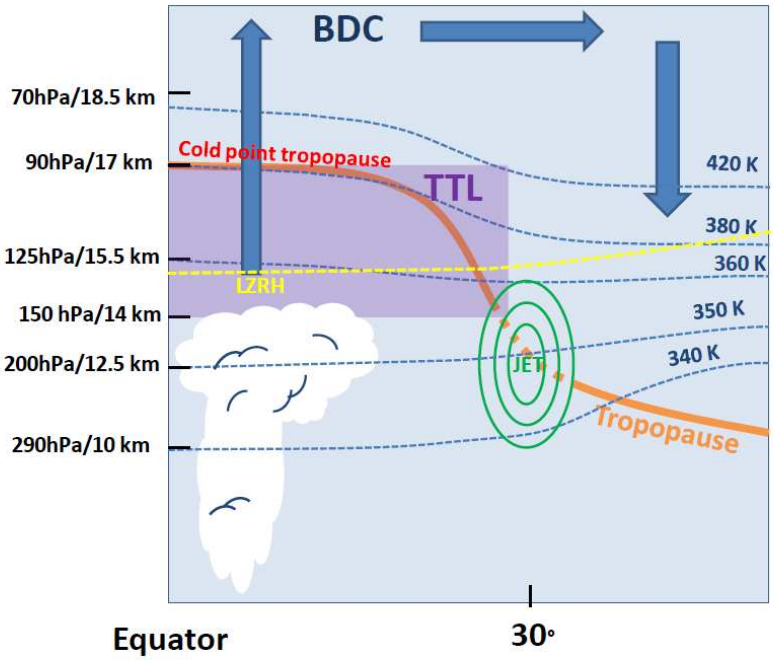

Fig. 2.5: A schematic of the tropical tropopause layer (TTL), shown as purple area. The level of zero radiative heating (LZRH) is presented as yellow dashed line in the lower TTL. The cold point tropopause is located at approximately 380 K in the tropics. The tropopause is approximated with the orange bold line. Different isentropes are shown with blue dashed lines for 340, 350, 360, 380 and 425 K. Green ellipses represent the subtropical jet core. The Brewer Dobson circulation is illustrated by the thick blue arrows.

Figure 2.5 shows the extension of the TTL based on the definition used for this study. The upper boundary of the TTL is located at the cold point tropopause or cold point (CP) temperature, which is based on the vertical temperature structure similar to the TTL definition from (Gettelman and de F. Forster, 2002). The CP temperature plays a crucial role in the exchange of air masses between the troposphere and the stratosphere as the transport of trace gases is mainly controlled by the temperature at the CP. Changes of the meridional extent of the upper TTL are presented and discussed in section 2.5 and in chapter 5 based on Lagrangian calculations.

2.3.2 Past and future changes of the TTL

Due to the fact that the TTL acts as a main entrance region for air masses carrying trace gases into the stratosphere, future changes in the structure of the TTL may also modify the transport (Fueglistaler and Haynes, 2005) and consequently trace gases like water vapor, which in turn affects the chemical composition of the stratosphere. Changes in the behavior

of the tropopause on longer time scales might be a relevant indicator of the anthropogenic climate change (e.g. Santer et al., 2003). Changes in the large scale meridional circulation may also effect the meridional extent of the TTL (Gettelman et al. (2009); Chapter 5).
The representation of the TTL has been analyzed in different Chemistry Climate Models (CCMs). Even though large differences exist among the models, i.e. in representing the cold point tropopause, the treatment of clouds and convection, they are able to reproduce the basic structure and some key properties of the TTL. Gettelman and Birner (2007) analyzed two CCMs from CCMVal-1 (CMAM and WACCM) and found that both simulations reproduced the correct TTL structure like the altitude of CP temperature or the location of the LZRH. Furthermore, different CCMs from CCMVal-2 were able to reproduce historical trends from reanalysis products like the tropical tropopause pressure decrease from 1980-1999 and the overall negative water vapor trend measured by HALOE from 1992-2004 (Gettelman et al., 2010).
Based on radiosonde data a negative temperature anomaly of the tropical lower stratosphere can be observed between 1979 and 2008 (Randel et al., 2009). However, this cooling trend is stronger between 30 and 70 hPa compared to the 100 hPa pressure level. Another observational based study, analyzing temperature anomalies of the tropical tropopause temperature based on NCEP reanalysis and radiosonde data, reported a strong cooling especially in the 1990s anticorrelated with Seasurface temperature (SST) anomalies in the underlying ocean, indicating a direct influence of the underlying ocean on the tropical lower stratosphere (Rosenlof and Reid, 2008). In contrast to the studies indicating a cooling of the tropical tropopause, Wang et al. (2012) showed by adjusting radiosonde data that the long-term cooling trends are less certain. Further, they report that the height of the CP temperature has increased more than previously thought. However, they argue that a decrease or an increase of the CP temperature are both physically plausible due to a tropospheric warming occurring simultaneously to a stratospheric cooling. Temperature observations of the tropical tropopause temperature were anomalously low after 2000 (Randel et al., 2006), especially over the warm pool region in the West Pacific (Rosenlof and Reid, 2008). Changes at the tropopause temperature trend near the year 2000, might be caused by the observed change of ozone trend showing a decrease after 2000, as well as to the stratospheric water vapor decrease by about 10 % after 2000 (Randel et al., 2006; Solomon et al., 2010). Based on an atmospheric model with coupled stratospheric chemistry, a striking change of the trend in the tropopause pressure and temperature was identified near the year 2000 as well. The model results indicate a slowdown of the decreasing tropopause pressure trend accompanied by a change of the tropopause temperature trend relative to the year 2000. Before, the temperature revealed a decrease after 2000 an increase again (Austin and Reichler, 2008). (Li et al., 2008) suggest that these changes are dominated by changes of the tropical upwelling, which in turn is influenced by the ozone concentration in the lower stratosphere. An comparison of ozone and temperature trends before the year 2000 in observations, CCMVal-2, CMIP3 and CMIP5 models was carried out by Young et al. (2013). They indicated that the relationship of the trends from climate models, which are partly analyzed within this study, are within the range of observations. Another important consequence of a stronger TTL upwelling might be a shorter stratospheric lifetime of chemical tracers due to a faster troposphere to

stratosphere transport (Randel and Jensen, 2013).
Future CCM simulations show a significant decreasing trend in the lapse rate tropopause of -23 hPa and an increase of the cold point temperature over the 21st century of 0.5-1 K per century (Gettelman et al., 2010, Figure 2.6). Additionally, CCMs project a "thinning" of the TTL (after the definition of Gettelman and de F. Forster (2002) from the level of main convective outflow to the CP temperature 12-18 km) of $\sim$ -1.7 hPa/decade in the vertical dimension, due to a simulated faster decrease in the Lapse Rate Minimum pressure compared to the Lapse Rate Tropopause Pressure. Further, an increase of water vapor is simulated in the lower stratosphere by 0.5-1 ppmv per century. Smaller but still significant changes for the future TTL were shown by Austin and Reichler (2008) based on an atmospheric model using coupled stratospheric chemistry with future GHGs scenarios from the Intergovernmental Panel on Climate Change (IPCC scenario A1B [1]). The authors suggest that the radiative effect due to ozone recovery in the future contributes to an increase in the tropopause temperature. But after 2040 the increasing SSTs caused by the increase in GHG concentration accompanied by a warming of the troposphere, plays an even larger role. Due to a warming of the tropical upper troposphere, the subtropical jets are strengthening, resulting in an increase of the mean tropical upwelling in the lower stratosphere (Butchart et al., 2010). One consequence of an increase in the tropical upwelling is a stronger upward TTL transport. This in turn effects the ozone concentration in the tropical lower stratosphere, which decreases and might lead to lower temperatures there in the future (Randel and Jensen, 2013). However, most CCMs predict a rising and warming of the cold point tropopause and an increase of stratospheric water vapor, recent observations do not demonstrate those simulated trends (Wang et al., 2012).
As the amount of trace gases in the lower stratosphere is controlled by the transport of air masses from the troposphere to the stratosphere and the minimum temperature, it is crucial to investigate the cold point temperature in more detail, which is the goal of the present study.

2.4 The cold point temperature

The CP temperature is the minimum temperature of the lower atmosphere. Usually the CP temperature is a good approximation for the tropical tropopause. The temperature of the CP is important, as it defines the amount of tropical water vapor that can enter the stratosphere (Holton and Gettelman, 2001). It was shown that the temperature minimum can only exist in radiative equilibrium, above the region, which is influenced by deep convection (Thuburn and Craig, 2002). The maximum altitude of tropical deep convection is observed to be not higher than 200-150 hPa (Gettelman et al., 2002a). Although the CP can in principle be decoupled from convection, Kuang and Bretherton (2004) showed a strong connection between the location of the convective cooling maximum due to uplift and the location of the CP using an cloud-resolving model. Furthermore, they found an increase in

[1] Balanced across all sources - best estimate temperature rise of 2.8°C until 2100.

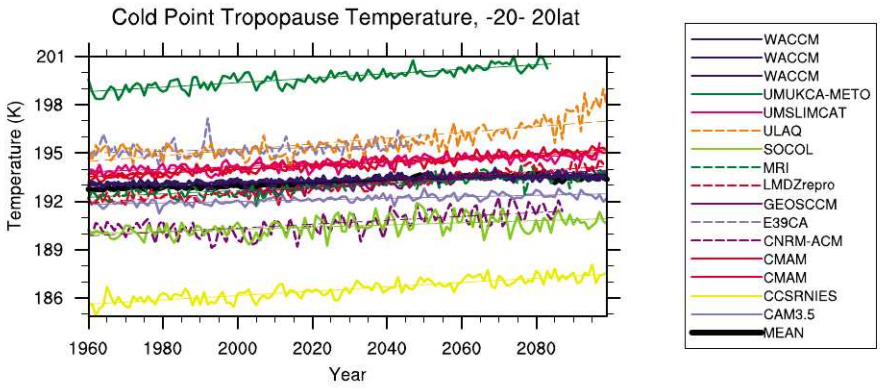

Fig. 2.6: Cold point temperature time series for future REF-B2 scenarios. Thin lines are linear fits. Multimodel mean (MEAN) is the thick black line (Gettelman et al., 2010).

the height of the cold point temperature with increasing SSTs, but no increase in the CP temperature at the same time, which might be probably due to ignoring the TTL ozone field that could produce further temperature changes. There is observational evidence that the temperatures in the TTL are affected by convections leading to significant cold anomalies in the TTL (Kim and Dessler, 2004). A relationship between frequent convection penetrations and low tropopause temperatures has been reported by (Gettelman et al., 2002b). However, the CP is more a stratospheric feature depending stronger on the photochemistry of ozone than on convection (Mehta et al., 2008). The CP temperature in the tropics varies on seasonal to interannual timescales largely due to variations in large scale ascent, which in turn is connected to the BDC, Quasi-Biennial Oscillation (QBO), ENSO and volcanic eruptions (Kuang and Bretherton, 2004; Randel et al., 2000, 2003, 2004; Zhou et al., 2001; Krüger et al., 2008). The influence of Volcanic eruptions were analyzed by Randel et al. (2000), they found a warming and lowering of the tropical tropopause after the eruption from El Chichon in 1982.

On a seasonal timescale the CP varies in its temperature and altitude from summer to winter. During NH winter the temperatures at the tropical CPT are lowest compared to the other seasons. This is caused mainly by enhanced wave driving during NH winter, which lifts and cools the tropopause (Holton et al., 1995), see section 2.2.1. Based on radiosonde data, Seidel et al. (2001) found that the CP is zonally and meridionally structured in different quantities like the temperature and potential temperature. From the equator to the poles, the cold point temperature is increasing, as well as the potential temperature of the CP. Zonally lowest CP temperatures occur over the maritime continent, which is associated with localized deep convection where the tropopause height decreases with decreasing atmospheric stability (e.g. Highwood and Hoskins, 1998; Seidel et al., 2001; Kim and Son, 2012). Seidel et al. (2001) further mention particularly that the highest CP levels with lowest pressure are not found over the western Pacific, but rather over Central America and Africa, as higher surface air temperatures can occur over the continents.

On the annual timescales the CP reveals variability in matters of temperature and its geo-

graphical distribution as well. Events like ENSO (Section 2.4.2) or the Indian monsoon are the most dominant source for climate variability. They have a large impact on the location and distribution of convection over the Pacific, which in turn influences the circulation and temperature in the tropical tropopause region (Fueglistaler and Haynes, 2005).

2.4.1 The Lagrangian cold point

Trajectory calculations are used to analyze the location, where air enters the stratosphere. This "entry point" point is given by the minimum temperature an air mass experiences along its trajectory, the so called Lagrangian cold point (LCP). It also specifies the location of minimum saturation mixing ratio of air masses entering the stratosphere. Thus, it can be also termed as the "dry point" or "dehydration point" as an air mass gets dehydrated to its minimum due to the temperature minimum. The location of the Lagrangian cold point is not coincident with the so termed "cold point", which refers to the lowest temperature in a given vertical profile like the Eulerian cold point (ECP) does. The LCP has systematically lower temperatures typically 2.5 K (and 4 K in potential temperature on the average) than Eulerian cold points due to horizontal transport of air parcels during ascent into the stratosphere through regions with a horizontal temperature gradient (Fueglistaler et al., 2005).
Jackson et al. (2001) was one of the first studies, calculating the transport in the TTL with trajectories based on large-scale meteorological datasets using 3D windfields. However, due to the application of forward trajectories, the LCP was not captured well as the trajectories stayed within the troposphere. That work was followed by several other Lagrangian studies like Fueglistaler et al. (2004) using ERA-40 data from the year 2001 as input for forward and backward trajectories analyzing the pathways of trajectories. The authors identified the West Pacific, being the main contributor for stratospheric air. Bonazzola and Haynes (2004) calculated large backward trajectory ensembles to determine pattern of transport for stratospheric water vapor during different ENSO phases. A comparison of trajectory model calculations based on ERA-40 with radiosonde data and satellite measurements was carried out from Fueglistaler and Haynes (2005). They found good agreement of the water vapor amount between observations and model calculations. Trajectory calculations based on a larger time period from 1979-2001 with ERA-40 data to estimate stratospheric water vapor mixing ratios was carried out from Fueglistaler et al. (2005). The authors showed improved estimates of stratospheric humidity compared to calculations from Eulerian tropical tropopause temperatures. The study from Krüger et al. (2008) showed a long-term climatology of LCPs and the dependence of the LCP temperature and distribution on natural variability using radiative heating rates as vertical velocity, highlighting also the differences among the kinematic and diabatic approach. Although improved performance was shown by Krüger et al. (2008) using the diabatic method compared to the kinematic method for ERA-40 data, Ploeger et al. (2010) demonstrated reduced differences between the two methods with ERA Interim data. Two different CCMs from CCMVal-1 were analyzed with a Lagrangian approach by Kremser et al. (2009). The authors showed a fairly well representation of the LCP distribution for the CCMs during different ENSO states. However, those CCMs had difficulties in reproducing the LCP temperature and in highlighting the main entrance

region for air masses into the stratosphere, the West Pacific.
Accompanied in the air, which is transported to the stratosphere also trace gases, which can contribute to the depletion of stratospheric ozone, are able to reach the stratosphere at the location of LCP. Hence, to better understand this transport the evolution of the LCP pattern is analyzed in more detail in the present study.
The density distribution and the temperature of the LCPs reveal a pronounced seasonal and annual cycle (Fueglistaler et al., 2005). Especially the temperature and hence, the amount of water vapor entering the stratosphere, largely depends on the conditions of the West Pacific area. Randel et al. (2004) found highest correlations of water vapor near the lower stratosphere and temperature anomalies in the West Pacific. LCP accumulations beside the area over the West Pacific are also found over South America and West Africa during all seasons. During NH summer a large amount of LCPs can be also determined over the Bay of Bengal, caused by the Asian Monsoon. Generally, highest LCP temperatures are observed during NH summer and lowest temperatures occurring during NH winter, which is linked to the annual cycle of zonal mean tropical tropopause temperatures. The western Pacific plays an important role as main entrance region for air masses traveling into the stratosphere during all seasons. Further results and discussion for the CP will be given in section 4.1.

2.4.2 The influence of ENSO

The cold point temperature for different ENSO phases based on the ERA Interim data, is presented in Figure 2.7 for the Eulerian (left) and Lagrangian (right) perspective during NH winter. The average CP temperature pattern for one ENSO neutral case is shown in Figure 2.7(a). Lowest temperatures are located over the West Pacific with 188.5 K, while the temperatures are increasing polewards. During the strong El Niño in 1997/98 (Figure 2.7(c)), the location of lowest temperatures is shifted to the east and reach slightly higher values (188.8 K). During the strong La Niña event in 1998/99 (Figure 2.7(e)) lowest temperatures are indicated with 186.8 K, which is 2 K lower and more pronounced over the West Pacific compared to ENSO neutral.
Similar to a varying structure and temperature of the ECPs, the distribution and the temperature of the LCPs is varying with underlying changing climate conditions as well. On the right side of Figure 2.7 the effect of ENSO on the geographical distribution and the temperature of the LCP is shown. The corresponding LCP pattern during ENSO neutral conditions is presented in Figure 2.7(b) revealing the main entrance region located over the maritime continent with minimum temperatures around 186 K. During El Niño (Figure 2.7(d)) the entrance regions of air masses traveling from the surface to the stratosphere is shifted to the East Pacific. The LCPs are distributed almost homogenously over the whole tropical area, indicating higher minimum temperatures compared to ENSO neutral (around 187 K). During La Niña (Figure 2.7(f)), the geographical distribution of the LCP is more pronounced and concentrated over the West Pacific region revealing lower minimum temperatures (around 185 K) compared to ENSO neutral.
Fueglistaler and Haynes (2005) and Krüger et al. (2008) investigated also other natural forc-

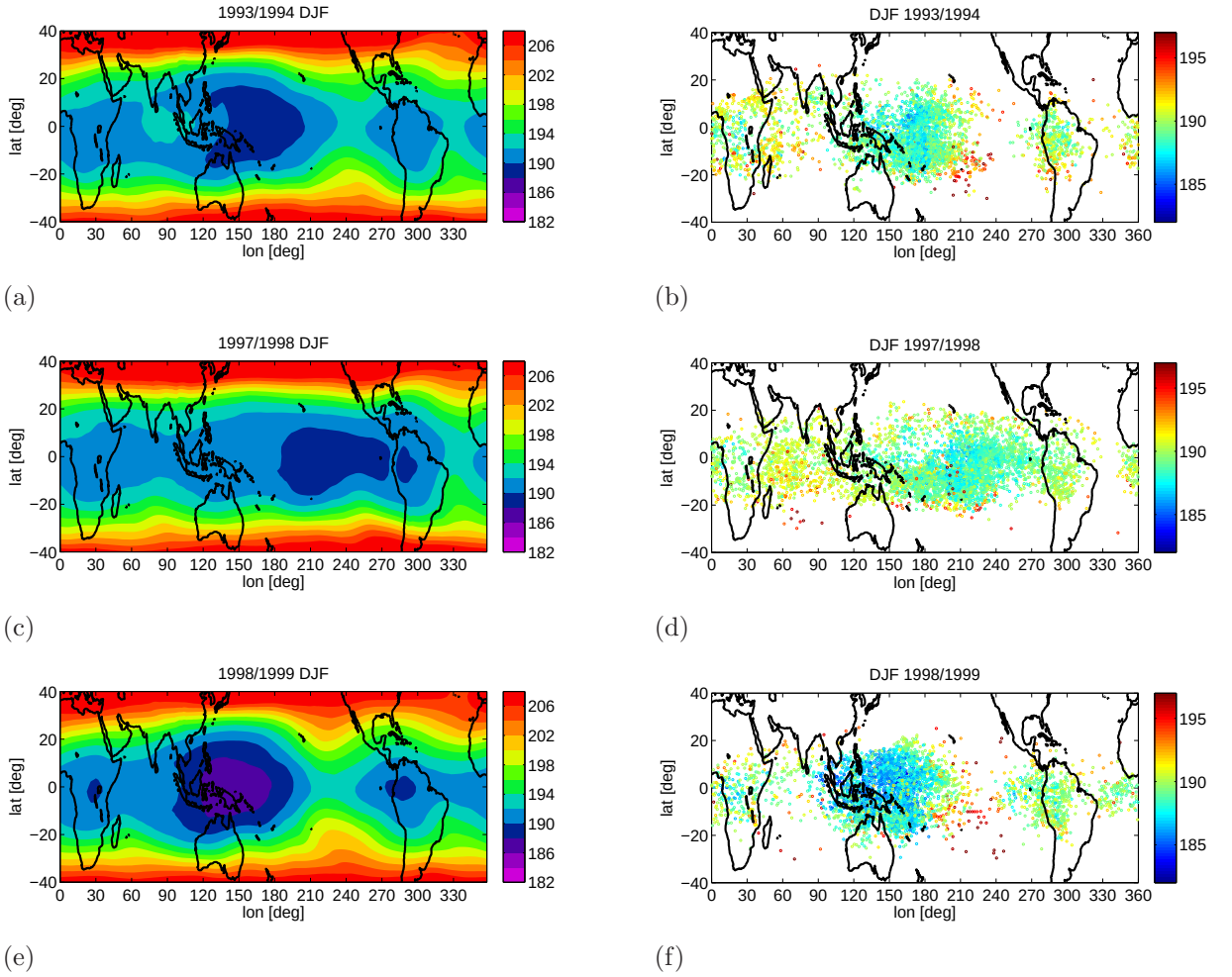

Fig. 2.7: Eulerian (left) and Lagrangian (right) cold point temperature for the different ENSO states during NH winter (ERA Interim), ENSO neutral 1993/1994 (a) and (b), El Niño DJF 1997/1998 (c) and (d) and La Niña DJF 1998/1999 (e) and (f).

ing factors beside ENSO, such as QBO, volcanic eruptions and the solar cycle. The analysis of the LCPs revealed an impact of natural forcings on the LCP temperature and pattern. A colder TTL and dryer stratosphere is reached during La Niña and QBO East north of the maritime continent. During el Niño and QBO West a warmer TTL and less dry stratosphere is analyzed based on trajectory results.

2.5 The tropical widening

Already Pittock (1988) states: "The most robust of the empirical climatic relationships and correlations is the argument that with a global mean warming the climatic zones will tend in general to move poleward".
Recently, a growing number of studies gave evidences for a widening of the tropical belt (e.g. Seidel et al., 2008; Davis and Rosenlof, 2012). However, the location of the boundaries of the

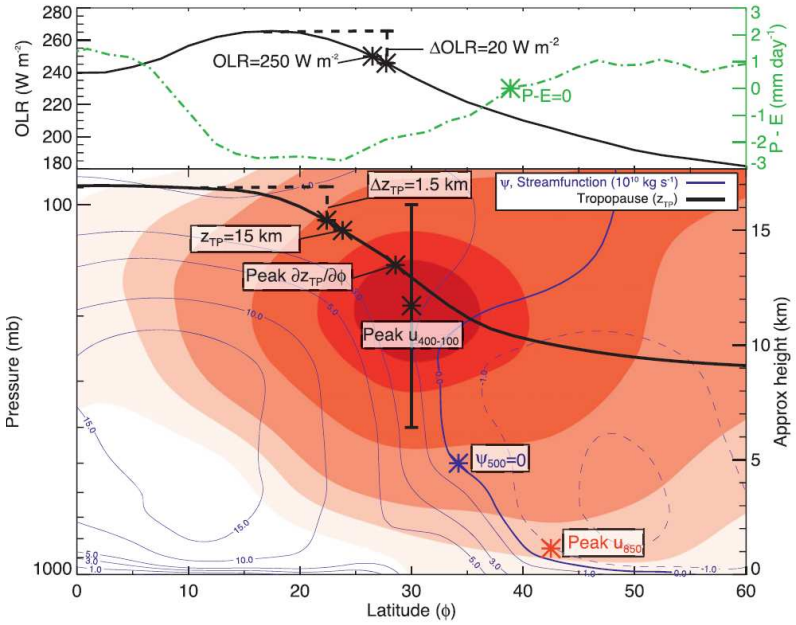

Fig. 2.8: Different metrics to diagnose the tropical edges are highlighted by asterisks on a monthly-mean zonal-mean cross section of atmospheric properties from the NCEP-NCAR reanalysis and NCEP OLR dataset for January 2008. The zonal-mean zonal wind is shaded (5 m/s contours), and the mean meridional streamfunction (ψ) based on the zonal-mean meridional wind is contoured in blue (Davis and Rosenlof, 2012).

tropics are not consistently defined. This inconsistency is due to the difficulties, defining a clear border between the subtropics and the tropics at different levels of the atmosphere. Between these two zones, atmospheric characteristics experience gradual modifications. Based on different indicators, varying definitions of the tropical boundaries exist, which all represent a measure of the width of the tropical belt (Reichler, 2009). Figure 2.2 visualizes a schematic diagram of different atmospheric features that are used to distinguish the tropics (Seidel et al., 2008). Dynamical indicators focus on the atmospheric circulation, like the lateral boundary of the Hadley cell or the position of the subtropical jet streams. Physical indicators apply characteristics like the amount of outgoing long wave radiation (OLR), the change of ozone concentration in the stratosphere or the thermally defined tropopause height. Figure 2.8 displays various thresholds in different properties of the atmosphere, which have been used to define tropical edges (Davis and Rosenlof, 2012). Further, Figure 2.8 visualizes the different latitudinal locations depending on the threshold ranging from 25° latitude for the tropopause height threshold at 15 km to 45° latitude for the latitude of peak wind at 850 hPa at around 1 km height. Table 2.1 summarizes different diagnostics identifying a broadening of the tropical belt, which are described in more detail in the following.

In the year 1992, Gibson (1992) presented results, showing a poleward movement of the subtropical wind maximum of 0.18° latitude per year between 1976-1991 on the SH and relates that to the consequences of the greenhouse effect. One of the first publications that

Diagnostic	Trend (lat/dec)	Data source	Reference
Lat. of subtropical wind max. (STWM) (SH winter)	1.8°	1976-1991 Austral. Bureau of Met. 500-hPa analyses	Gibson (1992)
Upwelling Branch of BDC	3°	1992-2001 satellite (HALOE)	Rosenlof (2002)
Poleward shift of jet streams	2°	1979-2005 satellite (MSU)	Fu et al. (2006)
Poleward shift of fronts	1.1°	1979-2003 satellite (TOMS)	Hudson et al. (2006)
Hadley Cell width	0.8° to 2°	1979-2005 ERA40, NCEP/NCAR, NCEP/DOE reanalysis	Hu and Fu (2007)
Frequency of high tropopause days	1.9° to 3.1°	1979-2005 radiosonde	Seidel and Randel (2007)
Poleward shift of jet streams	∼0.3°	1979-2001 ERA40, NCEP/NCAR reanalysis	Archer and Caldeira (2008)
Frequency of high tropopause days	0.5°	1979-2009 ERA40, NCEP/NCAR, NCEP/DOE reanalysis	Birner (2010a)
Poleward shift of subtropical jets	1.68°	1979-2009 satellite (MSU)	Fu and Lin (2011)
Poleward shift of jet streams	1.2°NH;2.1°SH	1979-2010 satellite (TOMS)	Hudson (2012)
1)Max. tropos. dry bulk static stability 2)Subtropical jet 3)Vertical average stream function	-0.5° to 0.9° 0.3° to 0.6° 0.4° to 2.0°	1979-2012 MERRA, ERA Interim, NCEP reanalysis	Davis and Birner (2013)
Hadley Cell width	<0.2°	1979-2005 CMIP3 historical	Johanson and Fu (2008)
Frequency of high tropopause days	0.71°	1958-1999 GFDL SST+Rad	Lu et al. (2009)
Hadley Cell width	0.17°	1979-2005 CMIP5 historical	Hu et al. (2013)
Hadley Cell width	0.27°	21st century CMIP5 RCP8.5	Hu et al. (2013)

Tab. 2.1: Tropical widening diagnostics, trends and data source referred from different observational and model studies for the recent past.

showed long-term trends for an indication of the tropical widening, was Rosenlof (2002). By analyzing the poleward extent of the upwelling branch of the BDC, based on satellite borne water vapor records in the lower stratosphere, the author found a widening of the upwelling region of ∼3° latitude per decade between 1992-2001.
The expansion of the Hadley circulation was analyzed by Hu and Fu (2007). Their results were based on different reanalysis datasets, and indicated that the Hadley Circulation experienced a significant expansion of about 2° to 4.5° of latitude in the time period from 1979 to 2005. Based on temperature changes in the troposphere and stratosphere, Fu et al. (2006) estimated a poleward shift of the subtropical jet streams. As the jet streams limit the poleward extent of the HC (section 2.2), they related this to a widening of the HC of 2° latitude between 1979 and 2005. Historical trends in the sub-tropical and polar jets were analyzed from Archer and Caldeira (2008). They identified a poleward movement of all jets between 1979 and 2001, accompanied by a weakening of the sub-tropical jets on both hemispheres and a strengthening of the poler jet on the SH. Another indicator for the width of the tropics was investigated by Hudson et al. (2006). They analyzed the variability of total ozone within different latitudinal regimes. The changes of total ozone were related to changes in the position of the subtropical and polar fronts. Hudson et al. (2006) observed a poleward movement of the subtropical and polar fronts by 1.1° latitude per decade between 1979 and 2003. Later, Hudson (2012) analyzed the location of jet streams at mid-latitudes using ozone data. The author found a significant poleward shift of the jet streams on both hemispheres of 3.7° and 6.5° latitude on the NH and SH between 1979 and 2010. Using different CMIP3 and CMIP5 models (Min and Son, 2013) suggest that stratospheric ozone depletion significantly contributed to the observed widening of the Hadley cell on the SH in the last decades. Another study from Seidel and Randel (2007) showed an increase in the frequency of occurrence of high tropopause days appearing in the subtropics. Their analyzes were based on radiosonde measurements and reanalysis datasets, resulting in an expansion of the tropical region of about 5° to 8° latitude between 1979 and 2005. However, Birner (2010a) suggested that tropopause statistics based on current reanalysis datasets may not be the best method to quantify long-term changes in the width of the tropical belt as the derived trends were not robust to different tropical edge definition methods. In his analysis he introduced an alternative tropopause height threshold definition relating the threshold of the tropopause to tropopause height statistics of the inner tropics. Using that threshold results in smaller but still significant widening trends of around 0.5°/decade for NCEP (1979-2009) and ERA40 (1979-2001) datasets. Nevertheless, the height of the tropopause is a variable that has often be neglected in the detection of climate change. In a study by Santer et al. (2003) it is shown that different reanalysis products indicate an increase in the global mean tropopause height of ∼1 to 2 hPa/decade. This result is also consistent with the resulting decrease in tropical lapse rate pressure estimated from radiosondes by Seidel et al. (2001).
A different possible effect on the width of the tropical belt was investigated by Grassi et al. (2012). They found a broader tropical area, when the index of the Pacific decadal oscillation shifts from positive to negative values due to disturbances in the meridional gradient of the temperature at the edges of the tropical belt.
Fu and Lin (2011) showed that the observed trend of lower-stratospheric temperature, has

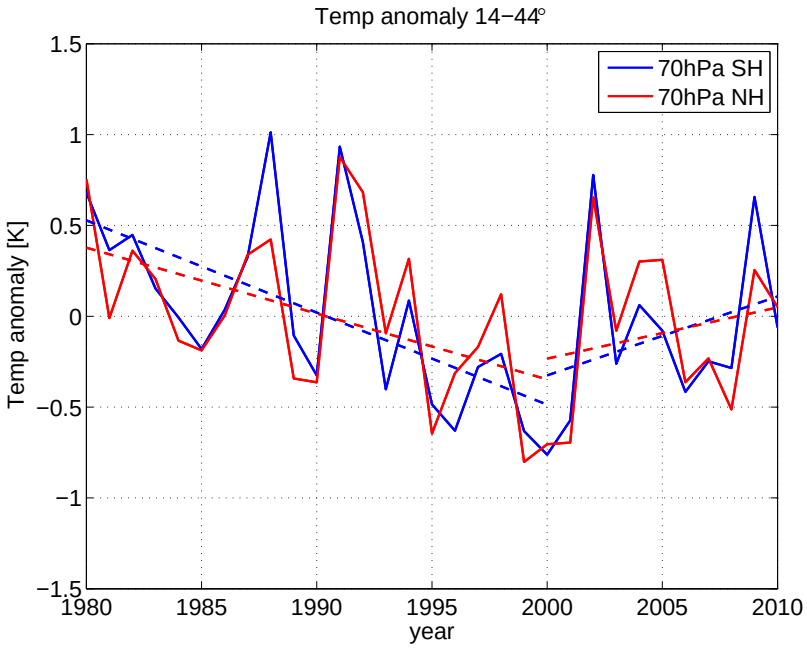

Fig. 2.9: Temperature anomaly using ERA Interim between 1979-2010 in 70 hPa in the subtropical midlatitudes between 14-44° NH (blue) and SH (red) and linear regression (dashed).

the characteristic of an enhanced cooling in the subtropical midlatitudes (between 15 ° and 45° north and south). This cooling in turn, they use as a measure for the extent of the poleward shifted jets in the subtropics. Based on satellite-borne microwave sounding unit (MSU) temperature data from 1979-2009 they found a widening of 1.68° latitude since 1979.

Figure 2.9 shows the temperature anomaly between 14° and 44° N and S, respectively, from the 70 hPa pressure level (lower stratosphere) using ERA Interim reanalysis between 1980-2010. The temperature anomalies for the NH (red) and SH (blue) are shown separately. A cooling from 1980-2000 can be observed followed by a slight warming after the year 2000. This result indicates a poleward shift of the subtropical jets prior to 2000, followed by a slight equatorward movement after 2000 again (this study; Fu and Lin, 2011). A recent study by Davis and Birner (2013) investigated more robust versions of existing diagnostics to define tropical edges. The authors used new reanalysis datasets from MERRA, ERA Interim and NCEP from 1979 to 2012. The resulting trends of a poleward shift of the tropical belt range from -0.5° to 2.0° latitude per decade (lat/dec) depending on the data and diagnostics, where smallest trends results from ERA Interim.

The cause of the widening of the tropics has been examined in a study by Lu et al. (2009). They showed that the widening can be replicated by an atmospheric general circulation model. They carried out sensitivity studies, where one simulation was forced by observed SSTs and sea ice, and the other was additionally forced by estimated radiative forcing from natural (solar and volcanic aerosol) and anthropogenic sources (well-mixed greenhouse gases, tropospheric and stratospheric ozone, and tropospheric aerosols). To define the borders of the tropics, they used the frequency of high tropopause days similar to Seidel and Randel

(2007). The authors concluded that the direct radiative forcing especially in matters of greenhouse gas and stratospheric ozone are the main force for the past trend of the widening and that SST forcings can be neglected. Analyzing different model output from AMIP2 and CMIP3 models, Johanson and Fu (2008) were able to identify a widening of the tropical belt in the 20th century as well. However, the simulated widening is weak compared to observations. Nevertheless, the widening is consistently simulated from most of the models.

The broadening of the tropical belt is not only a displacement within the tropics it also has global climate consequences. A poleward movement of the Hadley circulation is connected with a poleward expansion of the subtropical dry zones (Lu et al., 2007) and thus greater potential of droughts also in the midlatitudes (Hu and Fu, 2007; Birner, 2010a). A poleward movement of the subtropical jet streams has large influences on the development of storm tracks in midlatitudes (Birner, 2010a). In ensemble simulations of 15 coupled GCMs for the IPCC Fourth Assessment Report (AR4) scenario for the 21st century, a poleward and upward shift together with an intensification of the storm tracks was investigated by Yin (2005). The author connects the shifts of the storm tracks with changes in baroclinicity and the thermal structure of the troposphere. Furthermore, the author notes that it might be accompanied by shifts in surface wind stress and precipitation towards the poles and a shift towards more positive indicies of the Northern and Southern Annular Mode (NAM, SAM). A poleward shift of the subtropical jet streams could also lead to displacements of the global weather patterns, the temperature, precipitation and hydrologic cycle towards the poles (Hudson, 2012).
Lu et al. (2007) analyzed the width of the HC in simulations from the A2 scenario of IPCC AR4 models. The authors identified a consistent weakening and poleward movement of the HC in future model simulations of the 21st century. The authors suggest that besides the GHG-induced global warming, the widening could be also linked to stratospheric ozone depletion and climate variability. However, using GFDL models with radiative forcing from IPCC AR4, Lu et al. (2009) found that the widening trend of the tropical edges can be linked to direct radiative forcing and that SST forcing alone causes no significant change. In contrast to Rosenlof (2002) who identified a broadening of the upwelling branch of the BDC in the past, Li et al. (2010) detected a narrowing of the upwelling branch of the BDC and HC in future simulations. The authors analyzed two model simulations from GEOSCCM (A1b and A2) of the 21st century using IPCC GHG scenarios. Additionally they detected a strengthening of the BDC. However, Li et al. (2010) also noted that there is probably a close relationship between the narrowing of the ascending branch of the HC and the reported widening of the descending branch of the HC. Historical and future simulations of the Coupled Model Intercomparison Project Phase-5 (CMIP5) were analyzed by Hu et al. (2013). The authors detected a significant widening of the Hadley circulation of 0.15° lat/dec for the time period 1979-2005. Analyzing the extreme projected radiative forcing of RCP8.5 for the 21 st century, Hu et al. (2013) identified a significant widening of 0.27°/decade. Although the CMIP5 models seem to underestimate the observed widening trends, results of CMIP5 historical simulations suggest that anthropogenic forcing and the increase of GHGs factors explaining the observed and simulated trends.

In the present study a new indicator for the measure of the width of the upper TTL (see section 3.3.2) will be applied to analyze a possible change in the width of the transition between the troposphere to the stratosphere. The widening of the upper TTL will be analyzed and discussed for the present and past in chapter 5 and for the future simulations in chapter 6.

Chapter 3

Data, Model and Method

In this chapter the different datasets used for the study will be introduced. Also a short description of the trajectory model, which was applied to observational and model data will be given. One aspect of the present study is to evaluate and compare different global climate models with a Lagrangian point of view. Furthermore, the model setup and the method, which is used to evaluate the results of the trajectory model runs, will be presented.

3.1 Data

The reference data used in this study is based on the ERA-Interim reanalysis product. Different Chemistry Climate models (CCMs) participating in the IGAC/SPARC - CCMVal-2 initiative (International Global Atmospheric Chemistry / Stratospheric Processes And their Role in Climate - Coupled Chemistry Climate Model validation-2) are applied for this Lagrangian study. The major target of the CCMs from CCMVal-2 is the stratosphere, thus almost all applied CCMs use prescribed sea surface temperature (SST) from coupled climate model simulations. Additionally, one model run of the CMIP5 is provided for this study. Different to the CCMs, the models participating in CMIP5 include an interactive ocean, projecting changes in SST, sea-ice and the ocean circulation from a fully coupled atmosphere/ocean GCM.
For the trajectory calculations, a temporal and spatial high resoluted model output is necessary. Due to limited computing capacity and time, only some decades from the different climate models are considered. Using these different datasets, the climate models are validated for the past to create assumptions about the development of the future climate and the role of the ocean and the stratosphere therein.

3.1.1 ERA-Interim

ERA-Interim is a global reanalysis product of the ECMWF (European Centre for Medium-Range Weather Forecasts) (Uppala et al., 2008). ERA-Interim represents the time period from 1979 to the present in preparation to replace ERA-40 as a next-generation extended reanalysis product. In contrast to operational assimilations, the reanalysis assimilation model

is run throughout a time period without changing parameterizations or resolution. Thus, reanalysis datasets are more suitable for studies of a changing atmosphere on a longer timescale. This "Interim" product has many improvements compared to the previous product ERA-40. Systematic differences between observations and the model background are reduced, which leads to a better vertical stability in the temperature analysis (Dee et al., 2011). Furthermore, the velocity of the upward transport (the Brewer-Dobson circulation) in the tropical stratosphere is reduced to the half compared to ERA 40, but it is still almost twice as fast as reported by observations (Dee et al., 2011). Accordingly, it was shown that the mean stratospheric age-of-air using winds from ERA Interim improved significantly to more realistic values compared to ERA-40 winds (Monge-Sanz et al., 2012).
In contrast to ERA-40, now a 12 hour 4D-Var [1] is carried out, with a higher horizontal resolution (from T159 to T255) and an upgraded formulation of background error constraints. Some improvements have been made compared to ERA-40, like within model physics, which now include a new supersaturation scheme for ice microphysics (Tompkins et al., 2007), or an improved precipitation pattern, which was too strong over the tropical oceans bevore. Further, an automated scheme for correcting biases in the satellite radiance observations is included in ERA Interim (Dee et al., 2011). Mostly the same observations sets for the overlapping time period as for ERA-40 were used, apart from some exceptions like a new altimeter wave heights.
For this Lagrangian study, the 6 hourly data output from pressure levels with a horizontal resolution of 2° x 2° was applied. ERA Interim is now available on 37 standard pressure levels (23 for ERA-40), four of its vertical layers are situated approximately in the TTL region between 70 hPa and 150 hPa (at 70, 100, 125, and 150 hPa). For the presented calculations the temperature, meridional-, zonal- and the vertical wind fields on the pressure levels were used. The calculations were carried out for the available data from 1979 to 2011.

3.1.2 Chemistry Climate Models (CCMs)

Data from four different Chemistry Climate models (CCMs) were used from the SPARC CCMVal-2 initiative. The goal of CCMVal-2 is to improve the representation of physical and chemical processes in the CCMs. One important aspect to improve the understanding of CCMs is the comparison and validation of the CCMs reproducing past trends and past variability as well as the comparison of their ability to predict the future (see also SPARC, 2010).
In this study, the CCMs within the CCMVal-2 project are used to evaluate the evolution of the stratosphere under the influence of decreasing chlorofluorocarbons (CFCs) and increase of greenhouse gases (carbon dioxide CO_2, nitrous oxide N_2O and methane CH_4) in the future.
Several simulations have been proposed within the CCMVal-2 project and performed from most of the groups participating in CCMVal-2. One can distinguish between: REF-B1 simulations, "reproducing the past" and REF-B2 simulations, "making predictions".
The here presented REF-B1 transient run covers the near present and past from 1960-2006

[1] Compared to 3D-Var, in 4D-Var future observations are included by adding the time dimension.

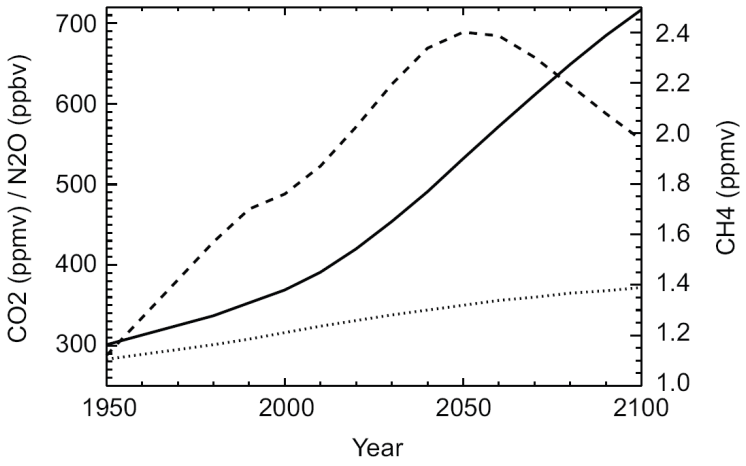

Fig. 3.1: SRES A1b scenario for surface CO_2 (solid), N_2O (dotted), and CH_4 (dashed) concentrations (SPARC, 2010, Chapter 2).

with forcing prescribed from observations. Those include anthropogenic and natural forcing, and are based on changes in trace gases, solar variability, volcanic eruptions, QBO, SSTs and sea ice cover (SIC).
The REF-B2 simulation considers the period from 1960-2100, at least for most of the models participating in CCMVal-2. It uses only the anthropogenic forcing including natural uncertainties obtained from climate simulations for SST and sea ice. Figure 3.1 shows the time evolution of the GHGs as applied for the scenarios from SRES A1b and A1 in the IPCC and WMO reports. CO_2 indicates more than a doubling by 2100 compared to 1950 (solid line), whereas CH_4 undergoes a trend reversal after 2050 (dashed) and N_2O (dotted) shows a trend with small growth rates. For more details of the simulations, see (SPARC, 2010, Chapter 2).
The provided data from the different model groups, analyzed in this study, is presented in table 3.1. Model data from four different CCMs were available, CMAM (Canadian Middle Atmosphere Model, Canada, Toronto), NIWA-SOCOL (National Institute of Water and Atmospheric Research - SOlar Climate Ozone Links, New Zealand, Lauder), E39CA (ECHAM4.L39(DLR)/CHEM/-ATTILA European Center HAMburg 4, Oberpfaffenhofen, Germany) and WACCM (Whole Atmosphere Community Climate Model, Boulder, USA). The REF-B1 scenario was available from all models, whereas the REF-B2 scenario could only be provided from CMAM and NIWA-SOCOL.

CMAM

Data from two different model versions were applied in this study. CMAM has a spectral resolution of T31/L71 with the uppermost computational level at 0.00081 hPa (90 km) and

Simulation	CMAM	NIWA-SOCOL	E39CA	WACCM
REF-B1	1990-1999	1990-1999	1990-1999	1990-1999
REF-B2	1990-1999	1990-1999	-	-
	2040-2049	2040-2049	-	-
	2090-2099	2089-2098	-	-

Tab. 3.1: Used model data from different CCMs.

a fully interactive stratospheric chemistry. The 6 hourly output data is used on standard pressure levels with a resolution of 5.6°(lat) x 5.6°(lon) on 41 vertical layers with a top at 0.01 hPa (80 km). The only CCM that was coupled to an ocean is the model version for the REF-B2 simulation from CMAM. The coupled NCOM 1.3 (NCar Ocean Model) ocean general circulation model has a horizontal resolution of 1.86° and 29 levels with a 50 m upper layer and 300 m layers in the deep ocean (Scinocca et al., 2008).

NIWA-SOCOL

The spectral resolution of NIWA-SOCOL is T30/L39. The uppermost computational level is placed at 0.01 hPa (80 km). Two different working groups within the CCMVal community contributed SOCOL (Solar Climate Ozone Links) with some differences in the model setup (Schraner et al., 2008). NIWA-SOCOL differs from SOCOL regarding the lower boundary conditions and some photochemistry details (SPARC, 2010, Chapter 2). For the NIWA-SOCOL model, SOCOL is a combination of the GCM MA-ECHAM4 and the chemical transport model (CTM) MEZON and includes a comprehensive representation of the chemistry of the stratosphere. The resolution of the used dataset is 12 hourly with 3.7°(lat) x 3.7°(lon) including 21 vertical levels up to 10 hPa (30 km).

E39CA

E39CA uses a spectral resolution of T30/L39 and has its uppermost computational level at 10 hPa (30 km). The dynamic part of E39CA is based on ECHAM4 with CHEM as stratospheric chemistry module. A Lagrangian mass conserving non-diffusive scheme ATTILA is used to transport tracers (Steil et al., 2002; Reithmeier and Sausen, 2002; Stenke et al., 2009). The applied dataset for this study is based on a 12 hourly data output with 3.7°(lat) x 3.7°(lon) on 21 vertical levels and top at 10hPa.

WACCM

The last CCM analyzed in this study is WACCM. The model has a spectral resolution of 1.9°(lat) x 2.5°(lon) with 66 vertical levels. The uppermost computational level of the model

lies in the lower thermosphere at 5.96 x 10 $^{-6}$ hPa (98 km). All physical parameterizations are included from the Community Atmosphere model (CAM 3.5) (Gent et al., 2009). MOZART3 provides the stratospheric chemistry for the fully interactive CCM, WACCM (Kinnison et al., 2007; Garcia et al., 2007). The data that was provided in this study is on a 6 hourly time interval and applied with the same resolution and number of vertical levels as described above.

3.1.3 Coupled Model Intercomparison Project Phase 5 (CMIP5) - Models

In anticipation of addressing open scientific questions that arose during preparation of AR4 on the IPCC, a new standard set of coordinated climate model experiments were set up within CMIP5 (Taylor et al. (2012); $http://cmip-pcmdi.llnl.gov/cmip5/$). The goals of the different model simulations are:

- to better evaluate if the simulations of the models are realistic for the recent past;
- to supply projections of climate change in the near (until 2035) and in longer terms (up to 2100 and beyond);
- to capture responsible factors causing differences in the model projections and to quantify cloud and carbon cycle feedbacks.

The historical CMIP5 runs represent simulations from 1850-2005. In this study they were applied from 1990-1999, including all forcings like atmospheric composition with CO_2 (anthropogenic and volcanic), solar forcing, emissions or concentrations of short-lived species and natural and anthropogenic aerosols or their precursors (Taylor et al., 2012).
The characteristics of the different Representative Concentration Pathways (RCPs-greenhouse gas concentration scenarios) experiments, are described in van Vuuren et al. (2011). Four different RCP scenarios were carried out within CMIP5 with different concentrations of

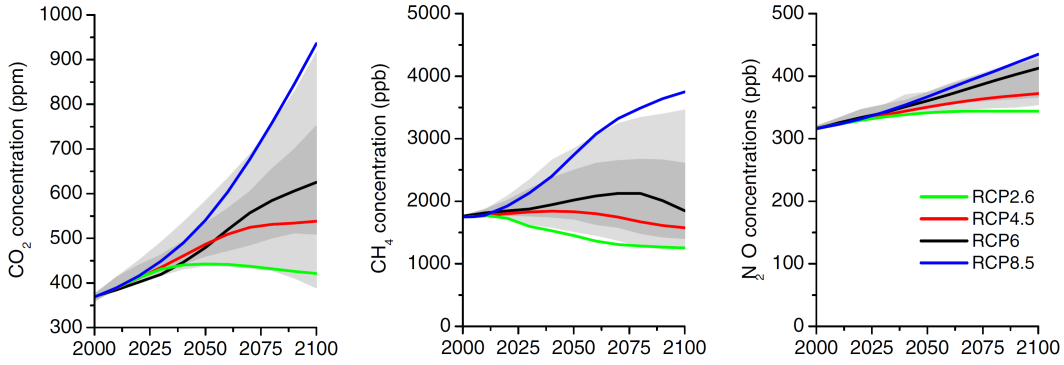

Fig. 3.2: Concentrations of GHGs for different RCP scenarios represented by different colors. Grey area indicates the 98th (light) and 90th (dark) percentile (van Vuuren et al., 2011).

GHGs leading to radiative forcing of 2.6, 4.5, 6 and 8.5 W/m^2 by the end of the century. They are representative in terms of emissions and concentrations developed and published by different scientific working groups and cover the time period up to 2100. The different concentrations of GHGs for the above mentioned RCP scenarios are presented in Figure 3.2. RCP8.5 is a scenario of "non climate policy", whereas the RCP2.6 scenario needs an "exact climate policy" for limiting emissions. In this study the RCP8.5 scenario was applied, where emissions and concentrations of the greenhouse gas considerably increase in time. Radiative forcing leads to 8.5 W/m^2 in 2100 without including any specific climate reduction targets, (see also Keywan et al., 2011). The concentration of CO_2 in the RCP8.5 scenario is almost three times higher in 2100 than in 2000. For CCMVal-2 REF-B2 scenarios the CO_2 doubles until the end of the 21st century (Figure 3.1).

MPI-ESM

In this study, output of the Max Planck Institute Earth System Model Low Resolution (MPI-ESM-LR) was used. The Atmosphere in MPI-ESM is based on the compounds of ECHAM6 with a spectral resolution of T63 with 47 vertical levels and model top at 0.01 hPa (80 km). The Max Planck Institute ocean model (MPIOM) uses 1.5° resolution and 40 vertical levels. Additionally, the land biosphere model JSBACH and the biogeochemical Model HAMMOCC are compounds of MPI-ESM. A separate coupling program (OASIS3) enables the exchange of information numerical codes representing different components of the climate system between ocean and atmosphere. Compared to ECHAM5/MPIOM the IPCC-AR4 model from Hamburg was expanded by the carbon cycle to make statements about the influence of climate change on the carbon cycle for the upcoming 5th assessment report from IPCC (Giorgetta et al., 2012).
For this study model output with a resolution of 1.85° (lat) x 1.875° (lon) using 26 vertical levels and top at 1 hPa (50 km) was applied. One historical run from 1990-1999, and the future runs for 2040-2049 and 2090-2099 from the RCP8.5 scenario were used (Table 3.2).

Simulation	MPI-ESM
Historical	1990-1999
RCP8.5	2040-2049
	2090-2099

Tab. 3.2: Used model data from MPI-ESM-LR.

3.2 Lagrangian transport model

Two different approaches are usually used to analyze the transport of air masses, the Eulerian and the Lagrangian approach. In the "Eulerian" perspective, a fixed point in space is observed where air masses are passing by. At this constant location, the evolution of different parameters of the air can be observed. With the "Lagrangian" approach in contrast, one

considers the changes in temperature or in other variables along the path of an air parcel. This path is called a trajectory. In the present study the Lagrangian method was applied. The objective of this work is to gain knowledge about the origin of air masses in the lower tropical stratosphere, which is done by analyzing large scale atmospheric transport. More detailed, air masses are analyzed along backward trajectories. Considering backward trajectories is a common approach to derive the history of air masses at a given location of interest, e.g in the tropical lower stratosphere. In contrast, forward trajectories give a better estimate of the region, where air masses arrive.
To avoid confusion, we describe the here used backward trajectories on the basis of forward motion and therefore, the numerical initialization (or start) point is called the trajectory end point and the numerical end point is labeled as the origin of the air mass or trajectory start point.

3.2.1 Numerical trajectory calculation

In reality, the exact path of an air mass is not known, but indicated by the windfield. To find a precise trajectory, it is useful to consider the problem as an "initial value problem". As the windfields exist on a finite grid, numerical approximations must be used to find a solution of the initial value problem.
A trajectory is then equivalent to a numerical solution of the differential equation 3.1, which describes the path of an air parcel over time. In a flow field u, each air parcel is moving during the time t along a path $x(t)$.

$$dx(t)/dt = u(x(t), t). \tag{3.1}$$

First, it is necessary to define a starting point of the trajectory, which equals the specification of the numerical initial value problem by setting $x_0 = x(t_0)$. Then, numerical methods can be applied to find a function $x(t)$, which fulfills the initial value problem defined by equation 3.1 and x_0.
Here, the Runge Kutta method is used to calculate an approximation of the trajectory. The numerical value x_n at time t_n is obtained using previous values x_m, $m < n$, in accordance to 3.1, where a reduction of the arising discretization error (see below) is obtained by the use of supporting points between t_n and $t_n + 1$.

In Figure 3.3 a real trajectory (solid curve) and its approximation (dotted curve) are exemplary given. Obviously, the approximated trajectory does not exactly correspond to the real path of the trajectory, which is caused by the discretization error, visualized by the short dashed lines in Figure 3.3. Figure 3.4 shows on the left a one dimensional function $x(t)$ within the interval $[t_n, t_n + h]$ and on the right, an approximation of the same function when applying the Runga Kutta method. Here, a fourth order method is shown, where four derivatives (f_1, f_2, f_3 and f_4) are combined to get the best estimate of the change of $x(t)$ in the interval $[t_n, t_n + h]$.

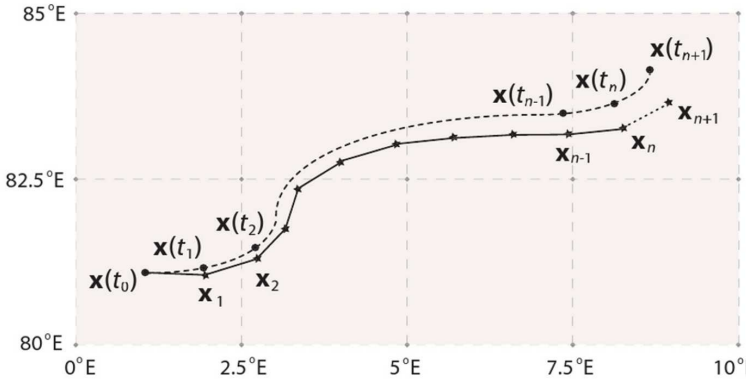

Fig. 3.3: Approximation for the path of a trajectory. The dotted curve represents the trajectory $x(t)$ for the time interval $[t_0, t_{n+1}]$, a numerical approximation is given by the solid curve (Tegtmeier, 2006).

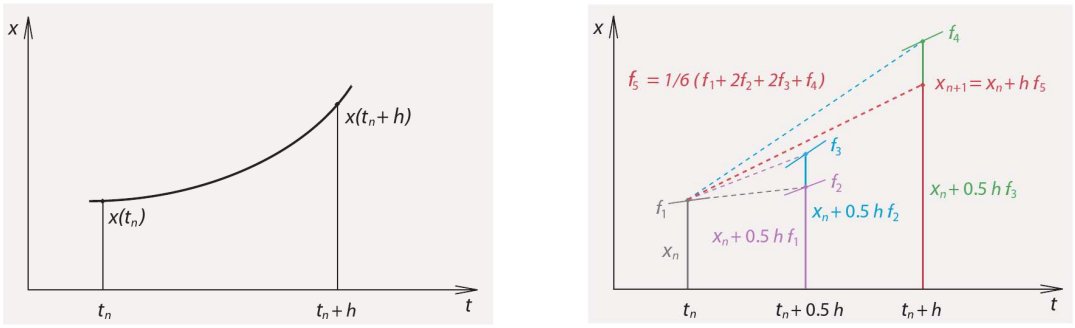

(a) (b)

Fig. 3.4: The function $x(t)$ for the interval $[t_n, t_n + h]$ (a), and the numerical approximation for the Runge Kutta method (b) (Tegtmeier, 2006).

The linear combination f_5 (red line) of these derivatives is used to determine the approximation x_{n+1}.
The integration steps of the numerical method are based on the meteorological variables at the integration positions. Within the routine of the trajectory model, a linear interpolation is being applied to determine the meteorological data as it is only available on a limited grid.

3.2.2 Vertical transport

There are two different ways to implement vertical transport in a numerical trajectory model. One can use the *kinematic* or the *diabatic* method (Schoeberl et al., 2003). The kinematic method is based on the continuity equation, whereas the diabatic method is based on the energy balance equation.
In the diabatic calculations, horizontal transport takes place on isentropic surfaces. The

cross-isentropic vertical motion $\dot{\Theta}$ is derived by the radiative heating rate through the energy balance equation. The vertical velocity is given by the potential temperature tendency.

$$\dot{\Theta} = Q\frac{\Theta}{T}, \tag{3.2}$$

with temperature T and $Q = \frac{J}{c_p}$, including diabatic heating rate J and specific heat capacity c_p.

In contrast, in the kinematic method, air parcels are moved along isobars driven by horizontal wind transport. The unit of the vertical coordinate is pressure, hence the vertical velocity ω is given by the pressure tendency. The vertical motion (Equation 3.3) is derived by integrating the continuity equation from surface pressure p_s to p and thus, the vertical velocity ω at pressure p is derived using the horizontal gradient ∇^h of the horizontal velocity V^h where u and v represent the horizontal wind components and ω_s=0 assuming a horizontal surface (Holton, 1992, Chapter 3.5).

$$\omega = \omega_s - \int_{p_s}^{p} \nabla^h \cdot V^h dp. \tag{3.3}$$

$$V^h = (u, v) \tag{3.4}$$

Horizontal winds dominate atmospheric motion, and thus, these wind fields are much larger than the dimension of vertical windfields. Hence, already small errors in the horizontal wind can lead to large errors in the vertical wind. Trajectories, numerically derived by the kinematic or the diabatic method, differ due to their unequal underlying initialization fields (diabatic heating for the diabatic method and horizontal wind for kinematic method) and the physical equations the calculations are based on (energy balance for the diabatic method and mass balance for the kinematic method). Thus, model results based on the two calculation methods do show differences like different pathways to the stratospheric overworld, while the real trajectory is unique. E.g. Ploeger et al. (2010) showed differences in the net heating fields derived from trajectory calculations in the upper TTL when using the two methods. Their results demonstrate that based on the diabatic method almost no subsidence occurs (because $d(\theta)/dt$ is positive in average), while with the kinematic method frequent subsidence is visible. As comparable measurements do not exist, the question which method is the actual more realistic one can not be answered.

3.2.3 Applied trajectory model

In this study, the trajectory model developed by Tegtmeier (2006) for polar studies, was used for the TTL. It is based on the Runge Kutta method and includes diabatic and kinematic transport as well. The model code was adapted to the purpose of the present study. In particular, import routines needed to be adapted due to the application of various model datasets using different resolutions in time and space.

Within this study, the trajectory model is used applying the kinematic method, since the model data used in the present study is mainly from GCMs where the trace gas transport in

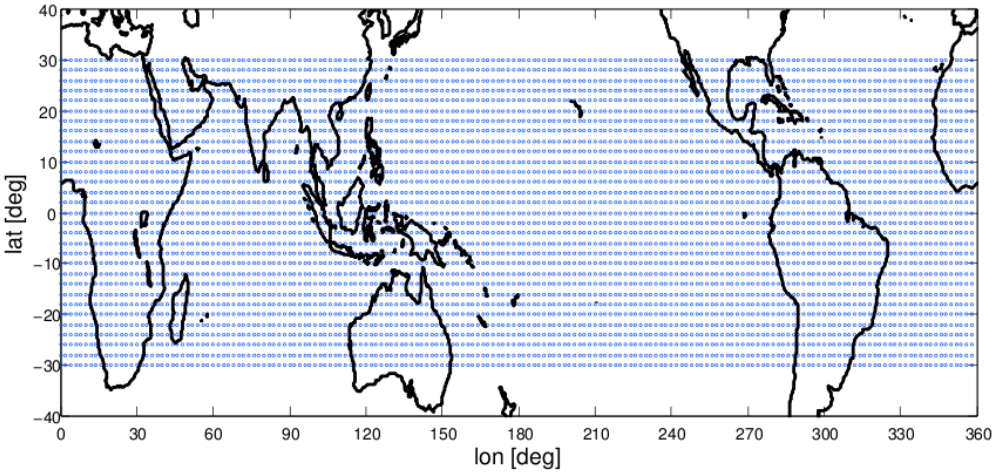

Fig. 3.5: Location of the initialization points of the trajectory model represented by the blue dots on a 2° x 2° grid from 30° S to 30° N.

the advection schemes is driven by vertical winds. The given vertical winds from the input data can be used directly to drive kinematic trajectories. Hence, in this study the kinematic method has been applied and vertical motion of an air parcel is calculated based on these vertical winds. The potential temperature is used as a measure of height for these quasi isentropic trajectory calculations (Chapter 4, 5 and 6).

3.2.4 Model setup

The back-trajectories were all started on the potential temperature level of 400 K (420 K for future simulations, chapter 6), which lies in the upper part of the TTL at around 18.5 km (19 km) (see chapter 2.3.1). For the backward calculation it is important that the initialization point lies above the cold point tropopause, which is at approximately 90 hPa or 17 km (see chapter 2.3.1). The trajectory model setup is on a 2° x 2° grid, spanning 30 ° S to 30° N, which results in 5580 trajectories for each run. The blue dots visualize the location of the initialization points in Figure 3.5.
The LCPs, calculated in this kinematic study, were reached in most cases within the first 30 days of the backward calculation. In order to span a whole season with well distributed LCPs and to get a good statistical coverage, the model was initialized at the end of each month of a season separately (Figure 3.6(a)). This means, e.g., for the winter season that the model is initialized at the end of February, January and December running for each initialization until the first of December.

To decide on the UTC starting time of the trajectory calculations, sensitive studies were carried out (Section 4.1.2). Resulting LCP patterns indicate that the distribution of the LCPs is sensitive to the different vertical windfields at initialization UTC time, which is found for the 6 hourly ERA-Interim reanalysis output. In order to not favor a certain UTC

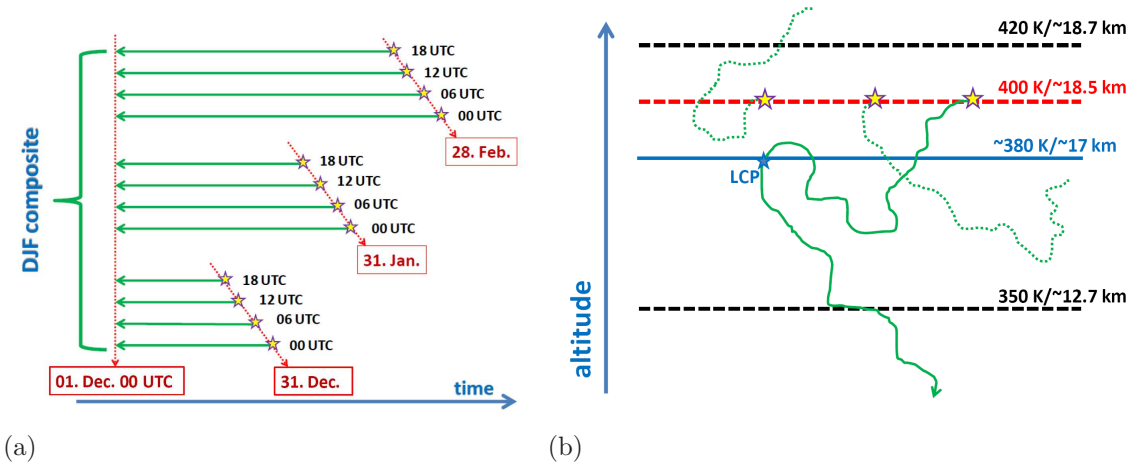

(a) (b)

Fig. 3.6: Schematic of initialization method for the trajectory model (a) and a visualization for the sample criteria of the trajectories (b), the green solid curve represents a trajectory that fulfills the sample criteria. The green dashed curve represent trajectories that are not considered. The sample criteria implies that only trajectories are considered that reach the 350 K at least once and stay below 420 K. Their dehydration point usually happens near the 380 K potential temperature level.

pattern connected to one particular UTC starting time, trajectory runs were initialized four times each month: at 00, 06, 12 and 18 UTC. The schematic in Figure 3.6(a) illustrates this initialization of the trajectory model. For each season, 12 model starts were initialized. The resulting LCP distribution for one season is then a composite of the results from these 12 model runs. Thus, 1548 model initializations for the ERA-Interim dataset are performed (between 1979-2011), which yields to a total of 8.637.840 trajectories with a computing time of ∼130 hours in total.

For the analysis of the trajectories only selected trajectories were considered, namely the ones fulfilling certain conditions. These are that trajectories need to reach at least once the 350 K θ level, which is the level of main convective outflow (at around 200 hPa or 12,5km). Furthermore, to analyze air masses traveling through the TTL and to avoid backflow from the higher stratosphere, only those trajectories are considered that stay below 420 K (440 K for future simulations). According to this selection the trajectories that travel from the troposphere to the stratosphere are considered to calculate the LCP, the coldest point of each trajectory and their geographical location (Figure 3.6(b)).

3.2.4.1 Annual averages

With the calculation of trajectories seasonal maps are obtained. In case for the NH winter season, months from two sequent years are considered. Hence, the method for the averaging of the annual means contributing to the time series need to be described in more detail, which is given here.

As mentioned before, ERA Interim data is available from Jan 1979 onwards. Thus, the first seasonal map for a trajectory run is available for the NH spring season (MAM) 1979. An

annual average is calculated by averaging over the four seasons of a year, beginning with NH spring. Hence, e.g., the annual average of the year 1979 results from an average of NH spring (MAM), summer (JJA) and fall (SON) of 1979 and winter (DJF) 1979/1980.
In case of the climate models the annual averages are calculated in the same way. However, as the climate model data of the year 2000 was only provided from NIWA-SOCOL REF-B2, for the other climate models the datapoint at the year 1999 was calculated based in spring, summer and fall averages of 1999 and the winter average of December 1999 and January/February 1999 (instead of January/February 2000)

3.3 Methods

3.3.1 Lagrangian cold point analysis

To derive the geographical distribution of the LCPs for one season of a year, the model setup method and sample criteria has been applied as described in section 3.2.4. Thus, the LCP distribution for a season is a composite of 12 LCP distributions at the different initialization times 00, 06, 12 and 18 UTC (for a 6 hourly dataset) and for each month of a season. This was applied for ERA-Interim, CMAM, WACCM and MPI-ESM. In case of a 12 hourly input, the composition for one season is accordingly composed by only 6 different LCP distributions with and initialization twice per day, 00 and 12 UTC and each month separately (NIWA-SOCOL, E39CA). The composite of the results from the different initialization conditions represent the average LCP distribution for a season. A composite of the seasonal LCP distribution in turn, represents the annual average LCP distribution.
As an example, Figure 3.7 shows the composite of the LCP distribution for DJF 1999/2000 for ERA-Interim including the different model start conditions (composition from 12 model starts as illustrated in Figure 3.6(a)). The minimum temperature of one trajectory, fulfilling the mentioned conditions, are marked by the colored dots.

3.3.2 Widening of the upper TTL

LCPs represent the location where tropospheric air masses enter the stratosphere. As air enters the stratosphere primarily in the tropics the LCPs represent the upper tropical tropopause layer (TTL) (section 2.3.1). Here, only the method of analyzing the LCPs will be presented. The obtained results of analyzing the widening of the upper TTL, are further described in chapters 5 and 6. Hence, to get the information about a possible widening of the upper TTL, the latitudinal distribution of the LCPs needs to be determined. For this analysis as well only those trajectories are considered that fulfill the above mentioned sample criteria (section 3.2.4). First it is important to define a threshold setting the border of the upper TTL properly, in order to derive a robust border of the width of the upper TTL region. In the next step, the change of the border of the upper TTL on long-term can be analyzed.
A simple method to derive a stable threshold, would be to count the number of the same

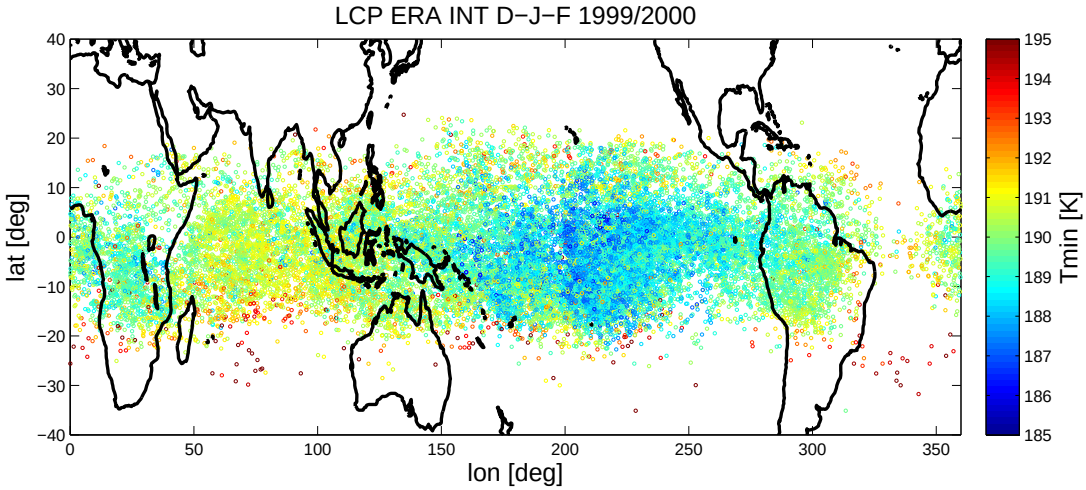

Fig. 3.7: Composite scatter plot of the temperature and geographical distribution of LCPs for ERA-Interim DJF 1999/2000.

amount of LCPs within the tropical belt, which then defines the width of the upper TTL. Due to the sample criteria the LCPs have to fulfill (section 3.2.4), the amount of trajectories reaching the LCP is varying for each initialization. Thus, the calculation of a certain percentile to choose as threshold for the upper TTL border, was found to be a good option. The percentile is a statistical measure to calculate a value (here: width of the LCP distribution) of a variable (here: the number of LCPs), below which a given percentage of observations (here: LCPs) fall, i.e. by taking the 90th percentile for example, the value of the width of the TTL can be determined, below which 90 percent of the LCPs may be found. Figure 3.8 presents one example of the tropical distribution of LCPs for a model initialization at 00 UTC from ERA-Interim DJF 1999/2000 (left side). Additionally, the latitudinal distribution of LCPs sampled in 2 ° bins is visualized (right side). The areas that represent possible thresholds for the border of the TTL, 90 and 70 percentiles, are roughly sketched with the pink and blue shaded regions around the equator.

After calculating the geographical and then the latitudinal distribution of the LCPs for each season, one can determine the width of the upper TTL in degrees North and South for each season by choosing a certain percentile. To find the most stable threshold of the border of the TTL, different percentiles of the LCPs were analyzed from the annual average LCP distribution, resulting in a certain value for the changing of the width of the upper TTL for each percentile.

The timeseries of the width of the upper TTL for ERA Interim from 1979-2010, based on different percentiles is presented in Figure 3.9. It is shown, depending on the percentile, certainly the width of the upper TTL is varying by approximately 5 ° latitude between the 70th and 90th percentile.

Figure 3.10 presents the change in the width of the upper TTL for the annual mean LCP distribution between 1979 and 2010 as a function of percentile. The significance of each

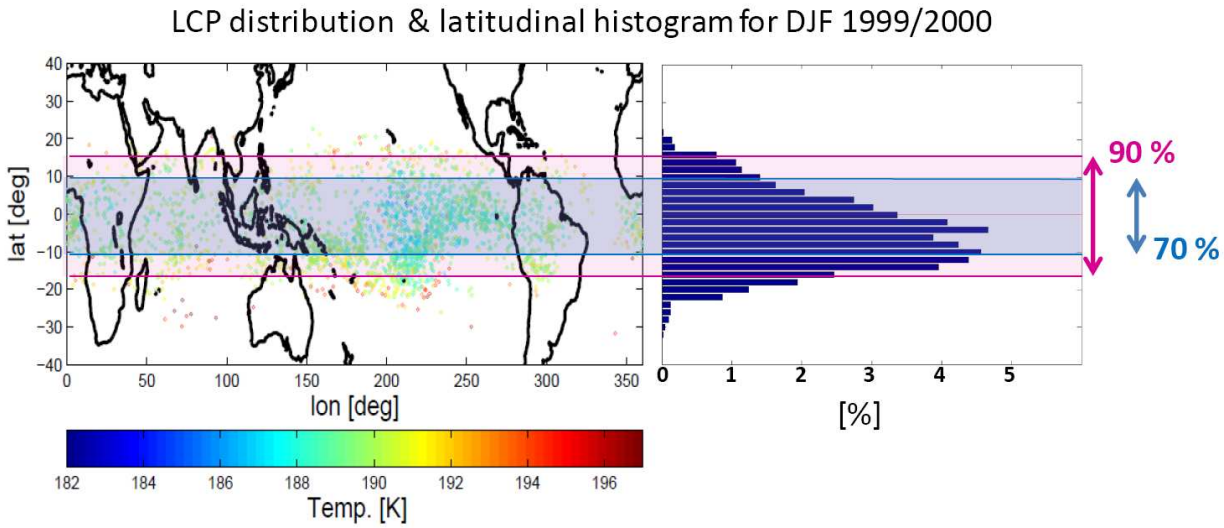

Fig. 3.8: Geographical distribution of LCPs for DJF 00 UTC 1999/2000 initialization (left side), corresponding histogram of the latitudinal LCP distribution (right side). The pink and blue shaded regions represent the 90th and 70th percentile of the LCP distribution.

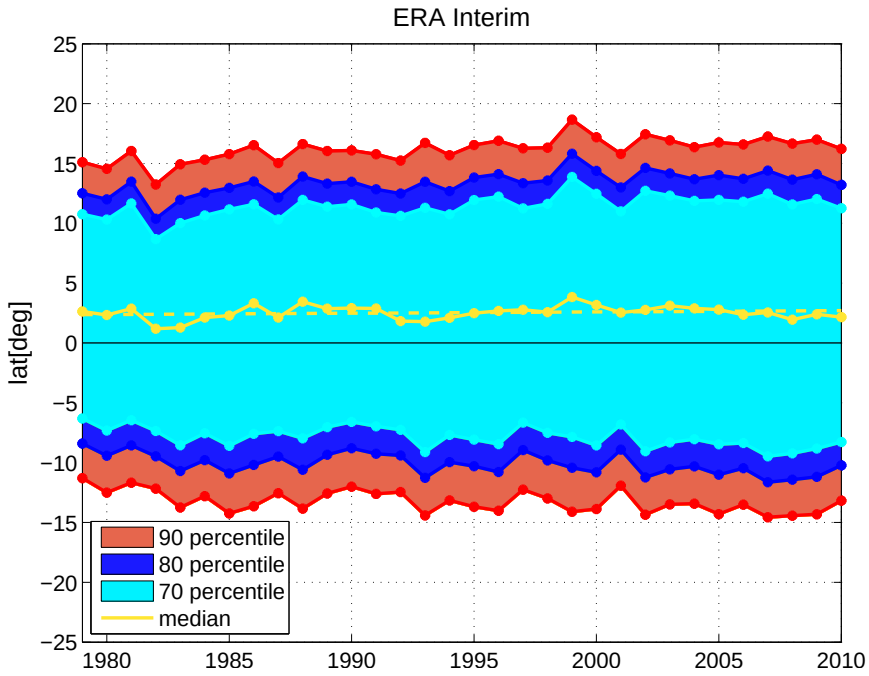

Fig. 3.9: Annual average width of the upper TTL represented by the 70th, 80th and 90th percentiles and the median of the LCP distribution for ERA Interim from 1979-2010.

value (within 95% significance level) is given by the blue lines. Ranging from smaller up to higher percentiles, the changing of the width of the upper TTL is increasing but also the error bars, due to the decreasing density of LCPs in the subtropics (see also Figure 3.7). The

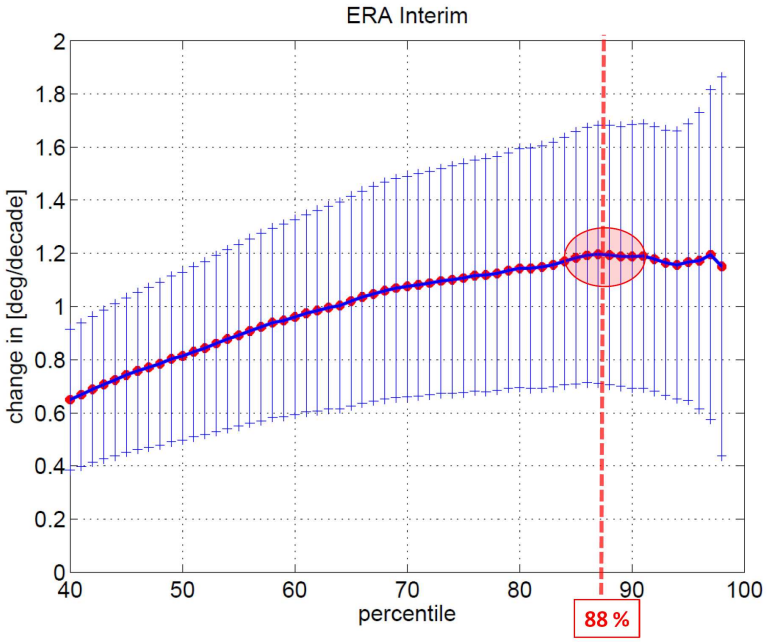

Fig. 3.10: Change of the width of the TTL (in degrees/decade) for the annual mean for different thresholds (percentiles), shown for the time period 1979-2010 for the ERA-Interim data. Red dots mark the value of the widening of the TTL, blue vertical lines mark the standard 1.96 σ (95%) error bars for each calculated percentile.

largest changes in the width of the upper TTL, is given by the percentiles between 85th and 90th. Also here the most stable interval of changes is visible. Consequently the threshold used as upper TTL boundary was found to be described by the 88th percentile of the LCPs distribution as best. To calculate the change in the width of the upper TTL, the gradient of the linear regression of the total width of the TTL for the 88th percentile is analyzed. The results concerning the longer term changes and the differences between seasons, hemispheres and the different model data, will be presented in chapters 5 and 6.

Chapter 4

TTL analysis

In this chapter, long-term climatologies for the upper TTL, analyzing the Eulerian and the Lagrangian cold points are presented based on the new ERA Interim product from the ECMWF for the time period 1979-2011 (section 4.1). Different CCMs from CCMVal-2 and one climate model from CMIP5 are analyzed likewise for the time period 1990-1999 (section 4.2). Differences and similarities between ERA-Interim and the climate models for the Eulerian and Lagrangian temperature patterns are determined. Furthermore, the geographical distribution of the LCPs on a seasonal and interannual cycle.

4.1 ERA-Interim

4.1.1 Eulerian cold point

The minimum temperature is determined by identifying the vertically lowest temperature of the 37 standard pressure levels of the ERA Interim assimilation, from surface (1000 hPa) to the upper stratosphere (1 hPa). This minimum temperature is called the Eulerian cold point. Typically, the CP temperature appears near 90-105 hPa (Randel, 2010). Due to application of the data on standard pressure levels (37 levels) and the lower vertical resolution compared to the model levels (60 levels), the temperature minima, at least for the ERA Interim dataset, are mostly found on the 100 hPa pressure level.

4.1.1.1 Climatology

The climatology for the tropical average annual CP temperature for 1979-2010 for the ERA Interim reanalysis is presented in Figure 4.1. The coldest region for the TTL, the so-called "cold trap" is visible over the West Pacific. In accordance to Figure 4.1, the lowest temperature in the annual mean reaches 190.5 K. The annual mean CP temperature within the tropics is adjusted almost meridionally symmetric to the equator. The temperatures are ranging from around 190 K to 202 K from the equator to 30° latitude. The region with lowest temperatures of 190 to 192 K over the West Pacific agrees with the location for the CP temperature from ERA 40 data analyzed for the time period 1979-2001 in Fueglistaler et al.

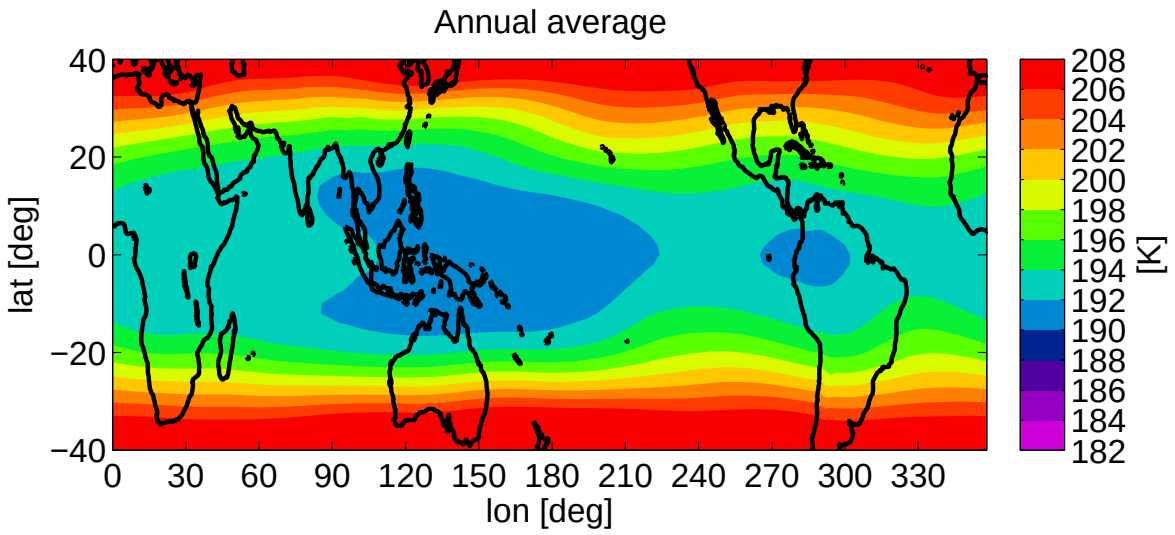

Fig. 4.1: Climatology of the Eulerian cold point temperature for the annual mean using ERA Interim 1979-2010; contour interval is 2 K.

(2005). But for ERA Interim lower temperatures on the annual average occur over South America compared to the ERA 40 pattern. A comparison of the tropical CP temperature using ERA-40 and ERA Interim data reveal generally 1 to 2 K lower temperatures in ERA Interim as well (Gettelman et al., 2010)

For the ERA-Interim dataset, from 1979-2011, the seasonal variation of the minimum temperature in the TTL is illustrated in Figure 4.2. The lowest CP temperature (188 K) occurs during NH winter (Figure 4.2(d)). The highest CP temperature minimum occurs during boreal summer with 192 K (Figure 4.2(b)), where the branch of lowest temperatures towards the Indian ocean is influenced by the Asian Monsoon, usually starting in June lasting until September (Kumar et al., 1999). The structure of the CP temperature distribution during NH fall (Figure 4.2(c)) mostly resembles the temperature pattern during NH summer with a lower temperature minimum of 191 K. The spatial structure of the CP temperature distribution during boreal spring (Figure 4.2(a)) seems to be more similar to the CP temperature pattern during NH winter indicating only a small area over the West Pacific with temperatures between 188 and 190 K.
In comparison to the Eulerian temperature fields shown for ERA 40 data in Fueglistaler et al. (2005), the CP temperature is generally similar centred for ERA Interim during all seasons (this study). A barbell structure of the lowest temperatures is visible during all seasons in ERA 40, which is not occurring during NH winter and spring for ERA Interim. Besides, during NH winter, a second centre of minimum temperatures is occurring over South America for ERA Interim, with similar low temperatures like over the West Pacific (Figure 4.2(d)). This phenomena is not occurring in the ERA-40 timeseries from 1979-2001 (Fueglistaler et al., 2005). Comparing the strength of the minimum temperatures, the results from ERA In-

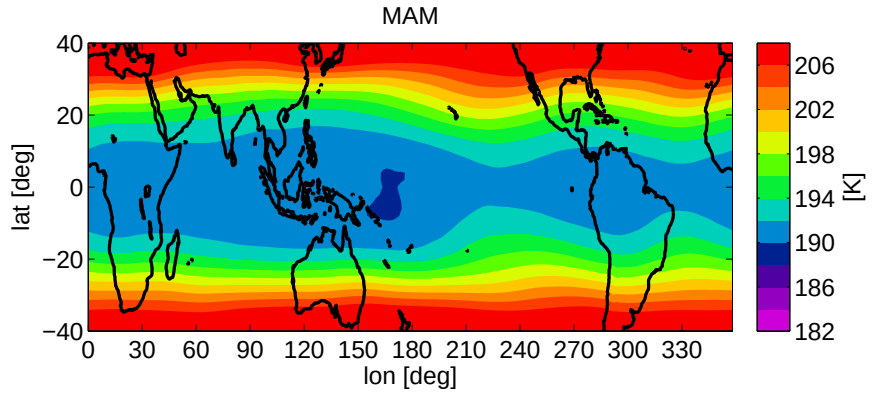

(a)

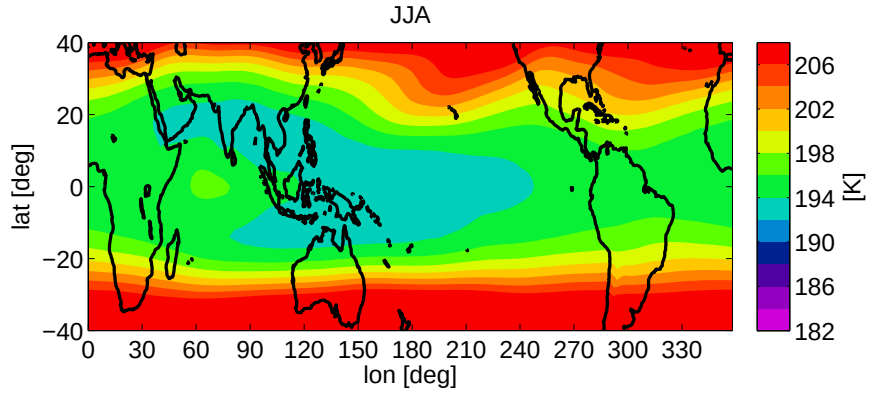

(b)

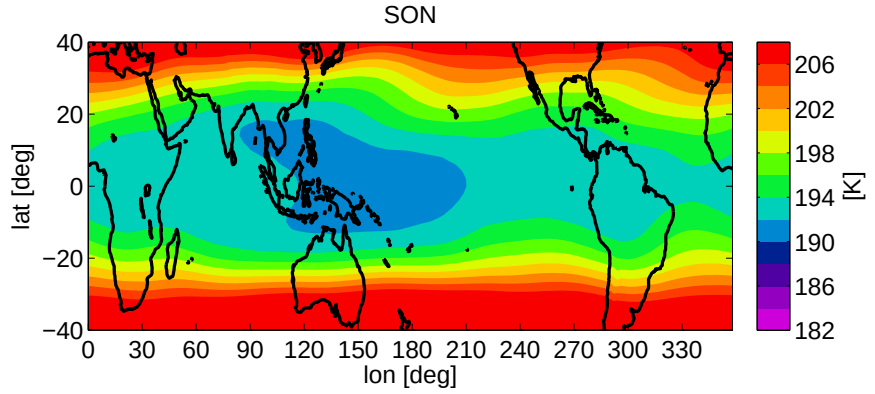

(c)

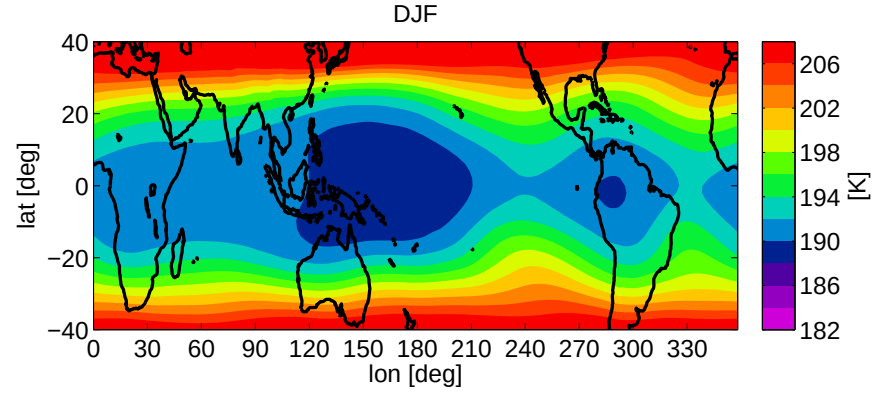

(d)

Fig. 4.2: Climatology of the Eulerian cold point temperature for different seasons using ERA Interim 1979-2010; contour interval is 2 K. MAM (a), JJA (b), SON (c) and DJF (d).

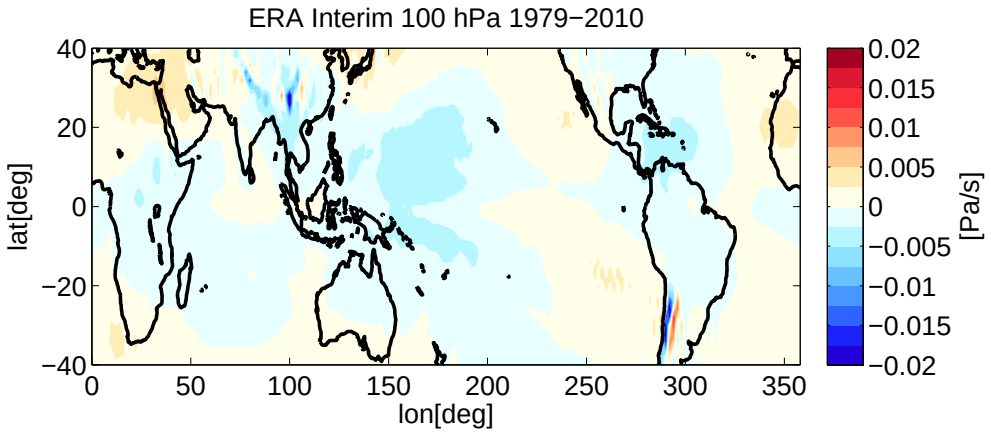

Fig. 4.3: Annual average vertical velocity in 100 hPa for ERA-Interim (1979-2010)

terim, presented in Figure 4.2, indicate lower minimum temperatures of 1 to 2 K compared to the results based on ERA-40 data.

4.1.2 Vertical wind fields

The resulting geographical pattern of the LCPs is also strongly depending on the vertical wind fields next to the TTL temperature in itself (Wohltmann and Rex, 2008; Krüger et al., 2008). For analyzing these effects more closer, the vertical wind fields on the annual average and at different UTC time with the resulting LCP pattern are investigated.
The annual average vertical velocity field in 100 hPa (16 km) using ERA Interim (1979-2010), is presented in Figure 4.3. On the annual average ascent regions are visible over the West Pacific, the Caribbean Sea and over Africa (blueish colors). Noisy patterns occur over South America and the Tibetan plateau probably affected by high altitude mountains, the Andenes and the Himalaya. Subsidence is apparent over North West Africa and the middle East, visible by the reddish color. Thus, ascent regions are in accordance with the main LCP accumulation regions (compare with Figure 4.8).

4.1.3 LCP sensitivity study

4.1.3.1 Vertical wind fields

Global maps of the climatological vertical wind fields in the 100 hPa layer of the NH winter season (DJF, ERA-Interim 1980-2010) are shown in Figure 4.4. Four different UTC times were used to initialize the trajectory model. The mean vertical wind for 00 UTC (Figure 4.4(a)), reveals a pronounced upward motion of air over the western Pacific and parts of South America, which is indicated by the blue colored area with negative units in [Pa/s] of the vertical velocity. However, over the maritime continent subsidence is modeled by the ERA Interim reanalysis 00 UTC product. The wind field for 06 UTC in 100 hPa is shown in

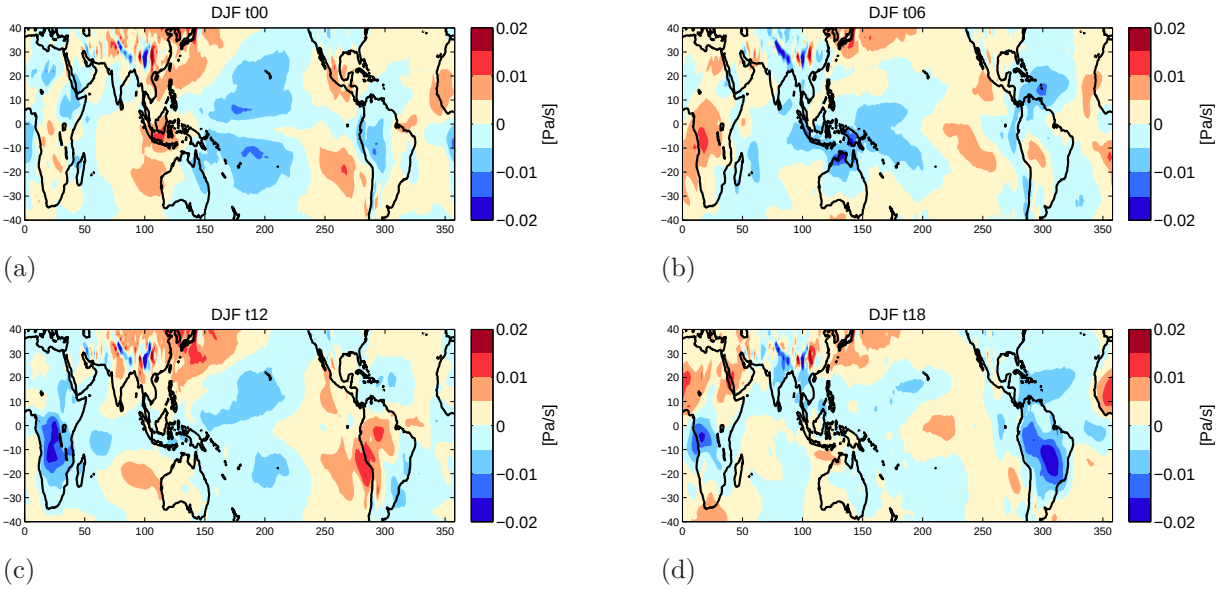

Fig. 4.4: Vertical velocity in [Pa/s] for different UTC time at 100 hPa for DJF 1979-2010 average (a) 00 UTC, (b) 06 UTC, (c) 12 UTC and (d) 18 UTC.

Figure 4.4(b). Upward motion is occurring mainly over the maritime continent, whereas a relatively strong subsidence is indicated over West Africa (colored red). The sign of vertical motion over West Africa changes for 12 UTC (Figure 4.4(c)). Relatively strong upward motion occurs at noontime over West Africa and downward motion over South America. This motion over South America changes for 18 UTC (Figure 4.4(d)). The pattern of the strongest vertical upward motions seems to propagate simultaneously with the local noon time, reflecting a pronounced diurnal cycle due to solar insolation. The vertical velocity in 100 hPa is clearly dominated by convection. Thus, the diurnal pattern must be also reflected in convection activity at 100 hPa. Indeed, tropical convection is observed to have a diurnal cycle, which is pronounced over land masses and weak over the oceans (Handon and Woodberry, 1993). This feature of a noticeable stronger vertical wind, hence convective activity, over the continents compared to the oceans is also visible in Figure 4.4. A maximum in brightness temperature, which stands for high convective clouds, over the continents around local noon time was found by Yang and Slingo (2001), which agrees with the strongest vertical velocity fields over the continents around local noon (Figure 4.4).

4.1.3.2 LCP distribution

Figure 4.5 shows the mean density of the different geographical distribution of LCPs for the four different starting times of the trajectory model for DJF 1980-2010. In Figure 4.5(a), the density of the occurrence of the LCPs for a starting time at 00 UTC of February 28 is presented. Most of the trajectories reach their temperature minimum over the West Pacific. The density distribution for a starting time at 06 UTC is shown in Figure 4.5(b). Here, still

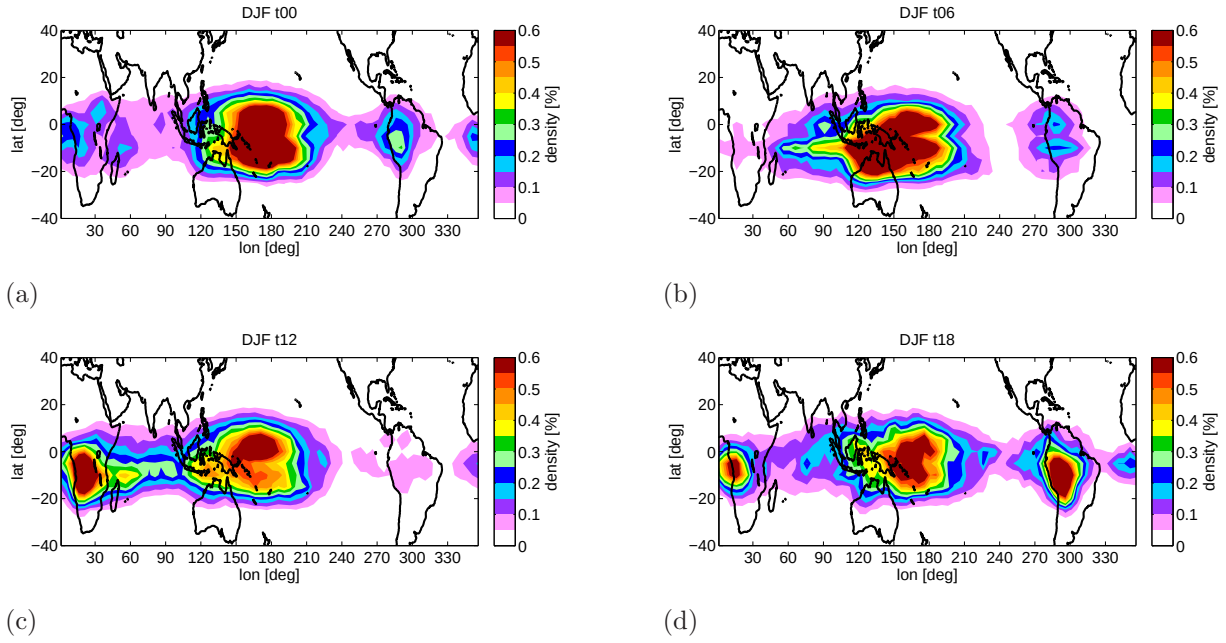

Fig. 4.5: Distributions of the LCPs relative density per 5° x 5° grid with contour interval of 0.05% regarding the different initialization time UTC for DJF averages 1980-2010 of the trajectory model runs. 00 UTC (a), 06 UTC (b), 12 UTC (c) and 18 UTC in (d).

most of the LCPs are located over the western Pacific, but with an enlarged area to West and to the East. For a model initialization at 12 UTC (Figure 4.5(c)), beside an accumulation of the LCPs over the western Pacific, which is a little smaller than for 00 UTC and 06 UTC, also a large amount of trajectories reach their entrainment point over West Africa. When initializing the trajectories at 18 UTC of February 28 (Figure 4.5(d)), a large number of LCPs appear over South America as well. The density of LCPs over West Africa decreases but is still existent.

These different diurnal patterns occur for all seasons with different starting times (not shown here). The main entrance region of tropospheric air masses reaching the stratosphere is the maritime continent. However, a large number of trajectories, which reach their coldest points, seems to shift their entrance regions towards local noontime, hence the location of maximum insolation of the model start. This may be connected with the existing vertical wind fields (compare with Figure 4.4) near the model start region (400 K, which is approximately at 100 hPa). One explanation could be that the trajectories are strongly influenced by the first time steps of the initial windfield. The vertical windfield for DJF 18 UTC shows a strong vertical upward motion over South America at 100 hPa, which is consistent with the maximum density of LCPs over this continent (compare Figure 4.5(d) and 4.4(d)). In Figure 4.4(b) an enlarged upward motion is apparent over the tropical West Pacific at 2 pm localtime, resulting in a large density of LCPs over the maritime continent (see Figure 4.5(b)).

4.1.3.3 Case study

To explain the connection between LCPs and the initialization wind field, single trajectories from different starting times (UTC), were considered. Figure 4.6 shows exemplary the behavior of several single trajectories starting over South America for different starting UTC times of February 28 th of 1996. For this sensitivity test, all trajectories are considered, which means the trajectories did not need to fulfill the conditions of the sample criteria as explained in section 3.2.4. The evolution of the potential temperature, starting at 400 K, is displayed for the following 90 days of calculation. Due to their different starting time at 00, 06, 12 and 18 UTC, the trajectories are initialized by different wind fields, resembling the average windfields shown for the average NH winter in Figure 4.4. Thus, the trajectories whose initialization location is above the South American continent are influenced by these wind fields respectively. It is expected that the trajectories, which were started at 00 UTC experience an upward motion due to the initialization field, which indicates a slight upward velocity over South America (Figure 4.4(a)). The resulting evolution of an exemplary number of trajectories started over South America are displayed in Figure 4.6. Approximately half of those trajectories, originate from the lower stratosphere. The other half comes from below and crossed the 350 K θ level. Thus, those trajectories fulfill the sample criteria and are considered afterwards in the LCP analysis. The trajectories initialized at 06 UTC and 12 UTC (Figure 4.6(b) and 4.6(c)) are expected to show an upward motion over South America. The single trajectories from 06 and 12 UTC (Figure 4.6(b) and 4.6(c)) behave similar to those from 00 UTC (Figure 4.6(a)). Some trajectories originate from above the initialization level and some from below, which reduces the LCPs fulfilling the criteria. The trajectories, which are initialized at 18 UTC (Figure 4.6(d)), experience at their first initialization step a strong upward motion, caused by the underlying meteorological wind field with a strong upward motion above South America (see Figure 4.4(d)). Thus, all the single trajectories originate from below and hence, fulfill the sample criteria. Figure 4.7 shows exemplary for DJF 1995/96, the average time of the trajectories to reach their minimum temperature. The trajectories were started for each month of a season individually. The majority of the trajectories reach their LCPs within the first 30-40 days.
The different behavior of these trajectories caused by their underlying wind fields could be the explanation of an accumulation of the LCPs in the respective area of relatively strong vertical upward motion at noontime, e.g. also visible in the accumulation of LCPs over West Africa for an initialization at 12 UTC (compare Figure 4.5(c) and 4.4(c)).
The effect of the initialization field on the LCP distribution has been analyzed within this study for ERA Interim. So far, these dependencies haven't been mentioned in any other study yet. Furthermore, other publications do not mention a favorized starting time of their Lagrangian calculations. In the following, the trajectories were calculated based on an average LCP distribution resulting from the trajectory initialization times 00, 06, 12 and 18 UTC.

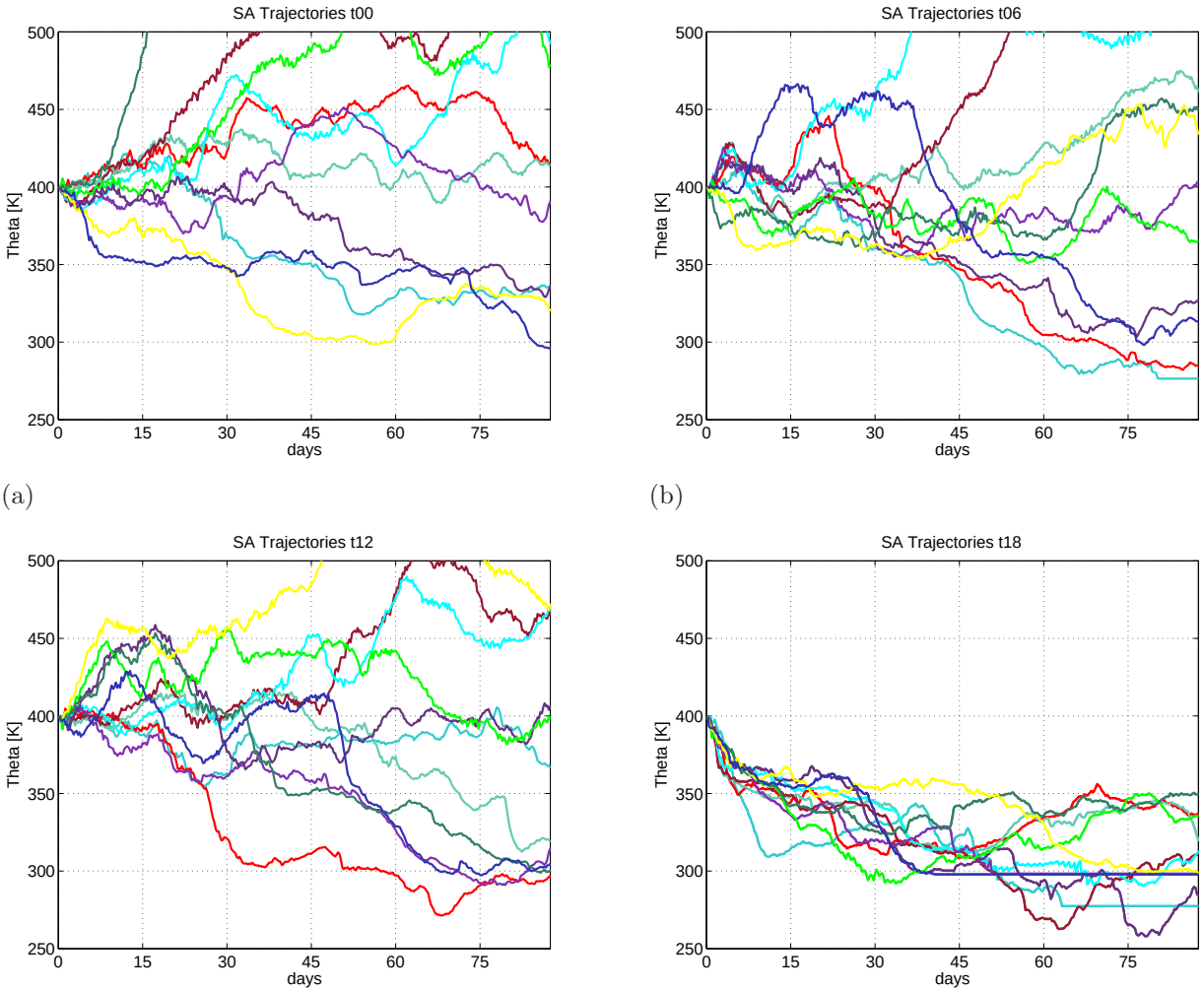

(a) (b)

(c) (d)

Fig. 4.6: Evolution of the potential temperature for different initialization times from randomly chosen single trajectories over South America in DJF 1995/1996. 00 UTC (a), 06 UTC (b), 12 UTC (c) and 18 UTC (d), different colors indicate different starting locations of trajectories over South America. Same colors indicate same location of trajectory start.

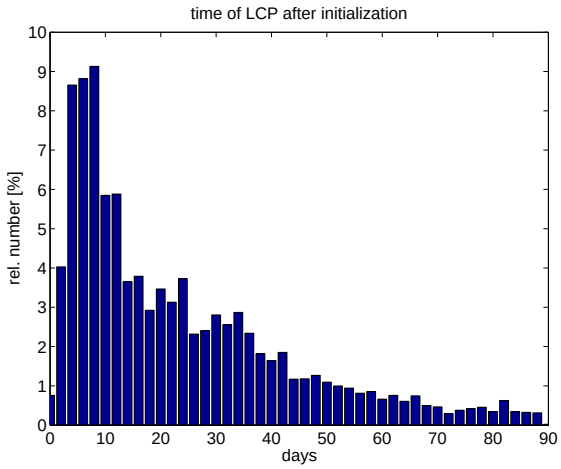

Fig. 4.7: Histograms of the time in days after initialization, when the LCP is reached for DJF 1995/1996.

4.1.4 Lagrangian cold point

In contrast to the Eulerian method, where the temporally evolution of atmospherical variables can be observed only at one constant spatial point, the Lagrangian method is useful to follow these variables along its' path the so called trajectory. After the trajectories are selected due to their sample criteria, they need to fulfill (see chapter 3.2.4), the lowest temperature of each trajectory is determined. Hereafter, the geographical distribution of the LCPs can be identified.

4.1.4.1 Climatology

The climatology of the Lagrangian temperature and the mean occurrences of LCPs for ERA Interim 1979-2011 is presented in Figure 4.8. The temperature of the LCPs (color shading) as well the relative frequency (white contour line) of the LCPs are sampled per 5° x 5° grid. This long term annual mean shows around the whole equator LCP temperatures lower than 192 K. Lowest temperatures occur over the maritime continent with minimum LCP temperatures of 189.5 K. Thus, most of the air masses reach their dehydration point over the tropical West Pacific, the so called "cold trap". That means most of the sampled air masses crossed the coldest region. Fueglistaler et al. (2005) showed a climatology of the LCP frequency based on ERA 40 data indicating similar locations for the main entrance regions of LCPs. Beside the high occurrence of LCPs with 0.6% over the West Pacific, two secondary maxima of the occurrence of LCPs exist over West Africa (0.4%) and South America (0.3%) in the present calculation, which are not visible in ERA 40 calculations by Fueglistaler et al. (2005). Figure 4.8 shows the climatology of the annual mean LCP temperature and density distribution. In the long term annual mean most of the trajectories enter the stratosphere in the western Pacific as indicated by the contour lines. Lowest LCP temperatures are reached with 190 K over the maritime continent. The location of this region is comparable to the

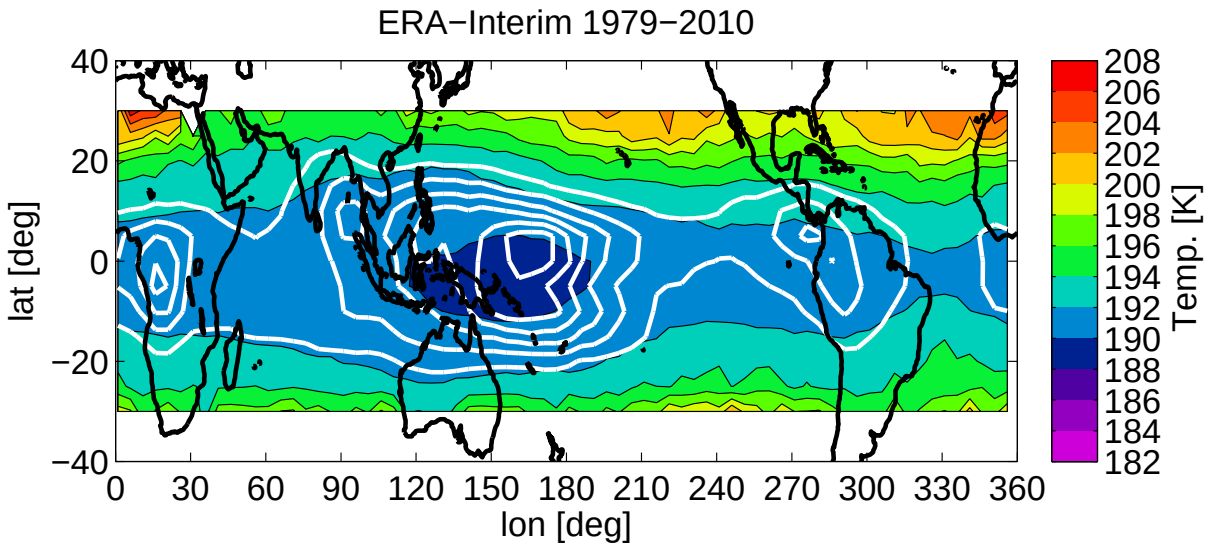

Fig. 4.8: Annual average climatology of the LCP temperature per 5° x 5° (ERA Interim 1979-2011). White contour lines display the density of LCP occurrence from 0.1% up to 0.7% with an interval of 0.1%.

coldest region presented in the Eulerian picture in Figure 4.2. The LCP temperature from ERA Interim indicates temperatures approximately 2 K lower compared to the Eulerian CP temperatures in Figure 4.1. Besides, it is also important to know at which vertical level the CP is reached. In the publication by Bonazzola and Haynes (2004), it was pointed out that the "cold point layer" extends from 360 - 380 K θ, showing average potential temperatures at 370 K for NH winter 97/98 and 98/99. The long term annual mean potential temperature of the LCPs for ERA Interim is presented in the appendix in Figure A.1. The cold point layer in the analyzed calculations, extends from 370 - 395 K θ in the annual average indicating lowest θ over the maritime continent. The seasonal distribution is shown in Figure A.2. During NH winter the CP layer is located at lowest altitudes in comparison to the different seasons (see Figure A.2(a)-(d)). The minimum potential temperatures (lowest altitudes) for LCPs is reached for DJF (360 K) and maximum (highest altitudes) for JJA (370 K).
In contrast to Bonazzola and Haynes (2004), who used large ensembles of 90-day backward trajectories for only 2 NH winter seasons using ECMWF data with 3D winds, in this study 32 NH winter seasons between 1979-2011 were analyzed and averaged for ERA Interim based on the kinematic method as well.

Figure 4.9 shows the seasonal average LCP temperature and occurrence analyzed per 5° x 5° grid. Figure 4.9(a) presents the climatology for NH spring. Lowest temperatures of 188.9 K occur above the West Pacific, South America and West Africa. Most air masses enter the stratosphere in the tropics over the West Pacific and over West Africa with 0.6%. A smaller maximum is visible over South America (0.3%). Figure 4.9(b) shows the climatology of LCP temperatures during NH summer. The average temperatures are highest during this season, and the coldest LCPs are located over the western Pacific as well with 191.2 K. The main

entrance region for air masses traveling from the troposphere into the stratosphere is over the western Pacific and over Bay of Bengal with 0.6%. In boreal summer air masses often reach their Lagrangian cold point over the Bay of Bengal, due to the anticyclone there, which appears during the Asian monsoon season. A large amount of air masses reach the stratosphere also over West Africa and Central America (0.3 - 0.4%). During NH autumn (Figure 4.9(c)), the lowest temperatures of 190.2 K exist over the West Pacific with a larger cold area compared to the NH summer season. The main entrance region for tropospheric air masses into the stratosphere is located over the tropical West Pacific as well (0.7%), but compared to the other seasons also the South American continent reveals high occurrences of LCPs with 0.5% and over West Africa with 0.4%. Figure 4.9(d) represents the LCP climatology for NH winter. This season shows the most intense pattern in LCP occurrence and temperature. This is caused by a generally more intense upward Brewer Dobson circulation in the tropical lower stratosphere during NH winter (Bonazzola and Haynes, 2004; Krüger et al., 2009). Lowest temperatures reach 187.5 K with the coldest region over the western Pacific accordingly with a large area of LCP frequencies reaching 0.7%. The cold point area is not exactly coincident with the region where most air masses enter the higher atmpsphere. The densest area of LCPs is shifted to the East compared to the cold point region over the maritime continent. Thus, fewer air masses are sampled directly in the coldest region. A similar behaviour of the displacement of the LCP density maximum and temperature minimum was shown by Krüger et al. (2008) for calculations based on ERA 40 heating rates. The authors showed the densest LCP area just south of the minimum CP temperature. A similar shift of the LCP density in respect to the lowest CP temperatures was shown by Fueglistaler et al. (2005) using ERA-40 data based on a kinematic method.

4.1.4.2 Spatial pattern

To better understand the LCP distributions during different seasons, the number of LCPs are tropically averaged in 5° longitude bins to highlight the zonal distribution of them (Figure 4.10). The black line represents the annual mean occurrence of LCPs from 1979-2010 for ERA-Interim. Between 120° and 180° East, 38% of the LCPs reached their lowest temperature in that region in the long term annual average. Results for the different regions are indicated by different colors. In NH winter most trajectories enter the stratosphere over the maritime continent with 45% (blue line). The maximum occurrence is shifted towards the East compared to the annual mean. During NH summer a large amount of air masses reach their cold point between 80° and 100° East (India/Bay of Bengal). Between 350° and 50° East (West Africa), largest occurrence of LCPs takes place in NH spring (green). (Krüger et al., 2008) calculated the LCP occurrence for ERA-40 and opECMWF data for the same region, resulting in 34% using vertical winds and 50-60% using diabatic heating rates of one single winter. A secondary peak over South America around 285 ° E is indicated using opECMWF 3 D windfields (Krüger et al., 2008). This peak is also visible in Figure 4.10, using ERA Interim data. However, comparing the NH winter 2001/2002 from this study, using ERA Interim with the one shown by Krüger et al. (2008) using ERA-40 and opECMWF reveals that the entrainment over South America is relatively smaller to the

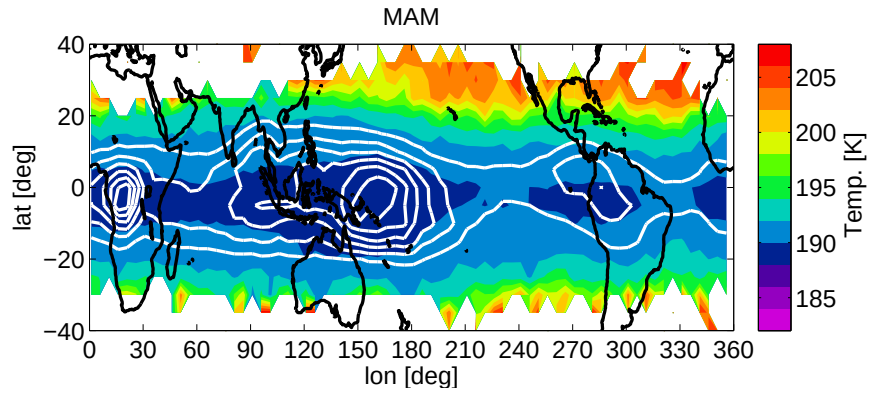

(a)

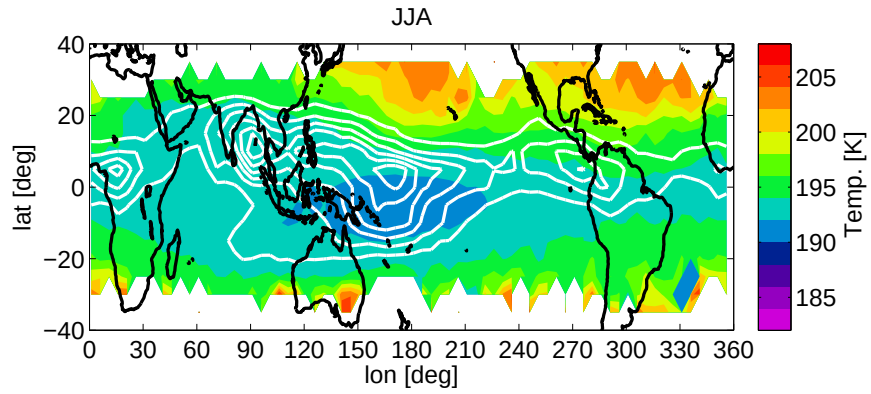

(b)

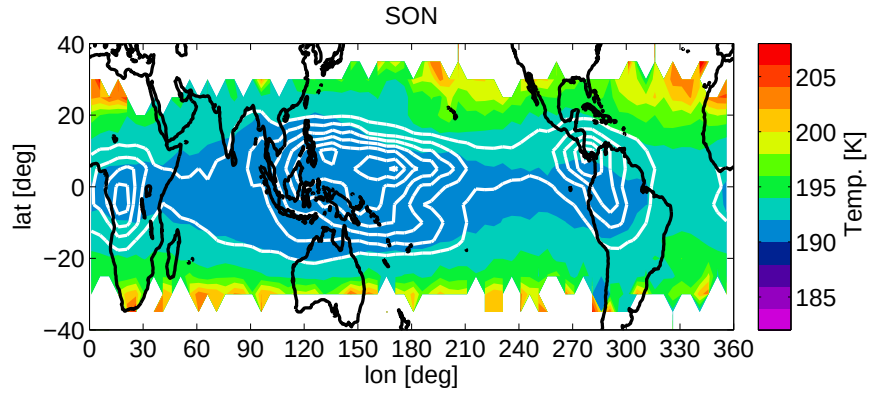

(c)

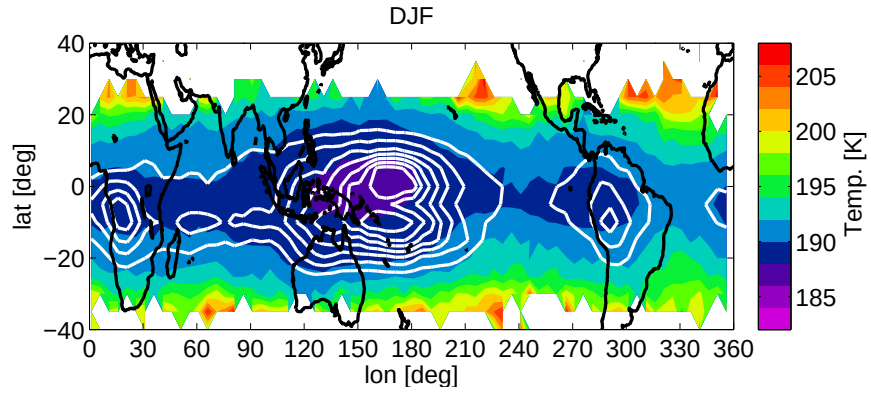

(d)

Fig. 4.9: Climatology of the LCP temperature for different seasons per 5° x 5° (ERA Interim 1979-2010). With contour lines display the density of LCP occurrence from 0.1% up to 0.7% with an interval of 0.1%: MAM (a), JJA (b), SON (c) and DJF (d).

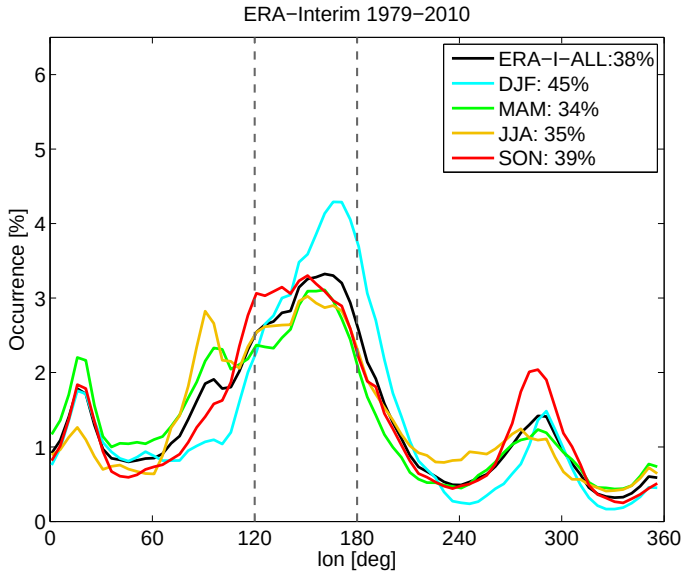

Fig. 4.10: Occurrence of LCP averaged inside 5° longitude bins (ERA-Interim 1979-2011). The number in [%] indicates the percentage of Trajectories reaching the stratosphere in the marked area between 120° and 180° East. The annual (black) and seasonal averages are represented in different colors (see legend).

entrainment over the West Pacific (not shown here) and for the average NH winter as well (Figure 4.10 blue curve). Furthermore, the accumulation of LCPs over West Africa around 20° E during NH winter for ERA Interim 2001/2002 (not shown here) and on the annual average (Figure 4.10), is not indicated in opECMWF and ERA-40 data (Krüger et al., 2008). A varying initialization method of the trajectories is not applied there and in other studies neither. This might be a possible explanation for neglecting an accumulation of LCPs especially over West Africa for an initialization time at local noon (12 UTC). It may however also reflect changes between the ECMWF assimilation models and techniques (Dee et al., 2011, e.g).

4.2 Global climate models

In this section, the ability of climate models to represent the basic structure of the upper TTL and the main entrance region into the stratosphere is investigated. Different seasons and regions are considered for the time period between 1990 and 1999. For the global models, basically, four different CCMs including full stratospheric ozone chemistry are analyzed. Most models within CCMVal-2 use a prescribed ocean, whereas CMAM REF-B2 is the only model, taking an interactive ocean into account. For comparison, the CMIP5 model MPI-ESM is analyzed as well, which is driven by observed GHG and ozone changes and uses an interactive ocean as well. Due to the large amount of data, the presentation of key results is chosen. More details, e.g. climatologies of the Eulerian cold point and the Lagrangian cold points for each model, are presented in the appendix (Figure A.3).

4.2.1 Eulerian cold point

As the Eulerian cold point temperature has a large impact on the LCP analysis of the climate models, Figure 4.11(a) presents the annual mean CP temperature for reanalysis and climate models between 10°N and 10°S. The average Eulerian cold point in Figure 4.11(a) varies for ERA-Interim between 191.5 K and 193 K. The two CMAM models, WACCM and the MPI-ESM simulations show similar temperatures (+/- 1.5 K) between 10°N and 10°S. The simulations from NIWA-SOCOL however simulate 2 to 5 K lower temperatures compared to ERA Interim. A warm Eulerian cold point bias appears in the E39CA model with temperatures 1 to 2 K higher than ERA Interim. There are several studies, reporting a cooling in the tropical tropopause especially from the 1990s onward, e.g. the work from Rosenlof and Reid (2008), which was based on reanalysis and satellite data. However, no trend is visible in the cold point for ERA Interim between 10°N and 10°S in Figure 4.11(a), which is consistent with results shown by Wang et al. (2012). They suggest that the reported decrease of CP temperature is not significant. By adjusting radiosonde data the authors determined less certain trends. That could be one reason why ERA Interim reflects no CP temperature decrease as it assimilates adjusted radiosonde data to produce their reanalysis product (Wang et al., 2012; Dee et al., 2011).
The behavior of the cold point tropopause temperatures simulated from different CCMs within the CCMVal-2 project, has been investigated by Gettelman et al. (2010). The differences between the models and ERA Interim show comparable characteristics of the cold point tropopause temperature between 20°N and 20°S, like in the temperature presented here. The models CMAM REF-B1, E39CA, NIWA-SOCOL REF-B1 and MPI-ESM reveal a strong peak in 1991, whereas ERA Interim, WACCM and the two REF-B2 simulations do not. Global maps of the climatology for the Eulerian cold point are presented in the appendix (Figures A.3(b)-(h)) for each climate model.

4.2.2 Vertical winds

As the Lagrangian study is performed based on the kinematic method, differences in the underlying vertical wind fields of the models can have a large impact on the simulated path of air masses. The strength of the vertical wind near the tropopause has been analyzed between 10°N and 10°S for each climate model (Figure 6.3(a)). At 100 hPa pressure level, ERA Interim has an average uplift of $-0.8 \cdot 10^{-3}$ Pa/s. E39CA indicates the weakest vertical velocity of $-0.2 \cdot 10^{-3}$ Pa/s, whereas the other climate models have the tendency to have slightly stronger vertical velocities compared to ERA Interim. The strongest vertical velocity is simulated for CMAM REF-B2 ($-1.3 \cdot 10^{-3}$) Pa/s. An intercomparison between the models and the multi model mean of the different climate models from CCMVal-2 project revealed as well stronger vertical velocities at 70 hPa in the tropics for NIWA SOCOL and weaker vertical velocities for E39CA compared to the multi model mean (Butchart et al., 2010).
The LCP temperatures are higher for E39CA and lower for the other climate models compared to ERA Interim. However, the strength of the cold or warm bias cannot be explained simply by the strength of the vertical velocity as NIWA SOCOL shows the strongest cold

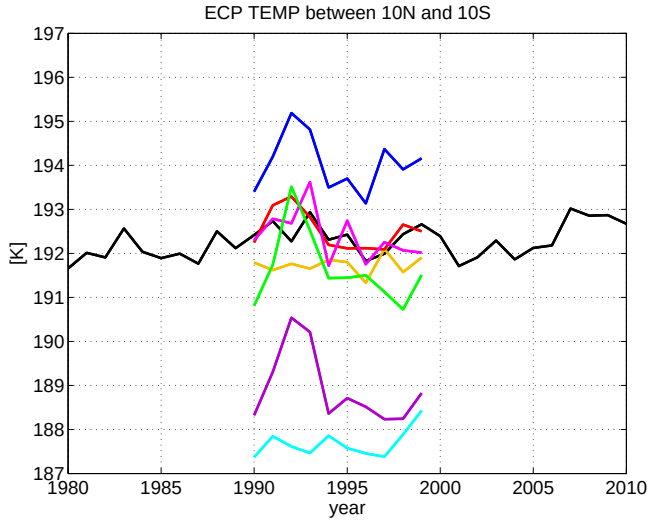

(a)

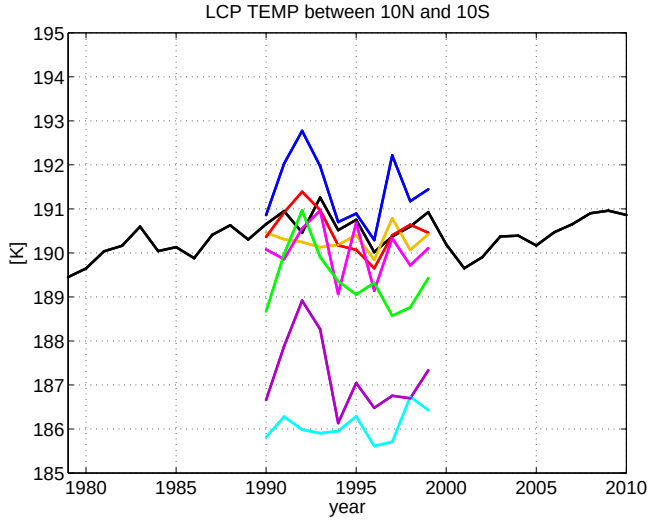

(b)

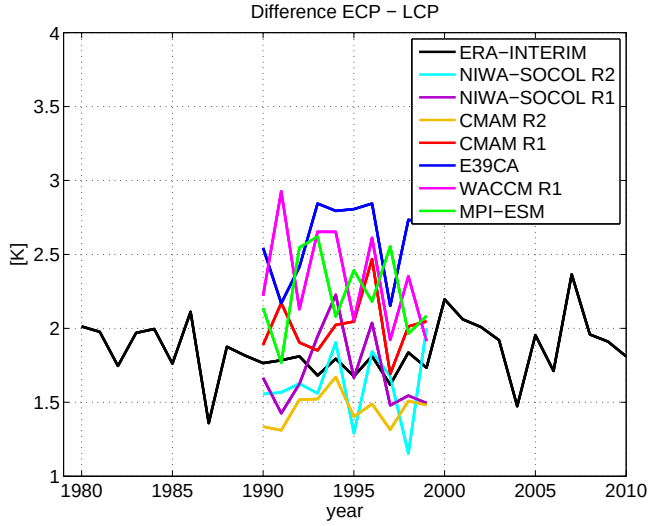

(c)

Fig. 4.11: Time series for the annual mean Eulerian CP temperature (a), Lagrangian CP temperature (b) and their difference (c) between 10°N - 10°S (ERA Interim, 1979-2011 and climate models, 1990-1999). See legend for color coding. Due to some missing values the Eulerian CP is not plotted for 1979.

bias to ERA Interim. The strong biases could be also attributed to the used model dynamics. In case of NIWA SOCOL, the applied semi-Lagrangian hybrid-transport-scheme could possibly have an effect on the much faster tape recorder and residual velocities (pers. comm. with Dan Smale - NIWA-SOCOL PI) compared to the other models within CCMVal-2 (SPARC, 2010, Chapter 5.). This could have an effect on the LCP temperature. The El Niño like pattern of the LCP distribution for NIWA-SOCOL REF-B1 and REF-B2, with an LCP accumulation over the eastern Pacific, rather than over the western Pacific as shown for ERA Interim (Figure 4.12(a) and (c), (d)) could arise from the climate model forcings. The NIWA-SOCOL model has a rather distinct atmospheric response to volcanic and QBO forcing (SPARC, 2010, Chapter 8.). This specific phenomena for NIWA SOCOL can be explained by the eruption of Mount Pinatubo and a stronger than normal QBO, which occurred in the early 90's.
The average vertical velocity fields in 100 hPa for ERA Interim and the different climate models is shown for NH winter in Figure A.4 and for NH summer in Figure A.5. Generally all models reflect an ascent region (blue) over the West Pacific and South America during NH winter (Figure A.4). Strongest ascent is indicated by CMAM REF-B2 and weakest by MPI-ESM, which is most similar to ERA Interim. During NH summer (Figure A.5) the strongest ascent region is located over East Asia and the China Sea according to ERA Interim. The climate models generally reproduce those ascent regions however, large differences exist among the models. CMAM REF-B2 simulates the strongest ascent region even spread over the Bay of Bengal and the tropical West Pacific. E39CA reproduces the ascent region over East Asia worse. WACCM and MPI-ESM reflect the location and strength of the ascent region best.

4.2.3 Lagrangian cold point

The time series of the Lagrangian cold point temperature between 10°N - 10°S is presented in Figure 4.11(b). The LCP temperature varies between 189 K and 191 K for ERA Interim. The climate models behave similar as for the Eulerian cold point analysis regarding their differences in the LCP temperature to ERA Interim. Highest LCP temperatures are simulated by the E39CA model and NIWA SOCOL reveals LCP temperatures up to 5 K lower than ERA Interim.
The differences between the Eulerian and the Lagrangian cold point is given in Figure 4.11(c). For ERA Interim, the LCP temperature is systematically ∼2 K lower than the Eulerian cold point. The CMAM REF-B1 simulation shows the smallest differences (∼1.4K) and largest differences are indicated by the E39CA model (∼2.5K). Analyzing ERA 40 data from 1979-2001, Fueglistaler et al. (2005) showed that the Lagrangian cold point is systematically about 2.5 K lower, than the cold point temperatures in the Eulerian perception.

4.2.3.1 Climatology

Figure 4.12 shows the annual mean LCP temperature between 1990-1999 for ERA-Interim (a) and the differences with the climate models (b)-(h). Lower LCP temperatures in the

climate models compared to ERA Interim are indicated by blueish colors, higher LCP temperatures are indicated by reddish colors. The E39CA model has a warm bias of 2 to 6 K, compared to ERA-Interim, which is increasing with distance from the equator. Only the temperature in the western Pacific region varies within +/- 1 K. The maximum frequency of LCPs in the West Pacific area compared to ERA-Interim is shifted to the Southeast visualized by the green contour lines (Figure 4.12(b)). Accordingly, less LCPs occur over the maritime continent up to the Bay of Bengal. In the two REF-B1 and REF-B2 runs from NIWA-SOCOL (c) and (d) a negative bias of the tropical LCP exists of -5 to -6 K, which is strongest over the West Pacific and decreasing polewards. Over the maritime continent up to 0.3% less LCPs occur, whereas in the East Pacific more entrainment into the stratosphere takes place. The two simulation runs from CMAM (Figure (e) and (f)) show only very small differences in the LCP temperature of +/- 1 K compared to ERA Interim. The difference of LCP occurrences over the maritime continent is up to 0.2%. However, over South America and India CMAM REF-B1 reveals up to 0.4% higher LCP occurrence than for ERA Interim, which does occur in CMAM REF-B2 simulations as well. Figure (g) presents the REF-B1 simulation of WACCM. The LCP temperature has a slight bias of -1 to -2 K within the tropics. In WACCM, the occurrence of LCPs is shifted to the East over the central and East Pacific and is higher with 0.4% more than ERA Interim. Further, less entrainment is simulated by WACCM over West Africa than compared to the other models. The MPI-ESM model (g), has an overall negative bias in the tropics between -1 to -2 K and simulates less LCPs over the whole Pacific (-0.5%), but 0.3% more over West Africa and 0.2% over South America in comparison to ERA Interim.
The global maps of the potential temperatures for the climate models between 1990-1999 is shown in Figure A.7. Lowest potential temperatures are simulated by CMAM REF-B1 with 360 K θ over the West Pacific, which is most similar to ERA Interim.
The structure of the LCP temperature (Figure A.6), as described above, is very similar compared to the structure of the Eulerian cold point (Figure A.3). It is visible from those that E39CA has an overall higher Eulerian CP temperature compared to ERA Interim, accordingly the LCP temperature from E39CA is higher compared to the LCP temperature from ERA Interim. Probable reasons for a warm bias might be deficiencies in transport in the TTL considering the differences from the Eulerian cold point (Figure 4.11(a)) (SPARC, 2010, Chapter 7.).
The two climatologies for the NIWA SOCOL simulations show lowest temperatures for the Eulerian cold point (Figure A.3(c) and (d)), which is also the case looking at the Lagrangian temperatures (Figure A.6(c) and (d)).

Figures 4.13 and 4.14 show the climatology of the average LCP temperatures for the NH winter (DJF) and summer (JJA) seasons 1990-1999. In general, the differences of the LCP temperatures for the different models compared to ERA Interim are in the same order in winter (Figure 4.13(b)-(h)) and in the summer seasons (Figure 4.14(b)-(h)) compared to the annual mean (Figure 4.12). The structure of the contour lines for the LCP occurrence are more noisy during NH winter and summer, due to a smaller amount of considered trajectories in the single seasons. Thus, differences in the LCP occurrence between the

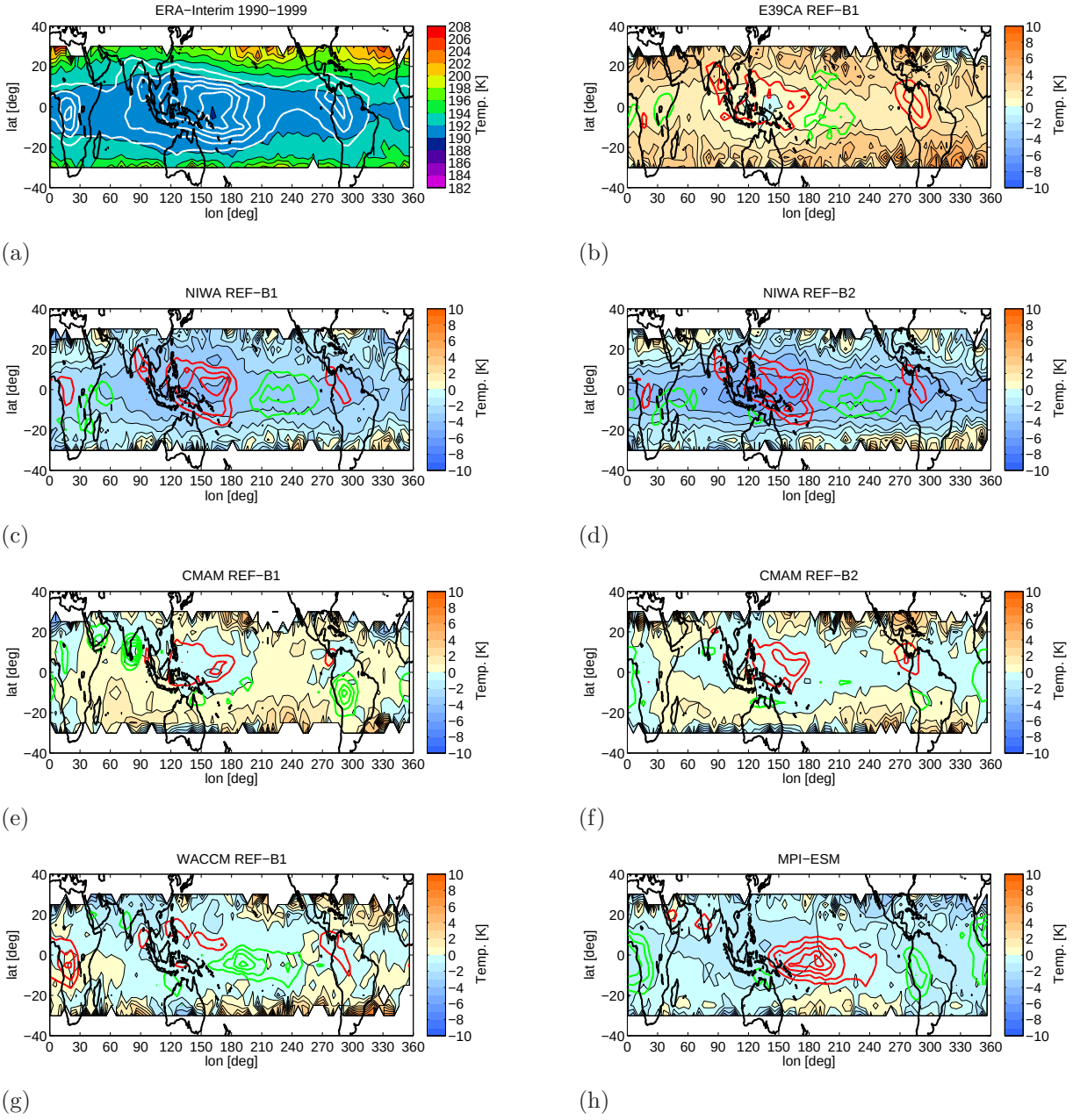

Fig. 4.12: Differences in the climatology of LCP temperature and occurrence from climate models to ERA-Interim (1990-1999) per 5° x 5°. Overlied with contour lines for the density of LCP occurrence in [%] red: less than ERA-Interim, green: more than ERA-Interim. (a) ERA-Interim, (b) E39CA, (c) NIWA-Socol REF-B1, (d) NIWA-Socol REF-B2, (e) CMAM REF-B1, (f) CMAM REF-B2, (g) WACCM, (h) MPI-ESM. The color interval is 2 K; for LCP occurrence and differences it is 0.1%. Ranging from 0.1% up to 0.7% for white contour lines in (a); between -0.5% and -0.1% red contours and 0.1% until 0.5% for green contour lines.

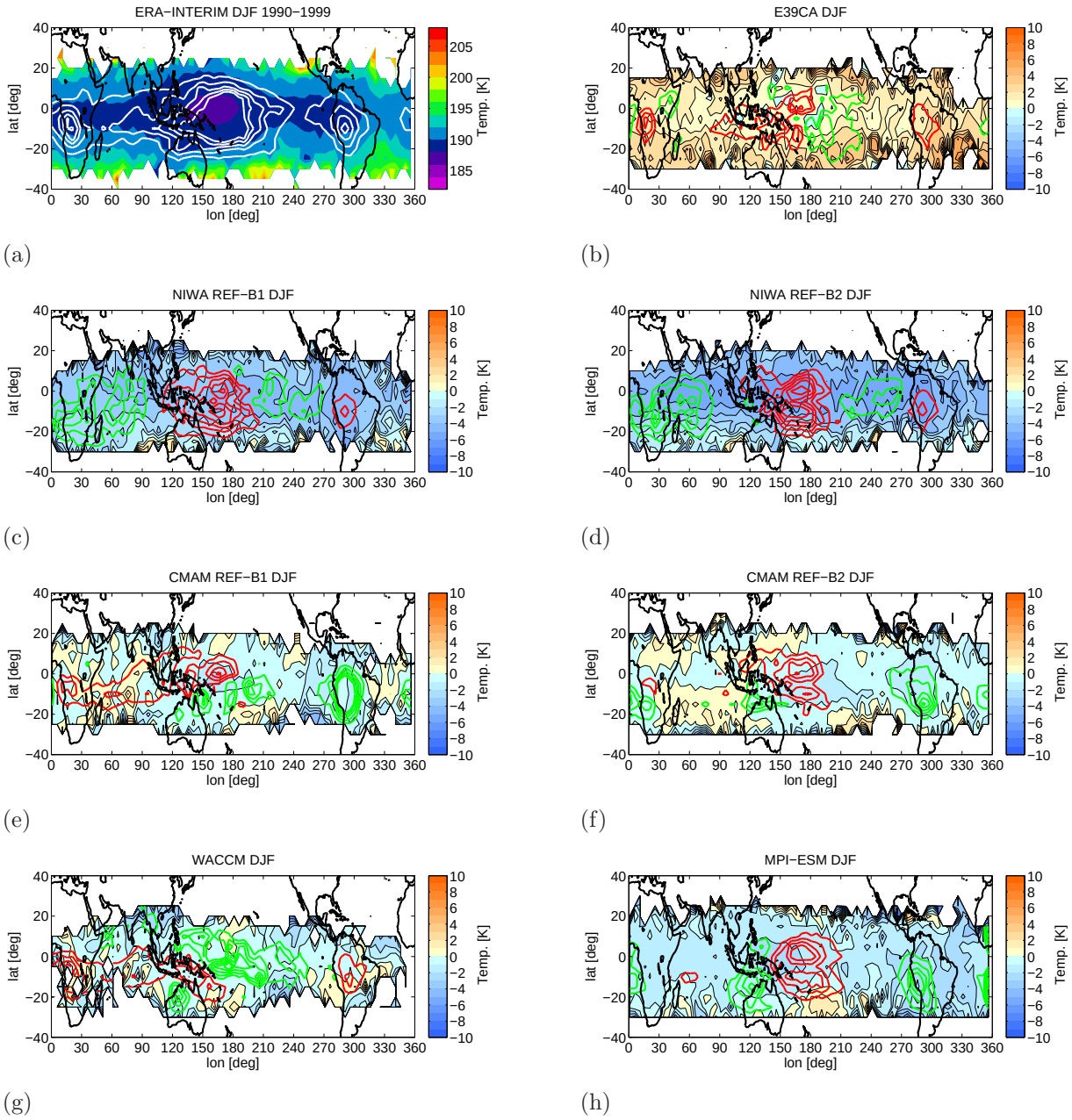

Fig. 4.13: Differences in the climatology of LCP temperature in DJF and occurrence from climate models to ERA-Interim (1990-1999) per 5° x 5°. Overlied with contour lines for the density of LCP occurrence in [%] red: less than ERA-Interim, green:more than ERA-Interim. (a) ERA-Interim,(b) E39CA, (c) NIWA-Socol REF-B1, (d) NIWA-Socol REF-B2, (e) CMAM REF-B1, (f) CMAM REF-B2, (g) WACCM, (h) MPI-ESM. Color and contour interval as for Fig 4.12.

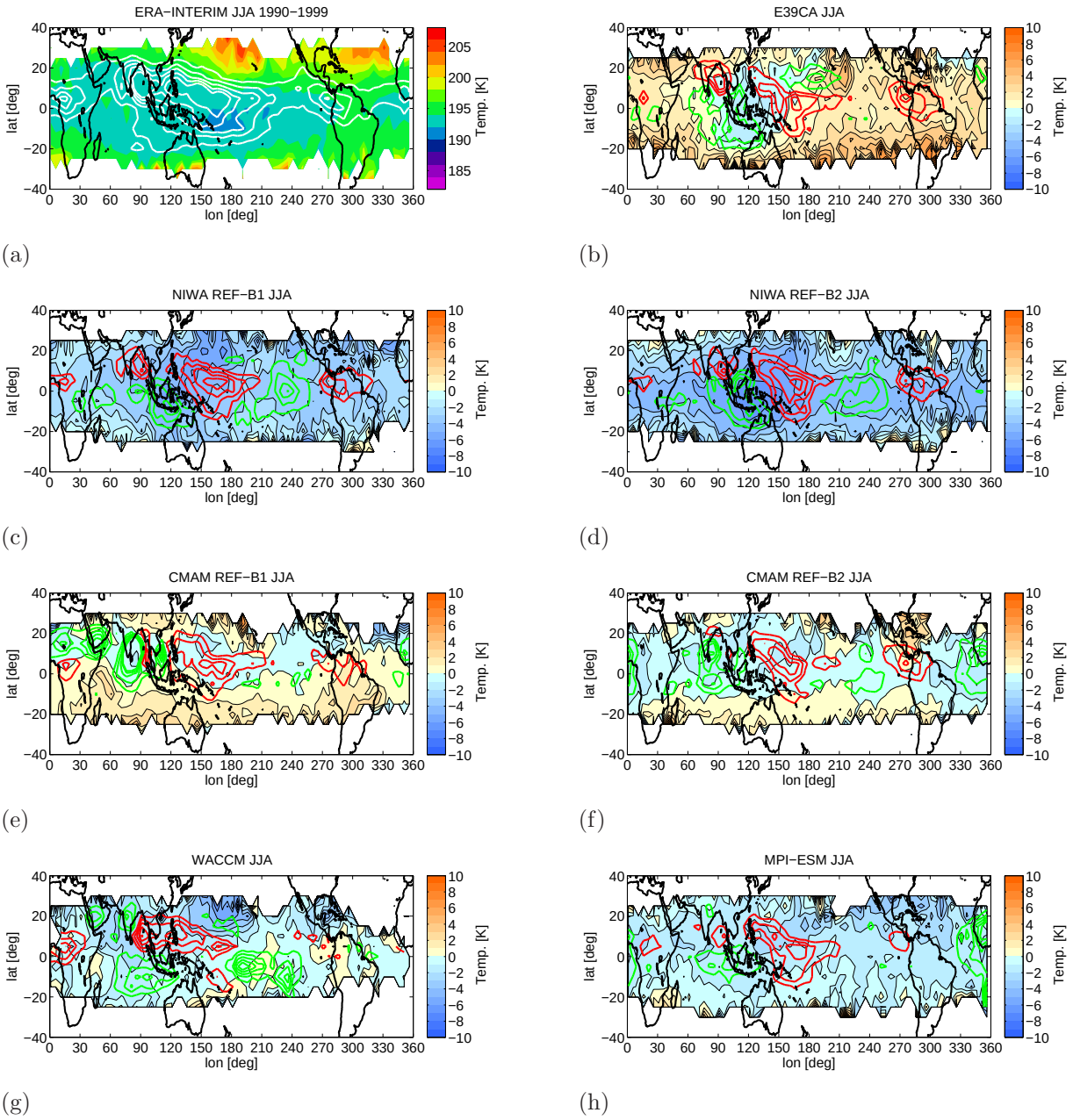

Fig. 4.14: Differences in the climatology of LCP temperature in JJA and occurrence from climate models to ERA-Interim (1990-1999) per 5° x 5° . Overlied with contour lines for the density of LCP occurrence in [%] red: less than ERA-Interim, green:more than ERA-Interim. (a) ERA-Interim,(b) E39CA, (c) NIWA-Socol REF-B1, (d) NIWA-Socol REF-B2, (e) CMAM REF-B1, (f) CMAM REF-B2, (g) WACCM, (h) MPI-ESM. Color and contour interval as for Fig 4.12.

climate models and ERA Interim (DJF: Figure 4.13(b)-(h) and JJA: Figure 4.14(b)-(h)) are more pronounced. The largest deviation in the LCP occurrence is visible in the western Pacific during DJF, where most of the models (except WACCM) simulate a lower frequency of LCPs. In the region over South America also large discrepancies are striking, especially for the two CMAM simulations and for the MPI-ESM (Figure 4.13(e), (f) and (h)). They indicate higher LCP frequencies over South America compared to ERA-Interim (Figure 4.13(a)).
For the NH summer season, the largest discrepancies in the LCP occurrence between climate models and the ERA Interim reanalysis data are visible over the West Pacific and the Bay of Bengal. The occurrence of LCPs is underestimated in all climate model simulations over the tropical West Pacific (red contour lines). In contrast to most of the other climate models, CMAM overestimates the LCP occurrence over the Bay of Bengal during NH summer (Figure 4.14(e) and (f)) (green contour lines). This might be probably due to the strong ascent in that geographical region, which is not indicated by the other models (see Figure A.5).

4.2.3.2 Spatial pattern

In Figure 4.15 the relative number of the zonally averaged LCPs within 5° longitude bins is shown for the period 1990-1999. The annual average (Figure 4.15(a)) and the seasonal (Figure (b)-(e)) LCP occurrence is presented for ERA-Interim and for the different climate models.
In the annual average, ERA Interim and the models agree with a main entrance region for air masses located between 120° and 200° E. NIWA-SOCOL simulates a quite zonally uniform distribution of LCPs highlighting this area least. Compared to ERA Interim, most climate models indicate an eastward shift of the main LCP occurrence. For ERA Interim 36% of all air masses reach the stratosphere in the area between 120° and 180° E. This amount is represented best from WACCM by simulating 39% of the air masses in that region. The other models indicate 5 to 13% less LCPs in this region. Due to the zonally uniform distribution from NIWA-SOCOL, both simulations show largest differences to ERA Interim.

The seasonal variability of the zonally averaged LCP distribution is shown in Figure 4.15(b)-(e). During NH spring ERA Interim indicates a maximum of LCPs between 80° and 110° E in the East Indian Ocean (Figure 4.15(b)). This accumulation is only reproduced by WACCM and CMAM REF-B1, whereas the other models do not highlight this region. In contrast to ERA Interim they indicate higher amounts of LCPs over the East Pacific and partly over West Africa. CMAM REF-B1 is able to capture the accumulation over the West Pacific best compared to the reanalysis. Discrepancies between ERA Interim and climate models appear during NH summer (Figure 4.15(c)) as well. An extremely high number of LCPs are simulated by CMAM REF-B1 (red) between 30° and 100° East in the Indian Ocean indicating a number twice as large as ERA Interim. The region over the West Pacific between 120° and 180° East is best represented by the model E39CA in comparison to ERA Interim. During NH fall generally it seems like discrepancies among ERA Interim and climate models are less striking (Figure 4.15(d)). However, the main entrance region for air masses in the

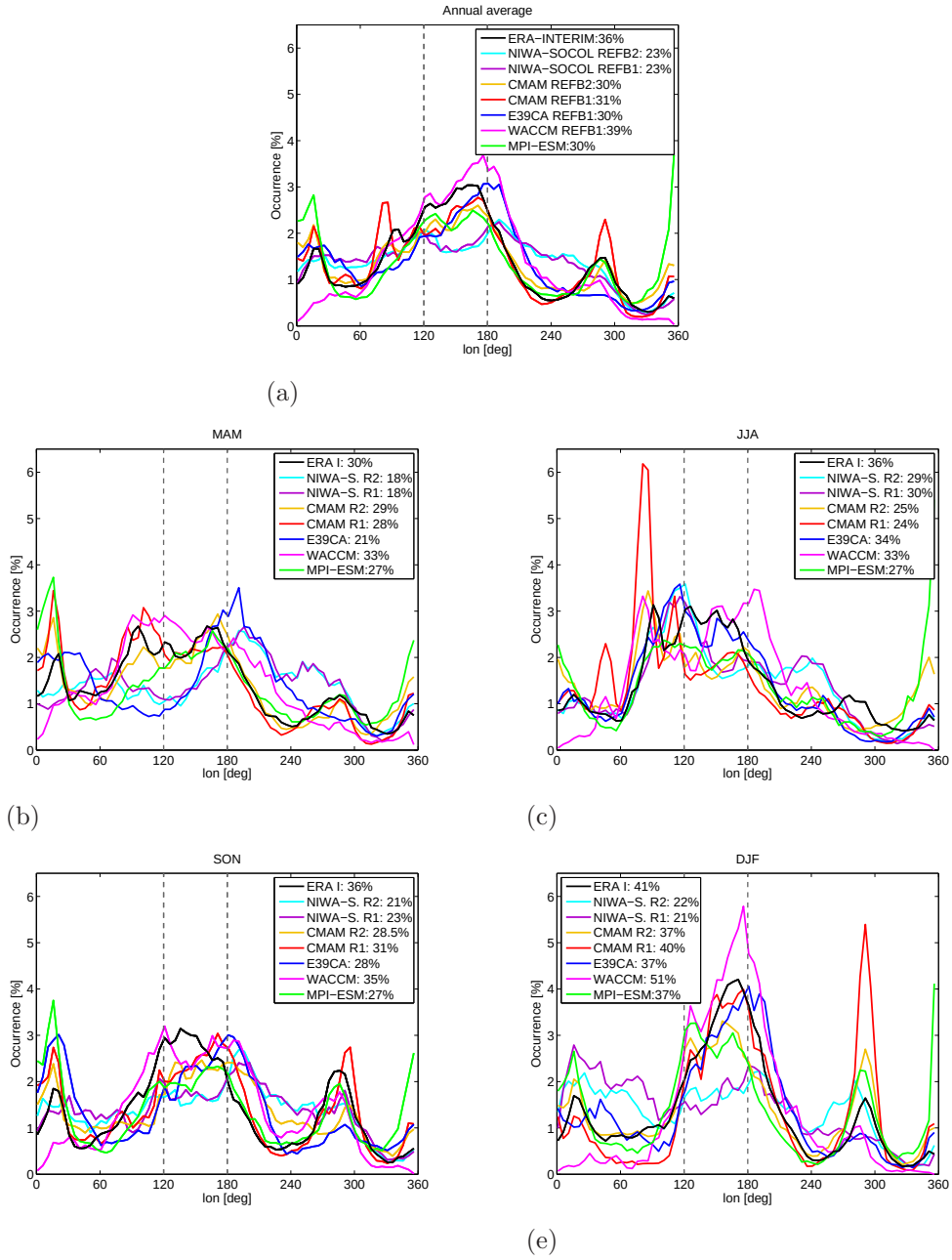

Fig. 4.15: Occurrence of LCP averaged inside 5° longitude bins for ERA Interim and climate models (1990-1999). Different colors represent the different models (see inset for color coding). Annual average (a) and the different seasons: MAM (b), JJA (c), SON (d), DJF (e). The number in [%] indicates the percentage of Trajectories reaching the stratosphere in marked area between 120° and 180° East.

West Pacific is simulated by the climate models to be stronger shifted towards the East compared to ERA Interim. For ERA Interim 36% of the air masses reach the stratosphere above the West Pacific. WACCM performs best in reproducing that amount but on the other hand indicates almost no LCPs between 0° and 60° E, which is shown by ERA Interim and the other models. During NH winter, largest entrainment is indicated over the West Pacific from ERA Interim. Most of the models (except NIWA SOCOL) are able to simulate the largest entrainment in the West Pacific during NH winter as well. ERA Interim reveals 41% of the air masses entering the stratosphere between 120° and 180° (Figure 4.15(e)). Highest amount is shown for WACCM with 51%, CMAM REF-B1 performs best by simulating 40%. Two further regional accumulations of LCPs are apparent over West Africa and South America with different intensities between the reanalysis and the climate models. CMAM REF-B1 simulates a striking occurrence rate over South America (260° and 320°), which is more than three times higher than for ERA Interim.
Overall, largest discrepancies appear during NH winter and summer among the climate models compared with ERA Interim. For the annual average and during NH fall, the climate models reproduce the occurrence of LCPs by ERA Interim best.

Inspecting the zonal distribution of the LCP, five entrainment regions covering the whole tropics can be distinguished and are newly defined (in contrast to the study by Krüger et al. (2008) and previous sections, but similar to Fueglistaler et al. (2004)): West Pacific (WP), East Pacific (EP), South America (SA), West Africa (WA) and the Indian Ocean (IN) (Figure 4.16). The time series of annual mean LCPs for these five regions is highlighted for ERA Interim and the different climate models in Figure 4.17. The upper panel represents the West Pacific (WP: 100° - 210°E [1]), the second panel the East Pacific (EP: 210° - 270°E),

[1]Note that the area of the West Pacific is now enlarged in contrast to the previous analysis.

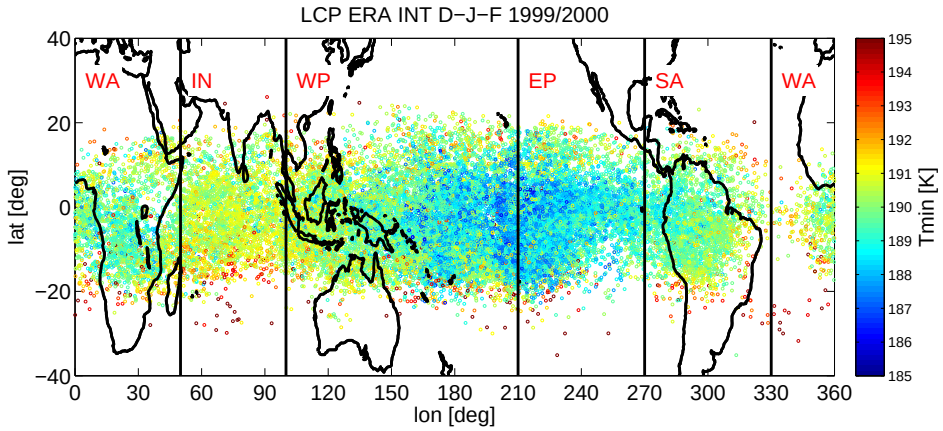

Fig. 4.16: Definition of geographical regions of the LCP distribution from ERA Interim DJF 1999/2000. West Pacific (WP) 100° - 210°, East Pacific (EP) 210° - 270°, South America (SA) 270° - 330° E, West Africa (WA) 330° - 50° E and Indian Ocean (IN) 50° - 100°E.

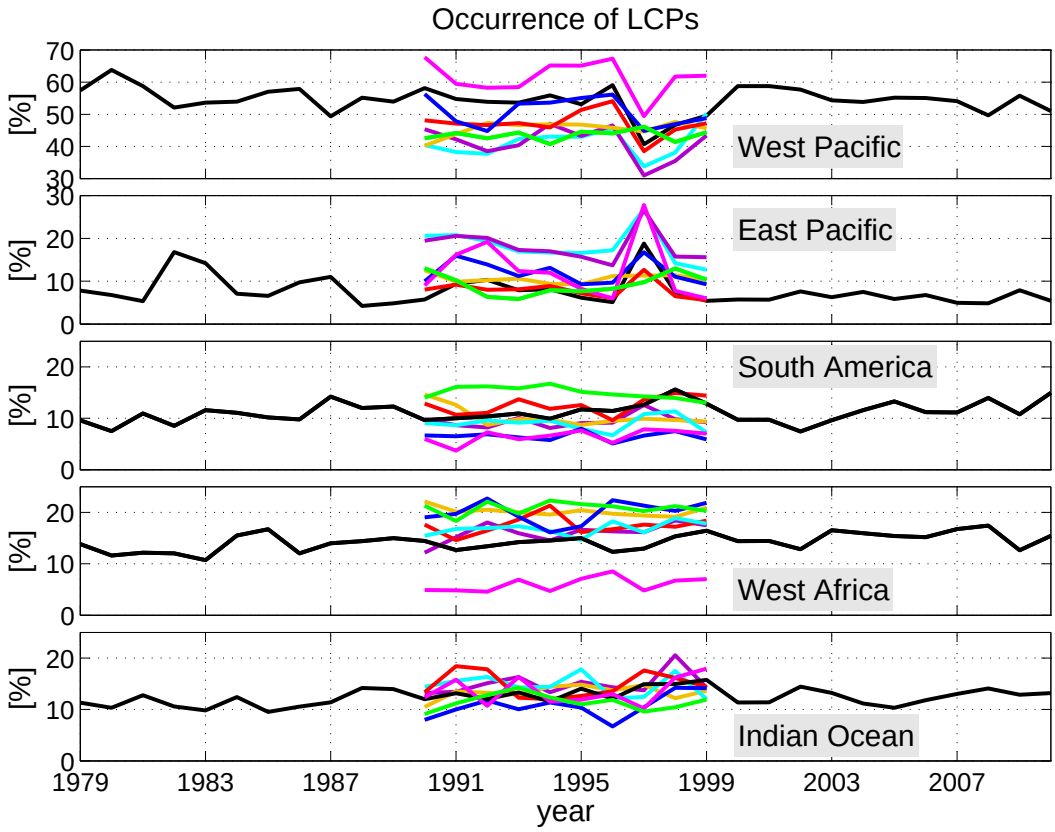

Fig. 4.17: Time series of annual average occurrence of LCPs inside 5 ° longitude bins for different regions. Number in [%] indicates the percentage of trajectories reaching the stratosphere (see legend with color codings from Figure 4.11(c).) First panel: West Pacific 100° - 210°, second panel: East Pacific 210°-270°, third panel: South America 270° - 330° E, fourth panel:West Africa 330° - 40° E, fifth panel: Indin Ocean 50° - 100°E.

the third panel South America (SA: 270° - 330°E), the fourth panel West Africa (WA: 330° - 50°E) and the lowermost panel the Indian Ocean region (IN: 50° - 100°E). Overall, the highest frequencies of LCPs occur over the West Pacific, where the highest amounts are reached by WACCM with around 60% (pink). The model from E39CA (blue) reveals similar amounts of LCPs as the reanalysis data (black) with around 55%. NIWA-SOCOL REF-B1 and REF-B2 (purple and cyan) reach up to 20% less LCPs in that region. In the East Pacific, CMAM REF-B1 and REF-B2 (red and yellow) agree best with ERA Interim, whereas the two NIWA-SOCOL simulations and to some parts WACCM overestimate the amount of LCPs by up to 10 %. The LCP amount over South America is reproduced closely by CMAM and NIWA-SOCOL in contrast to the other models, which simulate 5% to 10% more (MPI-ESM) and less (WACCM and E39CA) LCPs compared to ERA Interim. All climate models, except for WACCM, simulate up to 10% higher LCP frequency over West Africa. Overall the climate models performance is best over the Indian Ocean, where up to +/- 5% variations are found compared to ERA Interim.

In this annual mean time series, the interannual variability and the ENSO effect is visible as

well. The LCP occurrence for ERA Interim in the West Pacific varies between 50% and 65%, however for the year 1997 (strong El Nino), the LCP occurrence almost halfs and drops down to around 40% in the West Pacific. Most climate models, except CMAM REF-B2 (yellow) and MPI-ESM (green), which include both an coupled ocean, show a strong decrease of the LCP occurrence in the West Pacific in 1997 as well, but at the same time an increase of LCPs over the East Pacific. This behavior of an eastward shift of the LCP frequency to the central and eastern Pacific, which is typical for an El Niño event and is also visible in Figure 2.7(d).

4.3 Summary

Climatologies of the Eulerian and the Lagrangian cold point for ERA Interim and different climate models are highlighted in this chapter. The focus lies on the LCP occurrence to answer the question in which region and season most air masses reach the stratosphere and whether this coincides with lowest CP temperatures, hence the cold trap, where also enhanced tropical uplift in the upper TTL occurs. The behavior of the LCP temperature and distribution is analyzed for the annual and seasonal means using ERA Interim and climate models.

It is shown that some models have comparable characteristics of LCP temperature compared to ERA Interim. WACCM, CMAM REF-B1, CMAM REF-B2 and MPI-ESM are closest to the annual average LCP temperatures from ERA Interim (within +/-1.5 K). E39CA has a positive bias up to 2 K outside the maritime continent, whereas NIWA-SOCOL REF-B1 and REF-B2 have biases of -3 to -5 K, which increases towards the tropical West Pacific. The biases in the LCP temperatures are highly related to the Eulerian cold point climatologies and the vertical wind near the tropopause region at 70 hPa (section 6.2). Stronger vertical winds in the lower stratosphere tend to occur in models, which simulate lower CP temperatures compared to ERA Interim.

The annual average, where ERA Interim has the maximum LCP occurrence over the West Pacific, is well reproduced by the different climate models. However, they show discrepancies in the amount of entrainment over the tropical West Pacific during NH winter compared to ERA Interim (see also Figure A.8). During different seasons however, South America and West Africa are partly much stronger pronounced compared to ERA Interim. All climate models reproduce the shift of the accumulation of stratospheric entrainment points during NH summer from the West Pacific towards the Bay of Bengal (see also Figure A.9).

To summarize the results of the LCP frequencies, Figure 4.18 shows the relative number of LCPs in different regions, annually averaged over the years 1990-1999 for ERA Interim and all climate models. The analysis of the Lagrangian calculations revealed that most climate models reproduce a maximum entrainment of air into the stratosphere over the tropical West Pacific within 52% +/- 10%. Fueglistaler et al. (2004) indicated a larger occurrence of trajectories assuming their minimum saturation mixing ratio in the same region for the year 2001 using ERA-40 data. During NH winter 71% and during summer 67% of the trajectories reached their cold point in the WP, whereas in this study 60% and 52%

are analyzed respectively using ERA Interim data between 1979-2010 (Figure A.15). The differences probably appear due to the application of different ECMWF datasets and lengths of time series.
E39CA reproduces the annual LCP occurrence over the West Pacific of the reanalysis best (50.5%), however E39CA overestimates the number of LCPs in other regions, like the East Pacific and West Africa by 5% (Figure 4.18). NIWA-SOCOL and WACCM simulations reveal the strongest deviation compared to ERA Interim, especially over the Pacific and West Africa. The area over the Indian Ocean is reproduced best by all models.
By analyzing two different CCMs from CCMVal-1 using a Lagrangian approach for different reference years, Kremser et al. (2009) determined in contrast to the present work that the CCMs were not able to reproduce the highest entrainment over the West Pacific. However, the authors located a higher contribution of LCP occurrences over West Africa by the two CCMs compared to ERA-40 data, which is also one outcome of the results from this study. This may be due to the fact that enhanced vertical velocities (hence convective activity) together with pronounced LCP occurrences is detected during local noontime and especially over continents. In detail, ERA Interim revealed pronounced entrainment and strong vertical velocities especially for 12 and 18 UTC climatology over West Africa and South America, compared to earlier ECMWF based studies (e.g Kremser et al., 2009; Krüger et al., 2009; Fueglistaler et al., 2004). The different resulting LCP pattern due to a varying UTC starting time using ERA Interim data looks suspicious and should be addressed further in upcoming studies.

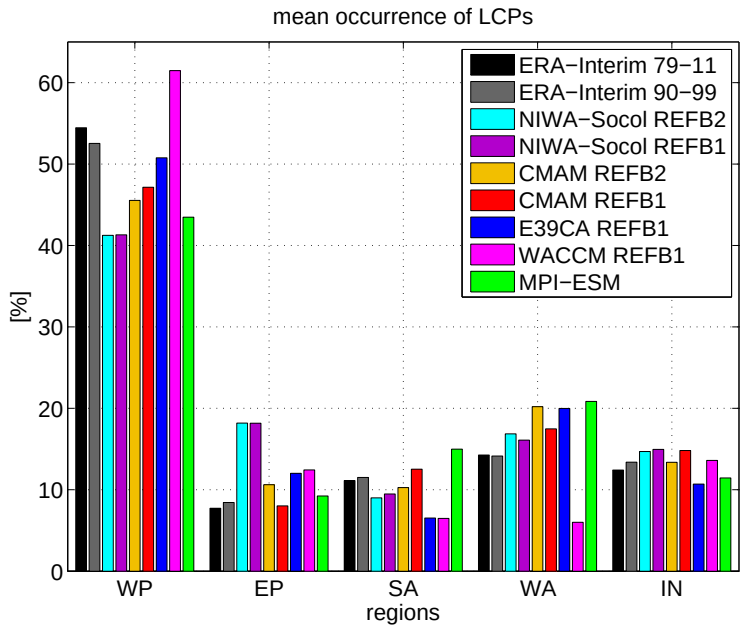

Fig. 4.18: Annual average occurrences of LCPs for different regions from ERA Interim and climate models. West Pacific (WP): 100°-210°E, East Pacific (EP): 210°-270°E, South America (SA): 270°-330°W, West Africa (WA): 330°-50°E and Indian Ocean (IN): 50°-100°W for 1990-1999, black bar represents ERA-Interim 1979-2011.

Chapter 5

Widening of the upper TTL

In this chapter the widening of the tropical belt is investigated using a new diagnostic, the meridional extension of the LCP distribution. Trajectory calculations based on ERA Interim (1979-2011), CCMVal-2 and CMIP5 (1990-1999) data are analyzed. LCPs represent the entrance region of air masses traveling from the troposphere into the stratosphere, and mark the upper boundary of the TTL (compare section 2.4.1). Hence, analyzing the meridional extension of these LCPs, the width of the upper TTL, as indicator for a changing tropical belt in the transition between the troposphere and the stratosphere, can be determined.
Different diagnostics have been applied mainly for the troposphere in the literature so far, to analyze the behavior of the tropical belt (Section 2.5). To set-up a stable method, here, a fix threshold for the border of the width of the upper TTL is determined, namely the 88th percentile in accordance with the annual average LCP distribution for the ERA Interim reanalysis (Section 3.3.2).
As described in section 2.4, the distribution of the LCPs reveals a seasonal cycle and interannualy variability (e.g. ENSO). Besides, natural variability influencing the LCPs, Fueglistaler and Haynes (2005) mentioned a broadening of the latitudinal density distribution of the LCPs based on ERA40 data (1979-2002), which could result from a change in the tropical upwelling. The intention of this chapter is to analyze this latitudinal distribution of the LCPs and the temporal evolution of the upper TTL widening in more detail using ERA Interim assimilation (1979-2011) and coupled climate models (1990-1999).

5.1 ERA-Interim

In the first part of this chapter the change of the width of the upper TTL is analyzed based on the LCP distributions of the ERA Interim assimilation (1979-2011). Because the width of the upper TTL varies similar to the distribution of the Lagrangian cold points, the evolution of this metric is analyzed for different seasons, hemispheres and different decades.

5.1.1 Variability of the width of the upper TTL

Largest variabilities of the latitudinal LCP distribution from ERA Interim is found for NH summer for the decade 1979-1989 (Table 5.1). Figure 5.1 shows a histogram of the LCPs for this decade, representing the interannual variability of the meridional extension of the LCPs. The LCPs have been counted inside 2.5° latitude bins and the relative amount is shown in [%]. Highlighted are the LCP distributions for 1979 (pink) and 1989 (blue). During NH summer most of the LCPs are located on the NH around 5° N. Overall, the meridional distribution extends mainly from ∼30° N to ∼20° S. While for 1979 the histogram shows a more narrow distribution, at least on the SH, the LCP distribution for 1989 is broader and more flat. However, this alone is no proof for a broadening of the upper TTL as the LCP distribution shows interannual variability as well. The goal is to find out if there is evidence for a significant change of the LCP distribution on a longer timescale, and thus, whether the upper TTL is broadening or if this is just by chance.

ERA-Interim	DJF	MAM	JJA	SON	annual
NH & SH 1979-2010	1.03 [0.65]	1.14 [0.79]	1.39 [0.7]	1.22 [0.72]	1.2 [0.49]
NH 1979-2010	1.00 [1.56]	0.84 [1.01]	0.31 [1.9]	0.56 [0.62]	0.68 [0.29]
SH 1979-2010	0.03 [1.18]	0.3 [0.47]	1.1 [1.06]	0.66 [0.53]	0.52 [0.29]
NH & SH 1979-1989	1.19 [3.98]	3.2 [2.98]	4.7 [3.3]	2.16 [3.14]	2.81 [2.34]
NH & SH 1989-1999	2.69 [3.12]	2.15 [5.08]	1.95 [2.94]	3.41 [3.75]	2.55 [2.44]
NH & SH 1999-2009	0.07 [3.36]	-0.49 [3.33]	1.34 [3.94]	0.11 [3.72]	0.26 [2.6]

Tab. 5.1: Change of the upper TTL (in ° lat/dec) represented by the 88 th percentile of the LCP distribution. Seasons, hemispheres and decades are analyzed separately. The 95 % confidence interval is calculated for each quantity and is displayed in the brackets. Significant changes are shaded in grey.

5.1.1.1 Annual average

The annually average width of the TTL from 1979-2010 for ERA Interim, defined by the threshold of 88th percentile (Section 3.3.2), is presented in Figure 5.2. The red shaded area represents the width of the upper TTL and the borders are visualized by the red curves at around 12° S for the southern and at around 15° N for the northern hemisphere. As can be seen, the median of the geographical LCP distribution is located on the Northern Hemisphere at around 2.5° N (green line). Thus, on the annual average most of the LCPs arise on the NH. This can be linked to the position of the rising branch of the Hadley circulation, which is located during most of the seasons some degrees north of the equator (Fueglistaler et al., 2009).

The temporal evolution of the absolute width of the upper TTL is shown in the lower graph of Figure 5.2. The total width of the TTL varies between 24° to 32° latitude. The linear

regression (blue dotted line) reveals a significant (1.96 σ level $\sim$ 95%) increase of the upper TTL width of 1.2 ° lat/dec for the time period 1979-2010 (see table 5.1). Considering the absolute width of the upper TTL, the broadest TTL is found in 1999, whereas the most

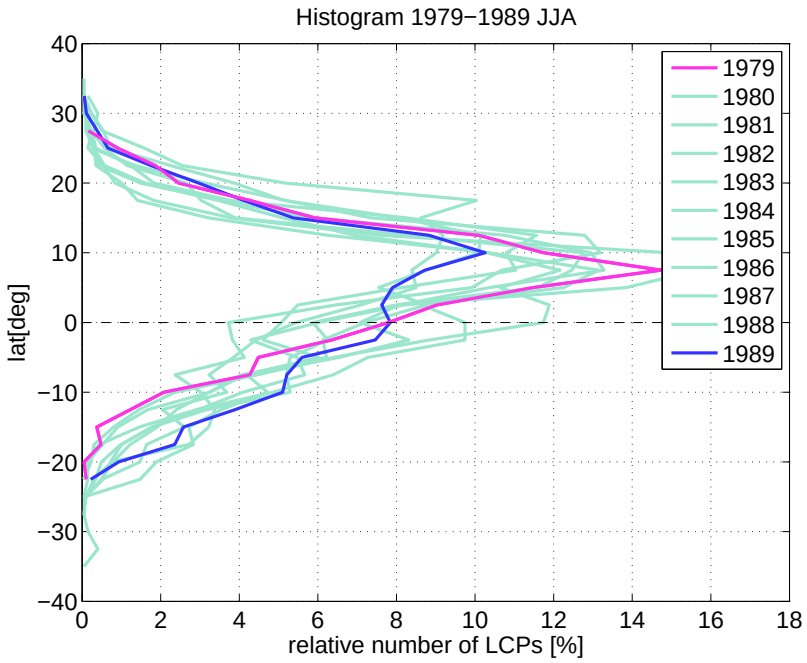

Fig. 5.1: Histogram for the LCP distribution for JJA ERA Interim 1979-1989 data.

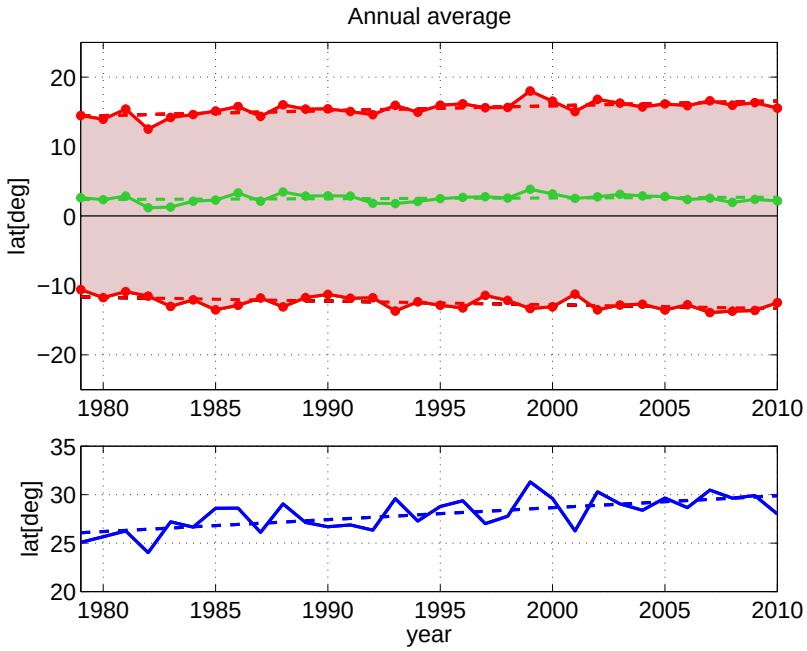

Fig. 5.2: Annual average width of the TTL represented by the 88 th percentile of the distribution of LCPs on the time scale from 1979-2010 (ERA Interim).

narrow TTL is found in 1982. This coincides with results of the tropical width analyzes carried out by Birner (2010a) and Lu et al. (2009), whose analysis of a tropical widening changes are based on the tropopause height using NCEP and ERA40 data. Birner (2010a) reported on a possible correlation between the width of the tropical belt and major volcanic eruptions and ENSO events. According to the author, minima of the width of the tropics are found after volcanic eruptions like El Chichon and Pinatubo in 1982 and 1991 respectively and anomalously large expansions after strong La Niña events as in 1999.

5.1.1.2 Seasonal cycle

The seasonal varying temperature and distribution of LCPs was shown in Section 4.1.4.1. Thus, one can assume that the width of the upper TTL has a seasonal cycle as well. Figure 5.3 shows the width of the upper TTL for the different seasons. During NH spring, the northern border of the upper TTL is located between 10° and 18° N (Figure 5.3(a)). On the SH, the border varies between 8° and 12° S. The total width is most narrow (around 26° latitude) and has the highest year to year variability of up to 30 %. An increase of the total width is demonstrated by the slope of the linear regression (blue dotted line). For NH spring the width of the upper TTL is most narrow in 1997 and broadest in 2000, meaning the LCPs are more accumulated within the tropics in 1997, while they are more spread out in the year 2000. During NH summer the upper TTL is broadest (Figure 5.3(b)). This is consistent with a poleward shift of the subtropical jets during that season (see also Birner (2010a)). The subtropical jets define the TTL borders laterally, they vary seasonally in their strength and position (Konopka et al., 2007). During NH summer the total width of the upper TTL amounts to 26° to 35° latitude between 1979-2010. 44 % of the LCPs are located between 8 and 20° N, thus the LCPs are mainly concentrated on the NH. Most of the air masses reach their LCP over the Bay of Bengal (compare Figure 4.9(b)), which is due to the Asian monsoon circulation. During NH fall, the highest amount of LCPs occur also on the NH (Figure 5.3(c)). However, compared to NH summer, the TTL region is slightly shifted towards the SH and the total width of the upper TTL amounts to 25° to 32°. In NH winter, the majority of the LCPs is located on the SH (Figure 5.3(d)), where the borders are located at around 10° N and 15° S. The total width varies between 20° and 30° latitude.
The presented migration of the upper TTL is consistent with the results by Birner (2010a) and is assumed to be related to the seasonal oscillation of the subtropical jets and location of maximum insolation.
Inspecting the total width of the upper TTL for each season and its linear regressions, a broadening of the upper TTL is identified for all four seasons (table 5.1). The strongest increase in the width of the upper TTL is indicated during boreal summer, with 1.39° lat/dec. Most of this signal is influenced by the SH (1.1° lat/dec). During boreal winter, the width of the upper TTL changes by 1.03° lat/dec. This change is mostly influenced by the NH revealing an increase of 1° lat/dec, whereas almost no change is indicated on the SH. During boreal spring, a positive change of 1.14° lat/dec is analyzed mainly due to the change of 0.84° lat/dec on the NH. During boreal fall, similar changes are shown on both

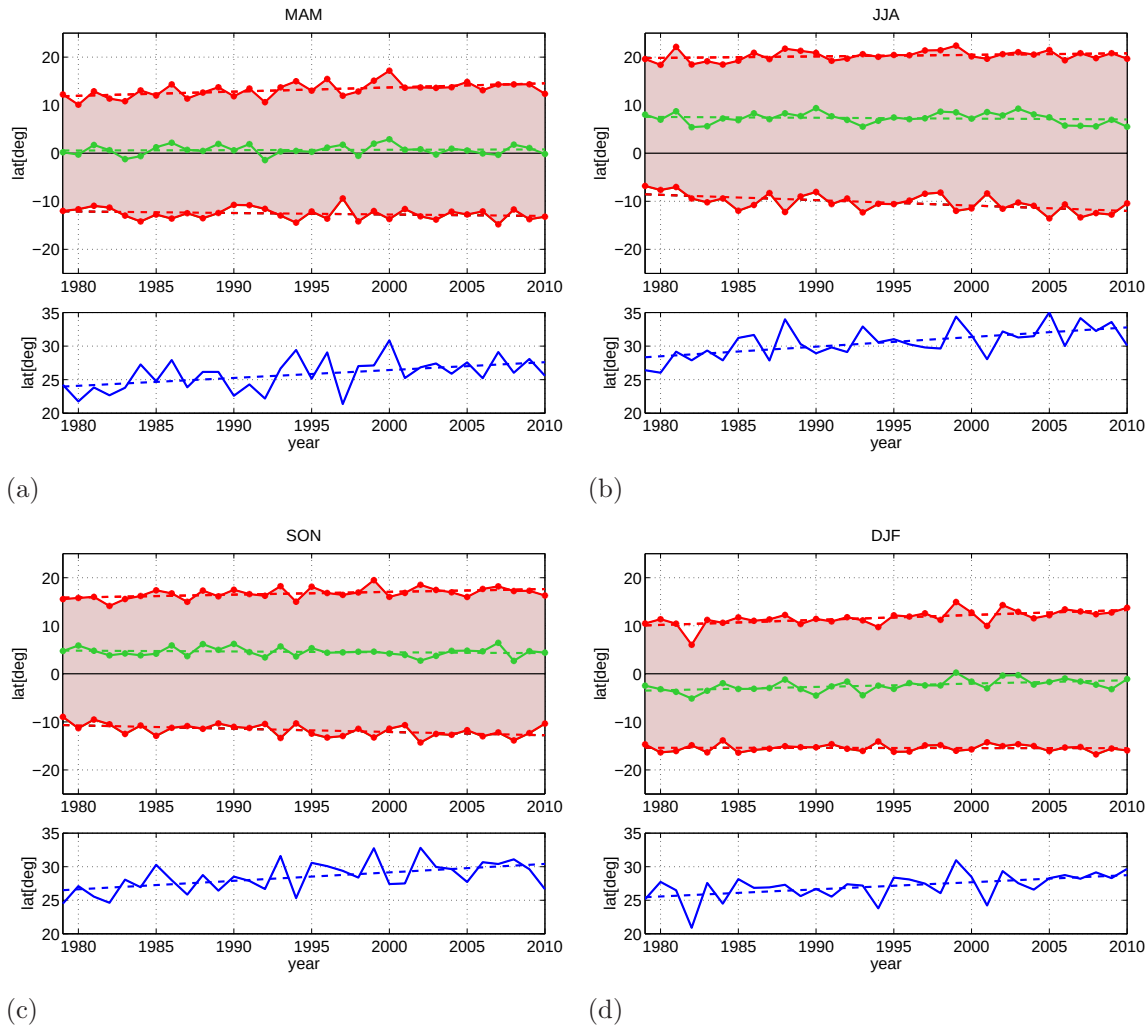

Fig. 5.3: Seasonal average width of the TTL represented by the 88 th percentile of the distribution of LCPs (red shaded area) from 1979-2010 during different seasons. The median of the distribution is presented by the green line. The total width of the 88 th percentile is shown in the lower panels (blue curve). Linear regressions for all curves are represented by the dotted lines with the corresponding colors. For MAM **(a)**, JJA **(b)**, SON **(c)** and DJF **(d)**.

hemispheres, which amounts to a total expansion of 1.22° lat/dec. All four seasons reveal significant results on the 2 σ level.
In general, the absolute change of the upper TTL is similar during all seasons. Seasonal differences occur by concerning the two hemispheres separately, discussed in the following section.

5.1.1.3 Hemispheric differencies

Table 5.1 shows the change of the width of the upper TTL on the northern and southern hemisphere separately. For the annual mean the NH reveals a slightly stronger widening

than the SH, which is significant on the 95 % confidence level. During NH winter and spring the broadening of the upper TTL is more pronounced on the NH. The same holds for the SH winter and spring, revealing a stronger change on the SH. For the NH summer and fall seasons the changes are weaker on the respective summer hemisphere. However, these seasonal differences on the hemispheres are not significant except for JJA and SON on the SH. Hemispherical differences of the expansion of the tropical belt have been noticed in previous studies as well. The observed varying expansion of the tropical belt on the two hemispheres depends on the underlying diagnostics that define the border of the tropics (Davis and Rosenlof, 2012). Some studies suggest a stronger widening of the tropopause on the SH, e.g. Birner (2010a), who found a significant widening trend based on the tropopause height diagnostic. This SH change could be possibly explained by the Antarctic ozone loss (Son et al., 2009; Davis and Rosenlof, 2012). Davis and Rosenlof (2012) showed that most diagnostics based on the tropopause show the largest tropical border expansion on the SH, whereas outgoing longwave radiation (OLR) based diagnostics show the strongest expansion on the NH. One explanation causing this feature is given by Davis and Rosenlof (2012). They suggest that the stronger trend on the NH is possibly due to more assimilated measurements on the NH effecting the hydrological cycle. However, for other metrics (e.g. latitude of peak wind at 850 hPa and most equatorward most latitude of zero crossing of mean meridional streamfunction at 500 hPa), Davis and Rosenlof (2012) investigated that the tropical belt growth is largest during summer and fall of each hemisphere. This is also the case analyzing the change of the upper TTL in this study.

5.1.1.4 Decadal changes

During the different time periods that have been analyzed for ERA Interim, decadal variability in the changing width of the upper TTL are detected. The data analyzed in this study covers the years 1979-2011, thus basically three decades. The results for the different decades are listed in Table 5.1. Noticeable is the fairly strong expand of the upper TTL during the first two decades (1979-1989 and 1989-1999) with a significant widening, whereas in the last decade (1999-2009) almost no change in the width of the upper TTL is apparent. On the annual average the TTL reflects a broadening of 2.81 °/dec during the first decade (1979-1989). The broadening of the TTL is strongest during NH spring and summer (3.2 and 4.7 ° lat/dec). During the second decade, 1989-1999 the upper TTL expanded again significantly by 2.55 ° lat/dec. The largest influence for the expansion arises during NH fall with 3.41 ° lat/dec, whereas NH spring and summer indicates minor expansions of the upper TTL with 2.15° lat/dec and 1.95° lat/dec (not significant). After the year 2000, the change of the upper TTL experiences a slowdown. During 1999-2009, the width of the upper TTL expands by 0.26 ° lat/dec on the annual average (not significant). During boreal summer, the upper TTL indicates the largest expansion of 1.34 ° lat/dec, during NH spring even a narrowing of 0.49 ° is showing up. However, none of the changes, occurring during the third decade, are significant on the 95 % level.
Before the year 2000 an increase of the water vapor content in the lower stratosphere is

reported by Rosenlof (2002). The author suggested that the widening of the tropical upwelling region could be a possible mechanism for this water vapor increase. Some studies report also about a slowdown of the growth of the tropical widening after the year 2000 (e.g. Birner, 2010a; Davis and Rosenlof, 2012). A reason for this phenomena might be the observed changes of the stratospheric circulation, which is related to the decrease of the water vapor content in the lower stratosphere after the year 2000. These atmospheric changes are correlated with a decrease of the cold point temperature in the tropics, a decrease of the ozone concentration near the tropopause after the year 2001 and an increase of the mean tropical upwelling (Davis and Rosenlof, 2012; Randel et al., 2006). However, the observed water vapor drop in 2000 is not well represented in model predictions based on Lagrangian calculations from ERA Interim or temperatures from radiosonde data (Fueglistaler et al., 2013). In contrast to Fueglistaler et al. (2013), who analyzed the stratospheric water vapor based on Lagrangian cold points, the results from this Lagrangian study reveal an indirect effect of the water vapor drop in 2000 by a narrowing of the TTL region. Most of the publications concerning the tropical widening are based on observational data prior to 2005, thus a possible slowdown of the tropical widening or even narrowing after 2000 was not reported in previous studies yet.

5.1.2 Spatial pattern

Concerning the LCP distribution pattern, large variabilities are striking within different regions. Due to seasonal effects, like the Asian Monsoon, changes in the LCP distribution over the year are notable within specific regions (e.g. the Indian Ocean). The width of the upper TTL within different regions during NH summer (JJA) and NH winter (DJF) is shown for ERA Interim (1979-2010) in Figure 5.4. The definition of the geographic regions from Section 4.2 (Figure 4.16) is applied in the following. Different thresholds are chosen to visualize the variability of the upper TTL-width.
During NH winter the median is mostly located on the SH, which implies a less variable border on the SH for almost all regions compared to the TTL-border on the NH. Exceptional is the East Pacific. There the median varies around the equator between 5°S and 5°N indicating larger variabilities on the NH as well (Figure 5.4(c)). Generally, during NH summer the LCP variability and accordingly the TTL border reveal high variability on the SH, the winter hemisphere, for all regions (Figure 5.4, lower panel). For those cases the variability on the SH is higher as the median of the LCPs lies on the NH.
The region with lowest LCP variability, among different percentiles, is indicated by the West Pacific (Figure 5.4(a) and (b)). On annual average the major part of tropopspheric air masses reach the stratosphere above the West Pacific with more than 50% (Figures 4.17 and 4.18). A slight displacement of the NH border towards the pole appears above the WP during NH winter (Figure 5.4(a)). Highest LCP variability is projected for the East Pacific on both hemispheres during NH winter and summer (Figure 5.4(c) and (d)). There annually averaged only 10 % of the LCPs reach the stratosphere from below (Figures 4.17 and 4.18). Above South America, the border of the upper TTL reveals a change towards the

South Pole during NH summer (Figure 5.4(f)). During NH winter the TTL border on the NH is located most equatorward above West Africa compared to other regions. However, a poleward migration of the NH edge is visible until the year 2010 (Figure 5.4(g)). During NH summer the TTL border on the SH reveals a poleward migration during the analyzed period as well (Figure 5.4(h)). A similar behavior is indicated over the Indian Ocean with a poleward displacement of the NH border during boreal winter (Figure 5.4(i)) and of the SH border during boreal summer (Figure 5.4(j)). Overall the upper TTL border on the NH tends to shift towards the pole during NH winter within all regions. Comparably there is a shift of the SH border towards the pole as well during NH summer.
The total width of the upper TTL for the defined regions during the different seasons and on the annual average between 1979 and 2010 is presented in Figure 5.5. The results are based on the 70th[1] percentile as threshold. In the West Pacific a significant positive change of the width of the upper TTL is revealed on the annual average with 0.99° lat/dec. A significant broadening is also identified during NH winter, summer and fall (Figure 5.5(a)). Over the East Pacific on the annual average a significant positive change of the TTL width is indicated by 0.89° lat/dec. However, the strongest positive change is appears during NH summer with 1.87° lat/dec but also during NH fall a significant broadening can be detected (Figure 5.5(b)). For South America a broadening of the upper TTL is significant on the annual average with 0.87° lat/dec during NH summer and fall. The most pronounced change appears during NH summer showing a broadening of 1.21° lat/dec (Figure 5.5(c)). Above West Africa smallest, but still significant changes of the upper TTL appear on the annual average with 0.67° lat/dec and also during NH fall 0.58 ° lat/dec (Figure 5.5(d)). Significant changes in the upper TTL are also revealed over the Indian Ocean on the annual average with 0.86° lat/dec. During NH summer and fall significant broadening is also detected with the largest change over the Indian Ocean during NH summer with 1.33° lat/dec (Figure 5.5(e)).
For the total width of the upper TTL, the largest variability is shown during NH summer over the Indian Ocean where the upper TTL width varies from 14° to 29° latitude. Note, howsoever, that the absolute width reveals now a more narrow upper TTL compared to the values in Section 5.1.1 due to the necessity to select a smaller percentile threshold for the regional analysis. The regions with least interannual variability of the LCP distribution is found over the West Pacific and West Africa. Here the differences of the total width of the TTL during different seasons is small compared to the other regions. On the annual average the total width over West Africa is most narrow and varies from 13° to 19° latitude, whereas the broadest upper TTL is found above West Pacific, South America and the Indian Ocean (17° to 23° latitude).

5.1.3 Discussion

The absolute width of the upper TTL based on the Lagrangian cold point analysis using the 88th percentile threshold for ERA Interim reanalysis ranges from 25° to 30° latitude.

[1]Due to a smaller amount of LCPs in single regions the 88th percentile could not be applied. This is also indicated by large differencies of the upper TTL border represented by the different percentiles e.g. large variability of the border of the upper TTL on the SH in the Indian Ocean Figure 5.4(j).

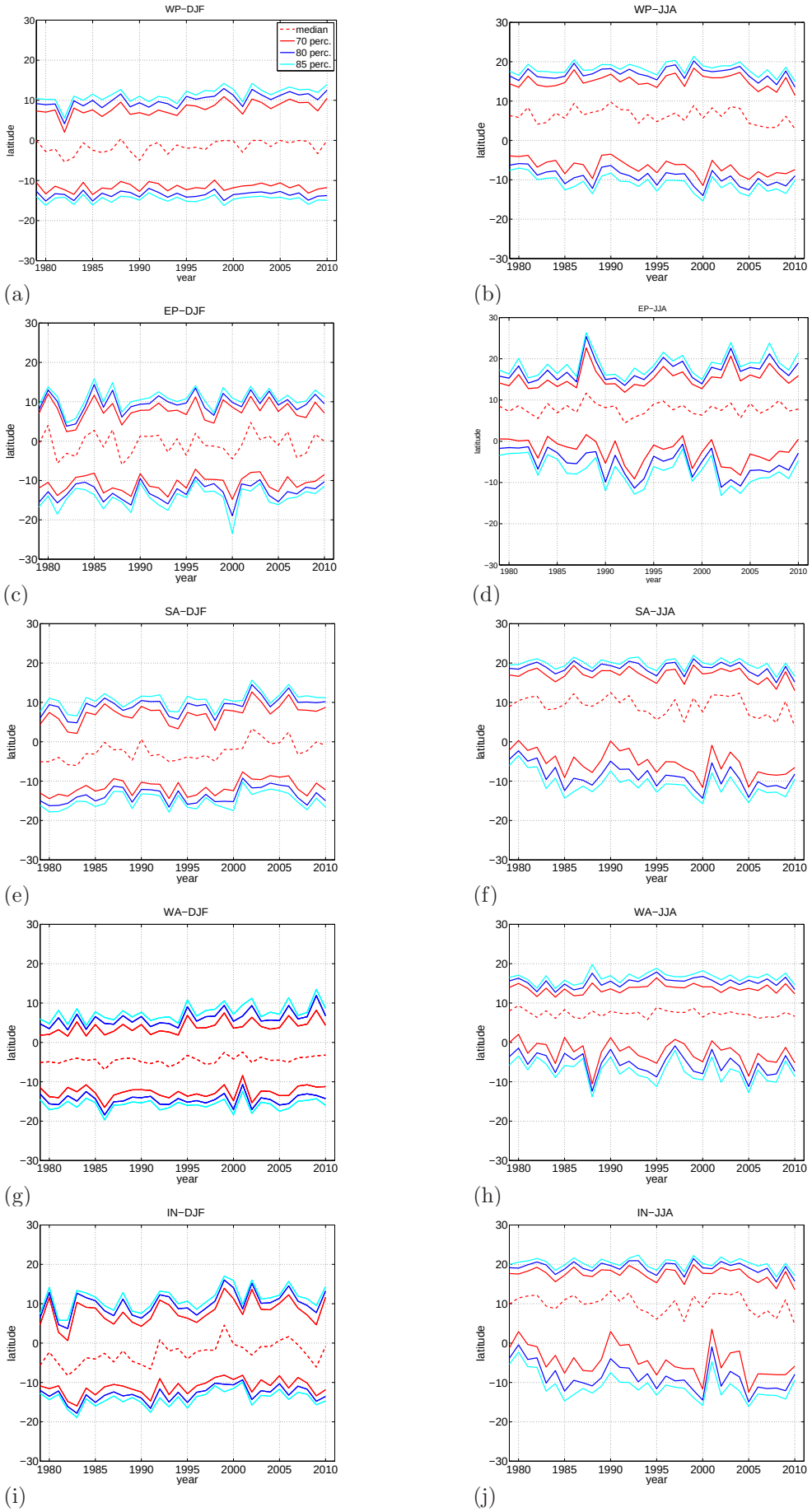

Fig. 5.4: Width of the upper TTL shown by the 70th (red) 80th (blue) and 85th (light blue) percentiles and the median (dotted) of the LCP distribution for different geographic regions for NH summer and winter for ERA Interim 1979-2010. West Pacific (100 - 210° E) (a) and (b), East Pacific (210 - 270° E) (c) and (d), South America (270 - 330° E) (e) and (f), West Africa (330 - 50° E) (g) and (h), Indian Ocean (50 - 100° E) (i) and (j).

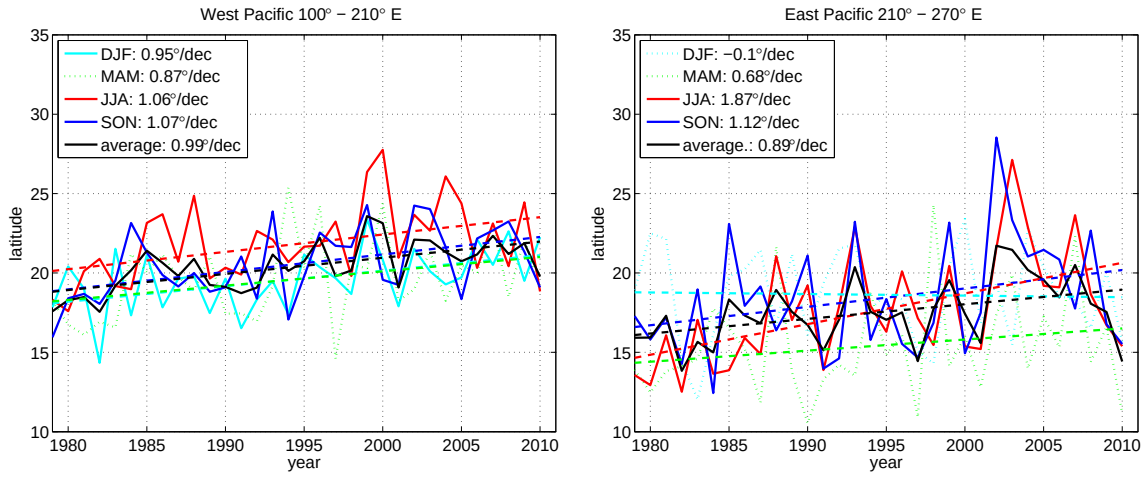

(a)

(b)

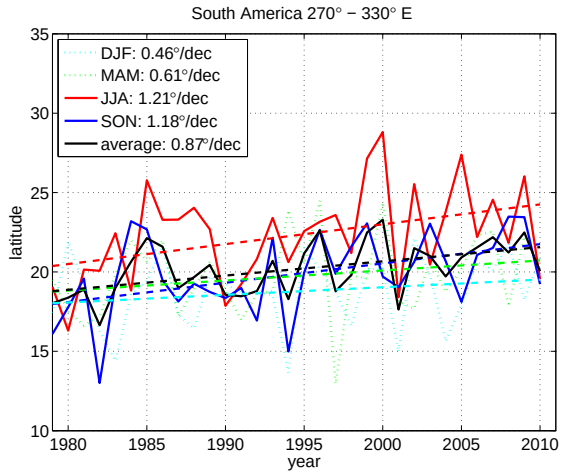

(c)

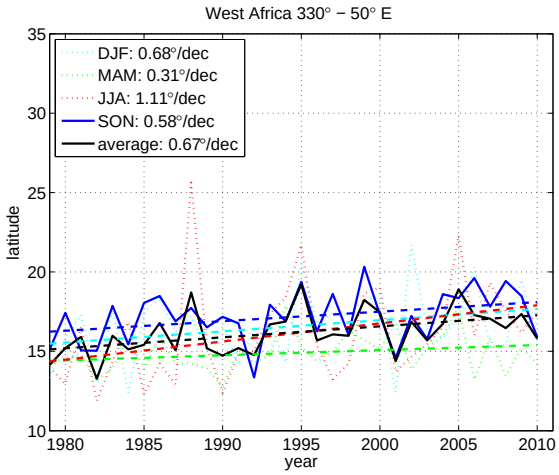

(d)

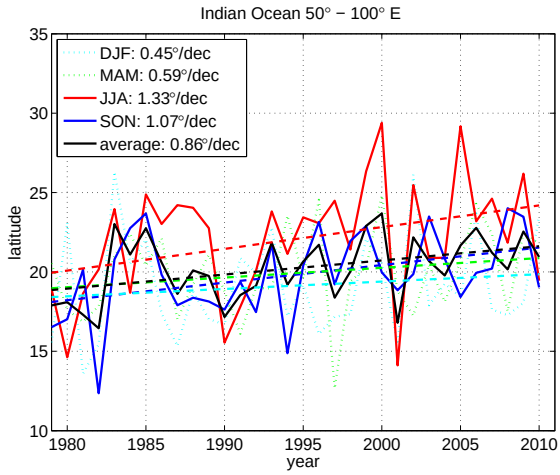

(e)

Fig. 5.5: Time series of the total width of the upper TTL represented by the 70 th percentile of the LCP distribution from 1979-2010 for ERA Interim within different geographical regions: West Pacific (100 - 210° E) (a), East Pacific (210 - 270° E) (b), South America (270 - 330° E) (c), West Africa (330 - 50° E) (d) and Indian Ocean (50 - 100° E). Significant changes within the 95 % confidence interval are indicated by solid lines, dotted lines imply no significance.

Depending on the season, this area is located more on the NH, during NH summer, and on the SH, during NH winter, covering the inner tropical region of the upper TTL. Whereas, other more tropospheric diagnostics, which are used to determine the tropical edges, enclose a broader region. Different widths representing the tropics are resulting by applying different diagnostics. The width of the Hadley circulation generally include a latitudinal band of 60° to 70° (Hu and Fu, 2007). Using the tropopause height diagnostic from Seidel and Randel (2007) the tropical borders cover 50° to 60° latitude. However, varying between different thresholds for the tropopause height, the width of the tropics can also range from 35° to 65° latitude (Seidel and Randel, 2007).
Though, the following question arises: is the meridional extension of the Lagrangian cold point, which is applied within this study as a metric to define a certain width of the upper TTL, really an adequate diagnostic?
Most of the characteristics, which are used to define tropical borders are located in the troposphere (e.g. jet-streams and the Hadley circulation; Section 2.5). The diagnostic of this study, is an important parameter to identify the main entrance region of air masses traveling from the troposphere into the stratosphere. It defines the cold point tropopause though, it connects the TTL with the upwelling branch of the BDC or the lower boundary of the tropical pipe (Plumb, 1996). The definition of the tropopause based on the cold point is reliable, when the lower stratosphere is not close of being isothermal, i.e., within the deep tropics (Highwood and Hoskins, 1998). Especially, in respect of transport processes between the troposphere and the stratosphere, the cold point tropopause is more relevant than the lapse rate tropopause (Selkirk, 1993; Mehta et al., 2011). Thus, even though different diagnostics and definitions for the total width of the tropics exist, they all represent a measure of one specific quantity of the width of the tropical belt.
Hence, when analyzing the broadening of the upper TTL it should be kept in mind that a poleward extension of the LCPs describes the cold point tropopause, which doesn't cover the whole tropical region but rather defines the inner tropics of the TTL. It is a stratospherical influenced metric for the main entrance region for tropospheric trace gases into the stratosphere. A change in the width of the upper TTL represents one consequence of the tropical broadening, which has not been investigated so far.

The results presented in Table 5.1 indicate that significant changes of the width of the upper TTL mostly exist, when the time interval is long and smooth enough. Thus, the change in the width of the upper TTL is significant considering the different seasons over the years 1979-2010 as well as for the annual average. The results for the annual average on the southern and northern hemisphere separately and of the two decades 1979-1989 and 1989-1999 show significances as well. Analyzing the change of the width of the upper TTL for different geographical regions, each region indicate significant positive changes between 1979 and 2010. On the annual average the upper TTL over the West Pacific reveals the largest change with 0.99° lat/dec. The East Pacific indicates the largest seasonal change of the upper TTL during NH summer by 1.87° lat/dec.
However, compared to previous studies, the change of the tropical widening deviates, which is probably due to differently applied diagnostics. (Davis and Rosenlof, 2012) pointed out

that especially subjective chosen diagnostics reveal a larger trend than the results from diagnostics, which are based on an objective threshold . The here detected significant change of 1.22 ° lat/dec for the upper TTL between 1979-2010 (ERA Interim data) based on an objective threshold, is larger than the trend obtained from objective methods by Birner (2010a) analyzing the tropopause height, who revealed a trend of -0.5 to +0.7 ° lat/dec (1979-2005) depending on the input data).

5.2 Global climate models

In the second part of this chapter the widening of the upper TTL is analyzed for the different climate models and is compared with ERA Interim assimilation for the time period 1990-1999. Firstly, the threshold for the tropical widening diagnostic is evaluated. The 88th percentile threshold is used for the climate models as for ERA Interim (except for WACCM: 78th percentile). Then, the width of the upper TTL is analyzed for the climate models with respect to the annual and seasonal cycles.

5.2.1 TTL widening diagnostic

Among the reanalysis and the different climate models moderate discrepancies appear concerning the resulting change of the width of the upper TTL dependent on different thresholds. The behavior of the climate models for different thresholds is shortly described in the following. Figure 5.6 shows the change of the width of the upper TTL for the annual mean LCP distributions for ERA Interim (a) and for the different climate models (b)-(h) as functions of percentile between 1990 and 1999. For all models, the change of the upper TTL width increases with percentile, but a clear positive change is only given by ERA Interim (a) and MPI ESM (h). For MPI-ESM this holds only up to a percentile of 94 %. For E39CA (b), the change slightly increases until the 83rd percentile and experiences a jump at the 90the percentile. Afterwards, the distribution is too irregular to define a clear border. The LCPs are uniformly distributed up to the 94th percentile of the LCP distribution for NIWA-SOCOL REF-B1 (c). When larger percentiles are applied, no clear border can be defined anymore. The same behavior is visible for CMAM (e), whereas a stable change occurs by using a percentile between 88 and 93.

The changes of the upper TTL width show different behaviors for the REF-B2 simulations (NIWA-SOCOL (d) and CMAM (f)). The REF-B1 simulations indicate almost all (except WACCM) an increasing width of the TTL, which is displayed by positive numbers for the change. In contrast, the REF-B2 simulations reflect in both cases a narrowing of the upper TTL. In comparison to all other model results, the change of the width of the upper TTL indicates large variances for WACCM (g) when the percentile is larger than 78. Up to the 78th percentile the width of the upper TTL indicates a narrowing, but the LCPs located more outside of the 78 th percentile seem to be not uniformly distributed and thus no TTL border can be defined.

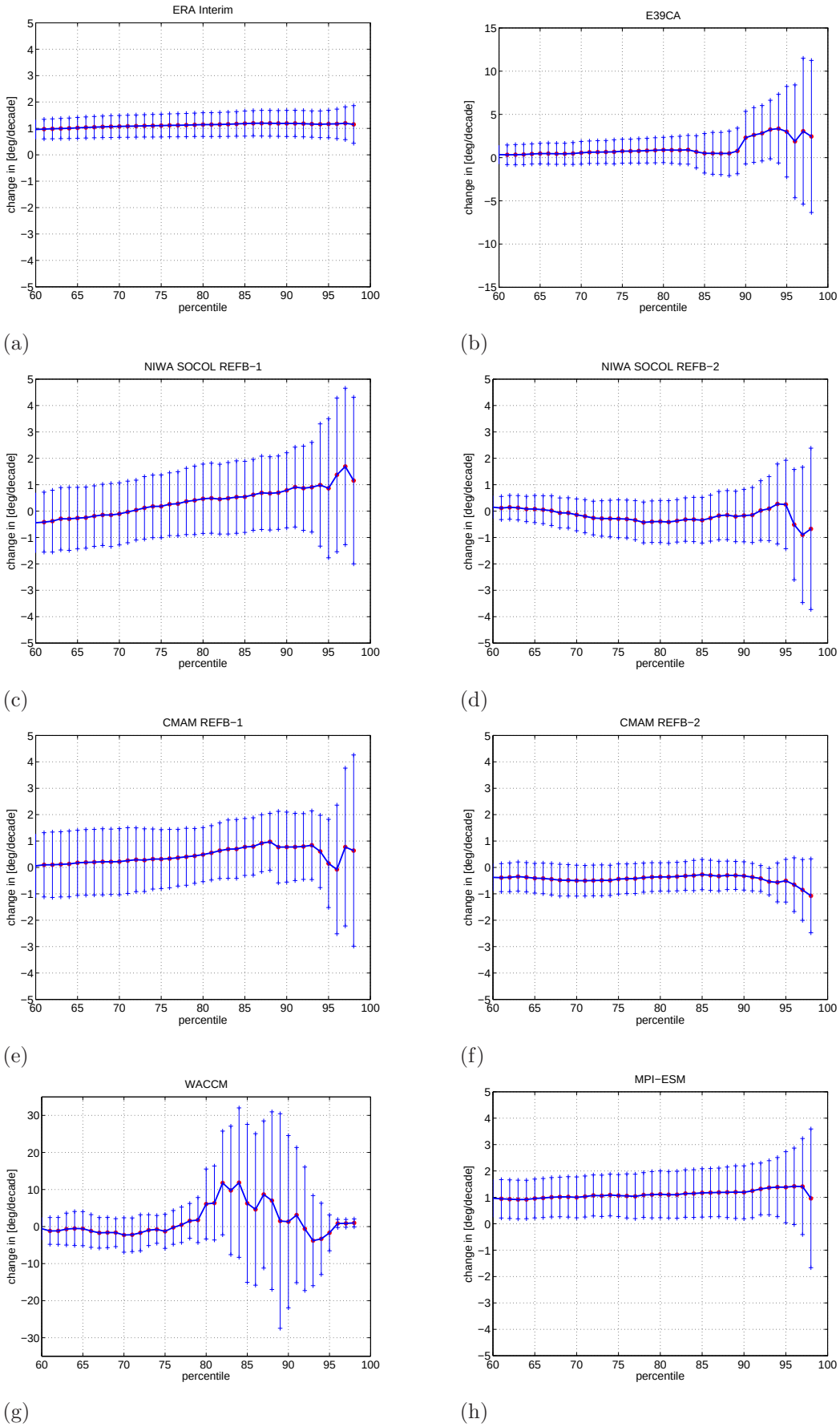

Fig. 5.6: Change of the width of the upper TTL (in $°lat/dec$) of the annual mean for different thresholds (percentiles) shown for the time period 1990-1999 for **(a)** ERA-Interim,**(b)** E39CA, **(d)** NIWA-SOCOL REF-B2, **(c)** NIWA-SOCOL REF-B1, **(e)** CMAM REF-B1, **(f)** CMAM REF-B2, **(g)** WACCM, **(h)** MPI-ESM. Red dots mark the value of the change of the TTL, blue vertical lines mark the 95 % level of the significance. (Note that there are different axis labelling for (b) and (h)).

For ERA Interim and the different climate models the 88th percentile as one joint threshold is chosen (for WACCM 78th percentile). Nevertheless it is important to mention that although for ERA Interim the 88th percentile is selected as most robust threshold, there might be more suitable thresholds to define the width of the upper TTL for the different climate models individually.

The results shown in Figure 5.6 lead to the assumption that due to the different behavior of the LCP distribution from the models, they all reveal a particular threshold, where the assumed change in the width of the upper TTL is most stable. However, due to an adequate number of LCPs for most models (not shown here), it is possible to define a clear border of the upper TTL up to the 93th percentile (except for WACCM). Figure 5.7 represents the width of the upper TTL based on different percentiles for ERA Interim and the climate models (70th: light blue; 80th: dark blue; 90th: red; median: yellow). ERA Interim and most of the climate models show an uniform change over the time period for different percentiles of the LCP distribution. However, small irregularities are indicated by E39CA (b). There, the width of the upper TTL, represented by the 90th percentile (red), reveals a more variable evolution on the SH compared to the 80th and 70th percentile. This indicates that there is a smaller number of LCPs on the SH than on the NH, increasing the variation of SH upper TTL border. Large discrepancies are shown for WACCM (g). There, the border on the NH reveals large discrepancies among different thresholds and thus, no clear border can be defined.

The results, presented in Figure 5.6 and 5.7, illustrated the diagnostic in defining the width of the upper TTL and the interannual variability of it for ERA Interim and different climate models. For most of the models (except WACCM) applying the 88th percentile threshold is within the limits of a stable definition for the borders of the upper TTL.

5.2.2 Annual average

Figure 5.8 shows the annual average width of the upper TTL between 1990 and 1999 for ERA Interim and climate models. The median of the LCP distribution is mostly located on the NH between 0° and 3° N. This means more LCPs are located on the NH. As WACCM is an outlier, due to the unrealistic representation of the NH edge of the upper TTL, it is not considered in the following description. The most equatorward edge for the 88th percentile of the LCP distribution is indicated by CMAM REF-B2 (14°N - 12°S). The most poleward edges are simulated by E39CA and NIWA-SOCOL REF-B1 (7° N to 15° S). The edges of the upper TTL for reanalysis and climate models are more confined on the NH (14° to 17° N), whereas they show a larger spread on the SH and varies between 10° S and 17° S. These locations of the hemispherical borders of the upper TTL coincide approximately with the latitude, where the gradient of the stratospheric tropical upwelling at 70 hPa changes from an increase of the vertical velocity to a decrease of the upward massflux between around 15° N and 10° S (SPARC, 2010, Chapter 4). The turn-around latitude, defined as where the upward mass flux becomes zero, is located beyond the borders of the upper TTL, further poleward at around 40° N and 35° S.

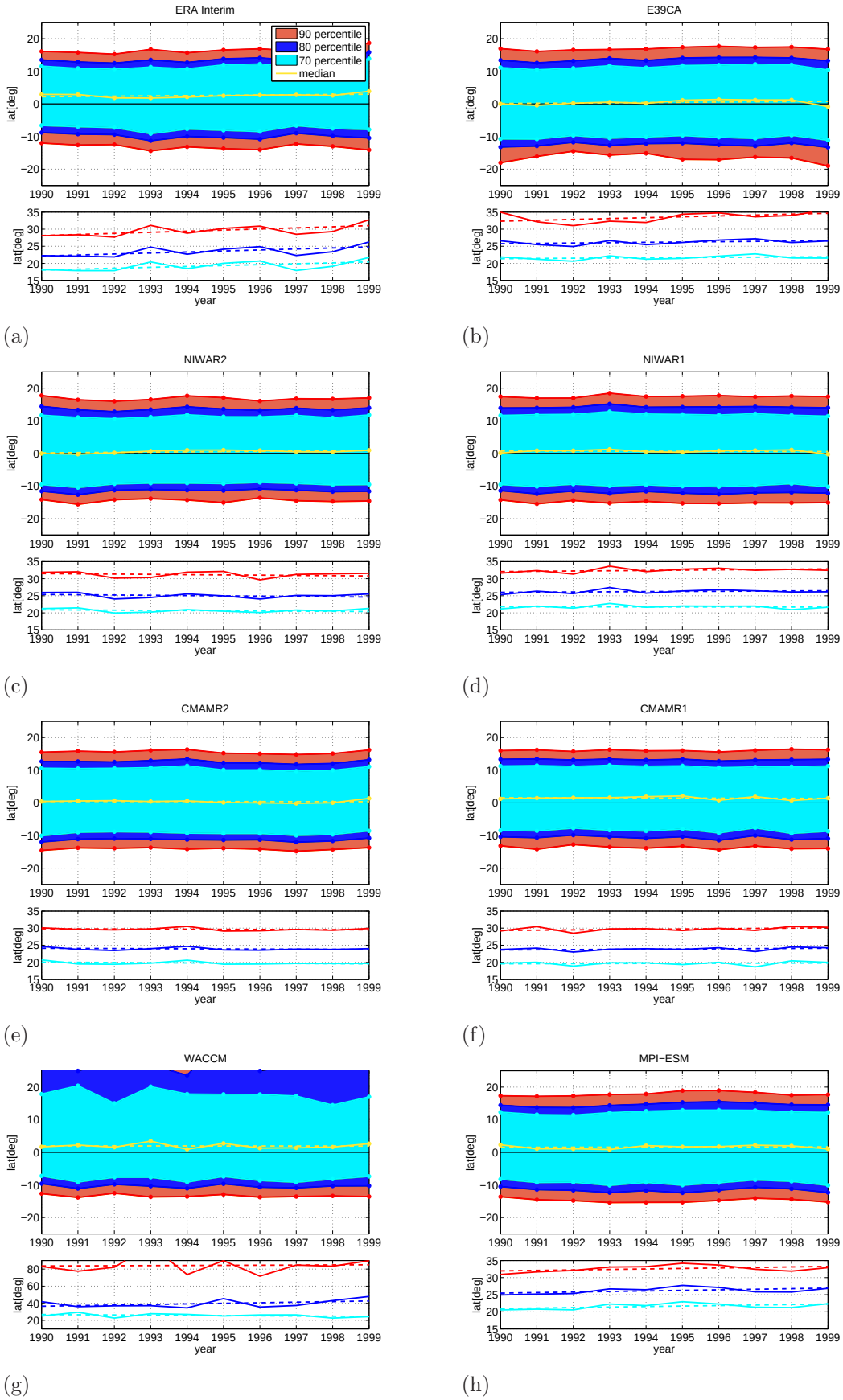

Fig. 5.7: Annual average width of the upper TTL represented by the 70th (cyan), 80th (blue), 90th percentiles (red) and the median (yellow) of the LCP distribution for ERA Interim and climate models 1990-1999. (a) ERA-Interim, (b) E39CA, (c) NIWA-SOCOL REF-B2, (d) NIWA-SOCOL REF-B1, (f) CMAM REF-B1, (e) CMAM REF-B2, (g) WACCM, (h) MPI-ESM.

The absolute width of the upper TTL varies between 26° and 33° latitude. The most narrow width is shown by ERA Interim and the two REF-B2 simulations. E39CA and NIWA-SOCOL REF-B1 reveal the broadest upper TTL. A significant positive change of the width of the upper TTL is indicated by ERA Interim with 2.84 ° lat/dec. The only climate model simulating a significant positive change of the upper TTL is the historical run of MPI-ESM. However, the change of 1.37 ° lat/dec is less than half of the change indicated by ERA Interim. The remaining REF-B1 simulations suggest a positive change of the upper TTL as well although it is not significant on the 95 % level. The REF-B2 simulations though simulate a negative change of the upper TTL.

5.2.3 Seasonal cycle

During NH spring 5.9(a), the deviation in the location of the upper TTL border on the SH is small between ERA Interim and the different climate models, whereas on the NH almost all climate models show a border located more poleward compared to the reanalysis. Hence, on the average the total width of the upper TTL is larger for all climate models during NH spring than for ERA Interim. The median of the LCP distribution for ERA Interim is varying around the equator, which is also reflected by the climate models. During NH summer (b), most of the climate models reveal an upper TTL border similar to ERA Interim on the NH, whereas the spread of the southern border is larger, varying between 9° and 15° S. The median of the LCP distribution is consistently located on the NH between 2° and 10° N for all models. During most of the time period, ERA Interim and CMAM REF-B1 reveal the location of the median further poleward. During NH fall (c), ERA Interim and climate models agree well with the edge of the upper TTL on the NH (15° to 18° N) apart from the outlier WACCM. The location on the SH shows a larger variability of the edges from 7° to 22° S. The median of the LCP distribution varies around 5° N for ERA Interim, whereas all climate models indicate a systematic southward shift towards the equator. During boreal winter (d) all models, seem to agree best with ERA Interim in matters of the width of the upper TTL . Due to the maximum insolation, the location of the median is located on the SH with a slight northward displacement for WACCM. The total width of the TTL varies between 22° and 32 ° latitude. Kremser et al. (2009) analyzed two CCMVal-1 CCMs (E39CA among them) with a Lagrangian approach for different NH winters. Although the authors do not mention it explicitly, the meridional extension of the LCPs of the CCMs is distributed more polewards as well indicating a more polewards TTL border. This is also analyzed for E39CA in the present study not only during NH winter but on the annual average as well (Figure 5.8).
During NH summer and fall the most narrow upper TTL width is simulated by CMAM REF-B2. During NH winter and spring ERA Interim, CMAM REF-B2 and NIWA-SOCOL REF-B2 are close-by showing the most narrow width. Seasonally, the most narrow width of the upper TTL appears during NH spring and winter. During NH summer the TTL width is widest for reanalysis and all climate models. Smallest deviations between ERA Interim and climate models are often found on the hemispheres, where most LCPs are located thus, the hemisphere the median appears. A striking feature of the shown results for the width of

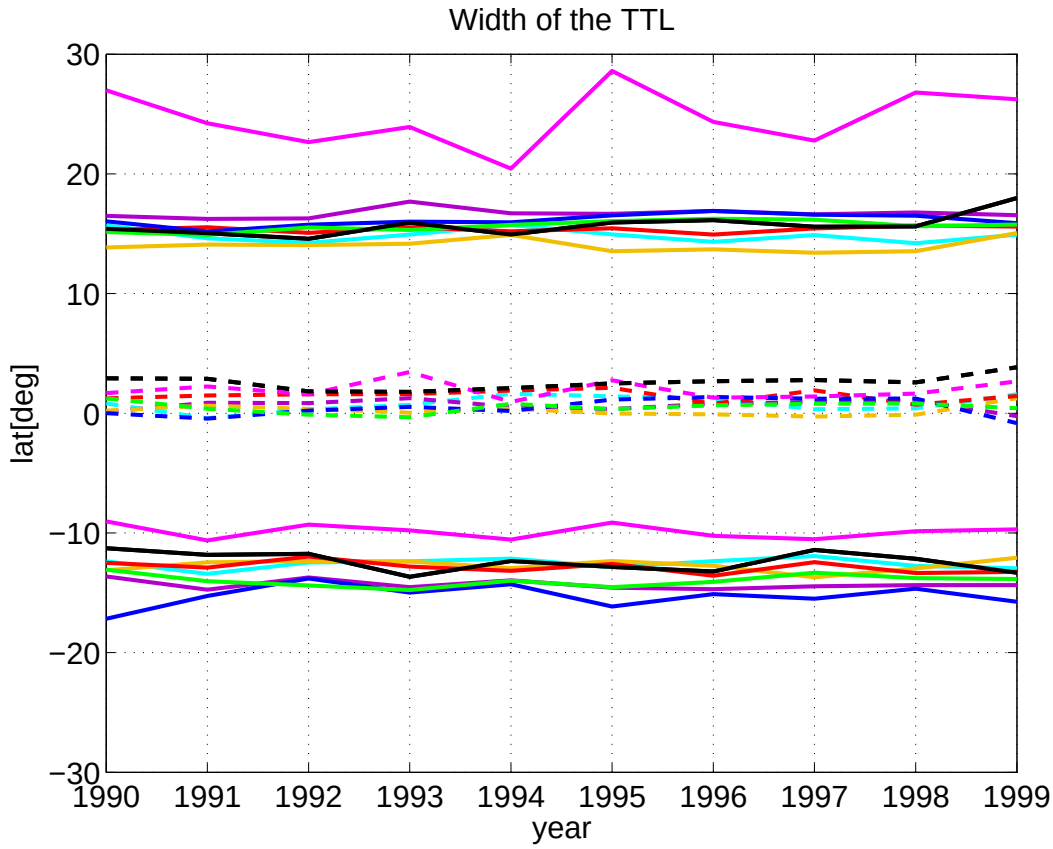

(a)

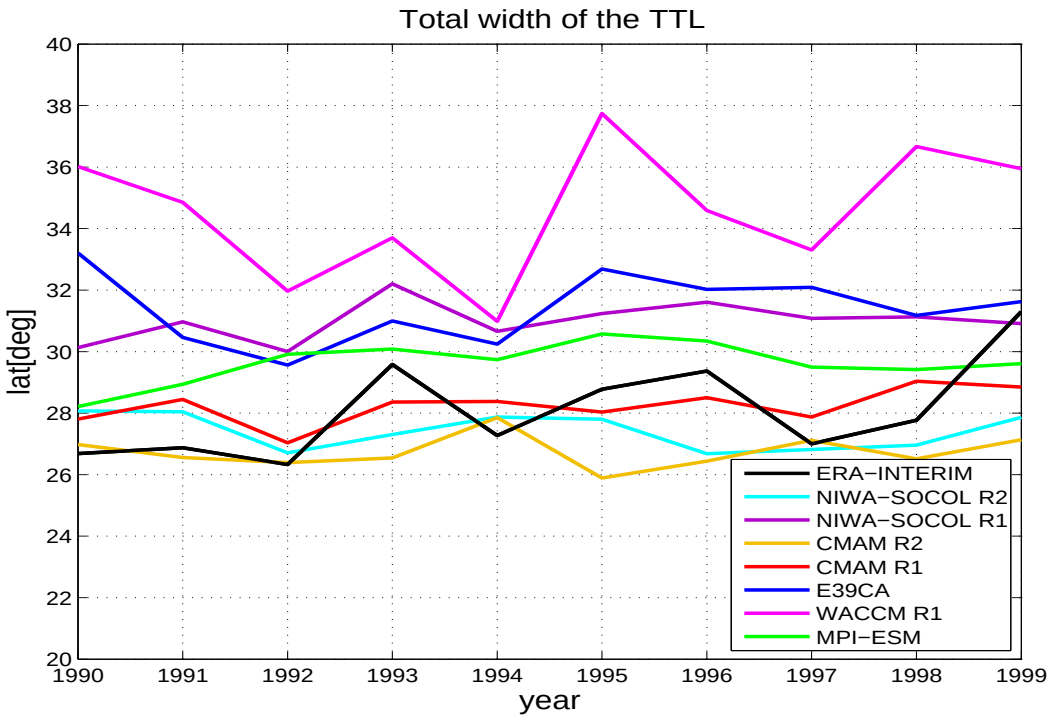

(b)

Fig. 5.8: Annual average borders of the upper TTL for ERA Interim and climate models from 1990-1999 (a) and the total width of the TTL respectively (b).

the upper TTL in Figure 5.9 is the well represented border of the upper TTL from WACCM on the SH whereas on the NH there seem to be large discrepancies (except for DJF). Due to a smaller percentile chosen for WACCM (78 %), the southern edge of TTL is located more equatorward than shown by the reanalysis and simulated by the other climate models.

A spatial change of the width of the upper TTL was tested within this study. Due to large variability of the spatial LCP distribution on the annual and seasonal average for all climate models a spatial analysis of the width of the upper TTL lead to large uncertainties. Further, the time period is too short to detect longterm changes or trends. However, an outlook for the upper TTL width, at least for the West Pacific the most robust LCP occurrence area, will be given in chapter 6 for the future simulations.

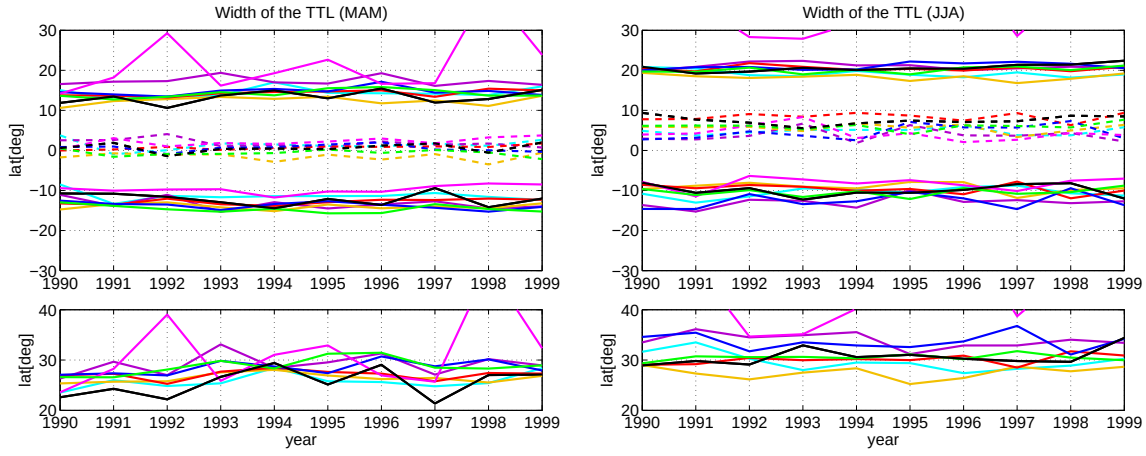

Fig. 5.9: Width of the upper TTL represented by the 88th (WACCM, 78th) percentile of the distribution of LCPs on the time scale from 1990-1999, seasonal averages for ERA Interim and climate models. See Figure 5.8 for color coding legend.

Changes of the upper TTL width between 1990-1999

The change of the upper TTL for the different climate models between 1990-1999 is presented in Table 5.2. Annually averaged, ERA Interim reveals a significant positive change of the upper TTL of 2.84° lat/dec between 1990-1999. All REF-B1 simulations and the historical run from MPI-ESM, indicate a broadening of the upper TTL as well. However, the REF-B2 simulations from CMAM and NIWA-SOCOL project a narrowing of the upper TTL area of -0.26° and -0.62° lat/dec. MPI-ESM indicates a significant meridional expansion of 1.37° lat/dec during that decade. Whereas, the changes by CMAM REF-B1 (0.97° lat/dec), NIWA-SOCOL REF-B1 (0.67° lat/dec), E39CA (0.49° lat/dec), CMAM REF-B2 (-0.26° lat/dec) and NIWA-SOCOL REF-B2 (-0.62° lat/dec) are not significant.
On a seasonal cycle, the models behave differently in matters of the strength of a changing TTL width. However, most of them agree with a broadening of the upper TTL, which is significant for ERA Interim during all seasons. WACCM, indicates large but unrealistic changes during NH spring, summer and fall. The changes in the upper TTL for the climate models mostly vary between 0.1° and 2° lat/dec between 1990 and 1999. A significant narrowing of the TTL region is indicated during NH fall by the two REF-B2 simulations by the NIWA-SOCOL and CMAM models. During NH summer NIWA-SOCOL REF-B1 and REF-B2 and E39CA simulate a narrowing of the upper TTL, however these results are not significant.
Compared to the annual average change in the width of the upper TTL, resulting from the ERA Interim reanalysis within the same time period, the models simulate a weaker change. For a different diagnostic, the width of the Hadley cell, Johanson and Fu (2008) found a significant widening of around 3° between 1979-2005 based on observational data (ERA40 and NCEP). The authors showed that various GCMs do simulate a significantly weaker widening of the tropical belt. Although a different diagnostic has been used in Johanson and Fu (2008), this discrepancy between observational data and climate models is also one result of the present study.

1990-1999	DJF	MAM	JJA	SON	annual
ERA Interim	2.72 [0.72]	3.2 [1.13]	2.39 [0.66]	3.04 [0.86]	2.84 [0.55]
CMAM REF-B1	0.88 [2.25]	0.25 [2.12]	1.49 [1.91]	1.27 [3.4]	0.97 [1.08]
CMAM REF-B2	0.02 [0.75]	0.14 [1.21]	0.63 [1.58]	-1.95 [0.97]	-0.26 [0.69]
NIWA-SOCOL REF-B1	1.31 [2.8]	1.27 [4.67]	-1.85 [2.3]	1.95 [3.41]	0.67 [1.39]
NIWA-SOCOL REF-B2	0.76 [2.55]	0.37 [2.77]	-0.7 [2.44]	-2.16 [2.12]	-0.62 [1.15]
WACCM	1.87 [5.41]	8.7 [15.88]	1.28 [18.09]	-5.72 [13.91]	1.53 [4.71]
E39CA	0.23 [2.91]	2.05 [2.7]	-0.47 [3.88]	0.13 [8.43]	0.49 [2.58]
MPI-ESM	1.11 [2.12]	1.8 [1.65]	1.66 [1.37]	0.21 [1.72]	1.37 [1.11]

Tab. 5.2: Change of the upper TTL (in ° lat/dec) for ERA Interim and climate models represented by the 88th percentile (WACCM 78th) of the LCP distribution between 1990 and 1999. Seasons, hemispheres and decades are analyzed separately. The 95% confidence interval is calculated for each quantity and is displayed in the brackets. Significant changes are shaded in grey.

5.3 Summary

In this chapter a new metric is applied to analyze the widening of the upper TTL in ERA Interim and different climate models. It is shown that a change of the edges of the upper TTL can be diagnosed by the meridional distribution of LCPs using trajectory calculations. A change of the meridional distribution is also an indication of a change in the tropical upwelling region (Fueglistaler and Haynes, 2005).
ERA Interim annual averages indicate a significant broadening of the upper TTL with 1.2 ° lat/dec between 1979 and 2010. The two hemispheres change almost uniformly on the annual average, whereas for the seasonal cycle the changes of the upper TTL between the hemispheres reveal differences as expected. It is also shown that the resulting temporal change in the TTL is highly depending on the considered time period. While a relatively strong change occurs in the first two decades 1979-1989 and 1989-1999 with 2.5° and 2.8° lat/dec widening respectively, only a small positive (non significant) change is detected for the decade 1999-2009. This might be due to a change of the stratospheric circulation around 2000 (Davis and Rosenlof, 2012), influencing also the stratospheric water vapor content (Randel et al., 2006)
Additionally, the change of the width of the upper TTL width within different geographical regions is analyzed for ERA Interim for the timeperiod 1979-2010. The area over the tropical West Pacific is the main entrance region of air masses traveling from the surface to the stratosphere. The analysis revealed that beside the whole tropical belt also a significant broadening within the West Pacific can be observed during all seasons and a change of 0.99° lat/dec on the annual average. Significant broadening of the upper TTL is also found for different seasons and regions and on the annual average for all geographical regions. Largest significant change is projected during NH summer over the East Pacific with 1.87° lat/dec. Figure 5.10 summarizes the annual average changes of the width of the upper TTL for ERA

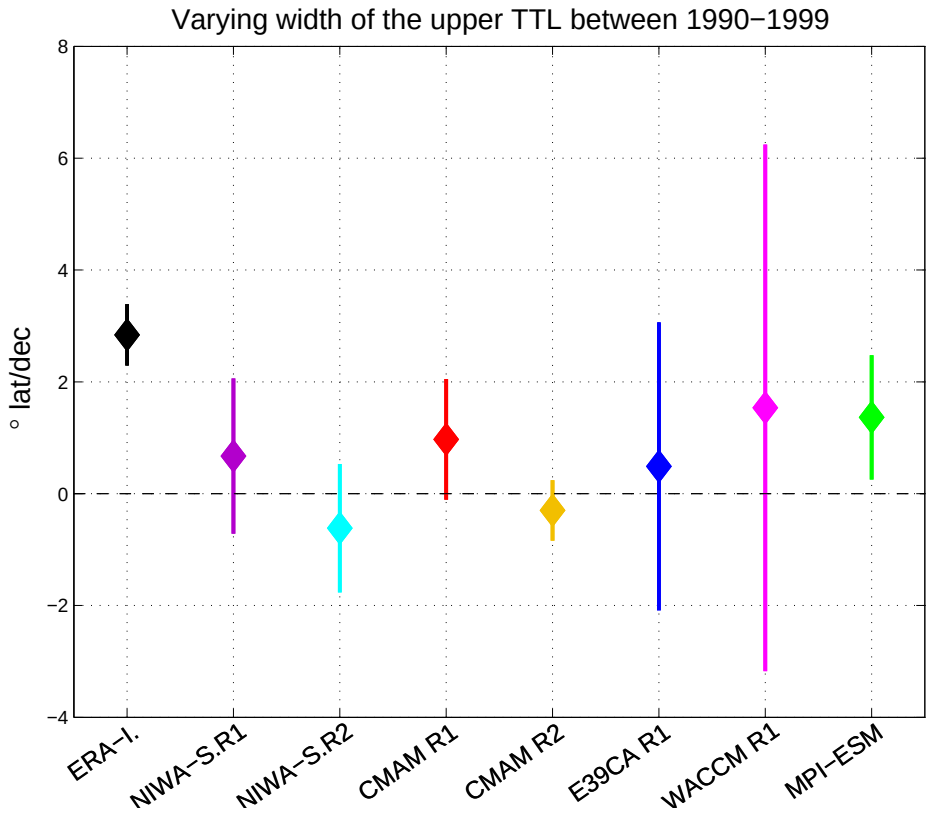

Fig. 5.10: Change in the annual mean width of the upper TTL [in ° lat/dec] shown for ERA Interim and different climate models from 1990-1999, applying the 88th percentile threshold. Vertical lines mark the 95 % level of the significance.

Interim and climate models between 1990 and 1999. The vertical bars represent the significance within the 95 % confidence interval. ERA Interim indicates a broadening of the upper TTL of 2.84° lat/dec for the 1990-1999 period. The REF-B1 models and MPI-ESM simulate a broadening of 0.5° to 1.4° lat/dec during the same period. Overall, the analyzed historical CMIP5 run of the MPI-ESM simulation showed the best agreement with ERA Interim performance representing a significant widening of the TTL. The two REF-B2 simulations indicate a narrowing of the TTL region. The REF-B2 scenario uses anthropogenic forcings only compared to REF-B1, where natural forcing is taken into account as well. The cause of a widening tropical belt has been investigated by Lu et al. (2009) who found that the increase of the width of the Hadley Cell is caused entirely by the direct radiative forcing related to GHG increase and stratospheric ozone depletion. Thus, in contrast to Lu et al. (2009), who showed that the broadening of the tropics can be attributed solely to anthropogenic forcings, the REF-B2 simulations analyzed within this study simulate a narrowing. This result indicates the importance of the role played by natural variability such as volcanic eruptions and ENSO on the meridional distribution of LCPs, hence on the width of the upper TTL. The expansion of the upper TTL are only significant for ERA Interim and MPI-ESM, whereas they are not for the CCMs. All models reveal a weaker widening of the upper TTL compared

to ERA Interim. Based on the Hadley cell diagnostic, a systematicly weaker widening of the tropical belt in GCMs compared to observations was also found by Johanson and Fu (2008). The authors argue that model responses to volcanic, GHG or ozone depletion forcing are probably too small and hence, underestimating the stratosphere troposphere coupling in the tropics.

Chapter 6

Future changes of the TTL

In this chapter future changes of the upper TTL are analyzed based on climate model simulations applying a Lagrangian approach. In the first part differences of the Eulerian cold points and the vertical velocity in the TTL between past and future are investigated. These fields are used as initialization for the trajectory calculations of the TTL. The resulting LCP temperature and their distribution and change in the future within different seasons, years and regions are presented. Furthermore, a possible change of the width of the upper TTL in the future is analyzed. Three future simulations, two from CCMVAL-2 REF-B2 (CMAM and NIWA-SOCOL), and one from CMIP5 (MPI-ESM) are analyzed for the decades 1990-1999, 2040-2049 and 2090-2099[1].

6.1 Eulerian cold point

The annual average cold point temperatures within 10°N-10°S for ERA Interim and the different climate models is presented in Figure 6.1. The evolution of the Eulerian cold point temperature in the inner tropics (solid line) for the three future simulations reveals a slight increase from the past (1990s) to the future (2090s). The average cold point temperature for CMAM REF-B2 (yellow) varies in the 1990s around 191.7 K and increases up to the 2090s decade to 192.7 K. The same amount of ∼1 K increase is also visible for MPI-ESM (green) from 192 K to 193 K. NIWA-SOCOL REF-B2 (light blue) reveals a somewhat smaller increase of ∼0.8 K from 187.7 K in the 1990s to 188.5 K in the 2090s. As mentioned before in Chapter 4, the NIWA-SOCOL model has a strong cold bias up to 5 K. The global maps for the Eulerian CP temperature of the future simulations is shown in Figure A.10.

6.2 Vertical velocity

The vertical velocity fields for future model simulations (CMAM REF-B2, NIWA SOCOL REF-B2 and MPI-ESM) at 100 hPa are presented in Figure 6.2. The average vertical

[1]For NIWA-SOCOL REF-B2 instead of 2090-2099, the decade 2089-2098 was provided and compared respectively.

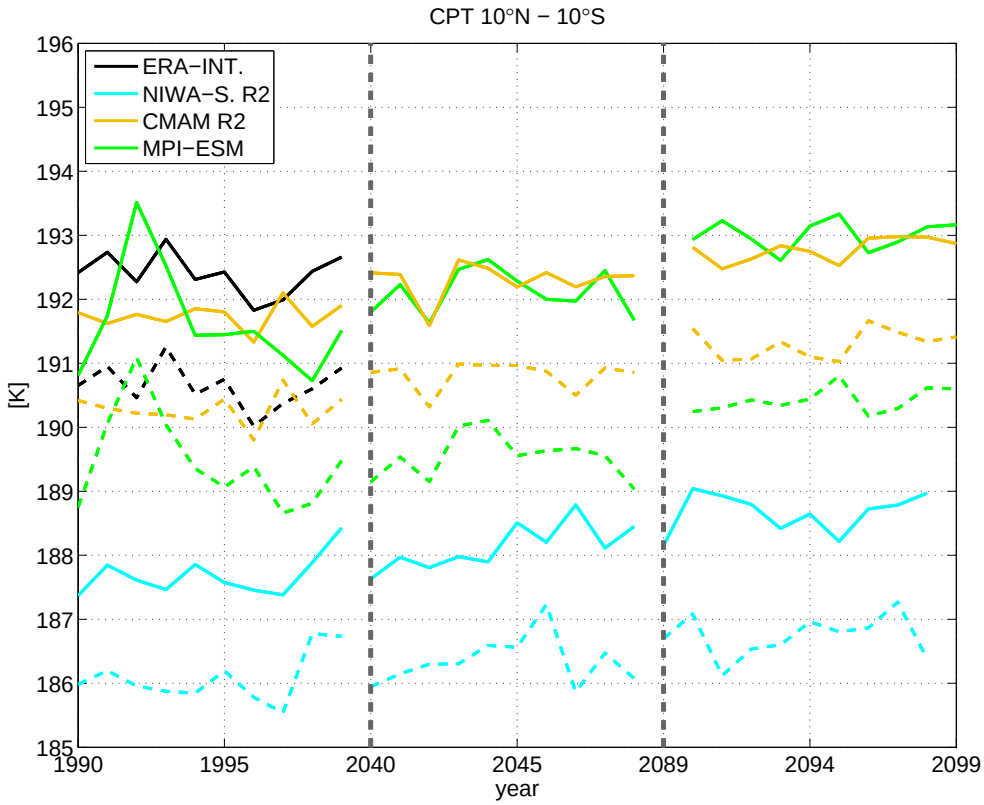

Fig. 6.1: Time series for the annual average Eulerian cold point temperature (solid) and the Lagrangian cold point temperature (dashed) between 10°N - 10°S, using ERA Interim, 1990-1999 and different climate models (1990-1999, 2040-2049, 2090-2099). For NIWA-SOCOL REF-B2 data from 2089-2098 were provided. See legend for color coding.

velocity for the climate models from 1990-1999 (left panel) are in good accordance with the ascent regions over the West Pacific and Africa as indicated by ERA Interim (Figure 6.2(a)). However, the pronounced ascent region over the Caribbean Sea, as shown by ERA Interim, is shifted towards the South and is located more over the South American continent for the climate models (Figure 6.2). The subsidence regions over North West Africa and the Middle East are also apparent in the climate models. Generally, the vertical velocity at the 100 hPa level near the tropopause is strongest in the CMAM REF-B2 simulation (upper row), where especially in the West Pacific the ascent is two times higher compared to ERA Interim but also the main ascent area is somewhat shifted to the SH tropics. The vertical velocity field of the climate model MPI-ESM (lower row) represents very similar magnitude and locations of subsidence and ascent as ERA Interim probably due to the fact that both models rely on the original ECMWF model code. The magnitude of vertical velocity from NIWA-SOCOL REF-B2 lies in between the two other climate models, but reveals stronger ascent in the central and eastern Pacific as well caused by the ENSO like pattern in the 1990s associated with an eastward shift of the main ascent region.

Analyzing 11 CCM simulations until 2100, Butchart et al. (2010) analyzed an increase of the tropical upwelling by 2% of the multi model mean per decade in the lower stratosphere. At

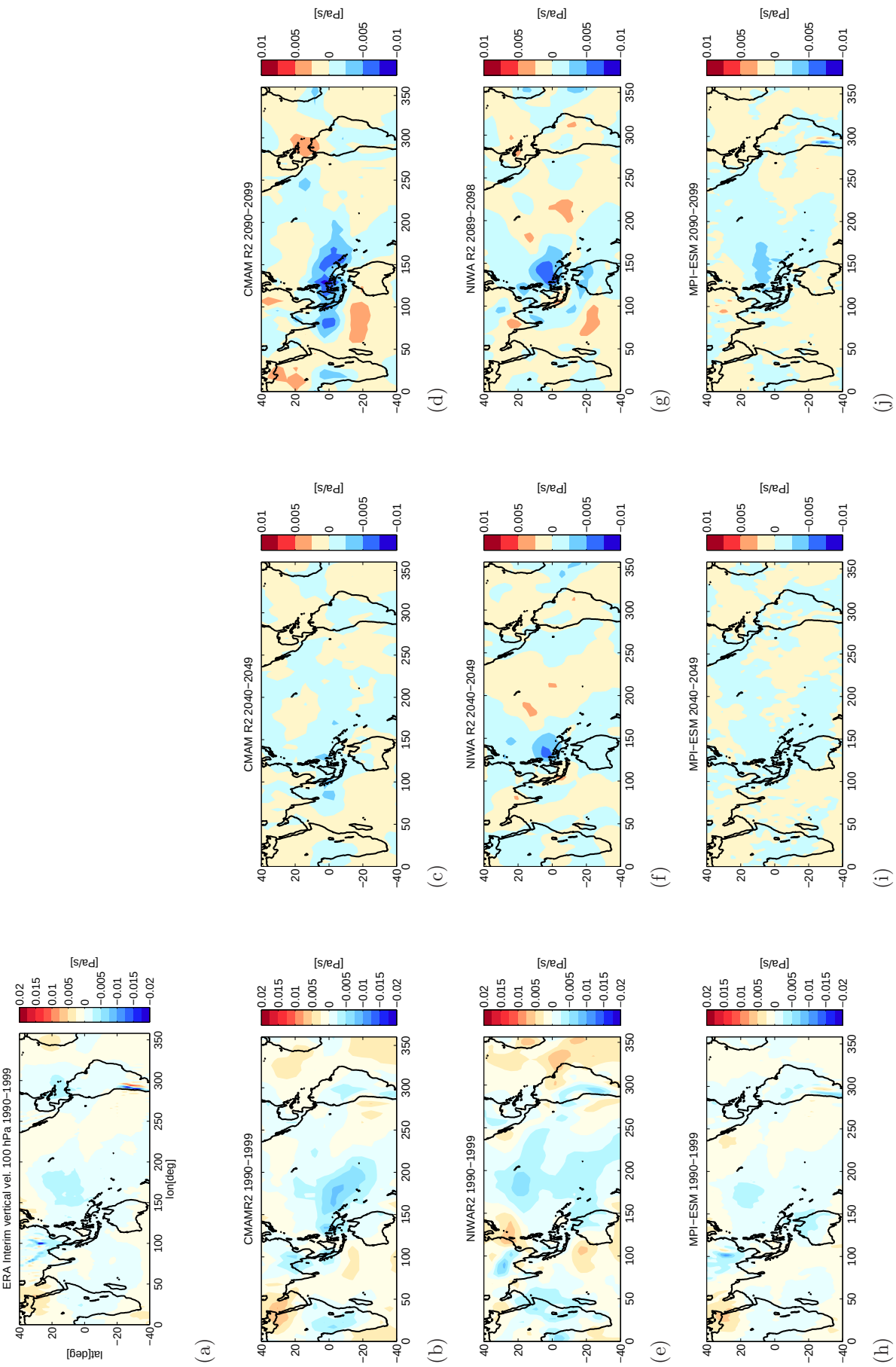

Fig. 6.2: Average vertical velocity at 100 hPa for ERA Interim, CMAM REF-B2, NIWA SOCOL REF-B2 and MPI-ESM, 1990-1999 Figure (a), (b), (e) and (h) and the differences to 1990-1999 for 2040-2049 and 2090-2099 for the particular model respectively is presented in Figure (c),(d); (f),(g) and (i),(j).

the 100 hPa pressure level this trend was indicated to be largest for CMAM (3%), but this trend decreases at the 70 hPa level to the half. The authors explained that the major part of this trend was forced by the parameterized orographic gravity wave drag of the models. The differences of the vertical velocity fields for the 2040s and 2090s compared to the 1990s period is shown in the middle and right panel from Figure 6.2. All models reveal an increase in the magnitude of the vertical velocity in the main ascent region, the West Pacific, towards the end of the 21th century. Strongest increase for the ascent region (up to -0.0075 Pa/s) but also for the subsidence regions (0.005 Pa/s) is projected for the two CCMs CMAM and NIWA-SOCOL.

The time series of the tropical averaged vertical velocity at 100 hPa for ERA Interim reanalysis (1979-2011) and all climate models (1990s, 2040s and 2090s) is presented in Figure 6.3(a). The magnitude of the average vertical velocity for ERA Interim varies around -0.0007 Pa/s. NIWA-SOCOL REF-B1 and REF-B2 and CMAM REF-B1 show similar strength of the vertical velocity. WACCM, MPI-ESM and E39CA reveal smaller vertical upward motions on average in the tropics. Strongest uplift is simulated by CMAM REF-B2. For all future model simulations the average tropical vertical velocity is strengthening at 100 hPa and 70 hPa pressure levels (Figure 6.3(b)). Strongest increase is visible for CMAM REF-B2, which might be due to the position of the strongest ascent area, which is located more equatorwards compared to the other two models (Figure 6.2). Hence, an increase of tropical deep convection in the future can probably be referred from that. A lifting of the tropopause under future climate conditions as analyzed by (Gettelman et al., 2010) using different CCMs, would cause an increase of the vertical velocity at the present tropopause height (around 100 hPa) due to an increase of tropospheric conditions.

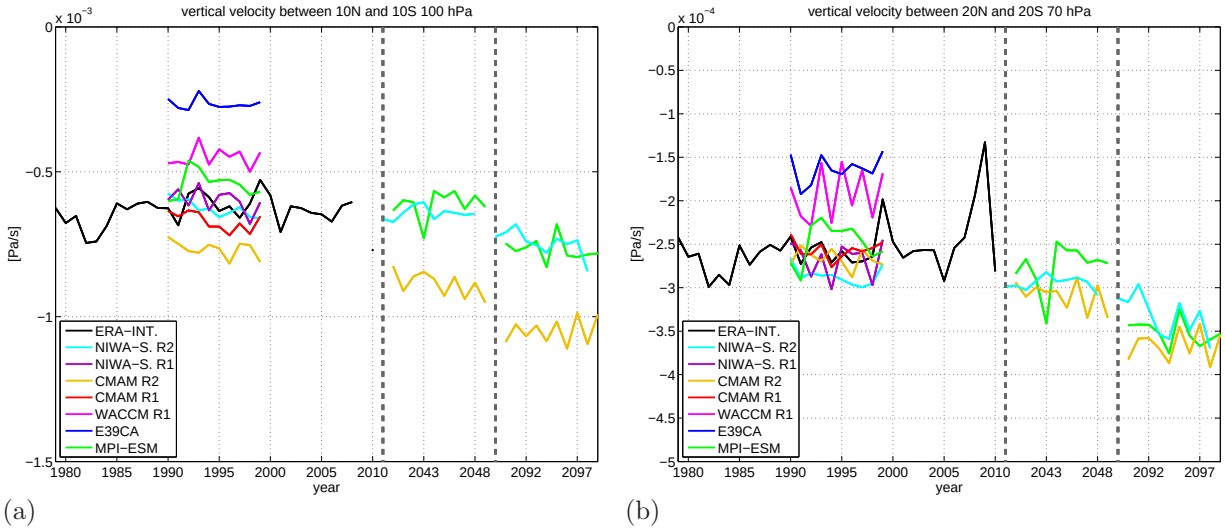

(a) (b)

Fig. 6.3: Time series of the annual average vertical velocity between 20°N - 20°S for ERA Interim (1979-2011) and for climate models 1990s, 2040s and 2090s at the 100 hPa (a) and 70 hPa (b) levels.

6.3 Sensitivity study

As already mentioned before, due to changing characteristics of the tropopause in the future, also the trajectory model setup needs to be adapted to the new atmospheric conditions. For the purpose of the present study, it needs to be ensured that trajectories cover the whole TTL region. As the tropopause height is projected to increase in the future (Gettelman et al., 2010; SPARC, 2010), the trajectories need to be setup at an higher altitude than the calculations carried out before (Chapters 4 and 5).
For the following Lagrangian calculations analyzing future model simulations, some sensitivity studies are presented that were carried out with model output from the CMAM REF-B2 simulations. This model was chosen representative as CMAM REF-B2 reveals the strongest increase in tropopause height compared to other CCMs (Gettelman et al., 2010; SPARC, 2010). Different trajectory model setups were applied for the different decades. The model setup and criteria were chosen to be the following:

1. Start at 400K θ level + fulfill 350 K criteria
2. Start at 420K θ level + fulfill 350 K criteria
3. Start at 420K θ level + fulfill 370 K criteria
4. Start at 450K θ level + fulfill 350 K criteria
5. Start at 450K θ level + fulfill 390 K criteria

For the first decade 1990-1999, criteria 1) to 3) are applied, but for the two following decades in the future, the 2040s and 2090s, where the tropopause is lifted to higher levels, criteria 1) to 5) are taken into account to analyze the differences between the model setup at 420 K compared to 450 K. Similar sensitivity studies were also tested for the two future simulations NIWA-SOCOL REF-B2 and MPI-ESM, which basically revealed the same results as for CMAM (not shown here).
The average trajectory sum[2] for CMAM REF-B2 fulfilling the criteria 1) to 5) for the annual average is presented in Figure 6.4. The average number for trajectories of one model start, fulfilling different criteria for ERA-Interim and all climate models, is illustrated in Figure A.11.

Applying the 1) model setup 400 K - 350 K (yellow), around 13,500 trajectories fulfill the criteria on average between 1990-1999. The number of trajectories is increasing strongly for the 2040s and the 2090s, where 19,000 are considered for the final analysis. Model setup 2) (dark blue) reveals 9,000 trajectories fulfilling the criteria during the 1990s, showing an increase up to 11,000 trajectories until the 2090s. Model setup 3) (purple) has similar values for the 1990s like criteria 1), but in contrast the number of trajectories increase in the future

[2]The sum refers to the number of trajectories, which were initialized originally to obtain one composite map of a season. 5580 trajectories are started for one model setup. For a season composite 3 (one per month) * 4 (different UTC times) = 12 model starts are carried out, resulting in 66960 trajectories.

slightly. Model setup 4) and 5) were only calculated for the 2040s and 2090s. Apparently, fewest trajectories fulfilling the condition are found for the criteria 4) (pink). Only 6,500 of the originally 66,960 trajectories on the average are able to travel through the 100 K thick layer of potential temperature θ in contrast to the 50 K θ and 70 K θ thick layers of criteria

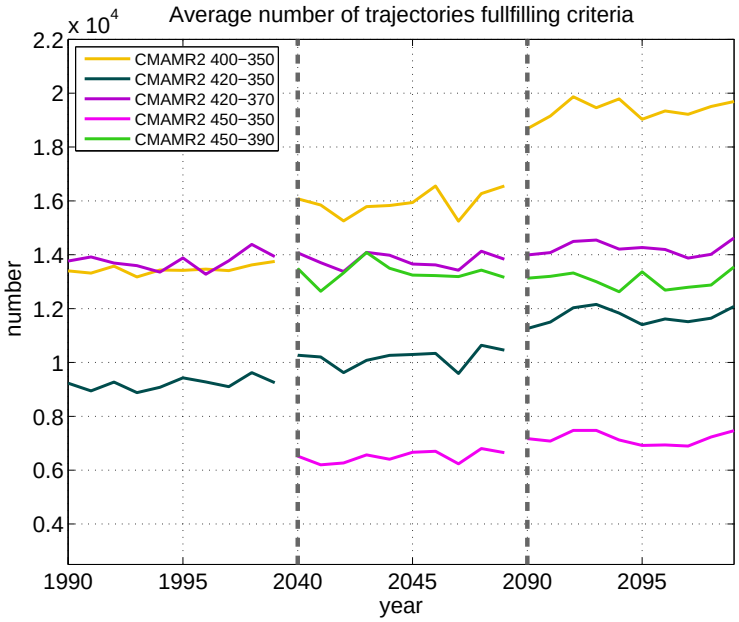

Fig. 6.4: Annual average number of trajectories fulfilling different criteria tested for CMAM REF-B2 composite analyses.

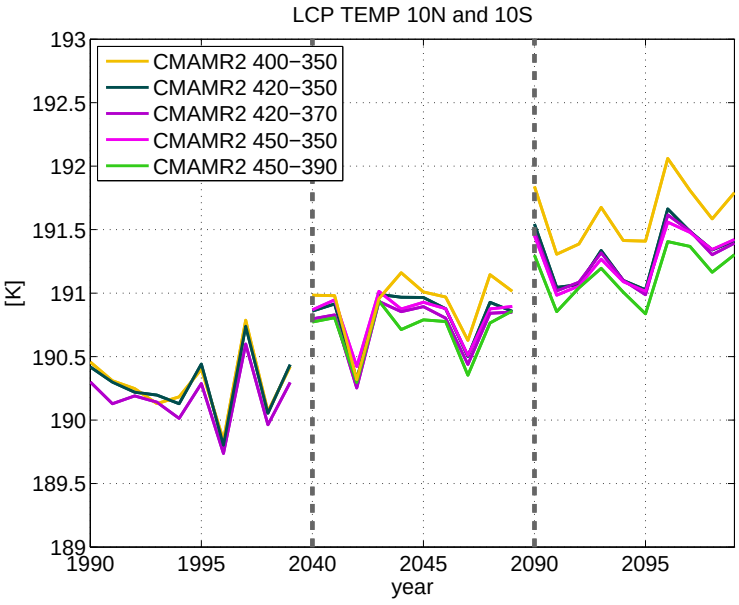

Fig. 6.5: Annual average LCP temperature for CMAM REF-B2 tested for different criteria represented by different colors.

1) and 3). Criteria 5) indicates similar numbers like criteria 3) during the 2040s but in contrast shows no increase in the number of trajectories in the 2090s, probably due to the lower criteria located at 390 K θ, which might be too high.
The average LCP temperature between 10°N to 10°S for CMAM REF-B2, where different model criteria are applied is displayed in Figure 6.5. The average LCP temperature between 1990-1999, is almost indistinguishable for the trajectories from criteria 1) to 3), which leads to the assumption of a robust model setup during that decade. However, for the 2040s and 2090s the differences of the LCP temperature between criteria 1) and 2) to 5) is increasing. A possible explanation of this result might be that starting at 400 K is already below the cold point tropopause, at least for the majority of the trajectories. Indeed, this assumption is supported by the global maps showing the potential temperature θ at the location of the LCP for the different climate models (Appendix Figure A.12 to A.14). It becomes clear that especially for the years 2090-2099, the LCP is located almost at the original initialization point at 400 K in some regions (e.g. North Atlantic). For criteria 2) 420 to 350 K most of the LCPs are located even above the 400 K level. Thus criteria 1) implies a too low trajectory start, to capture the right locations of the LCPs at least for the 2090s. Basically no striking difference can be derived for the LCP potential temperature maps for the future using criteria 2) and 3). Thus, the criteria 1) (yellow) doesn't "hit" the right cold point any more. The LCP temperature for criteria 1) is ∼0.3 K higher compared to criteria 2) to 5), which are within the same temperature range.
The result of this sensitivity study leads to the conclusion that the TTL is not captured well for the available future model simulations, when trajectories are started at the 400 K θ layer. Whereas, the 420 K θ layer as starting level is placed high enough to cross the LCP, hence the upper part of the TTL. During the 1990s a major part of the trajectories reach their LCP around the 360 K θ level, whereas during the 2040s and 2090s the LCP is located at higher levels (Figures A.12 to A.14). Hence, to compare the results of the different decades with each other using the most robust and similar criteria for all, the lower criteria of 350K is chosen. Using criteria 2) (420 K to 350 K) it is ensured to cover the lower part of the TTL, hence the whole vertical domain of the TTL during all decades. The increase of the tropical tropopause height is also reflected by an increase of the potential temperature of the LCP location in the inner tropics of 10-15 K θ, which can be equated to a decrease in the tropopause pressure of approximately 10 hPa from the 1990s to the 2090s (see Figures A.12, A.13 and A.14). CCMVal-2 models simulated a decrease of around 10 hPa between 1960-2100 from 105 hPa to 95 hPa (Gettelman et al., 2010). A striking strong gradient in the decrease of lapse rate tropopause pressure was especially simulated by CMAM REF-B2. Thus, with a trajectory start at 420 K θ, which lies at ∼18 km or ∼85 hPa, a good coverage of the TTL can be assumed.
Similar results as for CMAM REF-B2 sensitivity study exist also for NIWA-SOCOL REF-B2 and MPI-ESM (not shown here), leading to the conclusion that a model start at 420 K and the lower criteria of 350 K is feasible for the future model projections. Hence, for the following calculations, criteria 2) is applied for all future simulations:

- Start at 420K θ level + fulfill 350 K criteria

6.4 Lagrangian cold point

The LCP temperature as well indicates an increase in the inner tropical region (dashed lines in Figure 6.1). For CMAM REF-B2 (yellow) and MPI-ESM (green) a slight increase of approximately 1 K of the average LCP temperature is simulated from the decade 1990-1999 up to the decade 2090-2099. For NIWA SOCOL REF-B1 (light blue) also an increase of the temperature of approximately 0.5 K from the present to the future can be noted. Hence, the increase in Eulerian and Lagrangian cold point temperatures for the time period 1990-2100 is similar ranging between 0.5 to 1 K.
Results from the tropical average cold point temperature for several CCMVal-2 models are shown by Gettelman et al. (2010). The climate models generally project a slight increase of the cold point from 1960-2100 with 0.09 K/decade in the multi model mean. This number would lead to an increase of 0.99 K between 1990 and 2099, which is comparable to the increase of $\sim$1 K for the same period, calculated for the ECP and LCP in the present study.
Global anomaly maps of the average LCP temperature are presented for the different climate models simulating the future (Figure 6.6). The average LCP temperature overlied by density contour lines for the decade 1990-1999 (left row) and the differences to the 2040s and 2090s (middle and right rows) are presented for each model respectively (Figure 6.6). The overall pattern for all three climate models indicates an increasing LCP temperature in the future. CMAM REF-B2 (first row) reveals a temperature increase of 0.5 to 1 K for the 2040s, with a further increase of the LCP temperature of 1 to 1.5 K in the 2090s compared to the 1990s. The relative LCP density illustrates a slight decrease over the maritime continent (red lines), accompanied by an increase of the LCP density over the eastern Indian Ocean in the 2040s (Figure 6.6(b)). However, an increase of the LCP occurrence over the West Pacific and a decrease over West Africa and South America is projected for the 2090s (Figure 6.6(c)).

As already mentioned before (Chapter 4) an El-Niño like pattern of the LCP density distribution by NIWA-SOCOL REF-B2 is displayed during the first decade 1990-1999 (Figure 6.6(d)). During the 2040s and the 2090s the LCP temperature and occurrence illustrates more an ENSO neutral state again (see also Figure A.16(e) and (f)). Consequently, the differences between the first and the two following analyzed decades are largest in the western and eastern Pacific region. The LCP temperature reveals a decrease of 0.5 K over the West Pacific accompanied with an increase above the East Pacific of up to 2 K for the 2040s (Figure 6.6(e)). However, for the 2090s the LCP temperature displays an increase of almost the whole tropical area by 0.5 to 2.5 K compared to the 1990s (Figure 6.6(f)). The LCP density shows an ongoing increase for the 2040s and 2090s period over the West Pacific and a decrease above the East Pacific, caused by a shift of the main entrance region of air masses from the East to the West due to a more ENSO neutral or La Niña state compared to the 1990s again (Figure 6.6(e) and (f)). Another decrease of the LCP occurrence is projected over Africa and the western Indian Ocean in the 2090s.
Least changes for the future are projected by the CMIP5 MPI-ESM RCP8.5 simulation, although it includes the strongest GHG forcing. Between the 1990s and the 2040s the

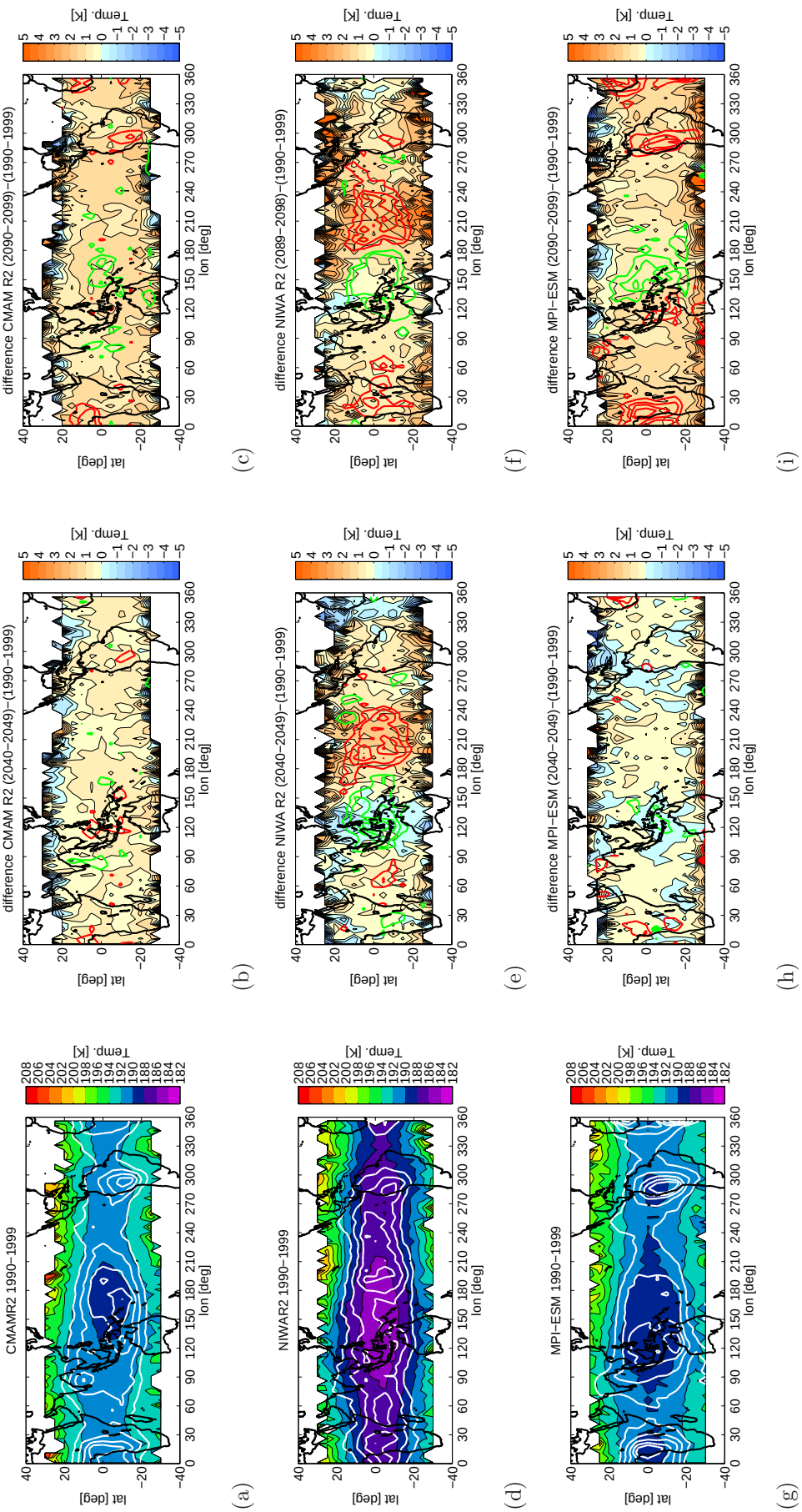

Fig. 6.6: Differences in the climatology of LCP temperature and occurrence for climate models from the past (1990s) to future (2040s and 2090s) for the annual average per 5° x 5°. Overlied with contour lines for the density of LCP occurrence in % red: less than in 1990s, green: more than in 1990s. CMAM REF-B2: (a) 1990s, (b) 2040s and (c) 2090s; NIWA-SOCOL REF-B2: (d) 1990s, (e) 2040s and (f) 2090s; MPI-ESM historical: (g) 1990s, RCP8.5: (h) 2040s and (i) 2090s. For 1990-1999 the color interval is 2 K; for LCP occurrence it is 0.1% (white contour lines) ranging from 0.1% up to 0.5% for (a), (d) and (g). Color interval for LCP temperature differences (2040s and 2090s) is 0.5 K; for LCP occurrence it is 0.05% red: from -0.05% and green: from +0.05%.

LCP temperature and density shows very small variations within the tropical region (Figure 6.6(h)). However, compared to the 1990s for the 2090s a distinct tropical warming of 1 to 1.5 K of the LCPs is striking, which is accompanied by (Figure 6.6(i)) an increase of the LCPs above the West Pacific and a decrease over West Africa and South America.
Overall, the climate models project a consistent evolution of the TTL for the 2090s period. Global maps of annual average LCP temperature and density for the future simulations during all decades are shown in the Appendix (Figure A.16). NH winter and summer seasons for the different future simulations are presented as well in comparison to the 1990s (Figure A.17 and A.18).

6.4.1 Spatial pattern

The relative number of the tropical averaged LCPs within 5° longitude bins for the three future model simulations is presented in Figure 6.7. The changes for the longitudinal LCP distribution from the 1990s to the 2090s is different between the climate models.
Three main LCP accumulation regions (West Pacific, West Africa and South America) persist throughout all three decades for CMAM REF-B2 and MPI-ESM. However, NIWA-SOCOL REF-B2 displays a more flat LCP occurrence over the whole tropical region during all decades on the annual average, except the maximum over the East Pacific during the 2040s (Figure 6.7(a)). Largest changes of the LCP distribution are illustrated by NIWA-SOCOL REF-B2 (light blue) due to the El-Niño like pattern during the 1990s, which is not present any more in the other two selected decades.
On the annual average, NIWA-SOCOL REF-B2 (light blue) and MPI-ESM (green) simulate the largest increase of the LCP occurrence over the West Pacific from 38.38% to 43.27% and from 41.44% to 48.07% (Figure 6.7(a)). In contrast CMAM REF-B2 (yellow) simulates a slight decrease of the LCPs in the 2040s from 44.7% to 44.38% followed by a increase in the 2090s to 46.04% compared to the 1990s. The same behavior of a decreasing occurrence of LCPs over the West Pacific in the 2040s followed by an increase in the 2090s again is visible during NH summer and fall for CMAM REF-B2 (Figure 6.7(c) and (d)) and for MPI-ESM during NH spring (Figure 6.7(b). NIWA SOCOL REF-B2 simulates a decrease of the LCP occurrence in the West Pacific during NH fall (Figure 6.7(d)). All climate models agree that the amount of LCPs is largest over the tropical West Pacific during NH winter throughout all decades except for NIWA-SOCOL REF-B2 during the 1990s period, which is due to the too strong model response on volcano and ENSO forcing (Dan Smale, pers. communication).

The future changes of the five main entrainment regions of air masses traveling from the troposphere to the stratosphere are highlighted in Figure 6.8. In the present section, Figure 6.8 extends Figure 4.17 by the future climate scenarios of the TTL based now on the model setup at 420 K, where the trajectories have to origin from 350 K θ (criteria 2).

Over the West Pacific (upper panel) the occurrence of LCPs for CMAM REF-B2 and MPI-ESM amounts to 39% to 45% during the 1990s and the 2040s. During the 2090s an increase is projected reaching an amount of 41% to 50% respectively of LCPs over the West

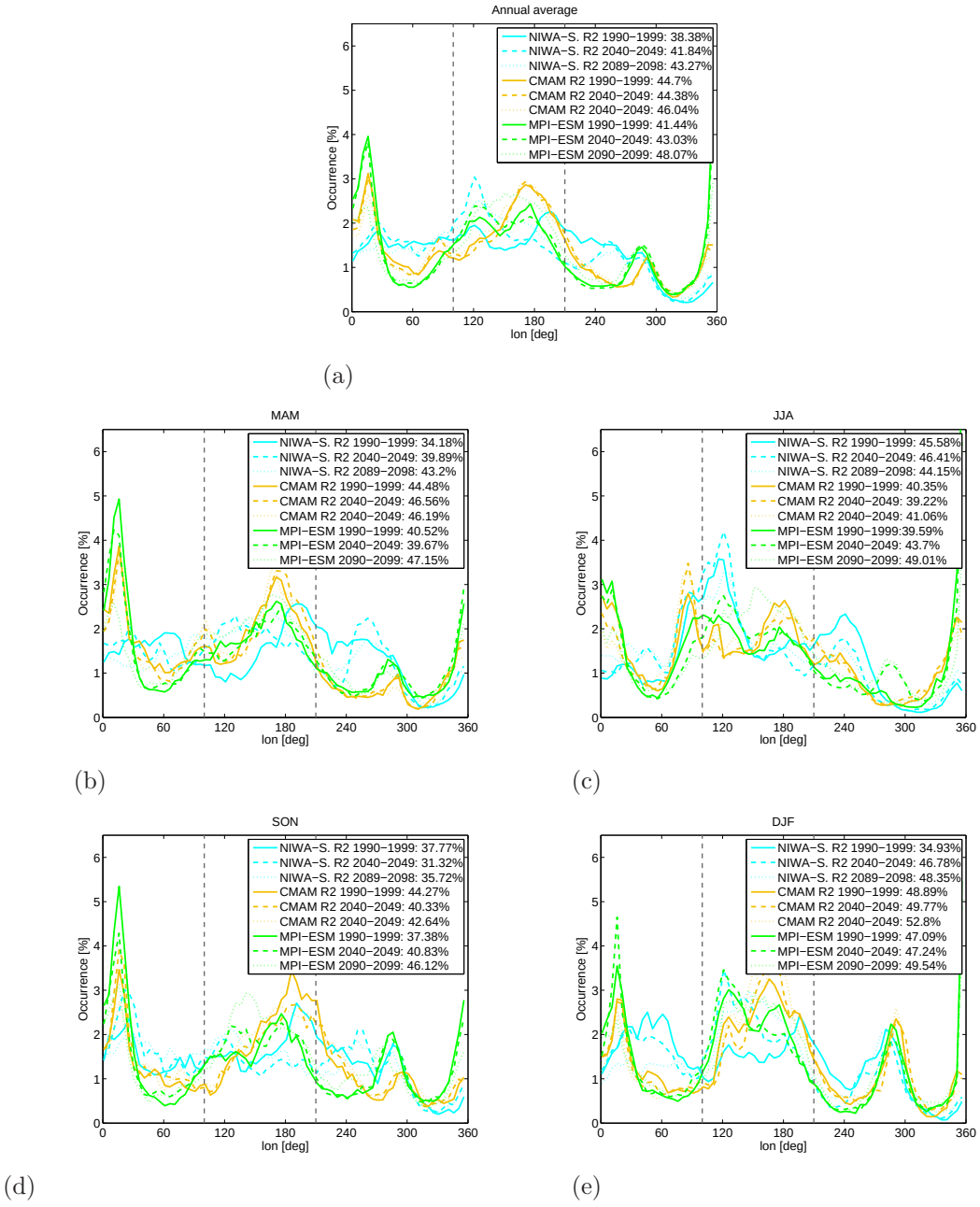

Fig. 6.7: Occurrence of LCP tropical averaged inside 5° longitude bins for ERA Interim and climate models (1990-1999, 2040-2049 and 2090-2099). The number in [%] indicates the percentage of Trajectories reaching the stratosphere from below in the marked area between 100° and 210° E. Different linestyles present the selected decades (see inset for color coding). (a) Annual average, (b) MAM, (c) JJA, (d) SON, (e) DJF.

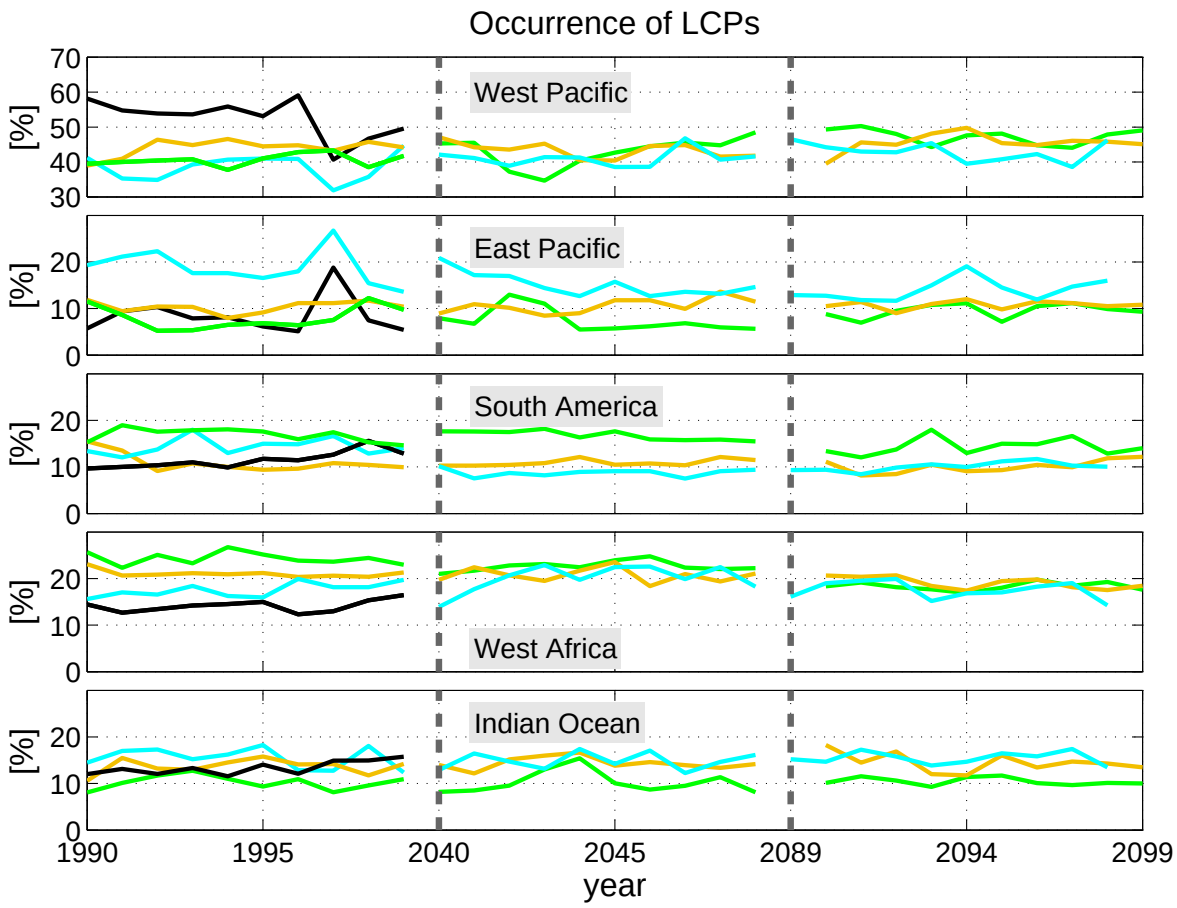

Fig. 6.8: Time series of annual average occurrence of LCPs inside 5 ° longitude bins for different regions for future simulations. Number in [%] indicates the percentage of trajectories reaching the stratosphere from below for ERA-Interim (black), NIWA-SOCOL REF-B2 (light blue), CMAM REF-B2 (yellow) and MPI-ESM (green). West Pacific 100° - 210°, East Pacific 210°-270°, South America 270° - 330° E, West Africa 330° - 40° E, Indian Ocean 50° - 100°E.

Pacific. For NIWA-SOCOL REF-B2 a slight increase of the LCP occurrence above the West Pacific is analyzed from 2040 onward. In the East Pacific region (second panel) a decrease of LCPs after 1999 is shown from NIWA-SOCOL REF-B2, whereas MPI-ESM indicates a slight increase in the amount of LCPs after 2040s. However, CMAM REF-B2 shows a roughly constant amount of LCPs within that region. The LCP accumulations over South America reveals a slight decrease of LCPs for MPI-ESM from the 1990s to 2090s and for NIWA SOCOL from the 1990s to the 2040s. CMAM REF-B2 indicates a more constant amount of LCPs of ∼9% to 11% over South America. In the geographical region over West Africa (fourth panel), NIWA-SOCOL indicates an increase of LCPs after 1999 followed by a decrease again after 2049. In contrast, the two other climate models MPI-ESM and CMAM REF-B2 reveal a slight decrease of LCP occurrence from 1990 onward until 2099, which is more pronounced for MPI-ESM (from ∼24% to 18%). Within the Indian Ocean region the

occurrence of LCPs varies among the models between 10% and 20%, but no distinct change in the amount of LCPs is obvious.

6.5 TTL widening

Here, a possible change in the expansion of the upper TTL -the cold point layer- is analyzed based on future simulations of different climate models (CMAM REF-B2, NIWA-SOCOL REF-B2 and MPI-ESM). The focus lies on the change of the meridional LCP distribution within three decades, one for the past in the 1990s and two decades in the future 2040s and 2090s.
The annual average width of the upper TTL for the climate models and ERA Interim is presented for the different decades in Figure 6.9(a). The borders of the upper TTL of the two hemispheres are determined using the 88th percentile of the LCP distribution as threshold (section 3.3.2). During the first decade, the northern edge is located between 13° to 16° N and the southern edge between 11° to 14° S. The median is clearly located on the NH around 2° N for ERA Interim, whereas for the climate models it is displaced towards the equator. This bias, which is simulated by all analyzed climate models within this study is also shown in Figure 5.8(a). For the future decades (2040s and 2090s) no distinct change is visible concerning the edges and the median of the LCP distribution.
The total width of the region in the upper TTL is illustrated in Figure 6.9(b). Between 1990-1999 the absolute width varies between 26 and 31° for ERA Interim and reveals a positive change. The variation of the total width for the climate models is smaller compared to ERA Interim during the first decade. The broadest TTL-width is simulated by MPI-ESM with 29° or 30° latitude. The most narrow upper TTL width is indicated by CMAM REF-B2 with 27° latitude, NIWA-SOCOL REF-B2 lies in between with 27.5° latitude. All climate models reveal an increase of the total width of the upper TTL from the 1990s to the 2090s of 1° to 2° latitude.

The seasonal cycle of the border and the width of the upper TTL for the future simulations, are presented in Figure 6.10. During the 1990s, the borders of the upper TTL in the two hemispheres and the median of the LCP distribution show only little deviations between reanalysis and models during boreal spring (Figure 6.10(a)). The borders of the upper TTL are located at around 13° for both hemispheres. The median is located at the equator, thus the LCPs are equally distributed in both hemispheres. The total width of the upper TTL is most narrow for reanalysis and NIWA-SOCOl REF-B2 (1990s), whereas MPI-ESM simulates an upper TTL, which is 3.5° broader (Figure 6.10(c)). During the 2040s CMAM REF-B2 reveals a slight displacement of the median towards the south, whereas no change is indicated from the other climate models. Towards the future (2090s) a clear displacement of the upper TTL border in the NH towards the pole is projected for all climate models, leading to an increase of the total width of around 2° latitude between the 1990s ans 2090s. During boreal summer the location of the upper TTL borders from MPI-ESM agree best with ERA Interim during the 1990s (Figure 6.10(b)). The median of the LCP distribution of

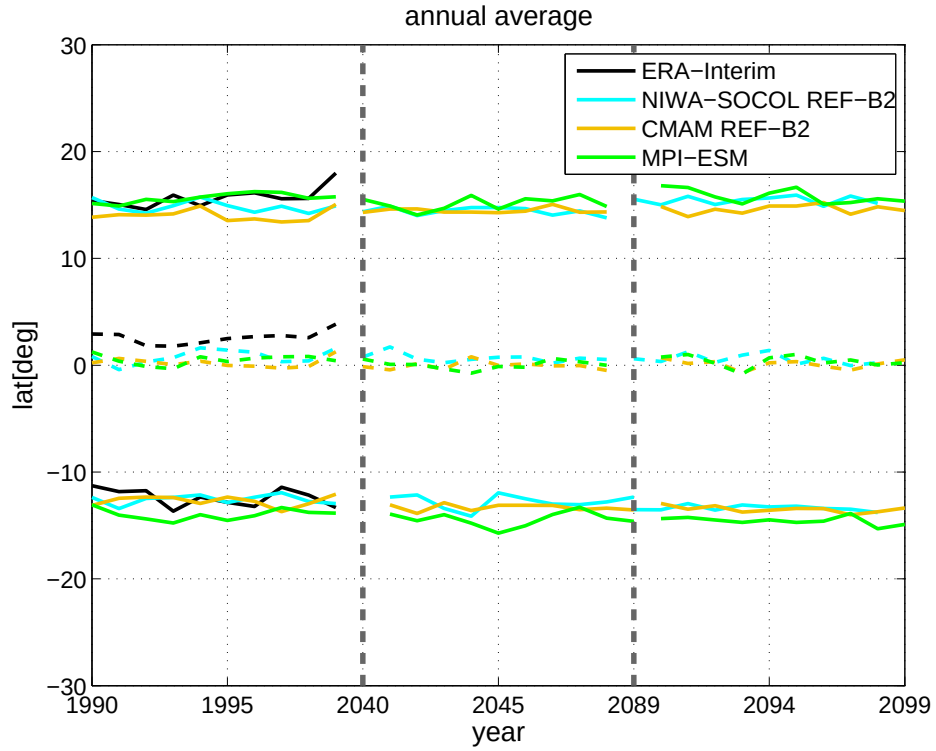

(a)

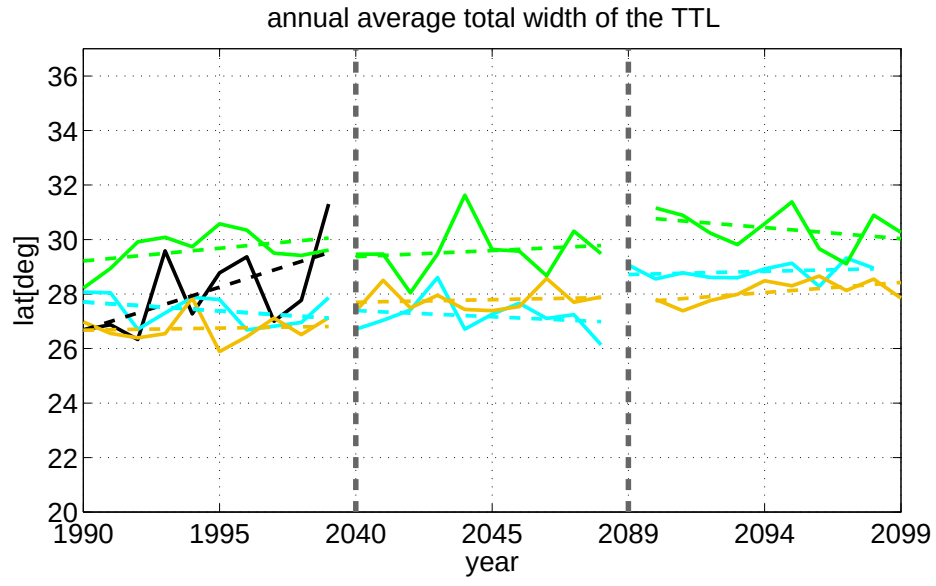

(b)

Fig. 6.9: Width of the upper TTL represented by the 88 th percentile of the distribution of LCPs for ERA Interim and climate models (past and future). In (a), the TTL region with defined borders on the NH and SH (solid lines) and the median (dashed) is shown. In (b) the total width of the TTL from the different models is shown (solid) with linear regression (dashed).

ERA Interim is located around 6° N during the first decade, whereas the median simulated from the climate models is located more equatorwards at 4° to 5° N. The location of the median during the 2040s and 2090s changes its position by moving towards the equator, which is consistent for all three climate models. During the 2090s period, the median is located around 2° to 3° N, which indicates a decrease of the LCP occurrences on the NH. Accordingly, an increase of LCPs in the SH occurs, which is accompanied by a displacement of the southern border towards the South Pole. For the total width of the upper TTL no distinct changes are projected until the 2040s. However, positive changes of 1° to 2° are projected for the 2090s period (Figure 6.10(d)). The most narrow upper TTL-width is simulated by CMAM REF-B2, whereas the broadest is simulated by MPI-ESM. Also for the future simulations, boreal summer reveals the broadest upper TTL width among all other seasons.
Largest discrepancies between ERA Interim and climate models is reflected by the median of the LCP distribution during NH fall (Figure 6.10(e) see section 5.2.3). The median from ERA Interim is clearly located on the NH around 5° N, whereas the median of the LCP distribution from the climate models is further South around the equator. Until the 2040s and the 2090s there is no distinct change visible concerning the border of the upper TTL. Corresponding to this, the total width reflects no consistent development towards a broadening or narrowing in a future climate. The width of the upper TTL varies between 24° to 33° latitude during all decades (Figure 6.10(g)).
During NH winter reanalysis and climate models project the location of the median on the SH between 2° to 5° S (Figure 6.10(f)). They agree well with the location of the NH border at ∼10°N. However, the most poleward position of the SH is illustrated by MPI-ESM around 18° S. For the 2040s no striking change is indicated neither in the position of the borders nor in the total width of the upper TTL compared to the 1990s. A shift of the median and the NH border towards the North by 0.5° to 3° latitude is obvious until the 2090s. The total width of the upper TTL region reveals a broadening for NIWA-SOCOL REF-B2 and CMAM REF-B2 until the 2090s, which in contrast is not projected in the MPI-ESM (Figure 6.10(h)).

6.5.1 West Pacific

As the West Pacific is the main entrance region for air masses reaching the stratosphere from below (40%-60%, see section 4.3), the area over the West Pacific is analyzed in more detail in this section. For the analysis the 70th percentile of the LCP distribution is chosen due to a smaller amount of LCPs in one single region, where the 88th percentile could not be applied any more (see also Section 5.1.2).
The annual average width of the upper TTL for the West Pacific, projected from the different climate models, is presented in figure 6.11. During the 1990s, the broadest upper TTL-width above the West Pacific is simulated by MPI-ESM with 23.2° latitude. The two REF-B2 simulations from NIWA-SOCOL and CMAM REF-B2 simulate a width of ∼22° latitude. During the 2040s the total width of the upper TTL within the West Pacific reveals an increase for CMAM with 0.7° latitude. However, NIWA-SOCOL REF-B2 indicates a

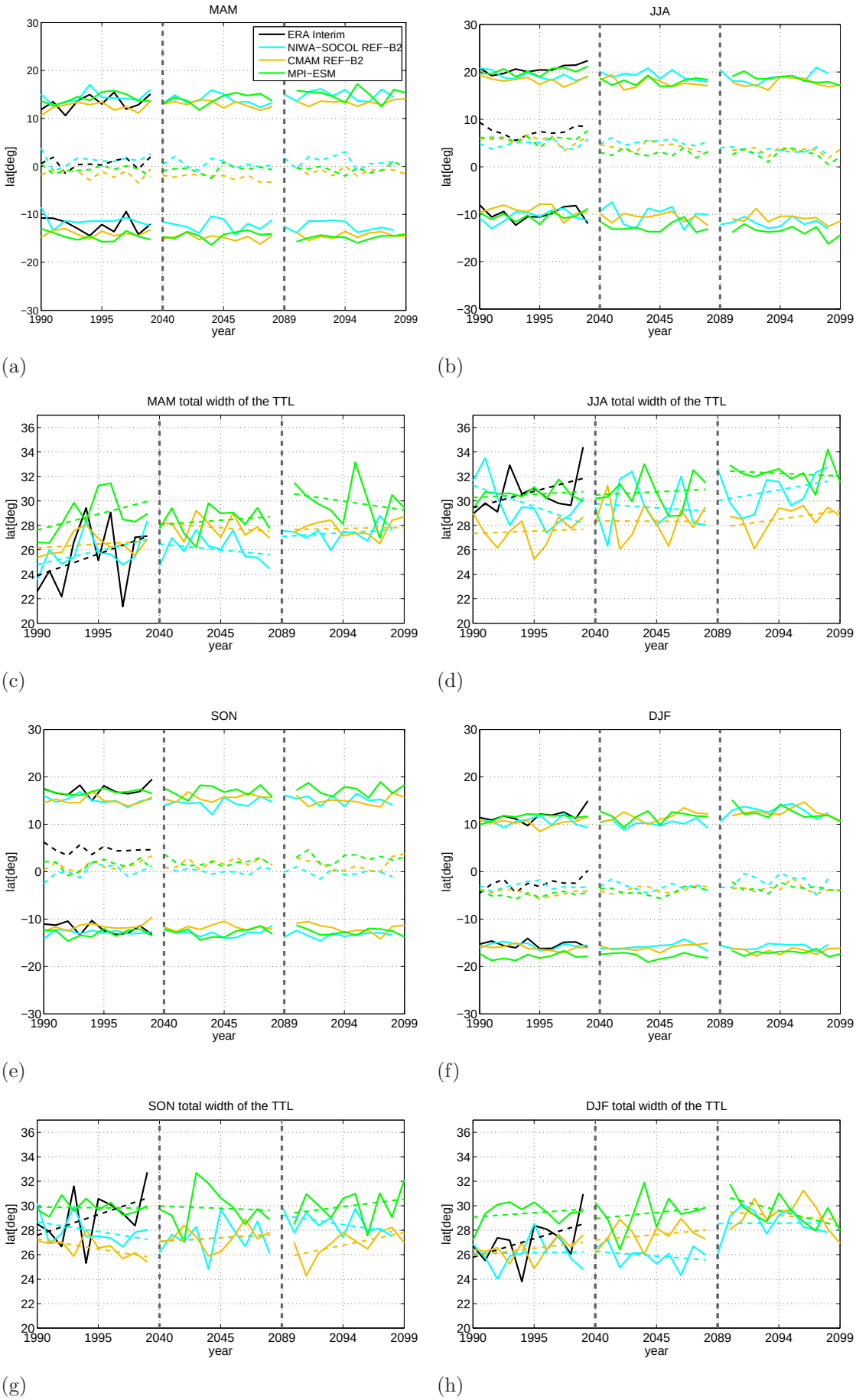

Fig. 6.10: Width of the upper TTL represented by the 88 th percentile of the LCP distribution for seasonal average of future simulations. For NH spring: (a) and (c), summer (b) and (d), fall (e) and (g) and winter (f) and (h).

decrease of 1.3° latitude and MPI-ESM shows only a change in the variability of the upper TTL width. From the 2040s until the 2090s all climate models reveal an increase in the width of the upper TTL of 0.7° latitude from MPI-ESM, 1.2° latitude from NIWA-SOCOL REF-B2 and 0.2° latitude from CMAM REF-B2.
Figure 6.12(a) shows the change of the average width of the upper TTL in the future simulations during NH winter. From the 1990s to the 2040s the average width reveals a narrowing of the upper TTL of 1.5° latitude for NIWA-SOCOL, whereas MPI-ESM of 0.1° latitude. In contrast CMAM REF-B2 shows a positive change of the upper TTL width of 0.9° latitude. From the 2040s towards the 2090s all climate models indicate an increase of the average width of further 0.7° latitude by MPI-ESM, 2.5° latitude by NIWA-SOCOL REF-B2 and 1.8° latitude for CMAM REF-B2.
During NH summer (Figure 6.12(b)) the simulations of MPI-ESM reveal larger changes compared to the winter season. From the 1990s to the 2040s MPI-ESM and CMAM REF-B2 simulate a positive change of the upper TTL by 1.2° and 0.9° latitude. NIWA-SOCOL REF-B2 indicates a decrease of the upper TTL width by 0.1° latitude. From the 2040s until the 2090s MPI-ESM and NIWA-SOCOL REF-B2 project an increase of the upper TTL width of 1.5° and 0.5° latitude, whereas CMAM REF-B2 indicates no change.
The changes of the width of the upper TTL over the West Pacific for NH fall and spring is shown in Figure A.20.

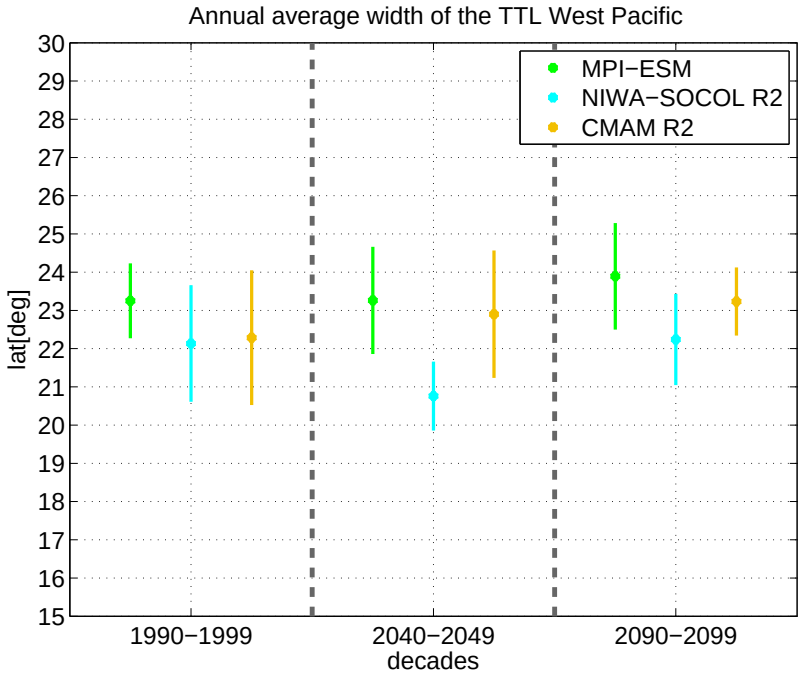

Fig. 6.11: Average annual width of the upper TTL above the West Pacific for climate models represented by the 70th percentile. Vertical lines indicate the variance (95 %) of the TTL-width.

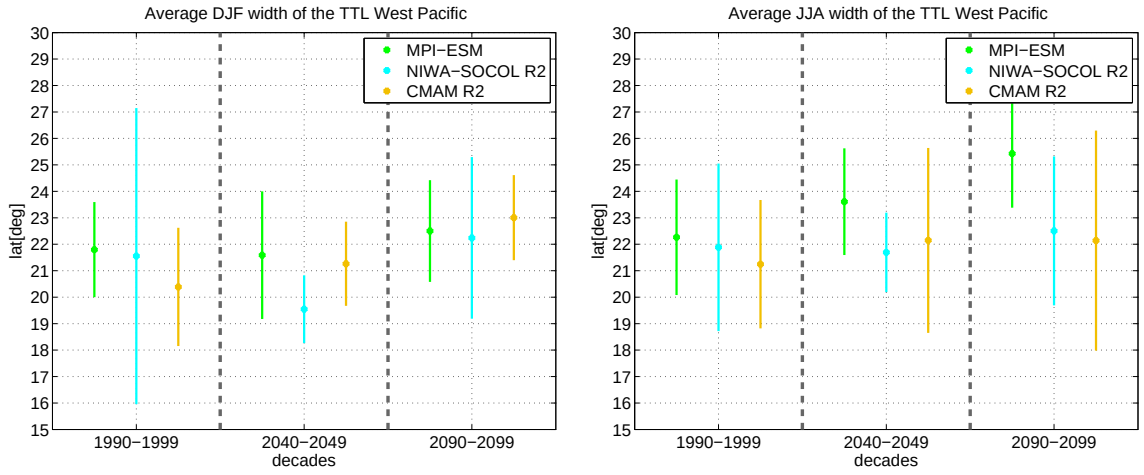

(a) (b)

Fig. 6.12: Average width of the upper TTL above the West Pacific during NH winter and summer for climate models represented by the 70th percentile. Vertical lines indicate the variance (95 %) of the TTL-width during NH winter (a) and summer (b).

6.6 Summary

In this chapter the future change of the upper TTL is analyzed with the help of different climate models. Changes between three decades are investigated in more detail. The 1990s, 2040s and 2090s are analyzed with data from the different models CMAM REF-B2, NIWA-SOCOL REF-B2 and MPI-ESM (historical and RCP8.5 scenarios). It is shown that the tropical CP temperature and LCP temperatures are projected to increase on the annual average of 0.5 K to 1 K between the 1990s and the 2090s, which is consistent among all three models. The Lagrangian results shown here are comparable to the future TTL analysis by Gettelman et al. (2010), who illustrated an increasing cold point temperature of 13 CCM REF-B2 simulations in climate models of $\sim$ 1 K between 2000 and 2099. The vertical velocity in the tropics at the 70 hPa and 100 hPa level from the climate models shows an increase towards the end of the 21th century, which is strongest for CMAM REF-B2 in the 100 hPa level revealing a doubling in the strength from 1990 to 2099.
Due to a projected higher tropical tropopause in the future (Gettelman et al., 2009, 2010), the trajectory model setup was adapted to the future tropopause properties. Strongest decrease of the tropical tropopause pressure is simulated by CMAM REF-B2 from around 100 hPa in the 1990s to less than 88 hPa by the end of the 21th century (Gettelman et al., 2010). Thus, carrying out a sensitivity study with CMAM REF-B2, the former trajectory start at 400 K θ, which is applied in chapters 4 and 5, is changed for all three climate models to a higher start level at 420 K θ for the future simulation data. The lower boundary criteria is kept at 350 K θ.
The LCP temperature and distribution is analyzed for the future simulations, resulting in an increase of LCP temperature, which is highest for NIWA-SOCOL in the East Pacific (1.5 K

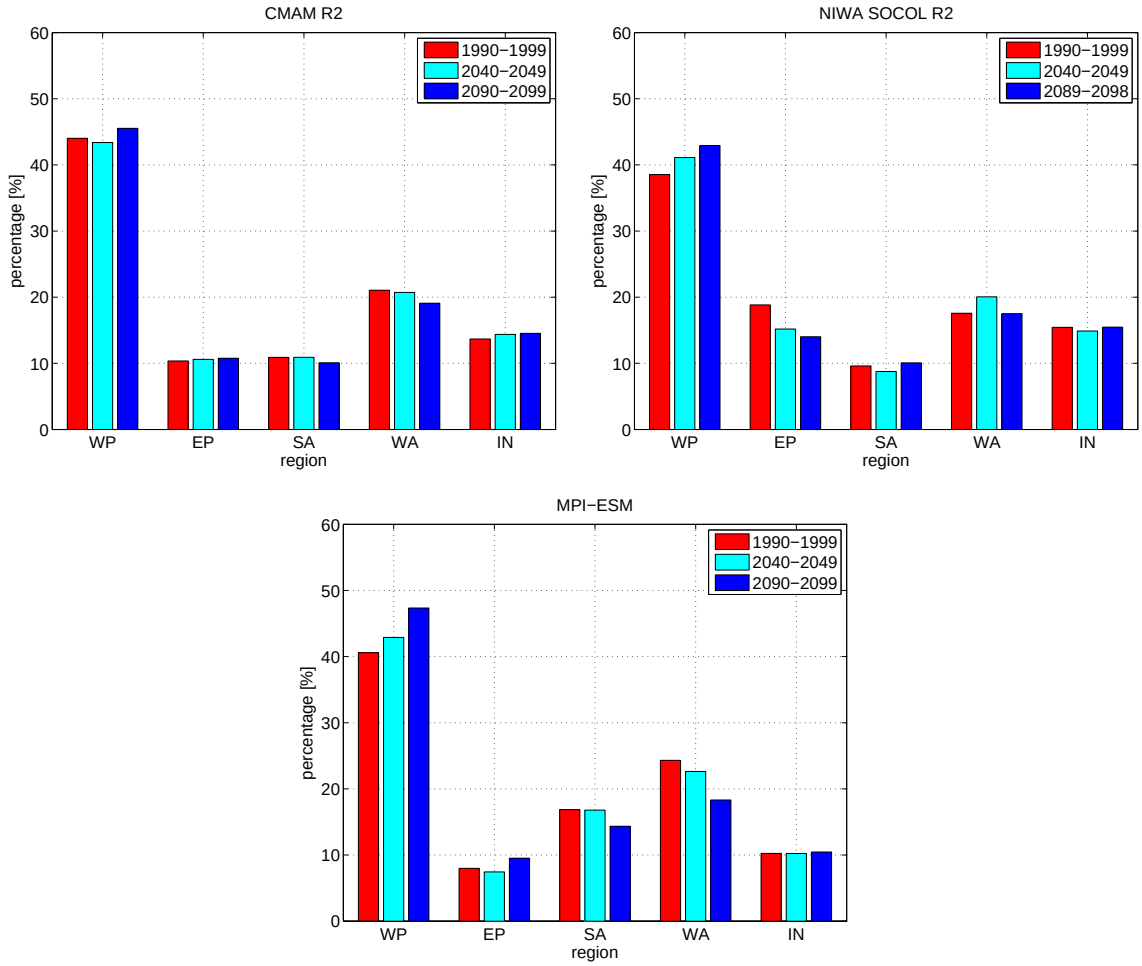

Fig. 6.13: Annual average occurrence of LCPs within different geographic regions for (a) CMAM REF-B2, (b) NIWA-SOCOL REF-B2 and (c) MPI-ESM for three decades 1990s, 2040s and 2090s.

to 2 K) and lowest for MPI-ESM in the West Pacific (1 K). All models simulate an increasing occurrence of LCPs over the West Pacific, where MPI-ESM projects the strongest increase until the 2090s. The strongest decrease of LCP occurrence overall is simulated by MPI-ESM over West Africa until the 2090s.

Figure 6.13 summarizes the relative number of annual average occurrences of LCPs in different geographical regions for the three decades and the three climate models separately. Overall, all climate models reveal the dominance of troposphere to stratosphere transport for the tropical West Pacific. All climate models project an increase of the LCP occurrence above the West Pacific by 2% to 8% until the 2090s, accordingly over other geographic regions especially over West Africa the occurrence of LCPs is decreasing. Above the East Pacific and Indian Ocean no distinct changes are visible, except for NIWA-SOCOL for the East Pacific (see Section 4.2.3.1 for details). The seasonal changes are shown in the Appendix (Figure A.19).

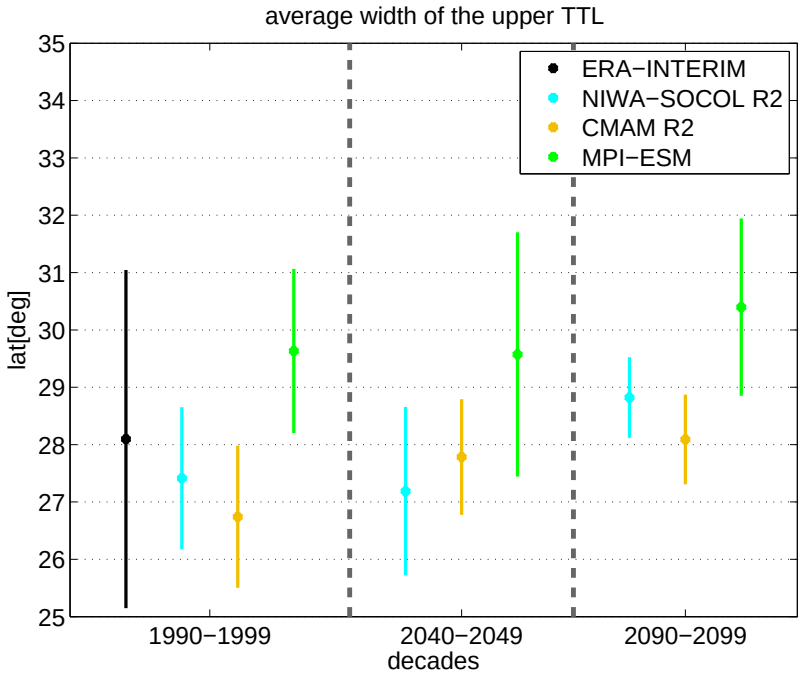

Fig. 6.14: Annual average width of the upper TTL for ERA Interim and climate models for the past and future represented by the 88th percentile. Vertical lines indicate the variance (95 %) of the TTL-width.

The upper TTL is analyzed also in matters of its poleward expansion. The annual average width of the upper TTL is displayed in Figure 6.14. For the past, the total width of the upper TTL of the three model simulations lies within the range of the detected upper TTL-width from ERA Interim, which gives confidence for the future model simulations. The three climate models show smaller variability within one decade compared to ERA Interim. All three climate models reveal an increasing width of the upper TTL from 1990 to 2099 of 0.5° to 1.5° latitude.
For the seasonal average a noticeable change is simulated during NH summer. All three climate models project a displacement of the median of LCP distribution and the SH border towards the South, hence an increase of LCPs on the SH. Additionally they also project a positive change of the width of the upper TTL. For NH winter CMAM REF-B2 and NIWA-SOCOL REF-B2 simulate a broader width of the upper TTL in the 2090s. No consistent change is projected for the NH fall season. However, NH spring reveals a positive change at least by NIWA-SOCOL REF-B2 and MPI-ESM from the 1990s to the 2090s.

Long-term changes of the position and strength of the jets and HC width were analyzed using different future projections of models within CCMVal-2 and compared with CMIP3 models (SPARC, 2010, Chapter 10). They demonstrated that models from CCMVal-2 and CMIP3 simulated a poleward expansion of the SH HC during the last decades of the 21th century. However, it was shown that the observed widening of the HC is larger than the simulated by the CMIP3 models, leading to the assumption that stratospheric ozone depletion, which is not included in many of those models, might be one explanation for this

discrepancy (Seidel et al., 2008).
The change of the upper TTL width within different geographical regions indicates most pronounced changes for MPI-ESM during NH summer with 2° latitude and during NH winter for CMAM REF-B2 of 2.1° latitude from the 1990s to the 2090s for the West Pacific. NIWA-SOCOL-REF-B2 reveals a decrease of the upper TTL width from the 1990s to the 2040s followed by an increase towards the 2090s during all seasons.
Under the conditions of a changing climate in the future the role of the West Pacific becomes even more pronounced due to an increase of the with of the upper TTL and simultaneously the increased possibility for warmer and hence more moist air masses reaching the stratosphere in that region from below.

Chapter 7

Conclusion

The tropical tropopause layer (TTL) is the main entrance region for climate and ozone relevant trace gases into the stratosphere. Once ozone depleting substances (ODS) reach the stratosphere, they can significantly contribute to ozone depletion. As a consequence, the originally harmful ultra violet (UV) radiation from the sun, absorbed by the ozone layer, can enter the lower atmosphere and reach the Earth's surface. Hence, it is crucial to investigate transport processes within the TTL, especially under the influence of increasing greenhouse gases (GHG) in a changing climate.
In this thesis, trajectory calculations were carried out to determine transport processes in the upper TTL, using ERA Interim and seven different climate model data for the recent past (1990s). In order to investigate changes in the TTL transport under future climate conditions, three climate models using future GHG and ODS scenarios until the end of the 21st century, were considered additionally. The Lagrangian cold points (LCPs) of each trajectory were analyzed to determine the entrainment region for tropospheric air masses into the stratosphere.
To investigate whether the recently observed broadening of the tropical belt is also reflected in the lowermost boundary of the stratosphere, a new diagnostic method for the upper TTL was presented in this study. Previous studies mainly focused on tropospheric characteristics like the position of jet streams or the width of the Hadley cell to define the tropical edges. In contrast, within this study the width of the upper TTL, which is mainly influenced by stratospheric characteristics, was analyzed by the spread of the meridional extension of the LCPs.

In the first result chapter (chapter 4), long-term climatologies of the Eulerian and Lagrangian cold points were derived using ERA Interim and different climate model data. In the following the questions from the introduction are repeated and answered.

- *How is the upper TTL represented in ERA Interim reanalysis?*
  Climatologies of the average Eulerian cold point (CP) were analyzed based on the new meteorological assimilation from ERA Interim for 1979-2011. On the annual average, the coldest region for the TTL, the so-called "cold trap", is located over the tropical West Pacific. The lowest temperatures, annually averaged, reach 190.5 K in that re-

gion. These temperatures generally agree in location with the CP from the ERA-40 CP climatology, which was presented by Fueglistaler et al. (2005) for the time period 1979-2001. However, this study reveals that ERA Interim has around 1 K lower CP temperatures over the tropical West Pacific. The minimum CP temperatures over tropical South America are more pronounced in ERA Interim and reveals 1 to 2 K lower temperatures compared to ERA-40 data. Seasonally, highest CP minimum temperatures of 192 K occur during NH summer over the West Pacific and the Bay of Bengal. During NH winter the minimum CP temperatures are lowest and more pronounced over the tropical West Pacific reaching 188 K. Compared to ERA-40 the minimum CP temperatures are generally 1 to 2 K lower during the different seasons as well.

- *Where is the main entrance region for trace gases into the stratosphere using ERA Interim?*
  The tropical LCP distribution was divided into 5 main entrainment regions. On the annual average, the main entrance region of tropospheric air masses into the stratosphere, is located over the tropical West Pacific (as defined by 100° to 210° E). More than 50% of the air masses reach the stratosphere in this geographic region. After the West Pacific, also West Africa (330° - 50° E) the Indian Ocean (50° - 100° E) and South America (270° - 330° E) play a secondary role as eintrainment regions. 11% to 14% of the air masses reach the stratosphere from below in these regions on the annual average. The East Pacific (210° - 270° E) contributes with less than 10% to the stratospheric air mass entrainment. During all seasons the West Pacific remains as main entrance region for air masses into the stratosphere. In NH winter this entrainment region is most pronounced indicating more than 60% of the air masses reaching the stratosphere from below. During NH spring and summer the amount reduces to 49% and 52%. During NH summer the Indian Ocean reveals the second largest air mass entrainment after the West Pacific. Whereas, South America contributes as second main region to the stratospheric air masses during NH fall.

- *How well do the different climate models reproduce upper TTL characteristics from ERA Interim?*
  In order to evaluate seven different climate models compared to ERA Interim, the LCP temperature and occurrence was analyzed. The annual average LCP temperatures from CMAM REF-B1 and REF-B2 and WACCM reveal the best agreements with ERA Interim within +/-1 K. NIWA-SOCOL REF-B1 and REF-B2 simulations indicate a negative bias of -3 K to -5 K. A smaller bias of -1 K to -2 K in the tropical region is simulated by MPI-ESM, whereas E39CA shows LCP temperatures up to 2 K higher compared to the reanalysis.
  In contrast to Kremser et al. (2009), who analyzed the main entrainment region with CCMVal-1 models for single seasons, the here analyzed CCMVal-2 models are generally able to reproduce the main entrance region above the tropical West Pacific on the annual and seasonal average. The model E39CA performs best indicating 1% less air mass entrainment into the stratosphere compared to ERA Interim above the

tropical West Pacific. The two CMAM simulations and MPI-ESM simulate slightly less entrainment of 4% to 8%, whereas the two NIWA SOCOL runs exceed even 11% less of stratospheric air mass entrainment. A higher entrainment compared to ERA Interim is projected by WACCM with 9%. While most climate models overestimate the occurrence of LCPs over West Africa by 2% to 7% on the annual average, only WACCM simulates less LCP frequency in that region by around 8% compared to ERA Interim. The Indian Ocean as entrainment region reveals the best agreement among the reanalysis and the different climate models indicating 10% to 15% of the air masses reaching the stratosphere from below within this region. Within the East Pacific, the two NIWA-SOCOL runs simulate an air mass entrainment into the stratosphere twice as large as for ERA Interim. Whereas, E39CA and WACCM underestimate South America as entrainment region.
During NH winter, all climate models, except the two NIWA SOCOL simulations, are able to reproduce the most pronounced main entrainment region for stratospheric air masses over the tropical West Pacific. Similar as on the annual average, E39CA performs best, followed by the two CMAM simulations and MPI-ESM underestimating this entrainment region by 4% to 10%, whereas WACCM overestimates the air mass entrainment by 17%. The two NIWA SOCOL simulations do not highlight the West Pacific during NH winter, which can be related to a too strong model response to the combined volcano and ENSO forcings leading to an El Niño like pattern and hence, more LCPs in the East Pacific. In contrast to the other climate models, CMAM REF-B1 simulates a twice as large tropospheric entrainment into the stratosphere over South America during NH winter compared to ERA Interim.
Overall, most of the climate models are able to reproduce the main entrance region for tropospheric air masses into the stratosphere over the West Pacific and the location of lowest minimum temperature.

In chapter 5 the broadening of the upper TTL was analyzed using a new method to define the meridional edges of the upper TTL for reanalysis and different climate model data. The following question arose and was answered in this chapter.

- *Is there a change in the width of the upper TTL in ERA Interim and climate models in the past and present?*
  Analyzing the poleward extension of the LCP distribution between 1979 and 2010, ERA Interim reveals a significant broadening of the upper TTL of 1.2° lat/dec on the annual average. While largest changes occur during the first two decades from 1979-1999, after 2000 no significant change is detected any more. This variation may be linked to observed changes in the stratospheric circulation indicating an increase in stratospheric upwelling and decrease of water vapor in the lower stratosphere from 2000 onward (Davis and Rosenlof, 2012; Randel et al., 2006). During NH summer a significant change of 1.39° lat/dec was determined indicating the largest change during all seasons on average from 1979-2010.

By investigating geographic regions separately, within each of them a significant broadening of width of the upper TTL can be detected on the annual average. However, the largest change appears in the West Pacific with 0.99° lat/dec between 1979-2010. Seasonally the largest change occurs in the East Pacific during NH summer with a broadening of the upper TTL of 1.87° lat/dec.
Overall, most of the climate models indicate a slight positive change of the width of the upper TTL between 1990-1999. However, the models tend to underestimate the revealed positive change from ERA Interim of 2.84° latitude during that decade by more than 50 %. Only MPI-ESM reveals a significant change with 1.37° lat/dec. Johanson and Fu (2008) investigated the widening of the tropical belt by analyzing the change in the width of the Hadley cell in CMIP3 models. The authors detected a systematically weaker change by the CMIP3 models compared to observations as well, which they related to a too weak model response to volcanic, GHG and ozone depletion forcing, underestimating the stratosphere troposphere coupling in the tropics.

In chapter 6, future changes of the TTL were investigated, using data from three climate models, driven with future GHG and ODS scenarios.

- *Does the TTL change in a future climate?*
  All three climate models project an increase of the average LCP temperature from the 1990s until the end of the 21st century by 0.5 K to 1 K. This result is consistent with an increasing CP temperature simulated by 13 different CCMs from CCMVal-1 of 0.1 K/decade, resulting to 1 K increase from the 1990s to the 2090s (Gettelman et al., 2010). Compared to the 1990s, all climate models project an increase of the LCP occurrence in the West Pacific accompanied by a decrease in other geographic regions towards the future. The largest change is simulated by MPI-ESM, with the percentage of air masses reaching the stratosphere above the tropical West Pacific increasing from 40% to 48% between the 1990s and the 2090s.
  A positive change of the width of the upper TTL between the 1990s and the 2090s is consistently simulated by the three models on the annual average. During NH summer a positive change of the upper TTL, and strikingly, a displacement of the LCP distribution towards the southern hemisphere is projected by all climate models. Analyzing the change of the width of the upper TTL above the West Pacific separately, a weak positive change from the 1990s to the 2090s is projected by all three climate models by 0.1° to 1° latitude. However, there seems to be no consensus among the climate models of a dominant season influencing this change. Further, the climate model projections indicate no significant results for the changes of the width of the upper TTL.
  Overall, the increasing LCP frequency, combined with a changing width of the upper TTL above the West Pacific, highlights the importance of this region as the main entrance gate for tropospheric air masses into the stratosphere also in a future climate.

Outlook

In this thesis, which was based on ERA Interim from 1979-2011 and different climate models, TTL characteristics were analyzed with a Lagrangian perspective. The results revealed that most of the analyzed climate models (CCMVal-2 and CMIP5) perform well in representing the main properties of the TTL like the CP temperature distribution and the main LCP occurrences. Due to computer time and space limitations of the trajectory calculations, only three decades of CCMVal-2 model data were available and analyzed. However, applying a longer-term time series would increase the robustness of the results and could better reflect possible long-term changes. The residence time of air masses in the TTL before they enter the stratosphere, is an useful diagnostic for the transport and chemical transformation of ODS. Due to limited time within this thesis, the investigation of this parameter was not possible, which should be included in future CCM studies. Furthermore, to test the sensitivity of trajectory calculations from CCMs using different vertical velocities like diabatic heating rates as well would be beneficial for further TTL diagnostics. As the heating rates were not available from the given climate models, this diabatic approach could not be tested within the present study. Future Lagrangian TTL studies should also consider that initializing the trajectory model with ERA Interim to a certain UTC time could lead to a mispresentation of the LCP frequencies.
The above mentioned suggestions could be applied for the next generation of CCMs, which will be available soon (end of 2013) within the new chemistry climate model initiative (CCMI).

Appendix A

Appendix

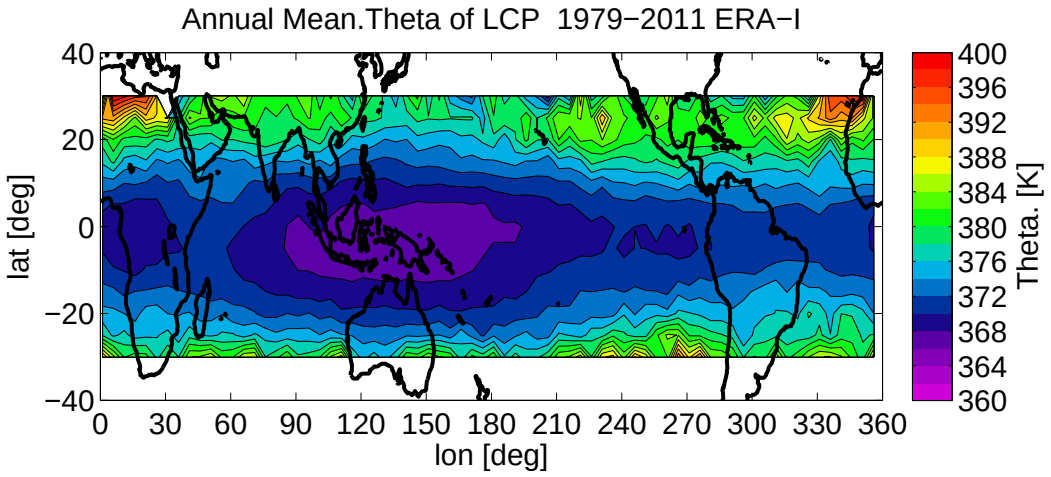

Fig. A.1: Annual mean of LCP potential temperatures for ERA Interim 1979-2010, color interval of 2 K.

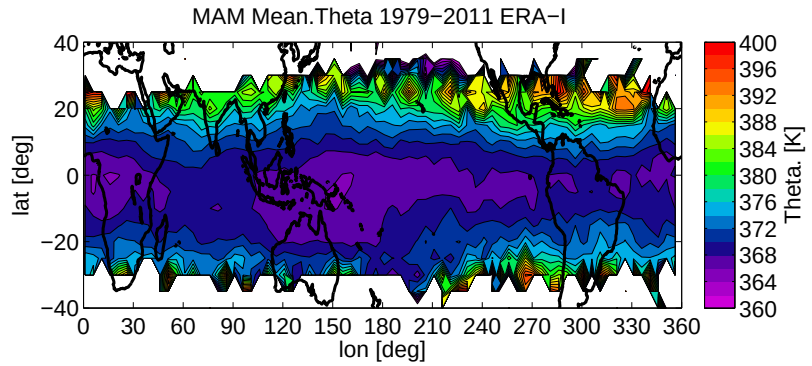

(a)

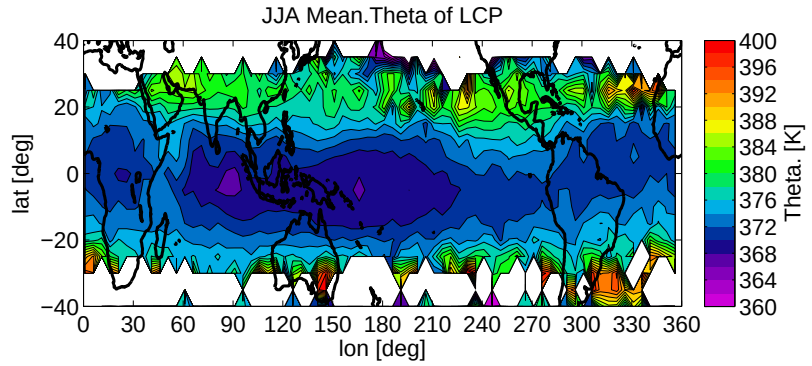

(b)

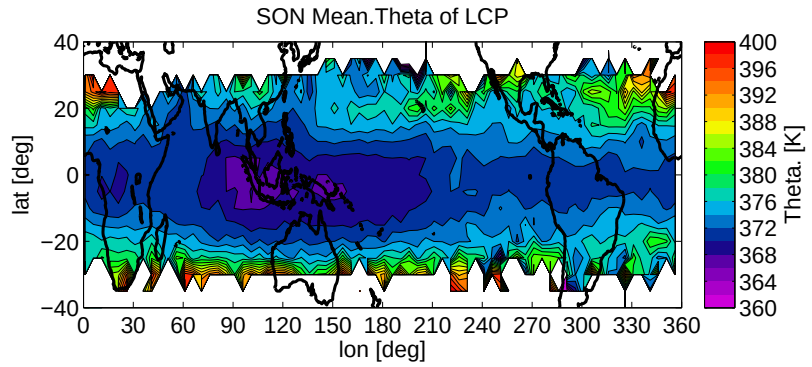

(c)

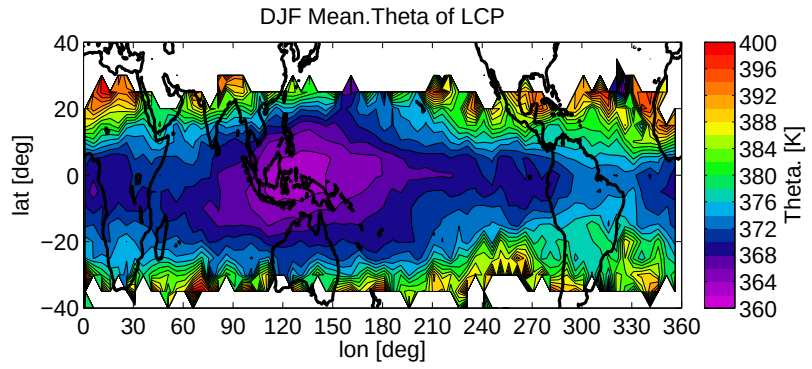

(d)

Fig. A.2: Sesonal mean of potential temperatures for LCPs from ERA-Interim 1979-2010 MAM: **(a)**; JJA: **(b)**; SON: **(c)**; DJF: **(d)**.

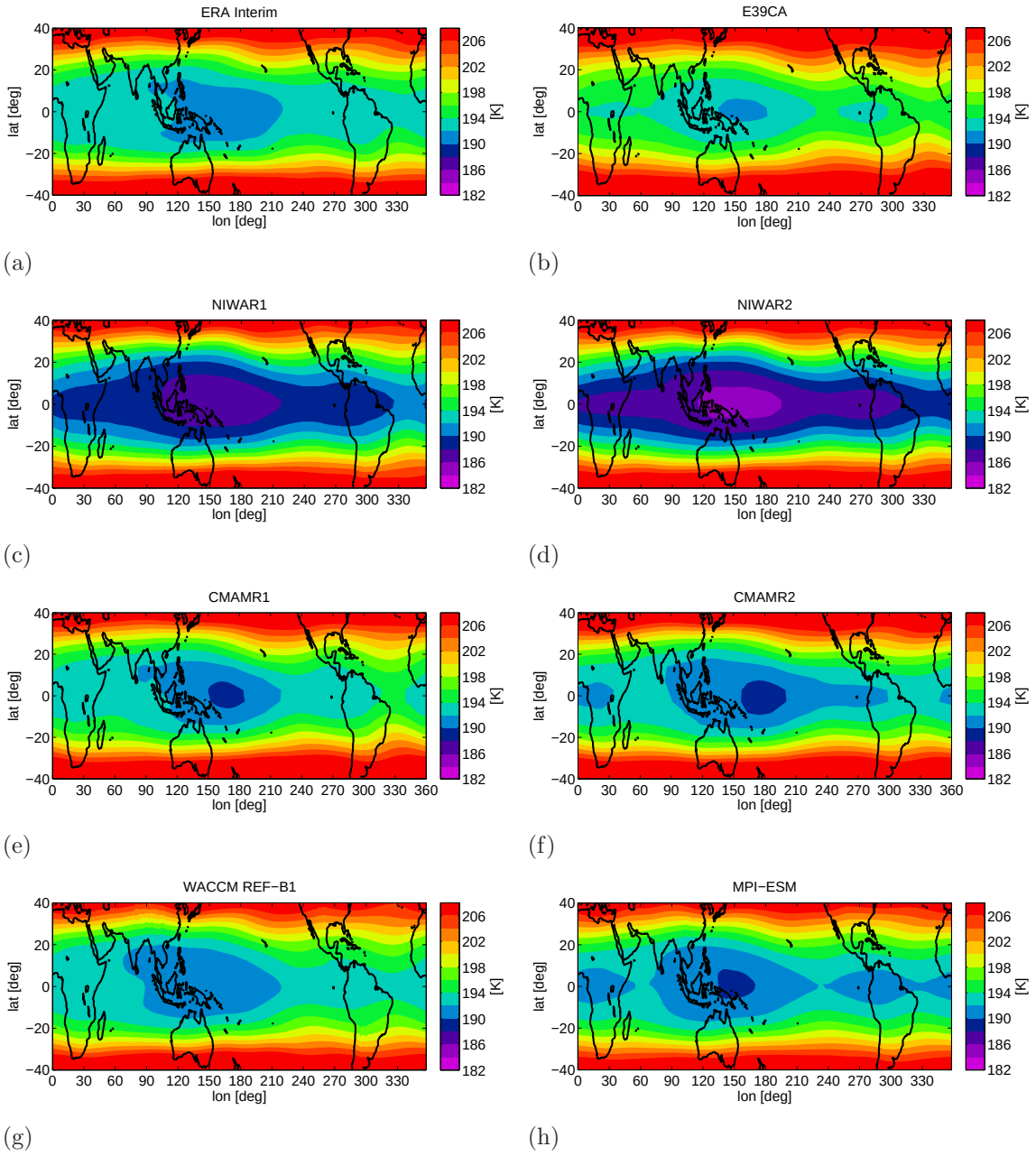

Fig. A.3: Climatology of the annual mean CP temperature for 1990-1999 for ERA Interim and climate models with a contour interval of 2 K.

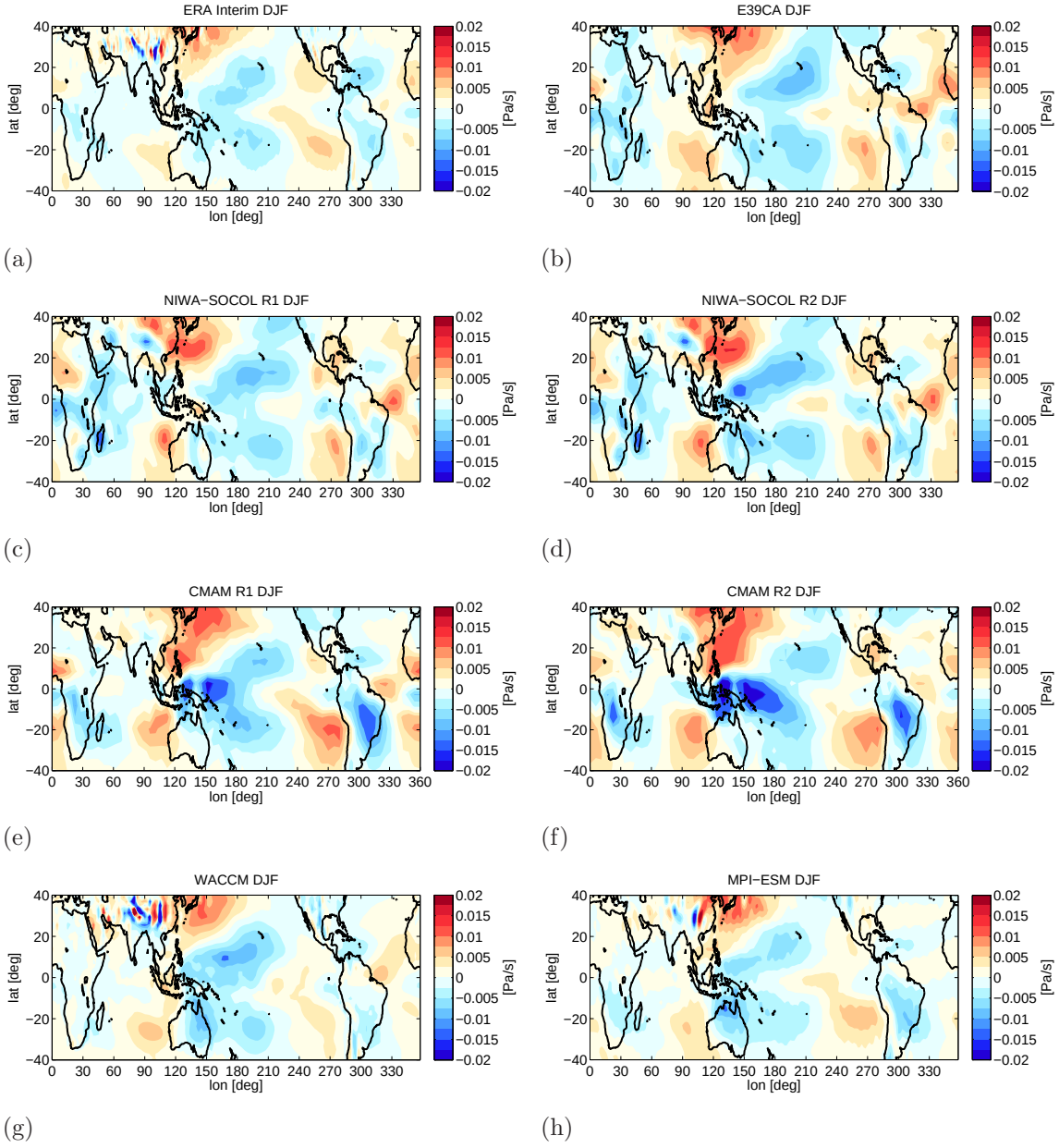

Fig. A.4: Climatology of the average vertical velocity at 100 hPa during NH winter for ERA Interim (1979-2010) and climate models (1990-1999).

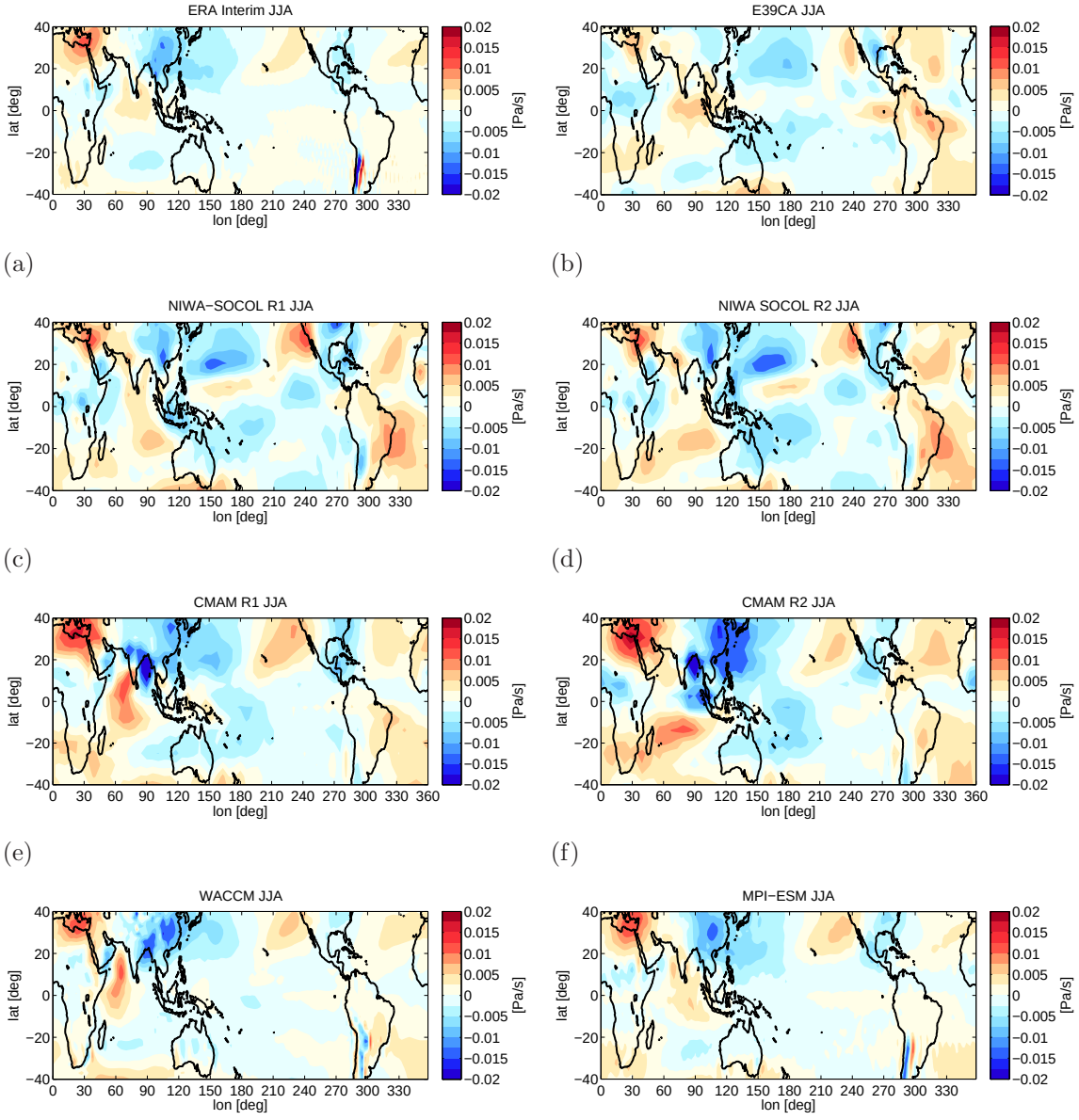

Fig. A.5: Climatology of the average vertical velocity at 100 hPa during NH summer for ERA Interim (1979-2010) and climate models (1990-1999).

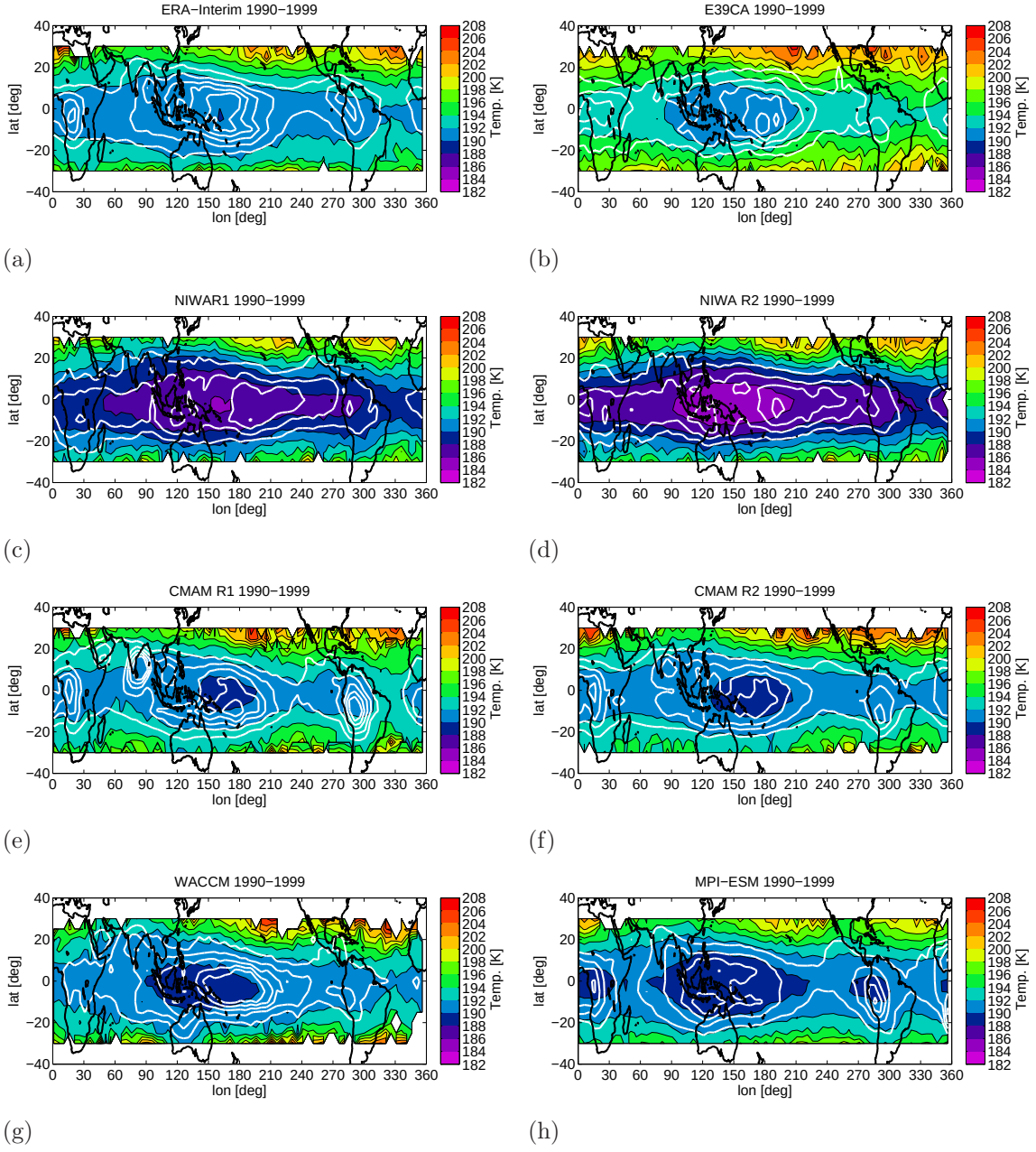

Fig. A.6: Long term climatology for the annual mean LCP temperature and occurrence for 1990-1999 per 5° x 5° from ERA Interim and climate models. White contour lines display the density of LCP occurrence from 0.1% with an interval of 0.1%.

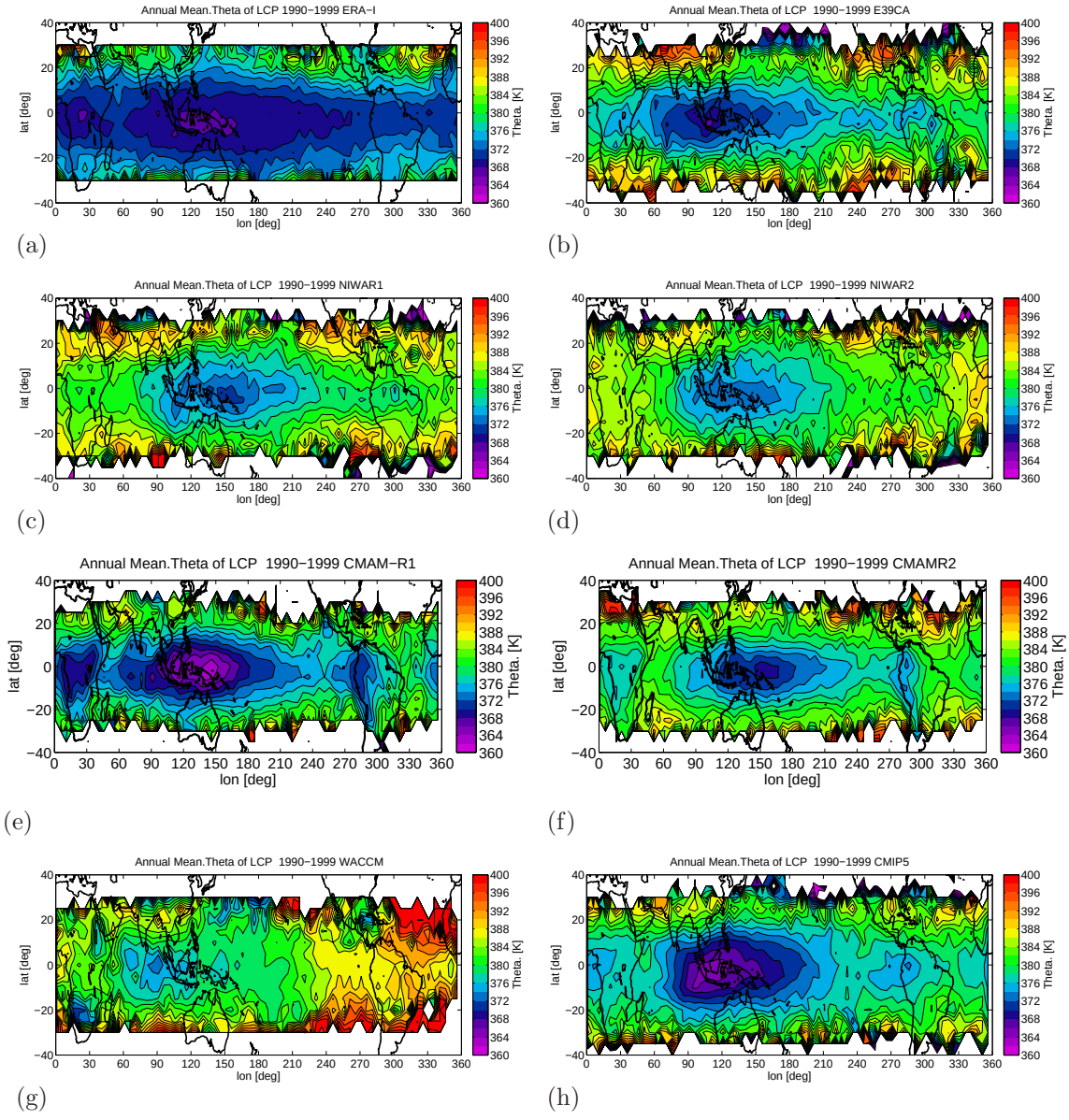

Fig. A.7: Annual mean of LCP potential temperatures for ERA Interim and climate models 1990-1999, color interval of 2 K.

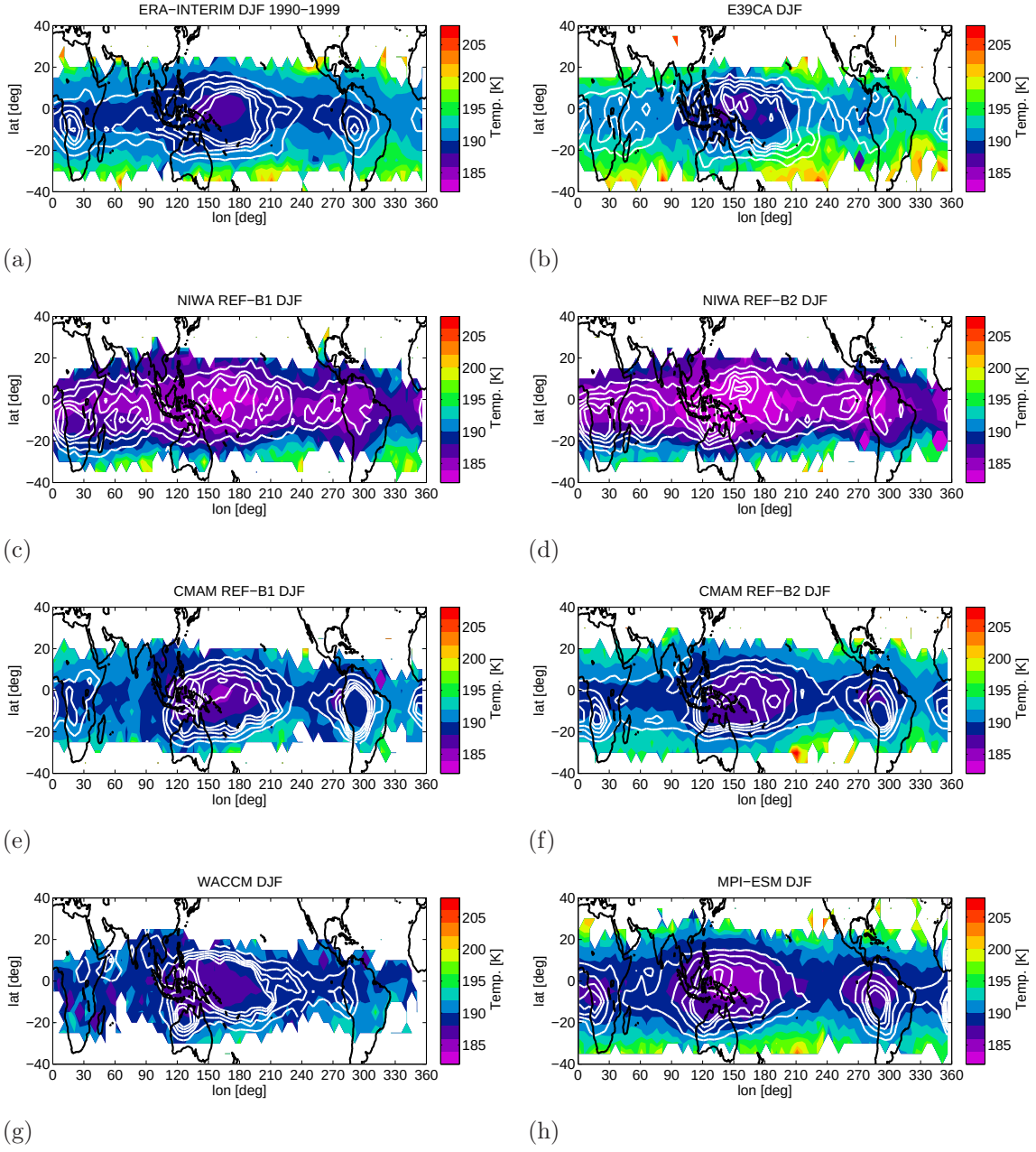

Fig. A.8: Long term climatology for LCP temperature and occurrence for DJF 1990-1999 per 5° x 5° for ERA Interim (a) and climate models (b)-(h). White contour lines display the density of LCP occurrence from 0.1% with an interval of 0.1%.

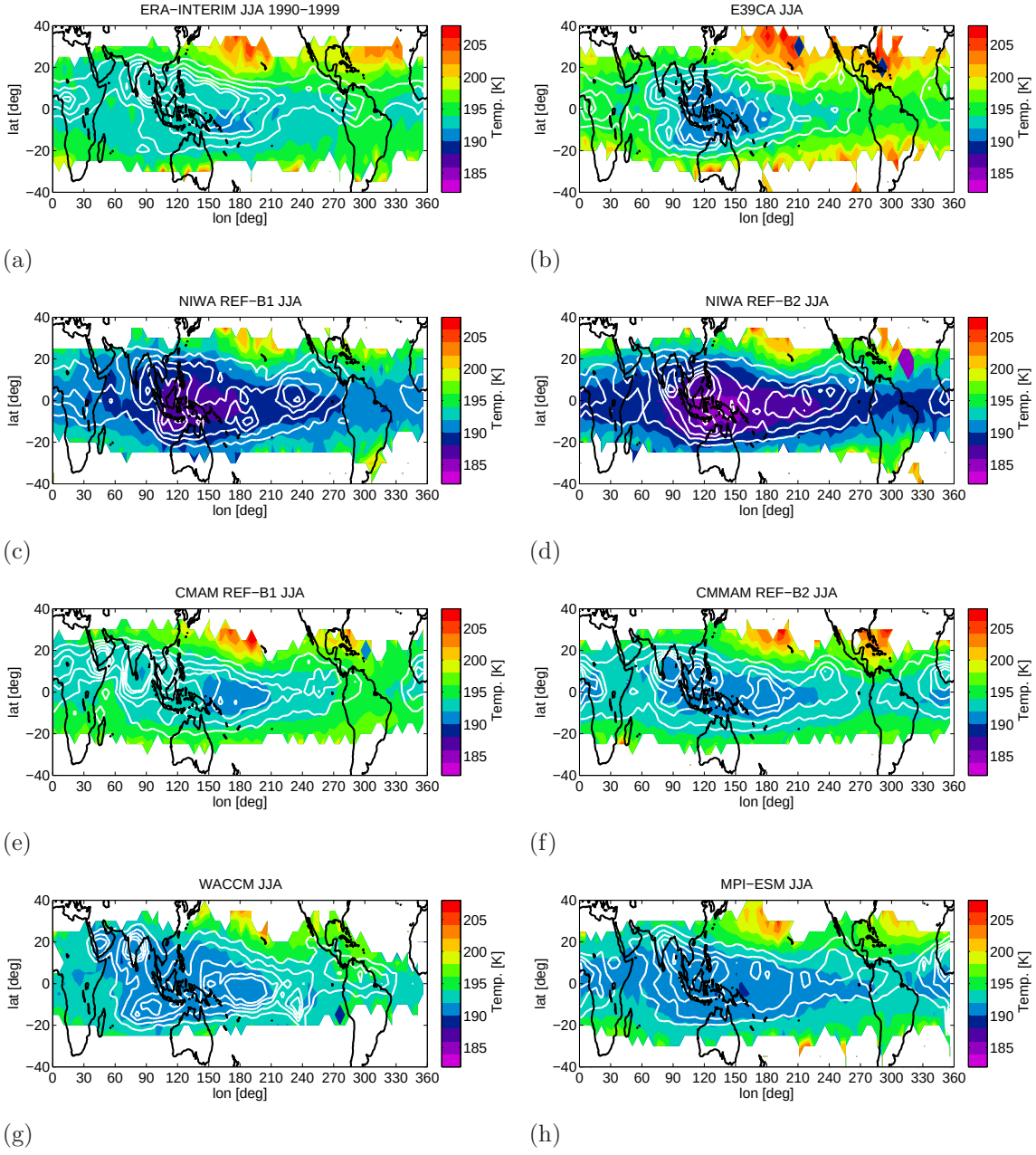

Fig. A.9: Long term climatology for LCP temperature and occurrence for JJA 1990-1999 per 5° x 5° for ERA Interim (a) and climate models (b)-(h). White contour lines display the density of LCP occurrence from 0.1% with an interval of 0.1%.

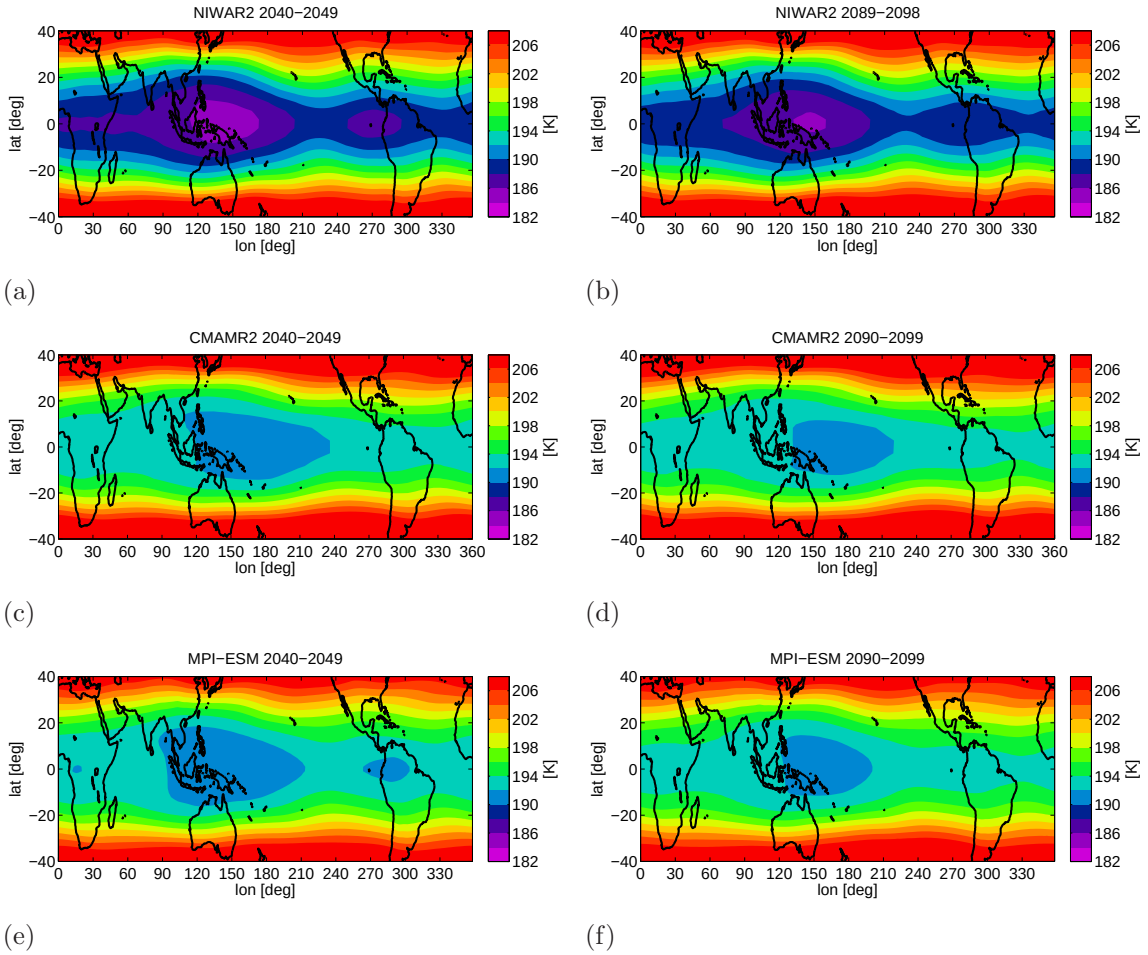

Fig. A.10: Climatology of the annual mean CP temperature for future simulations with a contour interval of 2 K.

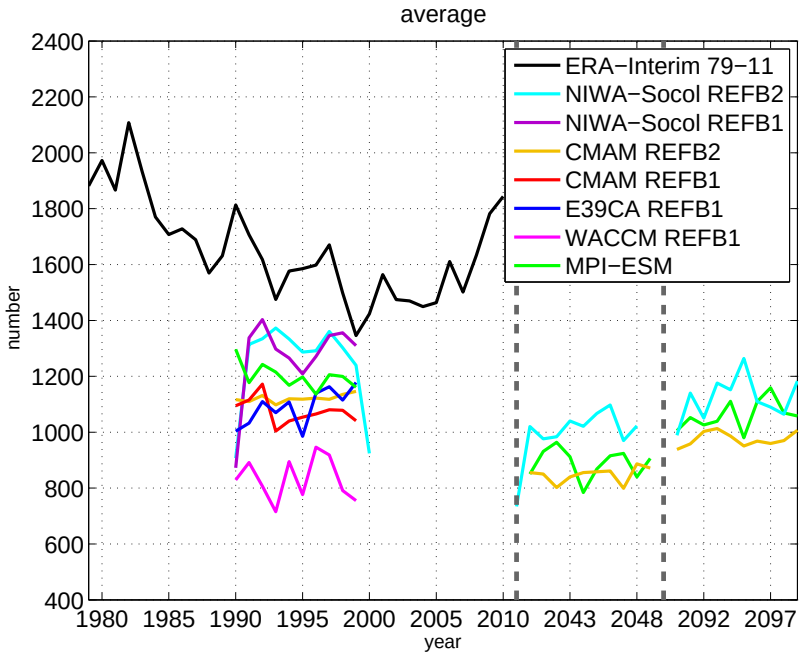

Fig. A.11: Average sum of trajectories fulfilling the criteria for one model setup.

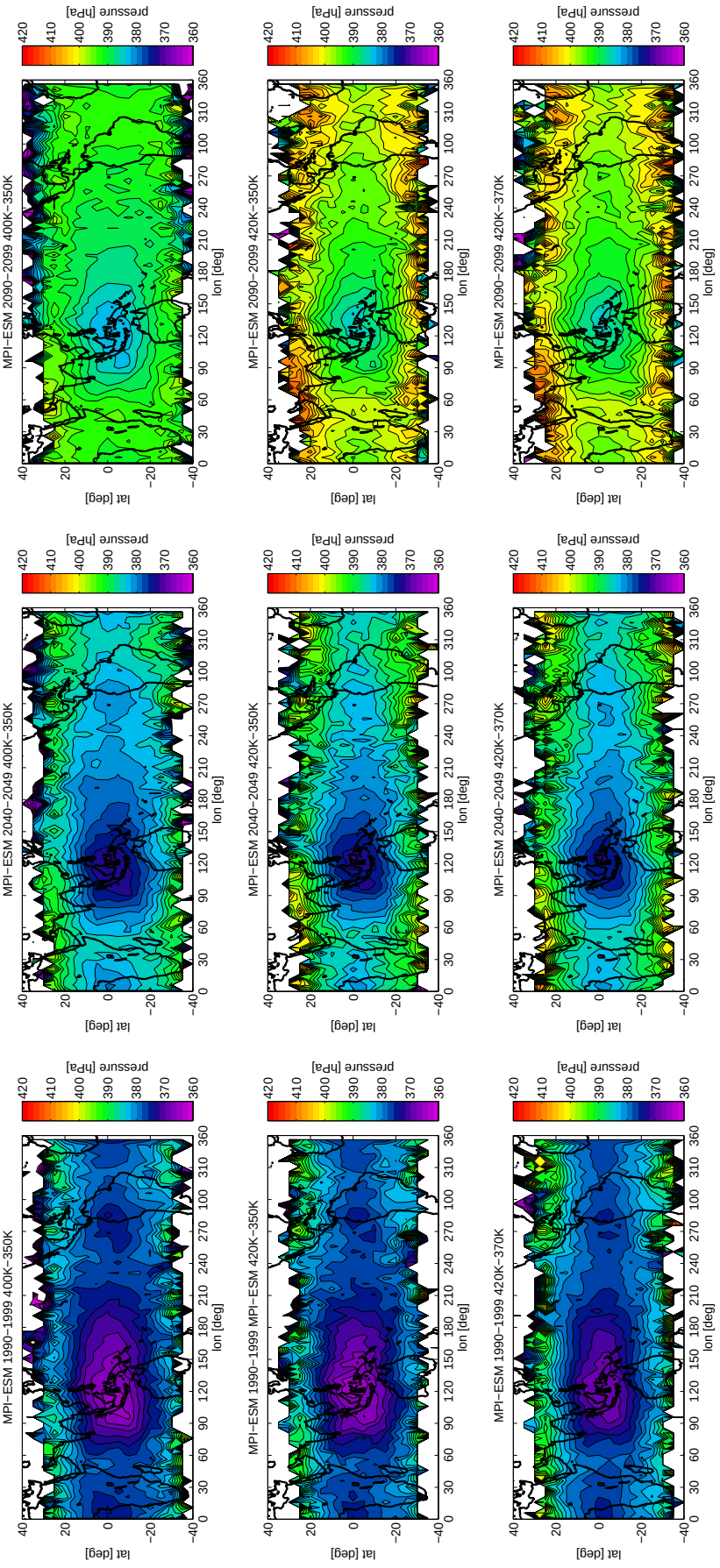

Fig. A.12: Annual mean LCP of potential temperatures for different criteria using MPI-ESM.

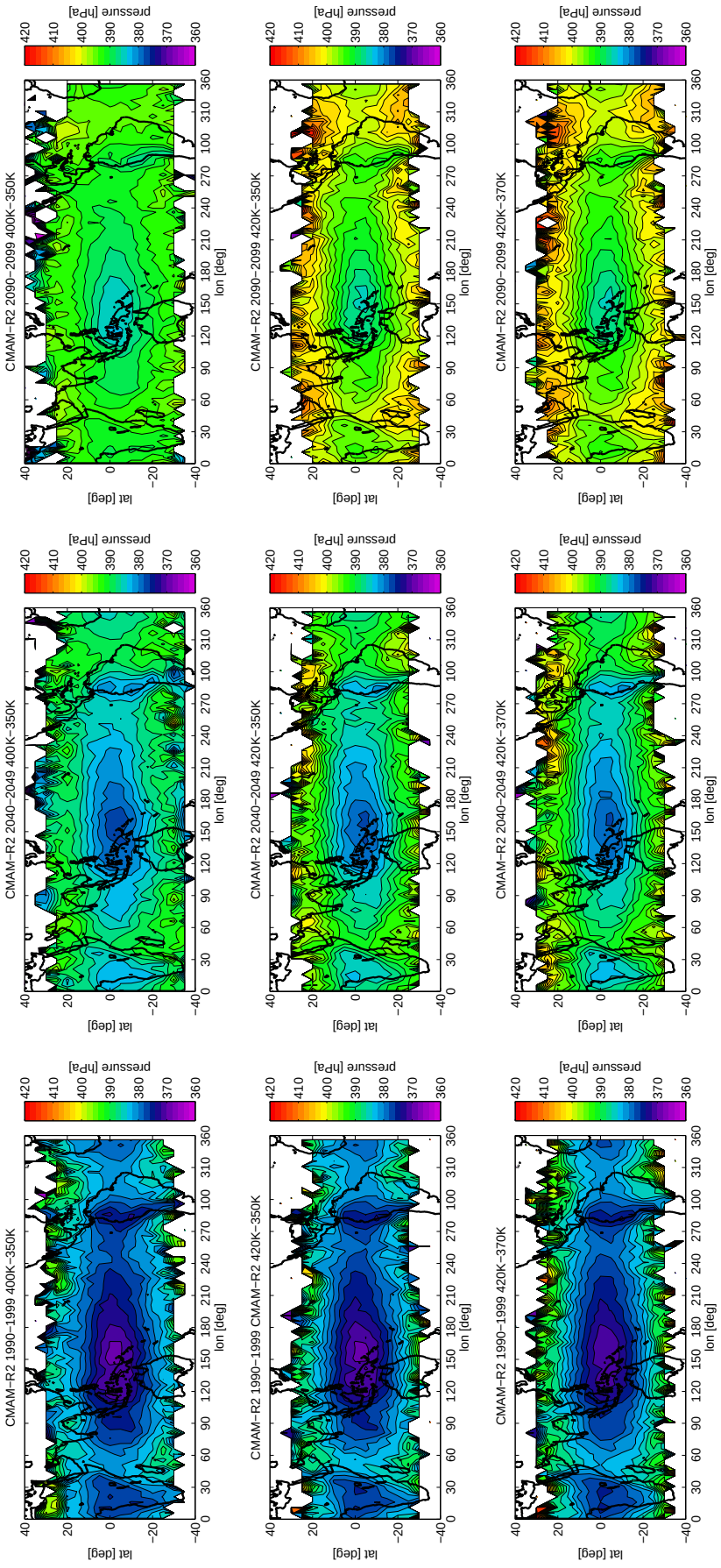

Fig. A.13: Annual mean LCP of potential temperatures for different criteria using CMAM REF-B2.

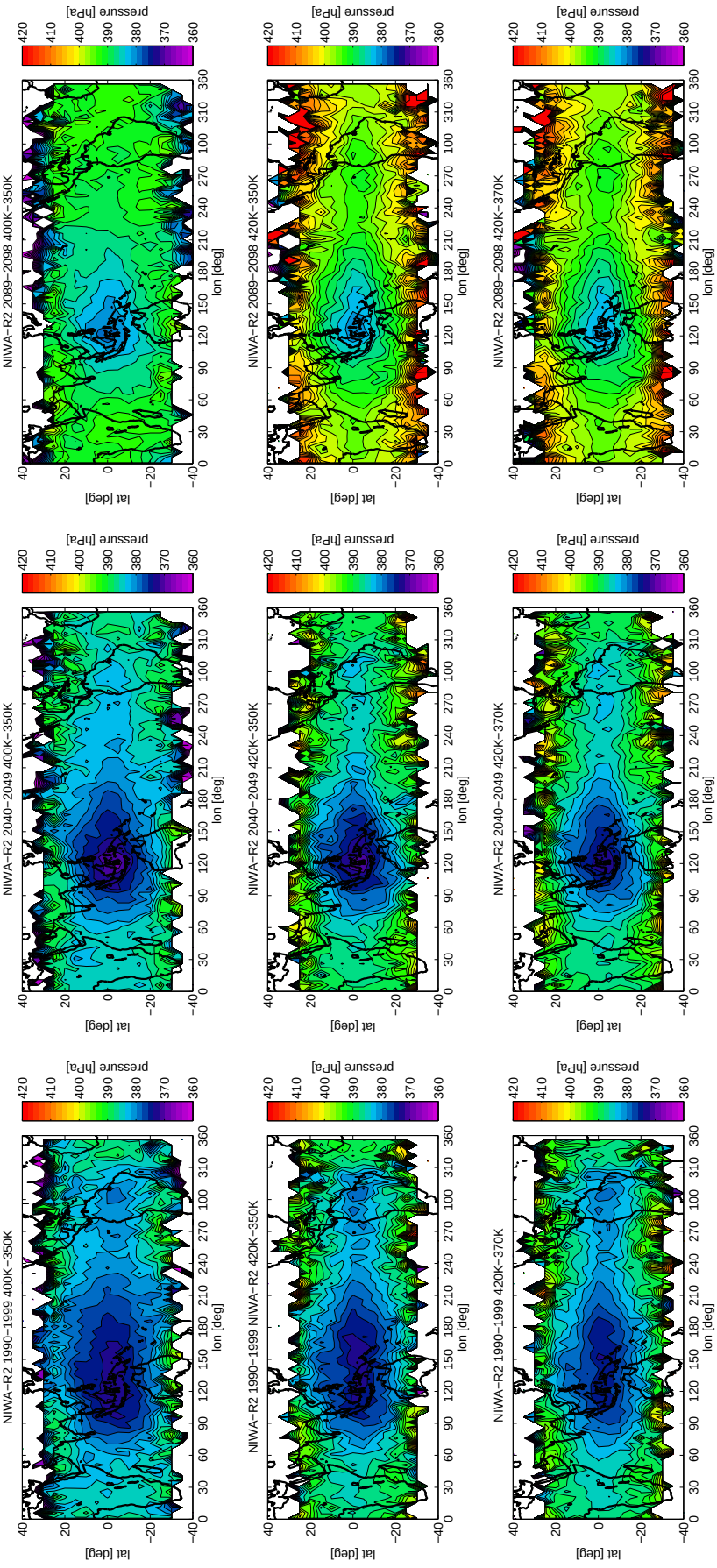

Fig. A.14: Annual mean LCP of potential temperatures for different criteria using NIWA-SOCOL REF-B2.

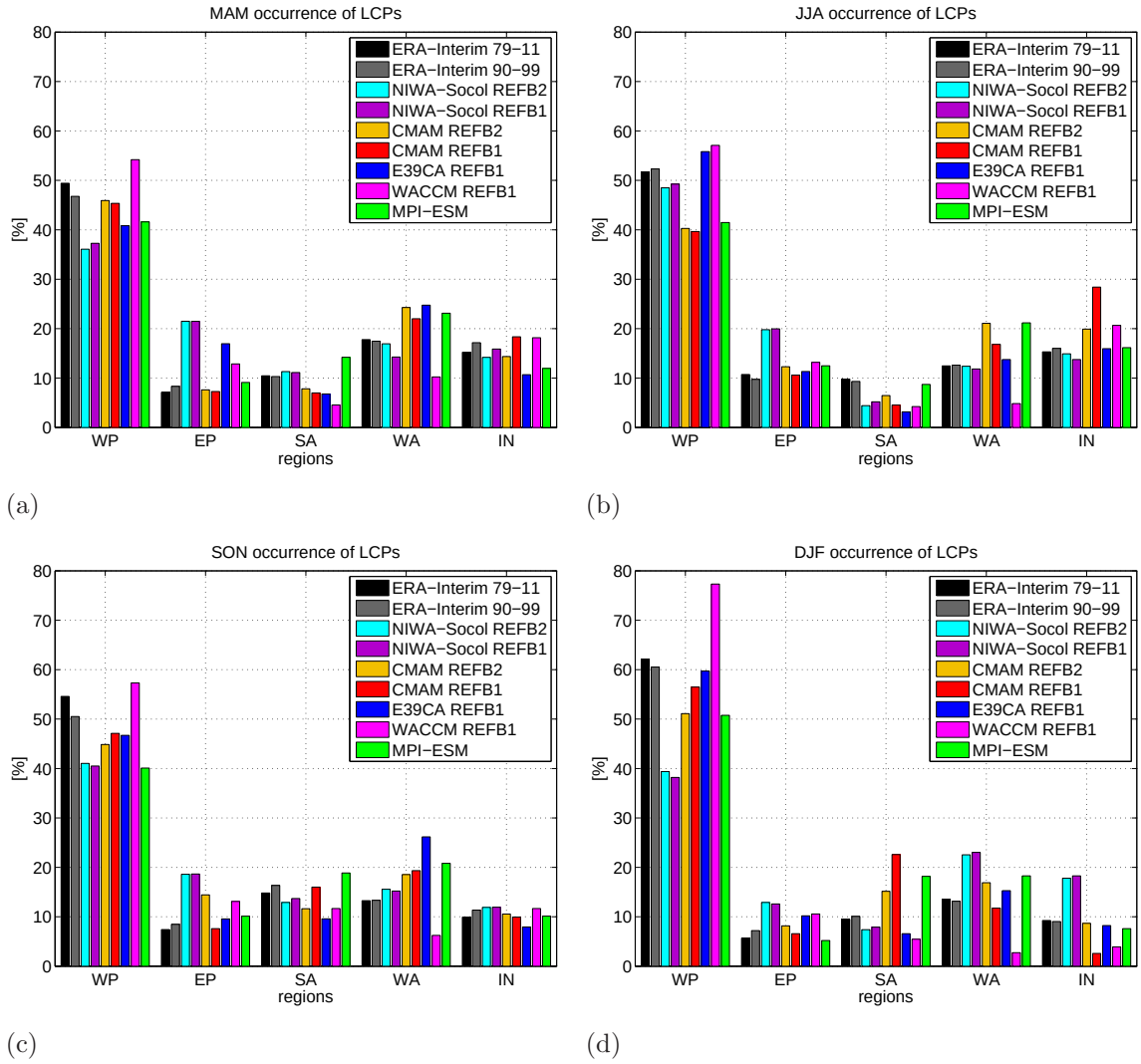

Fig. A.15: Average occurrences of LCPs for different regions from ERA Interim and climate models for different seasons. MAM (a), JJA (b), SON (c), DJF (d), West Pacific (WP): 100°-210°E, East Pacific (EP): 210°-270°E, South America (SA): 270°-330°W, West Africa (WA): 330°-50°E and Indian Ocean (IN): 50°-100°W for 1990-1999. Black and grey bars represent ERA-Interim 1979-2010 and 1990-1999.

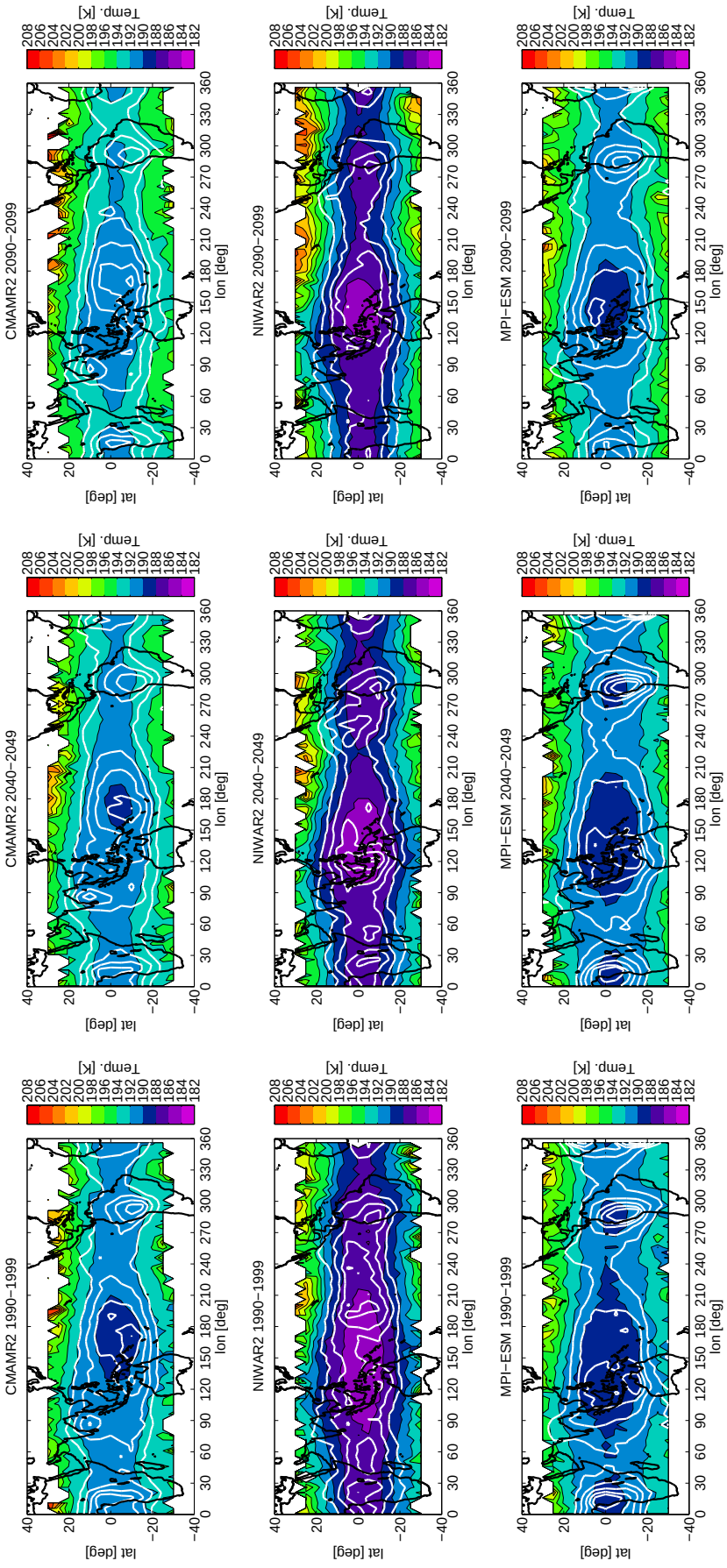

Fig. A.16: Annual average climatology of the LCP temperature and occurrence for future simulations per 5° x 5°. White contour lines display the density of LCP occurrence from 0.1% up to 0.7% with an interval of 0.1%.

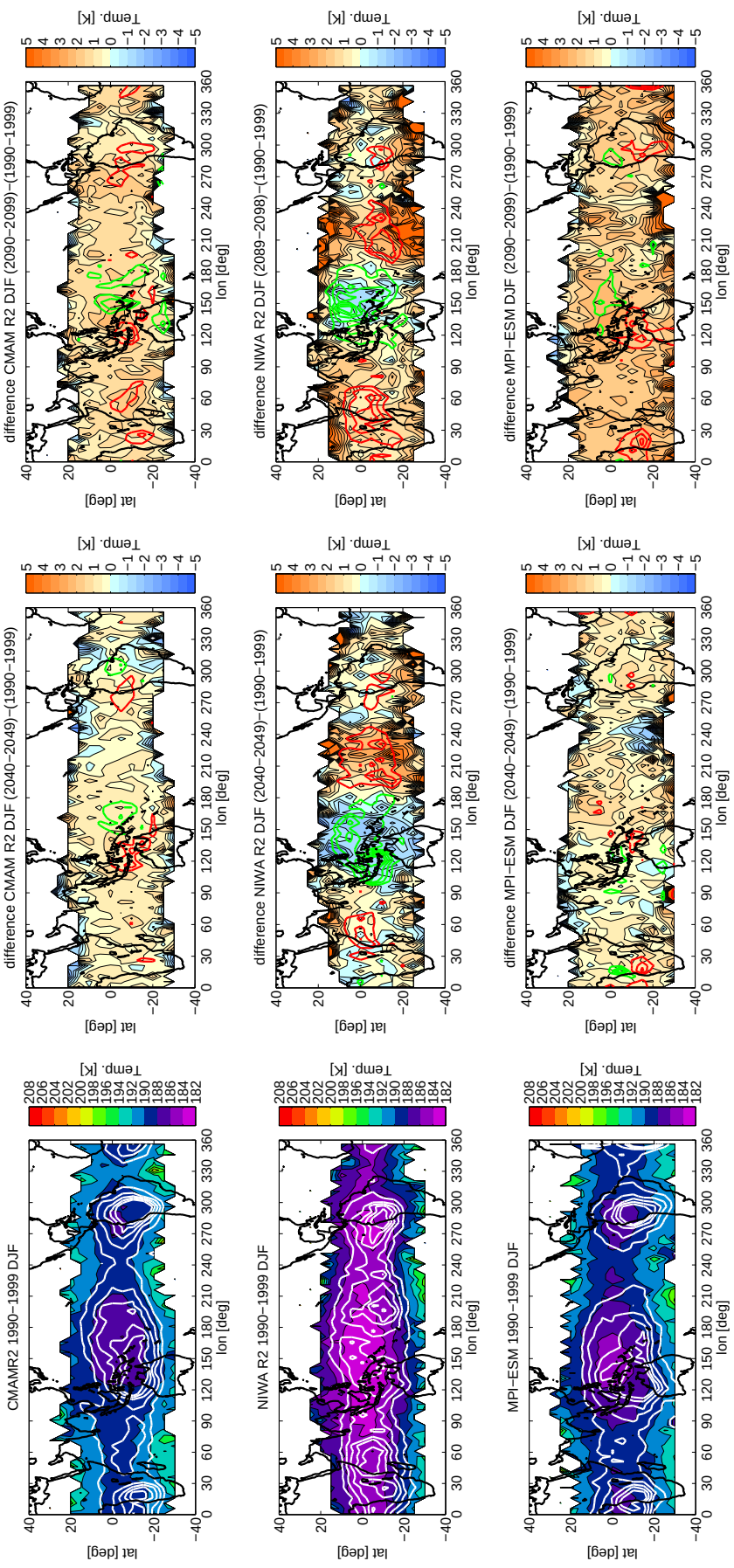

Fig. A.17: Differences in LCP temperature and occurrence for climate models from the past (1990s) to future (2040s and 2090s) for NH winter per 5° x 5°. Overlied with contour lines for the density of LCP occurrence in [%] red: less than in 1990s, green: more than in 1990s. CMAM REF-B2: (a) 1990s, (b) 2040s and (c) 2090s; NIWA-SOCOL REF-B2: (d) 1990s, (e) 2040s and (f) 2090s; MPI-ESM historical: (g) 1990s, RCP8.5: (h) 2040s and (i) 2090s. For 1990-1999 the color interval is 2 K; for LCP occurrence it is 0.1% (white contour lines) ranging from 0.1% up to 0.5% for (a), (d) and (g). Color interval for LCP temperature differences (2040s and 2090s) is 0.5 K; for LCP occurrence it is 0.1% (Note: different to annual average Figure 6.6) red: from -0.1% and green: from +0.1%.

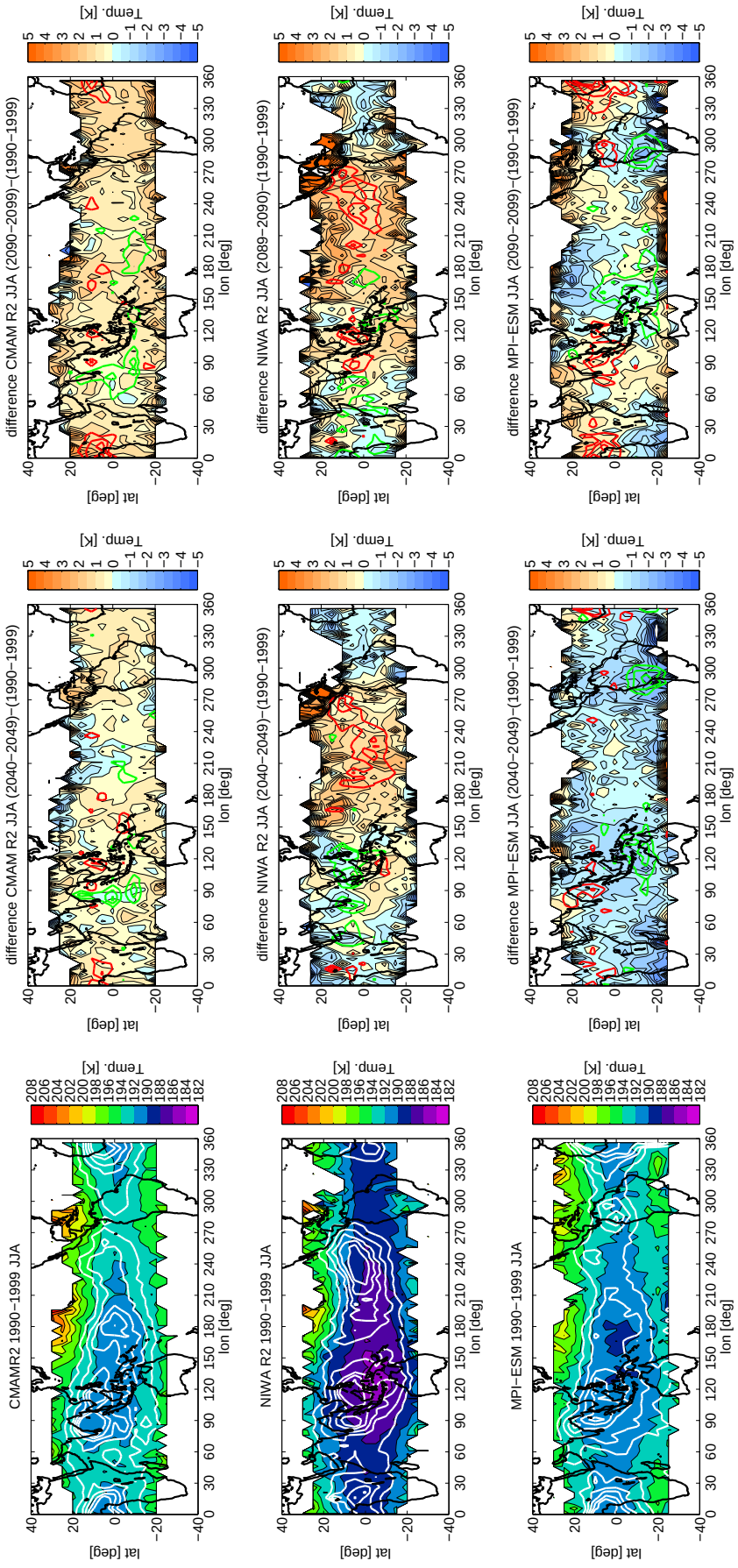

Fig. A.18: Differences in LCP temperature and occurrence for climate models from the past (1990s) to future (2040s and 2090s) for NH summer per 5° x 5°. Overlied with contour lines for the density of LCP occurrence in [%] red: less than in 1990s, green: more than in 1990s. CMAM REF-B2: (a) 1990s, (b) 2040s and (c) 2090s; NIWA-SOCOL REF-B2: (d) 1990s, (e) 2040s and (f) 2090s; MPI-ESM historical: (g) 1990s, RCP8.5: (h) 2040s and (i) 2090s. For 1990-1999 the color interval is 2 K; for LCP occurrence it is 0.1% (white contour lines) ranging from 0.1% up to 0.5% for (a), (d) and (g). Color interval for LCP temperature differences (2040s and 2090s) is 0.5 K; for LCP occurrence it is 0.1% (Note: different to annual average Figure 6.6) red: from -0.1% and green: from +0.1%.

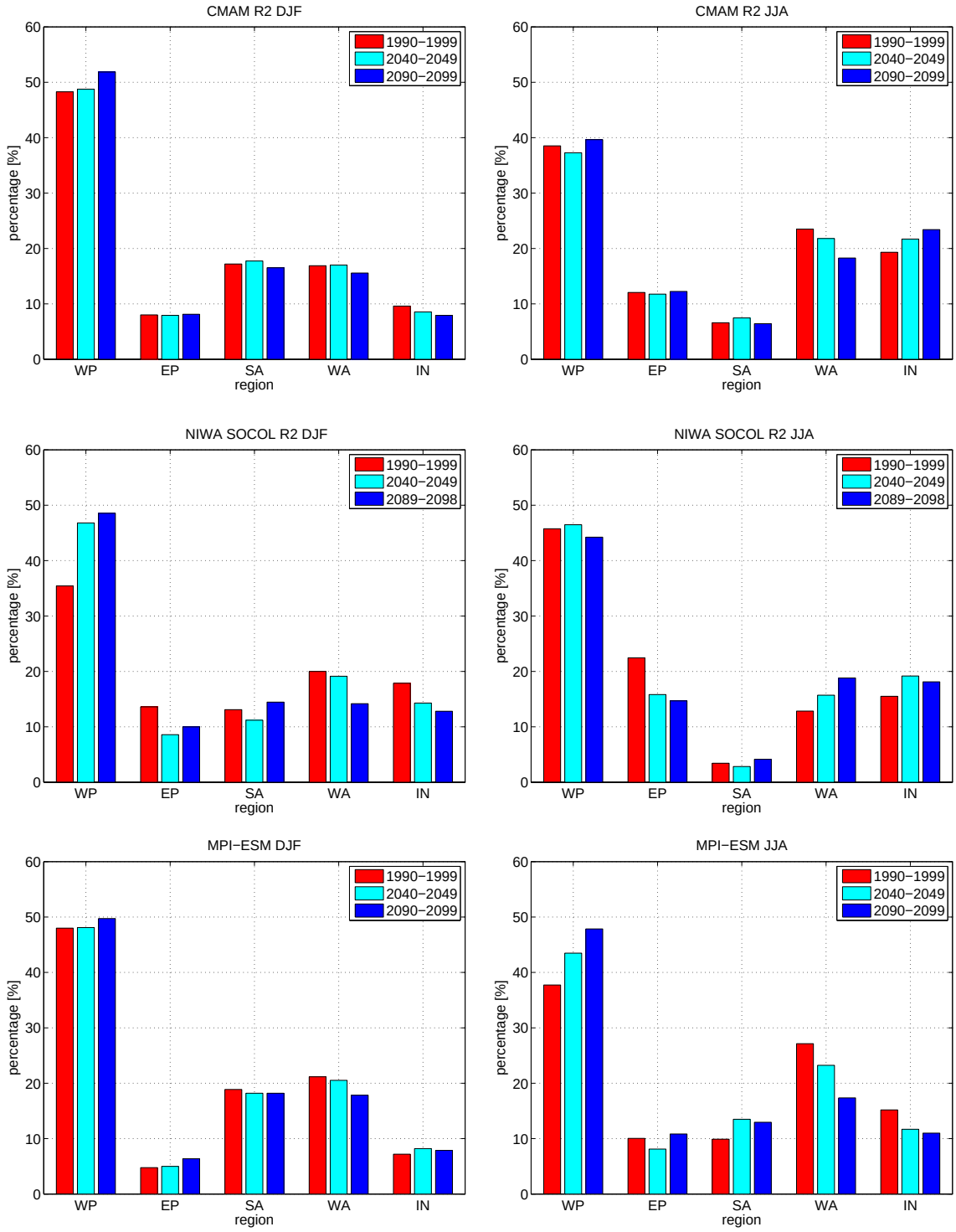

Fig. A.19: Seasonal average occurrence of LCPs within different geographic regions from future simulations for NH winter (left) and summer (right).

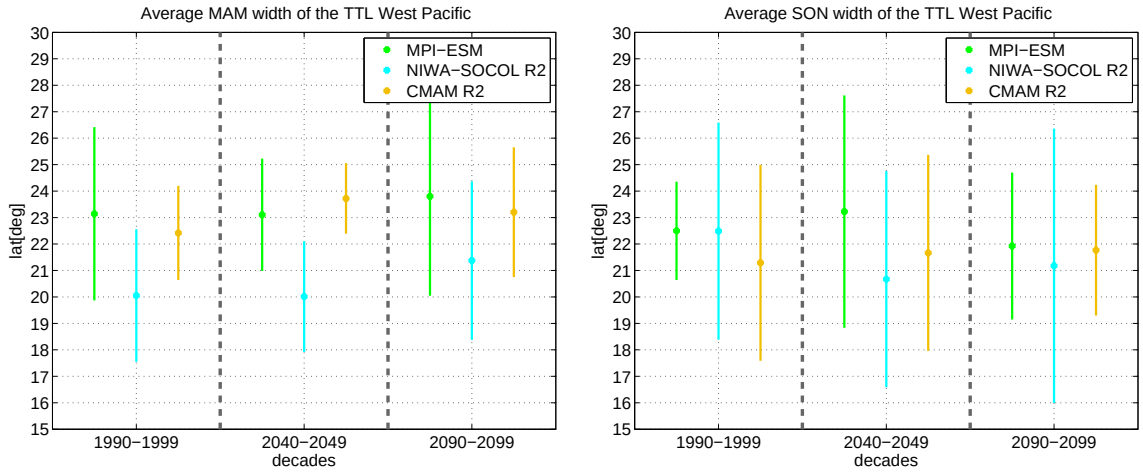

(a) (b)

Fig. A.20: Average width of the upper TTL above the West Pacific during NH spring and fall for climate models represented by the 70th percentile. Vertical lines indicate the variance (95 %) of the TTL-width during NH spring (a) and fall (b).

List of Figures

List of Tables

Abbreviations

A1B	IPCC scenario balanced across all sources
A2	IPCC scenario describing a very heterogeneous world
AMIP	Atmospheric Model Intercomparison Project
AR4	Fourth Assessment Report
ATTILA	Atmospheric Tracer Transport In a Lagrangian model
BDC	Brewer Dobson Circulation
CAM	Community Atmosphere Model
CCM	Chemistry-Climate Model
CCMVal	Chemistry-Climate Model Validation
CHEM	comprehensive chemistry module
CMAM	Canadian Middle Atmosphere Model
CMIP	Coupled Model Intercomparison Project
CP	Cold Point
CTM	Chemical Transport Model
CPT	Cold point tropopause
ECHAM	European Centre/ Hamburg model
ECMWF	European Centre for Medium-Range Weather Forecast
ECP	Eulerian Cold Point
ENSO	El Niño/ Southern Oscillation
ERA-Interim	ECMWF Reanalysis: global dataset from the ECMWF from 1979 to the present.
ERA-40	ECMWF Reanalysis: global dataset from the ECMWF from 1957 to 2002.
ESM	Earth System Model
E39CA	ECHAM4.L39(DLR)/CHEM/-ATTILA
GCM	General Circulation Model
GHG	Greenhouse Gas
GFDL	Geophysical Fluid Dynamics Laboratory
HALOE	Halogen Occultation Experiment (Satellite instrument)
HAMMOCC	Biogeochemistry component of MPI-ESM
HC	Hadley Circulation
IGAC	International Global Atmospheric Chemistry
IPCC	Intergovernmental Panel on Climate Change
ITCZ	Intertropical Convergence Zone
JSBACH	Land component of MPI-ESM

LCP	Lagrangian Cold Point
LZRH	Level of Zero Radiative Heating
MEZON	Model for the Evaluation of oZONe trends
MERRA	Modern Era Retrospective-Analysis for Research and Applications
MOZART3	Model for Ozone and Related Chemical Tracers, version 3
MPI-ESM	Max-Planck Institute Earth System Model
MPIOM	Max Planck Institute Ocean Model
MSU	Microwave Sounding Unit (satellite)
NAM	Northern Annular Mode
NCEP	National Centers for Environmental Prediction
NH	Northern Hemisphere
NIWA-SOCOL	National Institue of Water and Atmospheric Research - Solar-Climate-Ozone Links
OLR	Outgoing Longwave Radiation
ODS	Ozone Depleting Substances
PVU	Potential Vorticity Unit
QBO E/W	Quasi-Biennial Oscillation Easterly/Westerly phase
RCP	Representative Concentration Pathways (greenhouse gas concentration scenarios)
REF1	Historical reference simulation in CCMVal
REF2	Future reference simulation in CCMVal
SAM	Southern Annular Mode
SH	Southern Hemisphere
SPARC	Stratosphere-troposphere Processes And their Role in Climate
SRES	Special Report on Emissions Scenarios
SST	Sea Surface Temperature
TTL	Tropical Tropopause Layer
UTC	Universal Time Coordinated
VSLS	Very Short-Lived Substances
WACCM	Whole Atmosphere Community Climate Model
WMO	World Meteorological Organization

Bibliography

Archer, C. L. and K. Caldeira, 2008: Historical trends in the jet streams. *Geophys. Res. Lett.*, **33**, doi:10.1029/2008GL033614.

Austin, J. and T. J. Reichler, 2008: Long-term evolution of the cold point tropical tropopause: Simulation results and attribution analysis. *J. Geophys. Res.*, **113**, doi:10.1029/2007JD009768.

Birner, T., 2010a: Recent widening of the tropical belt from global tropopause statistics: Sensitivities. *J. Geophys. Res.*, **115**, doi:10.1029/2010JD014664.

Birner, T., 2010b: Residual circulation and tropopause structure. *J. Atmos. Sci.*, **67**, 2582–2600, doi:10.1175/2010JAS3287.1.

Bjerknes, J. and E. Palmén, 1937: Investigations of selected European cyclones by means of serial ascents. *Geofysiske Publikasjoner*, **12**.

Bonazzola, M. and P. H. Haynes, 2004: A trajectory-based study of the tropical tropopause region. *J. Geophys. Res.*, **109**, doi:10.1029/2003JD004356.

Brewer, A. W., 1949: Evidence for a world circulation provided by the measurements of helium and water vapour distribution in the stratosphere. *Q. J. Roy. Meteor. Soc.*, **75**, 351–363, doi:10.1002/qj.49707532603.

Butchart, N., et al., 2010: Chemistry-climate model simulations of twenty-first century stratospheric climate and circulation changes. *J. Clim.*, **23**, 5349–5374, doi:10.1175/2010JCLI3404.1.

Charney, J. G. and P. G. Drazin, 1961: Propagation of planetary scale disturbances from the lower into the upper atmosphere. *J. Geophys. Res.*, **66**, 83–109.

Davis, N. A. and T. Birner, 2013: Seasonal to multidecadal variability of the width of the tropical belt. *J. Geophys. Res.*, **118**, 7773–7787, doi:10.1002/jgrd.50610.

Davis, S. M. and K. H. Rosenlof, 2012: A multidiagnostic intercomparison of tropical-width time series using reanalyses and satellite observations. *J. Clim.*, **25**, 1061–1078, doi:10.1175/JCLI-D-11-00127.1.

Deardorff, J. W., G. E. Willis, and G. H. Stockton, 1980: Laboratory studies of the entrainment zone of a convectively mixed layer. *J. Fluid. Mech.*, **100**, 41–64.

Dee, D. P., et al., 2011: The Era-Interim reanalysis: Configuration and performance of the data assimilation system. *Q. J. Roy. Meteor. Soc.*, **137**, 553–597.

Dobson, G. M. B., 1956: Origin and distribution of polyatomic molecules in the atmosphere. *Proc. R. Soc. Lond., A*, **236**, 187–193.

Dobson, G. M. B., D. N. Harrison, and J. Lawrence, 1929: Measurements of the amount of ozone in the earth's atmosphere and its reaction to other geophysical conditions, Part III. *Proc. R. Soc. Lond., A*, 456–486, doi:10.1098/rspa.1929.0034.

Folkins, I., M. Loewenstein, J. Podolske, S. Oltmans, and M. Proffitt, 1999: A barrier to vertical mixing at 14 km in the tropics: Evidence from ozonesondes and aircraft measurements. *J. Geophys. Res.*, **103**, 22 095–22 102.

Fu, Q., C. M. Johanson, J. M. Wallace, and T. Reichler, 2006: Enhanced mid-latitude tropospheric warming in satellite measurements. *Science*, **312**, 1179, doi:10.1126/science.1125566.

Fu, Q. and P. Lin, 2011: Poleward shift of subtropical jets inferred from satellite-observed lower-stratospheric temperatures. *J. Clim.*, **24**, 5597–5603, doi:10.1175/JCLI-D-11-00027.1.

Fueglistaler, S., M. Bonazzola, P. H. Haynes, and T. Peter, 2005: Stratospheric water vapor predicted from the lagrangian temperature history of air entering the stratosphere in the tropics. *J. Geophys. Res.*, **110**, doi:10.1029/2004JD005516.

Fueglistaler, S., A. E. Dessler, T. J. Dunkerton, I. Folkins, Q. Fu, and P. W. Mote, 2009: Tropical tropopause layer. *Rev. Geophys.*, **47**, doi:10.1029/2008RG000267.

Fueglistaler, S. and P. H. Haynes, 2005: Control of interannual and longer-term variability of stratospheric water vapor. *J. Geophys. Res.*, **110**, doi:10.1029/2005JD006019.

Fueglistaler, S., H. Wernli, and T. Peter, 2004: Tropical troposphere-to-stratosphere transport inferred from trajectory calculations. *J. Geophys. Res.*, **109**, doi:10.1029/2003JD004069.

Fueglistaler, S., et al., 2013: The relation between atmospheric humidity and temperature trends for stratospheric water. *J. Geophys. Res.*, **118**.

Garcia, R. R., D. R. Marsh, D. E. Kinnison, B. A. Boville, and F. Sassi, 2007: Simulation of secular trends in the middle atmosphere. *J. Geophys. Res.*, **112**, 1950–2003, doi:10.1029/2006JD007485.

Geerts, B. and E. Linacre, 1997: The height of the tropopause. http://www-das.uwyo.edu/ geerts/cwx/notes/chap01/tropo.html.

Gent, P. R., S. G. Yeager, R. B. Neale, S. Levis, and D. A. Bailey, 2009: Improvements in a half degree atmosphere/land version of the CCSM. *Clim. Dyn.*, **34**, 819–833, doi:10.1007/s00382-009-0614-8.

Gettelman, A. and T. Birner, 2007: Insights into tropical tropopause layer processes using global models. *J. Geophys. Res.*, **112**, doi:10.1029/2007JD008945.

Gettelman, A. and P. de F. Forster, 2002: A climatology of the tropical tropopause layer. *J. Meteor. Soc. Japan*, **80**, 911–924.

Gettelman, A., W. J. Randel, F. Wu, and S. T. Massie, 2002a: Transport of water vapor in the tropical tropopause layer. *Geophys. Res. Lett.*, **29**, doi:10.1029/2001GL013818.

Gettelman, A., M. L. Salby, and F. Sassi, 2002b: Distribution and influence of convection in the tropical tropopause region. *J. Geophys. Res.*, **107**, doi:10.1029/2001JD001048.

Gettelman, A., et al., 2009: The tropical tropopause layer 1960-2100. *Atmos. Chem. Phys.*, **9**, 1621–1637.

Gettelman, A., et al., 2010: Multimodel assessment of the upper troposphere and lower stratosphere: Tropics and global trends. *J. Geophys. Res.*, **115**, doi:10.1029/2009JD013638.

Gibson, T. T., 1992: An observed poleward shift of the southern hemisphere subtropical wind maximum-a greenhouse symptom? *Int. J. Climatol.*, **12**, 637–640.

Giorgetta, M., et al., 2012: Climate and carbon cycle changes from 1850 to 2100 in MPI-ESM simulations for the Coupled Model Intercomparison Project phase 5. *J. Adv. Model. Earth Syst.*, **5**, 572–597, doi:10.1002/jame.20038.

Gottwald, M., et al., 2006: *SCIAMACHY, Monitoring the Changing Earth's Atmosphere.* DLR.

Grassi, B., G. Redaelli, P. O. Canziani, and G. Visconti, 2012: Effects of the PDO phase on the tropical belt width. *J. Clim.*, **25**, 3282–3290, doi:10.1175/JCLI-D-11-00244.1.

Handon, H. H. and K. Woodberry, 1993: The diurnal cycle of tropical convection. *J. Geophys. Res.*, **98**, 16,623–16,637.

Highwood, E. J. and B. J. Hoskins, 1998: The tropical tropopause. *Q. J. Roy. Meteor. Soc.*, **124**, 1579–1604.

Holton, J. R., 1992: *An Introduction to Dynamic Meteorology.* London, 83 pp.

Holton, J. R. and A. Gettelman, 2001: Horizontal transport and the dehydration of the stratosphere. *Geophys. Res. Lett.*, **28**, 2799–2802, doi:10.1029/2001GL013148.

Holton, J. R., P. Haynes, M. E. Mcintyre, A. R. Douglass, R. B. Rood, and L. Pfister, 1995: Stratosphere-tropopsphere exchange. *Rev. Geophys.*, **33**, 403–439, doi:10.1029/95RG02097.

Hu, Y. and Q. Fu, 2007: Observed poleward expansion of the hadley circulation since 1979. *Atmos. Chem. Phys.*, **7**, 5229–5236.

Hu, Y., L. Tao, and J. Liu, 2013: Poleward expansion of the hadley circulation in CMIP5 simulations. *Adv. Atmos. Sci.*, **30**, 790–795, doi:10.1007/s00376-012-2187-4.

Hudson, R. D., 2012: Measurements of the movement of the jet streams at mid-latitudes, in the northern and southern hemispheres, 1979 to 2010. *Atmos. Chem. Phys.*, **12**, 7797–7808, doi:10.5194/acp-12-7797-2012.

Hudson, R. D., M. F. Andrade, M. B. Follette, and A. D. Frolov, 2006: The total ozone field separated into meteorological regimes - part ii: Northern hemisphere mid-latitude total ozone trends. *Atmos. Chem. Phys.*, **6**, 5183–5191.

Jackson, D. R., J. Methoven, and V. D. Pope, 2001: Transport in the low-latitude tropopause zone diagnosed using particle trajectories. *J. Atmos. Sci.*, **58**, 173–192, doi:http://dx.doi.org/10.1175/1520-0469(2001)058⟨0173:TITLLT⟩2.0.CO;2.

Johanson, C. M. and Q. Fu, 2008: Hadley cell widening: Model simulations versus observations. *B. Am. Meteorol. Soc.*, **22**, 2713–2725, doi:10.1175/2008JCLI2620.1.

Keywan, R., et al., 2011: RCP 8.5-A scenario of comparatively high greenhouse gas emissions. *Clim. Chang.*, **109**, 33–57, doi:10.1007/s10584-011-0149-y.

Kim, H. and A. E. Dessler, 2004: Observations of convective cooling in the tropical tropopause layer in airs data. *Atmos. Chem. Phys. Discuss.*, **4**, 7615–7629.

Kim, J. and S.-W. Son, 2012: Tropical cold-point tropopause: Climatology, seasonal cycle, and intraseasonal variability derived from cosmic gps radio occultation measurements. *J. Clim.*, **25**, 5343–5360, doi:10.1175/JCLI-D-11-00554.1.

Kinnison, D. E., et al., 2007: Sensitivity of chemical tracers to meteorological parameters in the MOZART-3 chemical transport model. *J. Geophys. Res.*, **112**, doi:10.1029/2006JD007879.

Konopka, P., et al., 2007: Contribution of mixing to upward transport across the tropical tropopause layer (ttl). *Atmos. Chem. Phys.*, **7**, 3285–3308.

Kremser, S., I. Wohltmann, M. Rex, U. Langematz, M. Dameris, and M. Kunze, 2009: Water vapour transport in the tropical tropopause region in coupled chemistry-climate models and ERA-40 reanalysis data. *Geophys. Res. Lett.*, **9**, 2679–2694.

Krüger, K., S. Tegtmeier, and M. Rex, 2008: Long-term climatology of air mass transport through the tropical tropopause layer (TTL) during NH winter. *Atmos. Chem. Phys.*, **8**, 813–823.

Krüger, K., S. Tegtmeier, and M. Rex, 2009: Variability of residence time in the tropical tropopause layer during northern hemisphere winter. *Atmos. Chem. Phys.*, **9**, 6717–6725.

Kuang, Z. and C. S. Bretherton, 2004: Convective influence on the heat balance of the tropical tropopause layer: A cloud-resolving model study. *J. Atmos. Sci.*, **61**, 2919–2927, doi:10.1175/JAS-3306.1.

Kumar, K. K., B. Rajagopalan, and M. A. Cane, 1999: On the weakening relationship between the indian monsoon and ENSO. *Science*, **284**, 2156–2159.

Labitzke, K. and H. V. Loon, 1998: *The Stratosphere*. Springer, 179 pp.

Li, F., J. Austin, and J. Wilson, 2008: The strength of the brewer-dobson circulation in a changing climate: Coupled chemistry-climate model simulations. *J. Clim.*, **21**, 40–57, doi:10.1175/2007JCLI1663.1.

Li, F., R. S. Stolarski, S. Pawson, P. A. Newman, and D. Waugh, 2010: Narrowing of the upwelling branch of the brewer-dobson circulation and hadley cell in chemistry-climate model simulations of the 21st century. *Geophys. Res. Lett.*, **37**, doi:10.1029/2010GL043718.

Lu, J., C. Deser, and T. Reichler, 2009: Cause of the widening of the tropical belt since 1958. *Geophys. Res. Lett.*, **36**, doi:10.1029/2008GL036076.

Lu, J., G. A. Vecchi, and T. Reichler, 2007: Expansion of the hadley cell under global warming. *Geophys. Res. Lett.*, **34**, doi:10.1029/2006GL028443.

Malberg, H., 1997: *Meteorologie und Klimatologie*. Springer, 20-21 pp.

McIntyre, M. E. and T. N. Palmer, 1983: Breaking planetary waves in the stratosphere. *Nature*, **305**, 593–600, doi:10.1038/305593a0.

Mehta, S. K., B. V. K. Murthy, D. N. Rao, M. V. Ratnam, K. Parameswaran, K. Rajeev, C. S. Raju, and K. G. Rao, 2008: Identification of tropical convective tropopause and its association with cold point tropopause. *J. Geophys. Res.*, **113**, doi:10.1029/2007JD009625.

Mehta, S. K., M. V. Ratnam, and B. V. K. Murthy, 2011: Multiple tropopauses in the tropics: A cold point approach. *J. Geophys. Res.*, **116**, doi:10.1029/2011JD016637.

Min, S.-K. and S.-W. Son, 2013: Multimodel attribution of the southern hemisphere hadley cell widening: Major role of ozone depletion. *J. Geophys. Res.*, **118**, 3007–3015, doi:10.1002/jgrd.50232.

Monge-Sanz, B., M. Chipperfield, D. Dee, A. Simmons, and S. Uppala, 2012: Improvements in the stratospheric transport achieved by a chemistry transport model with ECMWF (re)analyses: identifying effects and remaining challenges. *Q. J. Roy. Meteor. Soc.*, **34**, doi:10.1002/qj.1996.

Pittock, A. B., 1988: *Actual and anticipated changes in Australia's climate*. 35-51 pp.

Ploeger, F., P. Konopka, G. Günther, J.-U. Grooss, and R. Müller, 2010: Impact of the vertical velocity scheme on modeling transport in the tropical tropopause layer. *J. Geophys. Res.*, **115**, doi:10.1029/2009JD012023.

Plumb, R. A., 1996: A tropical pipe model of stratospheric transport. *J. Geophys. Res.*, **101**, 3957–3972.

Randel, W. J., 2010: *Variability and Trends in Stratospheric Temperature and Water Vapor*, Vol. 190. The Stratosphere: Dynamics, Transport and Chemistry, Geophys. Monogr. Ser., 123-135 pp., doi:10.1029/2009GM000870.

Randel, W. J. and E. J. Jensen, 2013: Physical processes in the tropical tropopause layer and their roles in a changing climate. *Nat. Geosc.*, **6**.

Randel, W. J., F. Wu, and D. J. Gaffen, 2000: Interannual variability of the tropical tropopause derived from radiosonde data and ncep reanalyses. *J. Geophys. Res.*, **105**, 15 509–15 523, doi:10.1029/2000JD900155.

Randel, W. J., F. Wu, S. J. Oltmans, K. Rosenlof, and G. E. Nedoluha, 2004: Interannual changes of stratospheric water vapor and correlations with tropical tropopause temperatures. *B. Am. Meteorol. Soc.*, **61**, 2133–2148.

Randel, W. J., F. Wu, and W. R. Ríos, 2003: Thermal variability of the tropical tropopause region derived from gps/met observations. *J. Geophys. Res.*, **108**, doi:10.1029/2002JD002595.

Randel, W. J., F. Wu, H. Vömel, G. E. Nedoluha, and P. Forster, 2006: Decreases in stratospheric water vapor after 2001: Links to changes in the tropical tropopause and the brewer-dobson circulation. *J. Geophys. Res.*, **111**, doi:10.1029/2005JD006744.

Randel, W. J., et al., 2009: An update of observed stratospheric temperature trends. *J. Geophys. Res.*, **114**, doi:10.1029/2008JD010421.

Reichler, T., 2009: *Climate Change: Observed impacts on Planet Earth*. Elsevier, 145-164 pp.

Reithmeier, C. and R. Sausen, 2002: Seasonal to multidecadal variability of the width of the tropical belt. *Tellus B.*, **54**, 278–299.

Rosenlof, K. H., 2002: Transport changes inferred from haloe water and methane measurements. *J. Meteor. Soc. Japan*, **80**, 831–848, doi:10.1175/JCLI-D-11-00127.1.

Rosenlof, K. H. and G. C. Reid, 2008: Trends in the temperature and water vapor content of the tropical lower stratosphere: Sea surface connection. *J. Geophys. Res.*, **113**, doi:10.1029/2007JD009109.

Salawitch, R. J., D. K. Weisenstein, L. J. Kovalenko, C. E. Sioris, P. O. Wennberg, K. Chance, M. K. W. Ko, and C. A. McLinden, 2005: Sensitivity of ozone to bromine in the lower stratosphere. *Geophys. Res. Lett.*, **32**, doi:10.1029/2004GL021504.

Santer, B. D., et al., 2003: Behavior of tropopause height and atmospheric temperature in models, reanalyses, and observations: Decadal changes. *J. Geophys. Res.*, **108**, doi:10.1029/2002JD002258.

Schoeberl, M. R., A. R. Douglass, Z. Zhu, and S. Pawson, 2003: A comparison of the lower stratospheric age spectra derived from a general circulation model and two data assimilation systems. *J. Geophys. Res.*, **108**, doi:10.1029/2002JD002652.

Schraner, M., et al., 2008: Technical note: Chemistry-climate model SOCOL: version 2.0 with improved transport and chemistry/microphysics schemes. *Atmos. Chem. Phys.*, **8**, 5957–5974, doi:10.5194/acp-8-5957-2008.

Scinocca, J. F., N. A. McFarlane, J. L. M. Lazare, and D. Plummer, 2008: Technical note: The CCCMA third generation AGCM and its extension into the middle atmosphere. *Atmos. Chem. Phys.*, **8**, 7055–7074.

Seidel, D. J., Q. Fu, W. J. Randel, and T. J. Reichler, 2008: Widening of the tropical belt in a changing climate. *Nat. Geosc.*

Seidel, D. J. and W. J. Randel, 2007: Recent widening of the tropical belt: Evidence from tropopause observations. *J. Geophys. Res.*, **112**, doi:10.1029/2007JD008861.

Seidel, D. J., R. J. Ross, and J. K. Angell, 2001: Climatological characteristics of the tropical tropopause as revealed by radiosondes. *J. Geophys. Res.*, **106**, 7857–7878.

Selkirk, H. B., 1993: The tropopause cold trap in the australian monsoon during STEP/AMEX 1987. **98**, 8591–8610.

Sherwood, S. and A. E. Dessler, 2001: A model for transport across the tropical tropopause. *J. Atmos. Sci.*, **58**, 765–779.

Solomon, S., K. H. Rosenlof, R. W. Portmann, J. S. Daniel, S. M. Davis, T. J. Sanford, and G.-K. Plattner, 2010: Contributions of stratospheric water vapor to decadal changes in the rate of global warming. *Science*, **327**, 1219–1223, doi:10.1126/science.1182488.

Son, S.-W., N. F. Tandon, L. M. Polvani, and D. W. Waugh, 2009: Ozone hole and southern hemisphere climate change. *Geophys. Res. Lett.*, **36**, 1486–1489, doi:10.1029/2009GL038671.

SPARC, 2010: Report on the Evaluation of Chemistry-Climate Models SPARC Report No. 5. WCRP-132 WMO/TD-No. 1526.

Steil, B., M. Dameris, C. Brühl, P. J. Crutzen, V. Grewe, M. Ponater, and R. Sausen, 2002: Development of a chemistry module for GCMs: first results of a multiannual integration. *Ann. Geophys.*, **16**, 205–228.

Stenke, A., M. Dameris, V. Grewe, and H. Garny, 2009: Implications of lagrangian transport for coupled chemistry-climate simulations. *Atmos. Chem. Phys.*, **9**, 5489–5504.

Taylor, K. E., R. J. Stouffer, and G. A. Meehl, 2012: An Overview of CMIP5 and the Experiment Design. *B. Am. Meteorol. Soc.*, **93**, 482–498, doi:10.1175/BAMS-D-11-00094.1.

Tegtmeier, S., 2006: Variationen der stratosphärischen residualzirkulation und ihr einfluss auf die ozonverteilung. Ph.D. thesis, University Potsdam, 37 pp.

Thuburn, J. and G. C. Craig, 2002: On the temperature structure of the tropical substratosphere. *J. Geophys. Res.*, **107**, doi:10.1029/2001JD000448.

Tompkins, A. M., K. Gierens, and G. Rädel, 2007: Ice supersaturation in the ecmwf integrated forecast system. *Q. J. Roy. Meteor. Soc.*, **133**, 53–63, doi:10.1002/qj.14.

Uppala, S., D. Dee, S. Kobayashi, P. Berrisford, and A. Simmons, 2008: Towards a climate data assimilation system: Status update of ERA-Interim. *ECMWF Newsletter*, **115**.

van Vuuren, D. P., et al., 2011: The representative concentration pathways: An overview. *Clim. Chang.*, **109**, 5–31, doi:10.1007/s10584-011-0148-z.

Wang, J. S., D. J. Seidel, and M. Free, 2012: How well do we know recent climate trends at the tropical tropopause? *J. Geophys. Res.*, **117**, doi:10.1029/2012JD017444.

WMO, 1957: WMO Meteorology-A three dimensional science: Second session of the commission for aerology Report No. 4. 134-138 pp.

WMO, 2003: WMO Scientific Assessment of Ozone Depletion: 2002, Global Ozone Research and Monitoring Project Report No. 47 Geneva. 498 pp.

WMO, 2007: WMO Scientific Assessment of Ozone Depletion: 2006, Global Ozone Research and Monitoring Project Report No. 50. 572 pp.

Wohltmann, I. and M. Rex, 2008: Improvement of vertical and residual velocities in pressure or hybrid sigma-pressure coordinates in analysis data in the stratosphere. *Atmos. Chem. Phys.*, **8**, 265–272.

Yang, G.-Y. and J. Slingo, 2001: The diurnal cycle in the tropics. *Mon. Wea. Rev.*, **129**, 784–801, doi:10.1175/1520-0493(2001)129⟨0784:TDCITT⟩2.0.CO;2.

Yin, J. H., 2005: A consistent poleward shift of the storm tracks in simulations of 21st century climate. *Geophys. Res. Lett.*, **32**, doi:10.1029/2005GL023684.

Young, P. J., A. H. Butler, N. Calvo, L. Haimberger, P. J. Kushner, D. R. Marsh, W. J. Randel, and K. H. Rosenlof, 2013: Agreement in late twentieth century southern hemisphere stratospheric temperature trends in observations and CCMVal-2, CMIP3, and CMIP5 models. *J. Geophys. Res.*, **118**, 605–613, doi:10.1002/jgrd.50126.

Zahn, A., C. A. M. Brenninkmeijer, and P. F. J. van Velthoven, 2004: Passenger aircraft project CARIBIC 1997-2002, Part I: the extratropical chemical tropopause. *Atmos. Chem. Phys. Discuss.*, **4**, 1091–1117.

Zhou, X.-L., M. A. Geller, and M. Zhang, 2001: Cooling trend of the tropical cold point tropopause temperatures and its implications. *J. Geophys. Res.*, **106**, 1511–1522.

Acknowledgements

First I would like to thank PD Dr. Kirstin Krüger, who offered me the possibility to work at the GEOMAR Helmholtz-Zentrum für Ozeanforschung Kiel and supported me completing this thesis. Many thanks also to Susann Tegtmeier for helping to find solutions of computer problems and scientific questions. I would also like to thank Markus Rex, Thomas Birner and Robyn Schofield for offering ideas how to apply analysis methods. Further thanks go to Dan Smale, Michael Neish, Hella Garny, and Andrew Gettelmann providing model data and answering questions about the special model characteristics. Finally, I would like to thank everybody who accompanied me in the last few years not only at the important lunch breaks but also in social and private environment beyond the walls of GEOMAR.

Diese Arbeit wurde mit der Textverarbeitung LaTeX angefertigt.

Statement/Erklärung

Herewith I confirm that I wrote the present thesis independently and nothing else then the given references were applied.
I assure that this work to the obtainment of the degree of doctor has not been submitted anywhere else before.
I explain that the present work was prepared according to the principles for the protection of good scientific practise of the German Research Society.

Hiermit bestätige ich, dass ich die vorliegende Dissertation selbständig verfasst und keine anderen als die angegebenen Quellen und Hilfsmittel verwendet habe.
Ich versichere, dass diese Arbeit zur Erlangung des Doktorgrades noch nicht an anderer Stelle eingereicht worden ist.
Ich erkläre, dass die vorliegende Arbeit entsprechend der Grundsätze zur Sicherung guter wissenschaftlicher Praxis der Deutschen Forschungsgemeinschaft erstellt wurde.

Kiel, September 2013

(Viktoria Mohr)